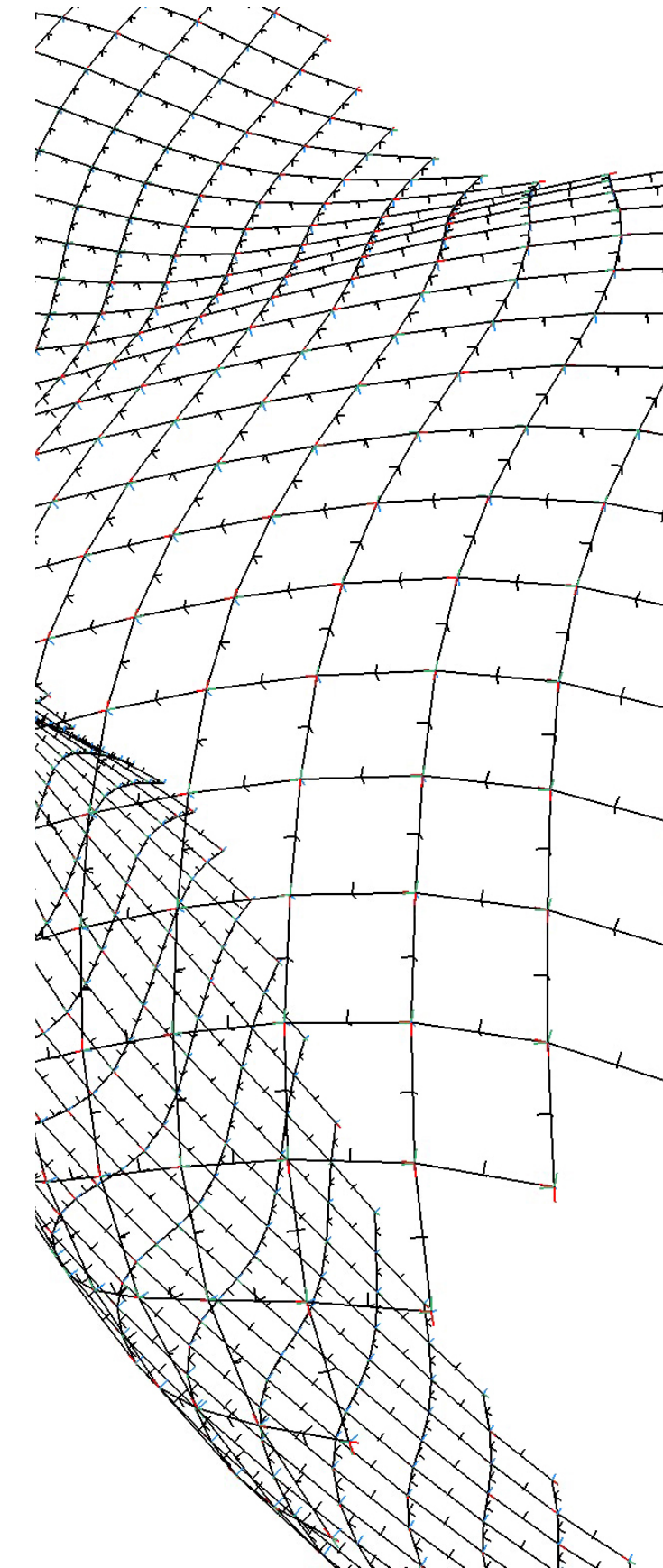
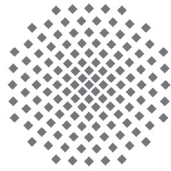


Jian-Min Li

## Timber Shell Structures

Form-finding and Structural Analysis  
of Actively Bent Grid Shells and  
Segmental Plate Shells.





Forschungsberichte

itke

aus dem Institut für Tragkonstruktionen  
und Konstruktives Entwerfen,  
Universität Stuttgart

Herausgeber:  
Professor Dr.-Ing. Jan Knippers

Institut für Tragkonstruktionen und Konstruktives Entwerfen:  
Forschungsbericht 42

**Jian-Min Li:**

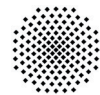
Timber Shell Structures. Form-finding and Structural Analysis  
of Actively Bent Grid Shells and Segmental Plate Shells.

Stuttgart, Juni 2017

ISBN 978-3-922302-42-1

D 93

© Institut für Tragkonstruktionen  
und Konstruktives Entwerfen  
Universität Stuttgart  
Keplerstraße 11  
D-70174 Stuttgart



Alle Rechte, insbesondere der Übersetzung, bleiben vorbehalten.  
Vervielfältigung jeglicher Art, auch auszugsweise, ist nicht gestattet.

# Timber Shell Structures

Form-finding and structural analysis of actively bent grid shells  
and segmental plate shells

Von der Fakultät Architektur und Stadtplanung der Universität Stuttgart  
zur Erlangung der Würde eines Doktor-Ingenieurs (Dr.-Ing.)  
genehmigte Abhandlung

Vorgelegt von  
**Jian-Min Li**  
aus Taipeh

Hauptberichter: Prof. Dr.-Ing. Jan Knippers

Mitberichter: Prof. Dr. Chris Williams

Tag der mündlichen Prüfung 23. Januar 2017  
Institut für Tragkonstruktionen und Konstruktives Entwerfen der  
Universität Stuttgart, 2017



## Abstract

Shell structures are structurally efficient but difficult to manufacture and thus expensive. Actively bent grid shells and segmental plate shells could be alternatives. The first kind utilizes bended members to form a continuously curved geometry and thus reduce the complexity of the joints. The second kind utilizes the stability inherited in trivalent geometries to be able to build a shell without using bending stiff joints. Both these two types of timber shell structures could largely reduce the construction cost. That is why they are chosen as the research topics.

The dynamic relaxation method (DR) is applied in this research as an important numerical method. It is used as the fundamental base for developing the form-finding tools of both actively bent grid shells and the segmental grid shells. A solver capable of the structural analysis of beam system is also developed here based on DR. Through the text, we show that DR could handle not only form-finding problems but also geometrically nonlinear analysis.

The dissertation consists of four parts. Part I is the introduction. Part II and Part III present both the form-finding and analysis techniques of these two types of timber shell structures. The last part is the conclusions.



## Acknowledgement

I would like to express my deep gratitude to my supervisor, Prof. Dr.-Ing. Jan Knippers. Because of his warm welcome and support, I could start one of the most important journey of my life. His instructions are always critical and inspiring. His smile, sense of humor and wise answers always give me strength.

I am also very grateful to Prof. Dr. Chris Williams, my co-advisor, for sharing his experience and knowledge. Discussing with him is like an adventure to me. Our meetings in Bath generated great influences in the development of this thesis.

To my colleague Petra Heim I want to thank for helping me to build my life in Stuttgart. I am very grateful to the precious friendship and the collegueship that I obtain from each member of ITKE. It nourishes me and makes me feel always at home in this big family.

For scholarship and funding I would like express my appreciation to DAAD and ForstBW.

To my dear parents and grandma in Taiwan I want to thank for their life-long supports and encouragement and for giving me such a wonderful childhood which is the very source of my character and strength. I also want to thank my dear sister and brother for providing me supports.

I want to thank my dear children Ruo-Yu and Jhih-Ran for giving me so much wonderful experiences. Without them, I might not know that life could be of so much bitterness and sweetness. They bring me not only pleasures but help me to know myself better.

At last, I want to thank my dear wife Sui and my parents-in-law for taking care of our children when I was not by her side. She is not only the initiator and the partner of this journey. She is my dearest friend and the best supervisor of my life.





## Table of Contents

PART I INTRODUCTION .....	13
Chapter 1 .....	14
1.1 The study of Timber Shell Structures.....	19
1.2 Structure of the Thesis.....	22
PART II ACTIVELY BENT GRIDSHELL.....	25
Chapter 2 .....	26
2.1 The study of actively bent grid shells.....	29
2.2 Mergence of form-finding and structural analysis .....	33
2.3 Contributions.....	34
2.4 Structure of Part II.....	36
Chapter 3 .....	37
3.1 Representation of an elastic grid system .....	37
3.2 Representation of motion .....	47
Chapter 4 .....	49
4.1. Introduction .....	49
4.2 Related work .....	50
4.3 Rotation formulations for DR.....	51
4.4 Co-rotation of beam-ends.....	56
4.5 Residuals of nodes.....	56
4.6 Optimized mass and inertia .....	57
4.7 Time interval independent.....	62
4.8 Kinetic damping .....	62
4.9 Algorithm .....	63
4.10 Numerical test cases .....	63
Chapter 5 .....	79
5.1 Introduction .....	79
5.2 Observation of convergence rate and stability .....	79
5.3 Influence of division.....	82
5.4 Method to speed up the convergence rate .....	82

5.5 Computation procedure .....	86
5.6 Test cases -- Comparison between DR and FEDR.....	88
Chapter 6 .....	91
6.1 Introduction .....	91
6.2 Related work .....	91
6.3 Assigning pre-stress .....	92
6.4 Node coupling .....	96
6.5 Test cases.....	99
Chapter 7 .....	106
7.1 Introduction .....	106
7.2 Projection method.....	106
7.3 Force method.....	124
7.4 Bending as a dominant factor in form-finding .....	128
PART III SEGMENTAL TIMBER PLATE SHELL.....	135
Chapter 8 .....	136
8.1 The study of Segmental Timber Plate Shells .....	136
8.2 Contributions.....	138
8.3 Structure of Part III.....	138
Chapter 9 .....	140
9.1 Trivalent polyhedron .....	140
9.2 Stability inherent from trivalent geometries.....	140
9.3 Patterns and Force Transfer.....	146
Chapter 10 .....	148
10.1 Introduction .....	148
10.2 Initial triangulation.....	149
10.3 Planarization.....	154
Chapter 11 .....	155
11.1 In-plane shear resistance .....	156
11.2 Axial force and out-of-plane shear resistance .....	158
11.3 Influence of screw orientation in plywood.....	161
11.4 Function of gaps .....	163

11.5 Bending stiffness in the joint.....	163
11.6 Minima distances and spacing of screws.....	164
Chapter 12 .....	166
12.1 FE-model .....	166
12.2 Failure criteria of a connection.....	168
12.3 Stress and failure criteria of plywood.....	170
12.4 Structural performance .....	174
Chapter 13 .....	177
13.1 Geometric compatibility for installation .....	177
13.2 Erection Process .....	177
PART IV CONCLUSION.....	181
Chapter 14 .....	182
14.1 Conclusion of Part II .....	182
14.2 Conclusion of Part III .....	184
14.3 Future work .....	185
Bibliography.....	188
List of Abbreviations.....	195
List of Notations.....	196
Curriculum Vitae.....	199



# PART I INTRODUCTION

## Chapter 1

### INTRODUCTION

#### Timber, a smart material

Human have been searching for an ideal building material and timber is a material designed by nature which fits many requirements very well. The highest tree in record is more than 100 m high. The tree foot must be able to take large forces resulted from gravity and wind. Due to severely survival

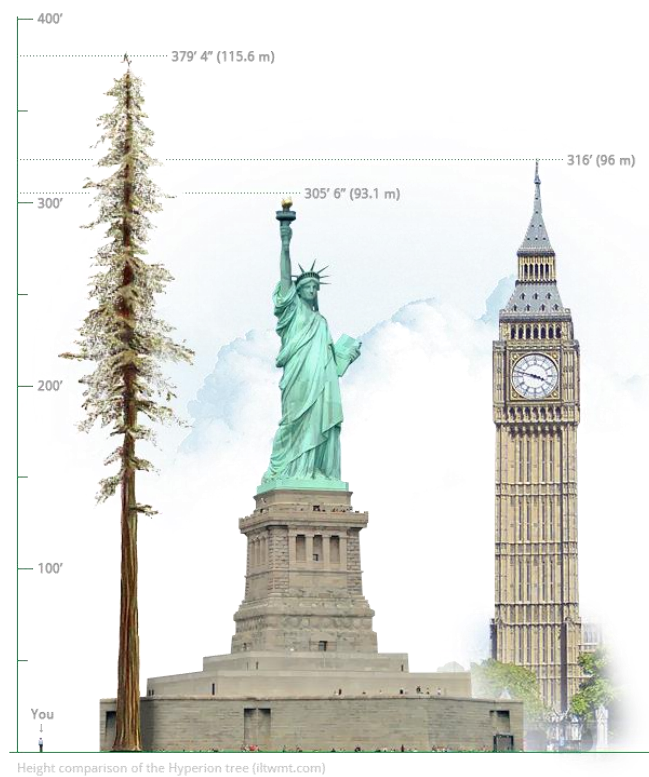


Figure 1.1: Hyperion, the tallest tree in the world and the comparison of the other famous buildings. (<http://iliketowastemytime.com/2012/10/01/oldest-tallest-and-biggest-trees-in-world>)



Figure 1.2: Spruce Goose, the largest air plane in history, has a wingspan of 97.5m and is entirely made of wood.

(<http://www.mission4today.com/index.php?name=ForumsPro&file=viewtopic&p=129981>)

competitions, trees have been developed to place their material in an efficient way such that they could remain strong and grow faster while consuming as less energy from the environment as possible (Figure 1.1).

On a micro level, the numerous cavities created by timber cell walls make wood a porous structure and thus optimize the tree section. They help to generate a larger section with the same amount of materials, which is more efficient to resist bending and buckling. Besides, timber is strong in the fiber direction and it can thus resist axial loads and bending moments efficiently. The relative weakness in the transverse direction gives timber an ideal machinability. Resin, the matrix of timber, also makes timber adhesive to each other while the original stiffness and strength are kept. These good machinability and adhesiveness enable users to generate various timber elements with different sections and geometries in a cost efficient way. Therefore, timber itself is not only a sustainable construction material, but also a smartly designed fiber reinforced composite material which is strong, light-weight and easy to process.

Even now, the largest aircraft in human history is still made of timber. It is Spruce Goose, a transport airplane built in the end of World War II, of a wingspan of 97.5m (Figure 1.2). This aircraft shows





Figure 1.3: The brine bath in Bad Dür rheim is a good example for showing the efficiency and the geometric variety of timber shell structures. (Kur- und Bäder GmbH Bad Dür rheim, <http://www.db-bauzeitung.de/150-jahre-db/in-die-jahre-gekommen-zum-db-jubilaem/#slider-intro-2>)

the tremendous advantages of timber. They are demonstrated by its strength, lightweight, machinability and adhesiveness. The principles and techniques of using timber-like materials to build structures continue to develop today. Artificial fiber reinforced materials such as glass fiber reinforced polymer (GFRP) or carbon fiber reinforced polymer (CFRP) are available today. The principles used in timber structure design can thus be applied in the design of artificial fiber reinforced composite structures and vice versa. This coherence connects the research of timber shells to a larger and more important research field of composite material structures.

#### Timber Shells, using smart material smartly

When building a structure, using materials smartly would be as important as using smart materials (Figure 1.3). For building a structure of a large span or cantilever, the most efficient way is to use shell behaviors. Due to the curved shell geometry, the out-of-plane load could be redirected and transferred into membrane forces. The maxima bending moment in the structure could then be largely



Figure 1.4: Double-curved laminated timbers are produced through steps. First, small linear profiles are laminated together with a nearly correct geometry. Second, the surfaces will be milled out to attain the exact geometry. (<http://resilientwood.tumblr.com/post/129299243257/centre-pompidou-metz>)

reduced. Because the internal forces in shells are mainly in the form of membrane forces, the most critical issues of member design would be about how to resist axial forces and local buckling. An ideal member in such case would be strengthened in the local axial direction, such as a timber member.

Since timber is easier to cut, bend and glue, there are diverse types of timber shell structures designed and built in accord with different design intents. Therefore, when it comes to building prototype structures, whose principles are newly invented or discovered such as in the bio-mimic studies, timber is often chosen as the ideal building material. A lot of experimental shell projects in this kind are built recently. Their common aim is to find innovative ways to build shell structures and smart ways to use materials.

Allowing using robot arms in pre-fabricating all structure elements of shell structures is another advantages of timber shell structures (Figure 1.4). Through the process of cutting, milling, and drilling, a curved linear element of changing sections or a plate element with a changing thickness and various

boundary geometries could be able to be fabricated with no difficulty while its high precision is attained. This promotes the trend of adopting timber shells as the main structures of freeform architectures.

### Challenges

There are many advantages of timber shells, but why are timber shells of large scales rare than those made of stones and steels? And why could they only be realized after the beginning of 20th century [1]? Looking into the challenges and difficulties may help us to answer these questions and they are deliberated in the three aspects as follows:

First is the challenge in connection design. As an orthogonal material, the strength of timber perpendicular to the fiber direction is much less than that parallel to fibers. This directly results in the difficulty of connection design. For example, around a pin hole the stress flow would be redirected such that the major direction of stresses is no more parallel to the fiber direction and it causes depressions or splits around the pin hole. The advantage of being an orthogonal material suddenly becomes a disadvantage (Figure 1.5) [2] [3].

Second is the challenge in structural analysis. The easiness of processing of timber brings many construction possibilities. However unconventional structures bring the challenge of structural analysis along. The analysis challenges may reflect in the joint simulation, the pre-stresses simulation and the multi-layered structure simulation [4] [5] [6] [7] [8].

Third is the challenge in form-finding. Because, for timber shells, it is more difficult to have bending stiff joints than other shell structures, timber shells rely more on their geometry, instead of on their joints, to gain the global and the local stabilities. Therefore, it requires more considerations when designing the geometry of a timber shell. Normally, each timber shell type has its corresponding form-finding strategy [9] [10].

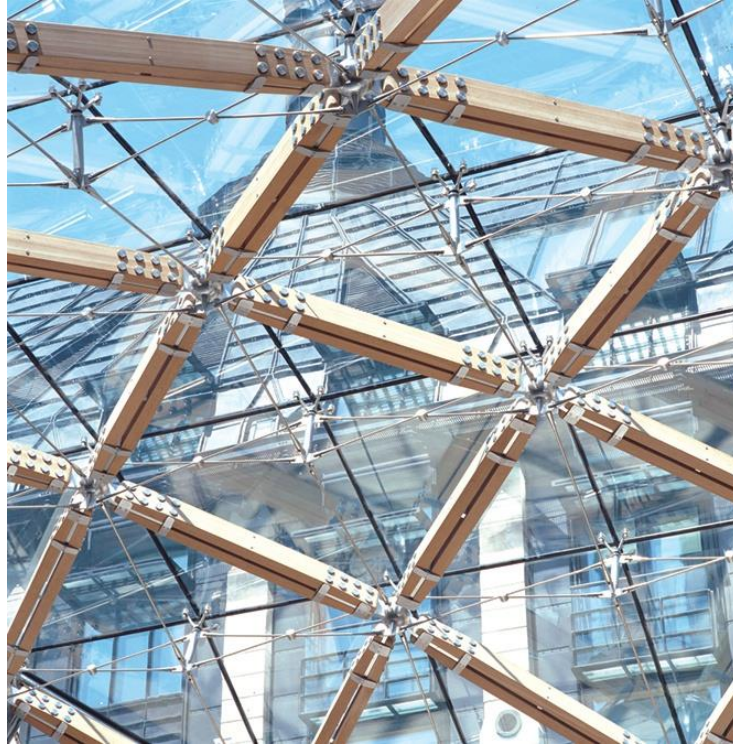


Figure 1.5: Portcullis House, London. Because the stress flow would be redirected around pin holes of a timber connection, the advantage of being an orthogonal material suddenly becomes a disadvantage. (<http://www.hopkins.co.uk/projects/5/100/>)

### 1.1 The study of Timber Shell Structures

Adhesive and joints have great influence to the evolution and the development of timber shells. Unlike shells made of stones, timber is light-weight and its self-weight is not much helpful to stabilize the structure [11]. Therefore, it is more challenging to design a connection in timber shells because the internal forces of a member in timber shells could not be always compressions. Tensions and bending moments occur once the uneven load such as those from wind or snow dominates. This might be the answer why the appearance of a stone shell of a large scale is much earlier than that of a large timber shell in human history.

A series of prototypes of timber shells emerged as the roof structures in the end of 18<sup>th</sup> centuries. Unlike the most common truss structures at that time, these roof structures mostly in the forms of domes or barrels were single layered [12]. Timbers were overlapped and connected by dowels or pre-cut into thin and long pieces and then bolted together (Figure 1.6). Or they were arranged in a

reciprocal way in a plane (Figure 1.7). All these methods enable a single layer timber structure to adopt a curved geometry and to extend the natural length limit of a timber.

These mechanical joined timbers were gradually replaced by laminated timbers with the improvement of the adhesives technology in the early 19<sup>th</sup> centuries [12]. With the popularity of improved glues, nails and screws, the timber construction technique gained large progress. The realization of the aircraft, Spruce Goose, built in 1947 is a well-known benchmark of timber shell technologies [13] [14].

A trend of exploring and re-discovering shell constructions started in 1960s [15]. Many new prototypes of timber shells were proposed and built at that time such as St.-Albert-Magnus-Kirche in Leverkusen (1967), Gardenschau Pavillion in Dortmund (1969), Expo Multihalle in Mannheim (1975) [1]. Form-finding techniques were again stressed and further developed in the project of Expo Multihalle. Unlike the form-finding works done by Gaudi with physical models only, the newly achievement of form-finding would be only possible with the help of computation techniques [16] [15].

In 1986, the largest span of timber shells reaches 160 m [17]. On the other hand, with the facilitation of computer aided design (CAD), some of the renown projects such as Solebad in Duerrheim (1987) and Toskana-Therme in Bad Sulza (1999) challenged complicated free-form geometries and dealt with thousands of custom-made members that each has a differently curved geometry and joint setting [12].

In the last decade, robot arms have been gradually integrated in the prefabrication process of complicated members of free-form timber shells. Without having this automatic production technique, some projects would not be possible or very difficult to realize due to the highly geometric complexity and the severe precision requirement. The highly precise processing of robot arms has made some joints such as finger joints, which were only possible in carpentry, now also realizable in timber shells [18]. The improvement of form-finding and structural simulation technologies push this trend further. Pioneer projects, such as ICD/ITKE Research Pavilions in Stuttgart (2010, 2011, 2016), Country Club in Yeosu (2010), Centre Pompidou in Metz (2010), Element House in Zurich (2014), Dieter-Paul Pavillon/Forstpavillion (2014), have shown that how rich the variety timber shell structures could bring.

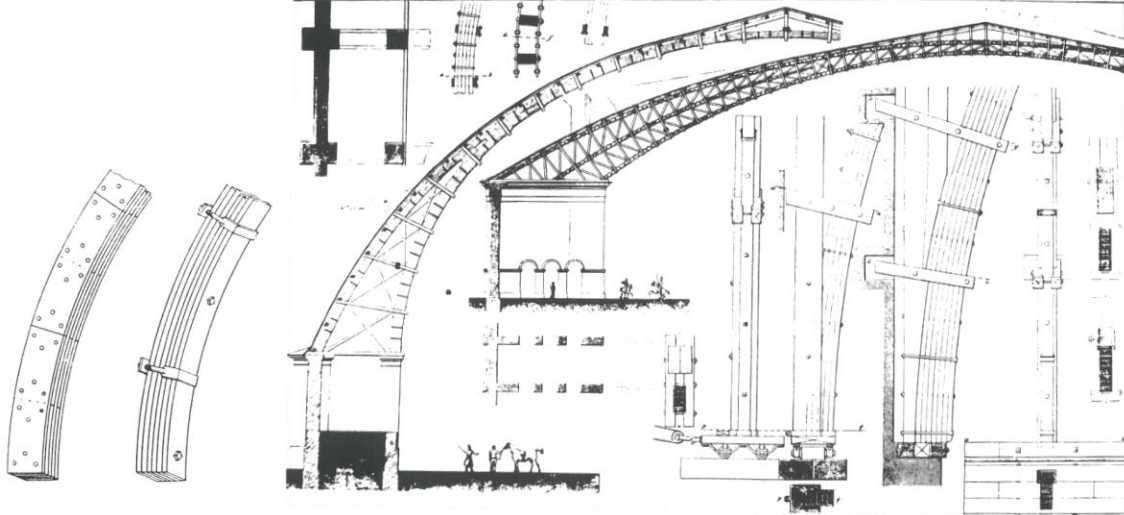


Figure 1.6: A timber construction type invented in the end of 18<sup>th</sup> centuries. Timbers were overlapped and connected by dowels or precut into thin and long pieces and then bolted together. (Müller, 2000)

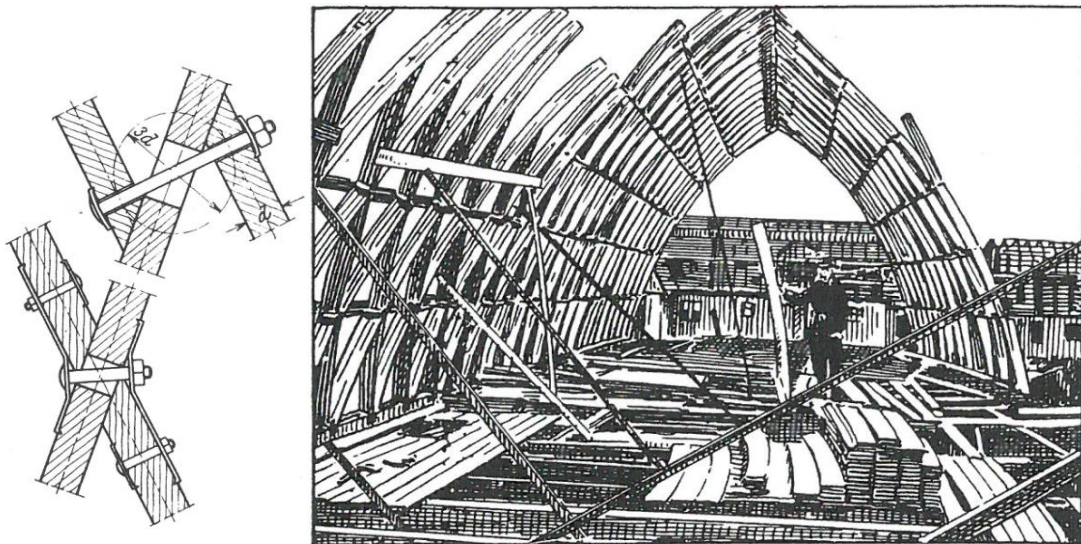


Figure 1.7 Timber were arranged in a reciprocal way into form a curved and single-layered roof. (Müller, 2000)

Since 2010, the team of University Stuttgart, consisting of the Institute of Building Structures and Structural Design (ITKE, Prof. Jan Knippers), the Institute of Computational Design (ICD, Prof.

Achim Menges) has undertaken a series of pavilion projects aimed at exploring the newest design theories and production technologies. Many of them are realized in timber shells. These projects focus on integrating biological principles into structural and architectural design and have attracted the attention of architects, engineers, and biologists. The new discoveries in bending-active principles, segmental composition methods, doubly layered porous structures and innovative connection designs are thus far the mainly highlighted contributions of this research program [5] [19] [8] [20]. In the same time, the team in Lausanne, Laboratory for Timber Constructions (IBOIS, Prof. Yves) also initiated several projects, which focus on folded plate structures, innovative timber connections and applications of bending-active principles in timber shells.

## **1.2 Structure of the Thesis**

Shell structures are structurally efficient but difficult to manufacture and thus expensive. Actively bent grid shells and segmental plate shells could be alternatives. The first kind utilizes bended members which are initially straight to form a continuously curved geometry and thus reduce the complexity of the joints. The second kind utilizes the stability inherited in trivalent geometries to build a shell structure composed of segmented panels without using bending stiff joints. Both these two types of timber shell structures could largely reduce the construction cost. That is why they are chosen as the research topics in this dissertation.

The dynamic relaxation method (DR) is applied in this research as an important numerical method. It is used as the fundamental base for developing the form-finding tools of both actively bent grid shells and the segmental grid shells. A solver capable of the structural analysis of beam system is also developed here based on DR. Through the text, we show that DR could handle not only highly geometrically nonlinear form-finding problems but also geometrically nonlinear analysis.

The dissertation consists of four parts. Part I is the introduction. Part II is about actively bent grid shells. Part III is about segmental plate shells. And the forth part is the conclusion. Some materials in this dissertation have been published in conferences or journals and are now reorganized in a way to better fit the dissertation structure and to show the coherence of the methodologies of the two kinds of timber shells.

Part II and Part III present both the form-finding and analysis techniques of these two types of timber shell structures. Since their strategies toward the structural solution are different, the developed methods are also different. For elastic grid shells, because the pre-stresses due to forming, both in the form-finding and structural analysis stages, is an important issue, an integral method is thus developed in this research such that both stages could be handles in one method, the dynamic relaxation method with six degrees of freedoms (DOF) per node. Part II illustrates the derivation of this 6DOF DR method and the further explorations of actively bent grid shells.

For plate segmental shells, the form-finding of trivalent polyhedrons and the structural analysis of specialized plate connection are of significance. Therefore, a from-finding method based on 3DOF DR has been developed in this research, and a custom-made program, using spring elements of a finite element method (FEM) software to simulate connections, is also developed here to do the pre-processing and post-processing of the structural analysis resulted from the FEM software. Both this form-finding technique and the structural analysis are shown in Part III. Since for plate shells the connection design has been a challenging task, an innovative connection design is also presented in Part III.

The last part is the conclusions, which digests the most important findings of this research work and points out several interesting directions for further works.





PART II ACTIVELY BENT  
GRIDSHELL

## Chapter 2

### INTRODUCTION

Using elastic and bendable strips to create daily objects had been an indispensable skill in pre-industrial times. By repeating weaving simple patterns, craftsmen could create various objects with double curved surfaces (Figure 2.1). These objects can fulfill simultaneously two ultimate tasks: to stay stable in shape as well as to take loads many times of the self-weight. An interesting phenomenon is observed here: A structure composed of strips in their highly bended states could form a stable and strong structure; the structure generates the shell behavior which is much stronger than the residuals arising from bending. The phenomenon and the principles observed here are applicable on a larger scale, such as spatial structures. A specific type of building structures thus emerges. They are actively bent grid shells.



Figure 2.1: Fish trap made of bamboo strips (71.1951.3.67 © musée du quai Branly / P. Gries, <http://masterpieces.asemus.museum/stories/view.nhn?id=165>)

Actively bent grid shells that are composed of slender, continuous and initially straight members going across each other at revolute joints have the advantages to generate curved spaces with uniform components. Unlike fabrics, when elastic grids adapt the shapes of double curved surfaces, there is no wrinkle generated (Figure 2.2). This is because elastic grids are free of the in-plane shear rigidity and thus are able to change the developed area and the included angles in each quad. This property makes elastic grids adaptive to both local and global changes in geometry and makes them as an ideal structure for free-form architectures.

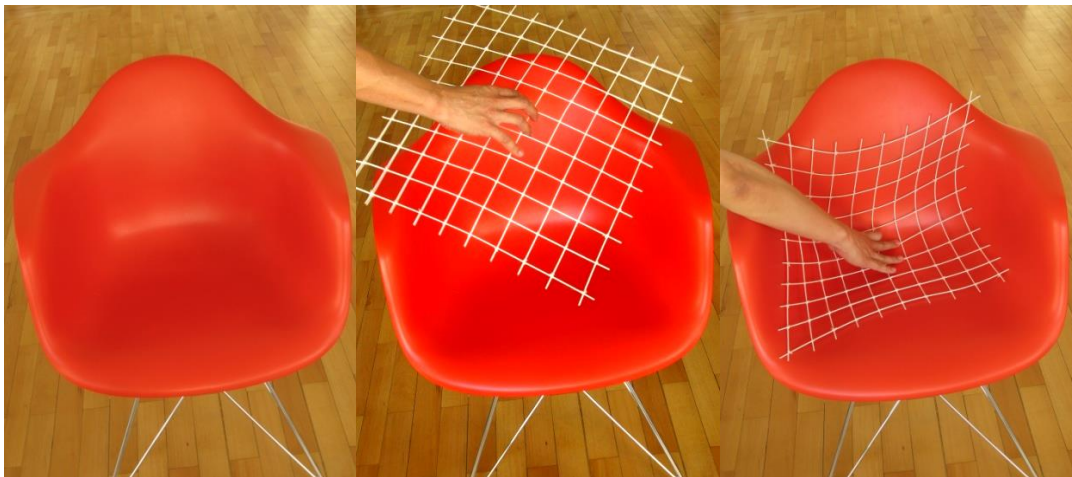


Figure 2.2: Elastic grids could adapt the geometries of free-form surfaces.

However, finding the right boundary conditions, including the cutting pattern, bearing positions, and bracing lengths, which lead to a specific geometry, is not an easy task. Designers have to keep equal grid lengths, minimize the residual forces, ensure the smoothness, and attain the desired geometry simultaneously. When in short of an appropriate numerical method designers have to return to physical models to find the boundary conditions. The complicated and multi-steps form-finding process makes this kind of structure less popular to architects/engineers and only a few building projects were realized.

The popularization of the non-uniform rational B-spline (NURBS) software and the geometrically nonlinear finite element analysis (FEA) program has recently removed some barriers of designing elastic grid shells; the NURBS software is used as a powerful tool to define free form surfaces while the geometrically nonlinear FEA program enables designers to simulate grid structures which undergo

large displacements and rotations. However, there are no approaches which can integrate the two parts together; the usual approach for designing elastic shells is to first derive a three-dimensional grid pattern with a form-finding method and then rebuild the corresponding structural model in a commercial FEA program. This twofold approach leads to the following two problems: First, elements might be over stressed in the structure design stage due to bi-axial bending and twisting, which are not fully considered in the form-finding process. Second, if geometric forms are directly transferred to structure models, there will be no bending pre-stresses in them. The rebuild of the pre-stresses of these highly bended models usually requires a complicated pre-stressing process and is one of the most critical challenges of the structure analysis of actively bent structures.

The attempt of using new fiber composite materials, such as glass and carbon fiber reinforced composite, in shell structures helps the research of elastic grid shells regain some momentum. Due to the large strength and stiffness ratio of these materials, a structure element of this type can be very flexible and take a relative large deformation while staying in the elastic range of the material [21]. But the most important factor of the revivification comes from the formation of a new research field called actively bent structures where the use of the bending mechanism is used to achieve global geometric integrity; curved structures can be realized with straight members because the bending mechanism naturally removes all kinked un-smoothness in the geometry. Besides, due to the bending mechanism, global movements can also be triggered by local actuations (Figure 2.3) and this property has the potential to be applied in kinetic structures.

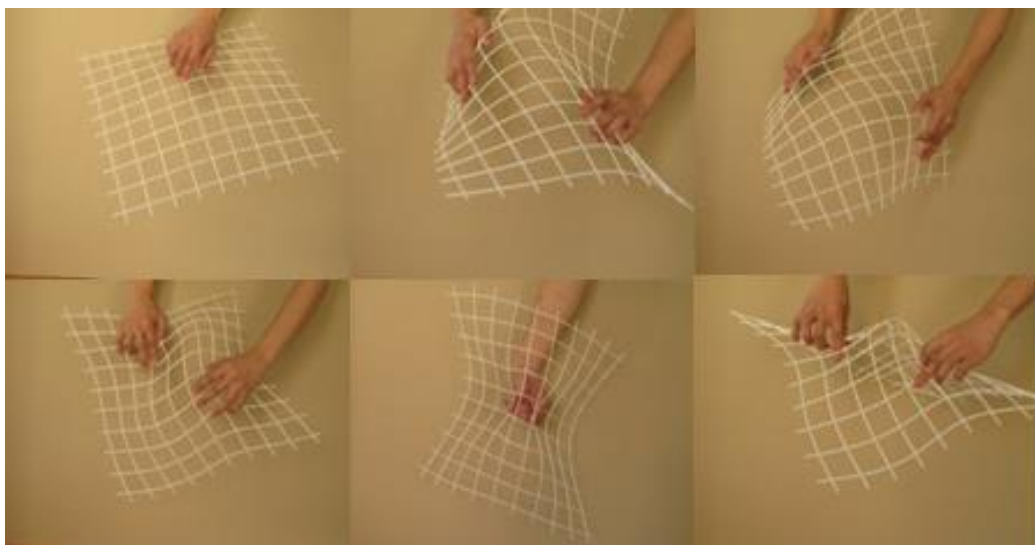


Figure 2.3: Global movements of an elastic grid shell can be triggered by local actuations

Today, even with so many new applications and achievements of actively bent structures, it still falls short of an effective approach which can precisely consider the structural behavior under given geometric constraints and there is neither a simple way which can easily solve the pre-stress issue. These two difficulties might be the most critical problems in the research of actively bent structures and are also the questions we like to answer the most.

### **2.1 The study of actively bent grid shells**

The first systematical research of actively bent grid shell was founded in 1970s by Frei Otto. Before that, similar building types had been seen in vernacular buildings and experimental projects of spans less than 20m. After the completion of Mannheim Multihalle in 1972 the largest span could reach 60m already (Figure 2.4). People started to notice the great potential of this type of structures. Because the stability issue of elastic grid shells is not very different to usual shell structures, most of the attention of the researchers have been placed in form-finding. The existing study of elastic grid shells, therefore with of the main focus in terms of form-finding methods, is reviewed in the following text.

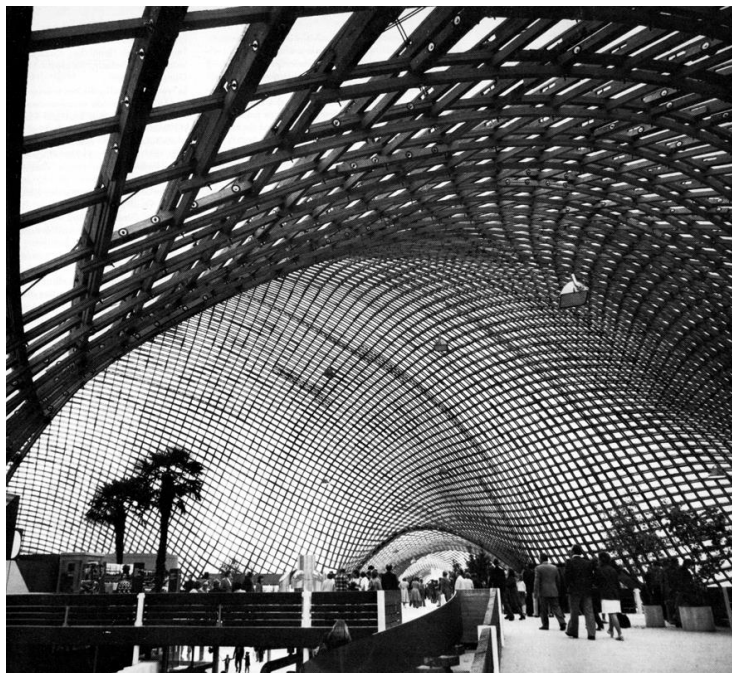


Figure 2.4: Mannheim Multihalle (<http://www.smdarq.net/case-study-mannheim-multihalle/#>)

### Chebyshev net

The method of the Chebyshev net, also known as the compass method, is a geometrical method. The drawing of the Chebyshev net starts from two arbitrary intersecting curves on a surface. Each curve is composed of segments with the same mesh width/grid length. The rest nodal points are only determined by finding intersection from two adjacent nodes with the same mesh width (Figure 2.5). The method was first seen in the work of P.L. Chebyshev in 1878 [22] and further researched by Frei Otto [15]. It has the advantage to adapt to free form surfaces. But it does not take account of bending behaviors of elastic materials. Elastic grid shells with the geometries derived in this way are not in static equilibrium and may transform to other shapes. This will bring additional stresses in members and extra difficulties for erection. Therefore, the results derived with this method usually need to be further adjusted with another form-finding method which is related to material properties [23].

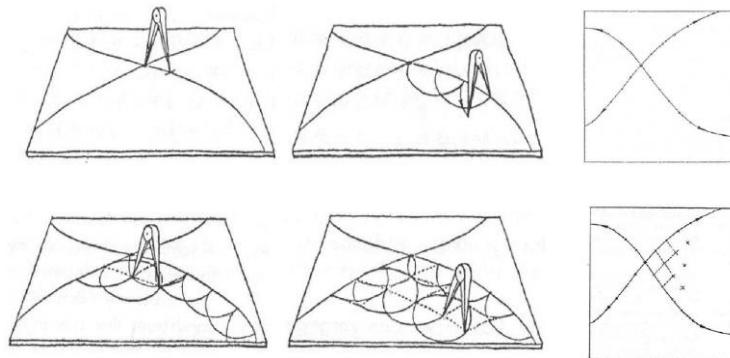


Figure 2.5: Drawing of a Chebyshev net (Frei Otto, IL 10 Gitterschalen)

### Hanging chains model

Hanging chains models can generate funicular geometries that have only tension forces while taking gravity load. Inverting the geometries of funicular, designers can get ideal shell geometries that have only compression forces when taking gravity load. The idea was first introduced by the physician Hook in the 17th century, further developed by the architect Gaudi in the 18th [24], and applied in the form-finding of grid shells by Frei Otto in 1970s [15]. The geometries derived in this way have good performance while taking gravity load, however when lateral or uneven loading is dominant,

this method loses its advantages. Besides, gravity load takes the main role in the formations of hanging chains models. This also limits possible geometries of elastic grid shells.

#### Pian's bending rod

Pian [5] proposed a method that uses equivalent shear forces of bending moment to model the in-plane bending behavior. The form of Downland Gridshell is found by using this bending rod properties [6] (Figure 2.6). This method was further developed to investigate spatially curved spline and grid shell structures, such as in the works of Barnes, Adriaenssens, Douthe and Li [25] [26] [27]. The team of Institut Navier also applied this method to design a grid shell in composite material (Figure 2.7). The form-finding in that case started from a specific cutting pattern and stopped while an aesthetic shape is reached in the cambering process [28].

#### Fallen elastic grids on a specific surface

Bouhaya also proposed a way of mapping continuous elastic grids on given surfaces. The dynamic explicit finite element analysis was used to simulate plane elastic grids dropped on imposed surfaces under the traction of gravity [29]. This method is able to create a grid shell structure complying with specific surfaces while taking bending behaviors into consideration. However, the traction by gravity will further twist grid geometries and lead geometries to follow the direction of gravity. This phenomenon will limit possible geometries and bring additional stresses in elastic rods.





Figure 2.6: Inner view of Downland Gridshell



Figure 2.7: Inner view of the Ephemeral Cathedral of Créteil (Jeu de lumière intérieur© CG-batiactu, <http://www.batiactu.com/edito/une-cathedrale-ephemere-en-forme-de-blob-a-creteil-35443.php?page=12>)

### Least strain energy state

Using the projection method and Pian's elastic rod model, Li and Knippers could derive grid layouts complying with specific surfaces 2011 [10]. Through the projection method, grid nodes are constrained only movable on the constraint surfaces/curves. When the elastic grid reaches its equilibrium, it naturally fulfills the given geometrical constraints. The equilibrium state is a state with the least strain energy in the solution domain defined by the constraints. Hernandez and Sechelmann introduced a similar way to derive the least strain energy state of an elastic grid on a specific surface by solving the overall potential function, which is also based on Pian's elastic rod model [30].

This thesis work takes the approach of finding the least strain energy state of an elastic grid under given geometric constraints and expand the dynamic relaxation method (DR) to have 6 degrees of freedom (DOF) per node such that the Euler-Bernoulli beam element can be employed and thus biaxial bending and torsion effects can be considered. After removing the geometric constraints and adding bracing and support conditions, the grid structure could transform to a load-bearing structure and the pre-stress built during the form-finding is correct for succeeding structural analysis.

## **2.2 Mergence of form-finding and structural analysis**

Most of the existing from-finding methods are based on form-finding structure models, where stiffness properties of profiles or of joints are usually very low compared with the stiffness properties of the built structures. When the stiffness properties become very low or even zero, the structure will change its form largely with the external forces.

For example, the use of hinges (zero stiffness in joints) in form-finding models is to diminish the bending forces in the structure and to find a form which takes the load mainly through axial forces. By further changing the member stiffness, two kinds of form-finding models can be derived as follows: First, when the member stiffness is similar as that of the built structure, the resulting form-finding model is a hanging chain model [15]. Second, when the member stiffness is very low compared with that of the built structure and the unstrained length is assumed to be zero, then the resulting form-finding model is a force density model [31].

Therefore, the essentials of form-finding and of structural analysis are the same. They are all to find the equilibrium states of structure systems. The only difference is that the stiffness properties considered in a form-finding model is much different from the real stiffness properties of a built structure.

As a result, if there is a numeric method which can find equilibrium states of both systems, whether of very low stiffness properties from a form-finding model or of real stiffness properties of a built structure, this method shall be applicable for both form-finding and structural analysis. In this research, we show that dynamic relaxation is one of such method, which can simulate structures of various stiffness properties of profiles and joints.

### **2.3 Contributions**

This thesis describes a general scheme for the form-finding and analysis of elastic grid shells. We use elastic properties in material and the projection method to derive smooth grid patterns according to given free-form surfaces. Other contributions of this work is listed below in detail.

#### Simulation of elastic beam systems of large rotations and displacements with six DOF dynamic relaxation

We show dynamic relaxation (DR) is a reliable and convenient method for simulating elastic beam systems which undergo large rotations and displacements. The Euler-Bernoulli beam element is integrated in our scheme such that biaxial bending and torsion mechanism can be considered. Our integration formulas for the rotational movement are expressed in a central difference form which makes the formulas easier to be comprehended and used.

Different from some previous research, where the inertia is expressed as a 3x3 matrix, the inertia in our scheme is expressed as a scalar. We show the necessity of using a scalar inertia and point out that if a matrix inertia is used, the rotation equation of motion stays no longer linear and the second term in the rotation equation of motion has to be considered.

#### Easy way of pre-stressing and coupling of elastic grid shell models

We develop a new technique to assign the pre-stresses of bending and twisting in one step. A complex pre-stressing process, which is common for the simulation of actively bent structures, is thus prevented. This method significantly expands our freedom in selecting a starting geometry; we are no longer restricted from beginning in an unstrained state. Instead, we can select a geometry that is closer to static equilibrium or that facilitates the assignment of constraints. This pre-stress technique is not only valid for explicit integration methods but also valid for implicit integration methods. That means all commercial FEA software can apply this technique when it allows users to access the database to assign the initial orientations.

A general method for coupling nodes is also presented in this work such that revolute joint, hinge and fixed joint can be easily simulated. Unlike the previous research, our method is based upon an equilibrium configuration and thus should be more stable and efficient.

#### Improving efficiency and stability by using fictitious lengths and fictitious section area

According to our research, the calculation efficiency and stability reach their best performance when nodes have similar stiffness in three major directions. By using this character, we develop a new technique to speed up the convergence rate. The convergence rate is optimized by using fictitious section areas and fictitious lengths to adjust the node stiffness such that they are similar in three major directions.

#### Form-finding by manipulating geometric constraints and material stiffness

We show that the projection method is an effective method to enforce geometric constraints (curve constraint and surface constraint) to elastic grids. We also point out that the mass matrix will induce numerical instability with geometric constraints and need corresponding adjustments. We also find that an elastic grid system with the stiffness of a construction profile is easily trapped in a potential well of a kinked geometry in the form-finding process. And the way for guiding the system through potential wells is by setting the profile stiffness in a special way where the ratio between the transverse stiffness and the axial stiffness is large enough such that the bending mechanism will dominate the process and remove all kinks in the geometry.

This enlarged stiffness ratio is not only important for stabilizing the form-finding process but also a very powerful tool to explore geometric patterns. Starting from free drawings, which are full of kinked lines, designers are able to generate smooth and continuous geometries without defining curves and surfaces.

## **2.4 Structure of Part II**

The structure of Part II unfolds as below: in chapter one, we illustrate the current state of the study, our research interest and our contribution. In chapter two, we introduce the necessary fundamental knowledge of the field of structure simulation of large displacements. In chapter three, we demonstrate our simulation method – 6DOF DR. In chapter four, we propose a unique way to speed up the convergence rate by using fictitious elements. In chapter five, we demonstrate how to assign pre-stresses which arise from bending geometries and how to simulate revolute joints and other important joints. In chapter six, we propose to use the projection method and the force method as form-finding methods to apply geometric constraints. In chapter seven we conclude the research and reflect on future works.

## Chapter 3

### BACKGROUND

There are many ways to calculate deformations of structures which undergo large rotations and displacements. Instead of solving the static state directly, the method adopted in this research is a dynamic approach--the static state is solved by damping a dynamic system to an equilibrium state.

The motion of structures can be described by means of equations of time and space. For simpler structures we can solve their equation of deformation at any specific time point as long as we know the give boundary condition. However, for complex structures this equation is only solvable numerically. The numerical procedure for solving the equation of motion is first to discretize the structure into finite elements and then to discretize the motion into time steps.

In the following sections we will introduce how to discretize a grid structure into systems of nodes and elements and how to discretize its motion in a central difference form in respect to time axis.

#### 3.1 Representation of an elastic grid system

An elastic grid structure is composed of elastic, continuous, and initially straight members which go across each other and connected with revolute joints: A long linear member can be discretized into a sequence of nodes which are connected by beam elements (Figure 3.1); a joint is realized by coupling the jointed nodes of the crossing members (Figure 3.2). In this way, the structure is discretized into nodes and beam elements. The description of the deformation of a continuous member is thus simplified to the description of the node positions and the node orientations of the discretized system.

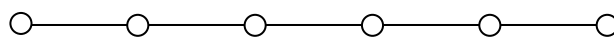


Figure 3.1: A discretized member consists of nodes and beam elements.

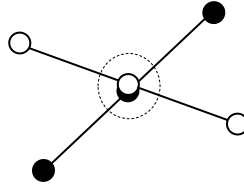


Figure 3.2: A jointed crossing structure consists of four beam elements and six nodes. The joint is realized by coupling the overlapping nodes.

In our model, nodes are the only objects considered in the equations of motion (translational motion and rotational motion). These nodes possess masses and moments of inertia which are subjected to the resultant forces and the resultant torques respectively. The nodes will shift and rotate freely if no force is exerted. Once the internal forces of beam elements are applied, the node movements will be coupled and the individual nodes will behave as an integral structure.

In our model, every node has six degrees of freedom, three for the rotation motion and three for the translation motion. If the jointed nodes are coupled in all six degrees of freedom, the result is a rigid joint. If only the translation degrees of freedom are coupled, the result is a hinge joint. If two rotation degrees of freedom and three translation degrees of freedom are coupled, the result is a revolute joint. The detail procedure for coupling is illustrated in Chapter 6.

### 3.1.1. Orientations and coordinate systems

#### Node orientations

As illustrated previously, nodes are the only objects considered in the equations of motion. A node position can be described by a three-dimensional vector  $\vec{d}$

$$\vec{d} = \begin{bmatrix} d_1 \\ d_2 \\ d_3 \end{bmatrix}$$

And a node orientation can be described by a 3x3 orthogonal matrix  $\mathbf{R}$

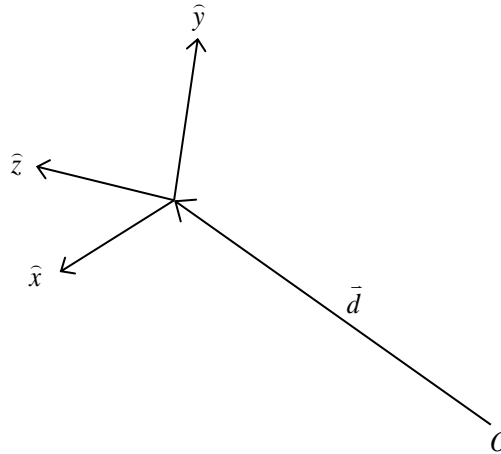


Figure 3.3: A node orientation is represented by three orthogonal unit vectors. The node position is presented by a three-dimension vector  $\bar{d}$  .

$$\mathbf{R} = [\hat{x} \ \hat{y} \ \hat{z}] = \begin{bmatrix} x_1 & y_1 & z_1 \\ x_2 & y_2 & z_2 \\ x_3 & y_3 & z_3 \end{bmatrix}$$

where  $\hat{x}$  ,  $\hat{y}$  , and  $\hat{z}$  are three orthogonal vectors pointing in the local x, y and z-directions (Figure 3.3). The nine values in the matrix are not independent with each other; having known the initial orientation and three rotation angles all components of the matrix can be derived [32]. Therefore, an orientation has only three independent variables. Instead of using rotation angles, throughout this thesis, the matrix form is used to describe orientations because the coordinate transformation and the rotation update could be represented in a compact manner.

### Beam-end orientations

The internal forces of a Euler-Bernoulli beam element is determined by its beam-end positions and its beam-end orientations. A beam-end is always connected with a node and has the same position. Therefore, there is no need to define a new position vector for a beam-end. However, a beam-end orientation may not coincide with the node orientation and thus there is a need to define a specific



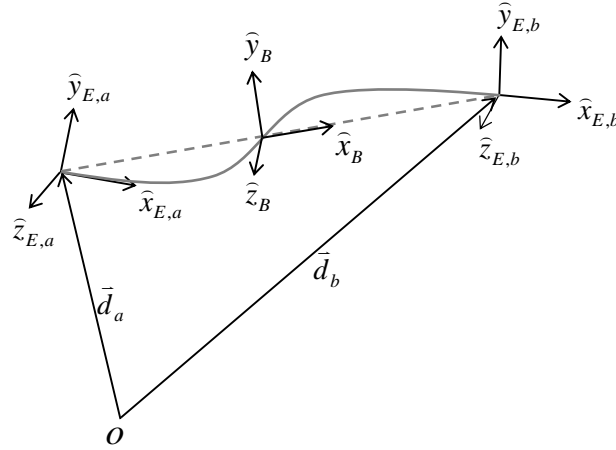


Figure 3.4: A beam element is related to two beam-end orientations and one beam orientation. The x-direction of a beam-end orientation is always parallel to the deformed center line of the beam. A beam element is always connected to two nodes at both ends and the nodes have their own orientations, which are not shown in this figure for simplicity.

orientation for a beam-end. There are two beam-ends for each beam element, and for each beam-end, a corresponding beam-end orientation is defined.

A beam-end orientation is not an independent orientation; it will co-rotate as a rigid body with the corresponding node to which the beam-end is located (Figure 3.4). The co-rotation is realized in our scheme by using the same transformation matrix to update the node orientation and the corresponding beam-end orientations (the detailed procedure is illustrated in Chapter 3). The pre-stresses due to bended and twisted geometry can be assigned to the system by setting specific initial beam-end orientations (the detailed procedure is illustrated in Chapter 6).

### Beam orientations

Before calculating the internal forces of a beam element, the two beam-end orientations have to be transferred from the global coordinates to the local beam coordinates. Therefore, there is a need to define additional orientations for beam elements, named beam orientations. A beam orientation is not an independent orientation; it can be completely determined by the beam-end orientations of its two beam-ends [33].

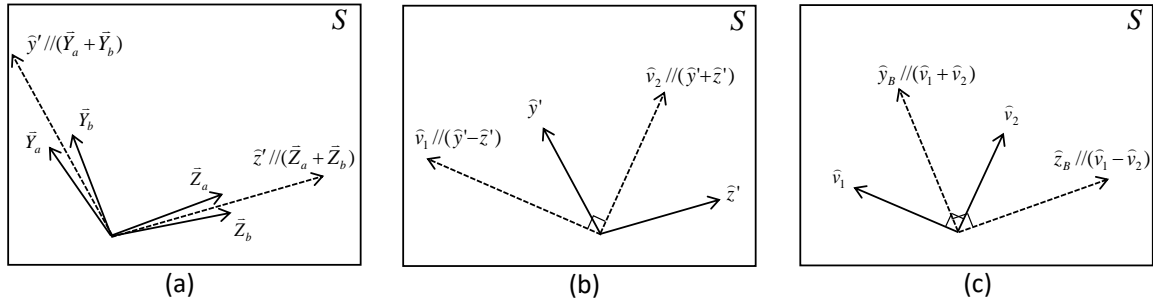


Figure 3.5: (a) Projected vectors  $\bar{Y}_j$  and  $\bar{Z}_j$  and their sum on plane S; (b) orthogonal vectors  $\hat{v}_1$  and  $\hat{v}_2$ ; (c) composition of vectors  $\hat{y}_B$  and  $\hat{z}_B$

The local x-direction  $\hat{x}_B$  of a beam orientation is defined as

$$\hat{x}_B = \frac{(\bar{d}_b - \bar{d}_a)}{|\bar{d}_b - \bar{d}_a|} \quad (3.1)$$

where  $\bar{d}$  is the position of a beam-end and its subscript marks the specific end (Figure 3.4).

The local y- and z-directions of a beam element,  $\hat{y}_B$  and  $\hat{z}_B$ , can be defined by the ‘‘average’’ of the two beam-end orientations. The derivation is divided into three stages: First, the vectors  $\bar{Y}_j$  and  $\bar{Z}_j$  are derived by projecting  $\hat{y}_{E,j}$  and  $\hat{z}_{E,j}$ , the local y- and z-directions of the two beam ends, to the plane S, which is normal to  $\hat{x}_B$  (Figure 3.5.a)

$$\begin{aligned} \bar{Y}_j &= \hat{y}_{E,j} - (\hat{y}_{E,j} \cdot \hat{x}_B) \hat{x}_B \\ \bar{Z}_j &= \hat{z}_{E,j} - (\hat{z}_{E,j} \cdot \hat{x}_B) \hat{x}_B \end{aligned}, j = a, b \quad (3.2)$$

where j denotes the two beam ends. Second, the averaged vectors  $\hat{y}'$  and  $\hat{z}'$  are derived with the projected vectors

$$\begin{aligned} \hat{y}' &= (\bar{Y}_a + \bar{Y}_b) / |\bar{Y}_a + \bar{Y}_b| \\ \hat{z}' &= (\bar{Z}_a + \bar{Z}_b) / |\bar{Z}_a + \bar{Z}_b| \end{aligned} \quad (3.3)$$

$\hat{y}'$  and  $\hat{z}'$  are already close to the final solution. However, they are not necessary perpendicular with each other and thus need further adjustment. Third, to ensure orthogonality, two orthogonal vectors  $\hat{v}_1$  and  $\hat{v}_2$ , shown in Figure 3.5.b, are thus composed and normalized

$$\begin{aligned}\hat{v}_1 &= (\hat{y}' + \hat{z}') / |\hat{y}' + \hat{z}'| \\ \hat{v}_2 &= (\hat{y}' - \hat{z}') / |\hat{y}' - \hat{z}'|\end{aligned}\tag{3.4}$$

and are used to compose the local y-and the local z-directions of the beam element as shown in Figure 3.5.c

$$\begin{aligned}\hat{y}_B &= \frac{\sqrt{2}}{2}(\hat{v}_1 + \hat{v}_2) \\ \hat{z}_B &= \frac{\sqrt{2}}{2}(\hat{v}_2 - \hat{v}_1)\end{aligned}\tag{3.5}$$

### Remarks

- 1) Nodes are the main subjects in motion. They possess masses and moments of inertia which are subjected to the resultant translational forces and the resultant rotational forces (torques) respectively. There is no specific requirement for the initial node orientations.
- 2) Beam-end orientations are deployed to calculate the internal forces of beam elements and always co-rotate with the corresponding nodes like a rigid body. Pre-stresses of bending and torsion can be assigned by assigning specific initial beam-end orientations.
- 3) A beam orientation is determined by the positions and the orientations of the two beam-ends. Internal forces of a beam elements are calculated according to its beam orientation. The local y-and local z-directions of a beam orientation are defined by the “average” of the two beam-ends.

### 3.1.2 Included angles

The included angles are used to compute shears, torsions, bending moments of a deformed beam element. Their geometric definitions are shown in Figure 3.6 and are calculated as follows

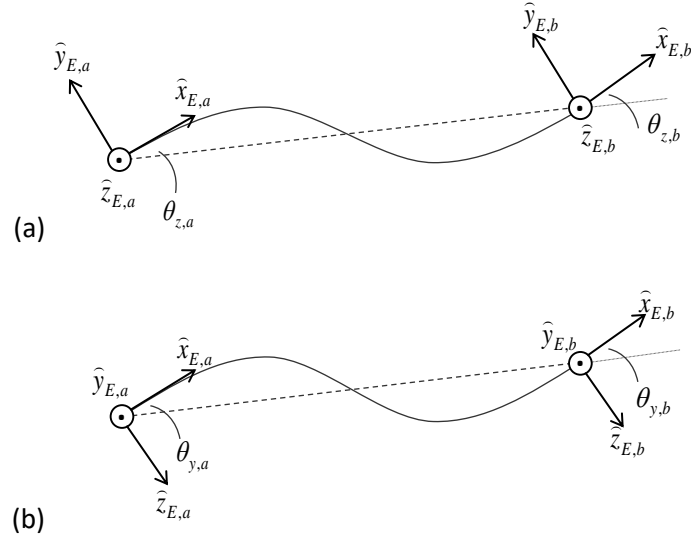


Figure 3.6: (a) Definitions of included angles,  $\theta_{z,a}$  and  $\theta_{z,b}$ ; (b) definitions of included angles,  $\theta_{y,a}$  and  $\theta_{y,b}$

$$\theta_{z,j} = \hat{x}_{E,j} \cdot \hat{y}_{E,j}, \quad j = a, b \quad (3.6.a)$$

$$\theta_{y,j} = -\hat{x}_{E,j} \cdot \hat{z}_{E,j}, \quad j = a, b \quad (3.6.b)$$

$$\theta_{x,b} - \theta_{x,a} = (\hat{y}_{E,a} \cdot \hat{z}_{E,b} - \hat{y}_{E,b} \cdot \hat{z}_{E,a}) / 2 \quad (3.6.c)$$

where  $\theta$  are included angles,  $\hat{y}_j$  and  $\hat{z}_j$  are the local y- and the local z-directions of the beam-ends, and  $j$  denotes the two beam-ends.

Another way to derive included angles is to calculate the rotation vector of the beam-end orientation in the beam coordinates

$$\theta_{x,j} = \frac{R_{32} - R_{23}}{2 \sin \Delta\theta} \cdot \Delta\theta, \quad j = a, b \quad (3.7.a)$$

$$\theta_{y,j} = \frac{R_{13} - R_{31}}{2 \sin \Delta\theta} \cdot \Delta\theta, \quad j = a, b \quad (3.7.b)$$

$$\theta_{z,j} = \frac{R_{21} - R_{12}}{2 \sin \Delta\theta} \cdot \Delta\theta, \quad j = a, b \quad (3.7.c)$$

where  $R_{mn}$  is the component, at the  $m$ -th row and  $n$ -th column, of the rotation matrix  $R$ , which is the  $j$ -th beam-end's orientation represented in the beam coordinates, and  $\Delta\theta$  is the corresponding rotation angle, which is calculated as

$$\Delta\theta = \arcsin\left(\frac{(R_{23} - R_{32})^2 + (R_{31} - R_{13})^2 + (R_{12} - R_{21})^2}{2}\right) \quad (3.8.a)$$

Another way to compute the rotation angle is often to be seen in references

$$\Delta\theta = \arccos\left(\frac{R_{11} + R_{22} + R_{33} - 1}{2}\right) \quad (3.8.b)$$

According to our research, when the rotation angle approaches zero, both Equation 3.8.a and Equation 3.8.b generate numerical instability (the result of Equation 3.8.b is much worse than that of Equation 3.8.a). The solution is to replace Equation 3.8.a with its Tylor expansion.

### 3.1.3 Internal forces/ beam-end reactions

We use the Euler-Bernoulli beam theory to build up the relationship between the internal forces and the end displacements. Following the same procedure, other type of beam elements can be easily adopted in our scheme, for example the Timoshenko beam element.

The displacement of an Euler-Bernoulli beam element has 12 degrees of freedoms and can be expressed by a vector  $\bar{q}$

$$\bar{q} = [\Delta_{x,a} \quad \Delta_{y,a} \quad \Delta_{z,a} \quad \theta_{x,a} \quad \theta_{y,a} \quad \theta_{z,a} \quad \Delta_{x,b} \quad \Delta_{y,b} \quad \Delta_{x,b} \quad \theta_{x,b} \quad \theta_{x,b} \quad \theta_{z,b}]^T \quad (3.9)$$

where  $\Delta$  is a translation displacement,  $\theta$  is a rotation displacement, subscript  $a$  and  $b$  mark the two beam-ends, and subscripts  $x$ ,  $y$  and  $z$  mark the three local directions of the beam (Figure 3.4). The internal forces (end reactions) acting on the two beam-ends can be expressed as a vector  $\bar{r}$

$$\bar{r} = [f_{x,a} \quad f_{y,a} \quad f_{z,a} \quad \tau_{x,a} \quad \tau_{y,a} \quad \tau_{z,a} \quad f_{x,b} \quad f_{y,b} \quad f_{x,b} \quad \tau_{x,b} \quad \tau_{x,b} \quad \tau_{z,b}]^T \quad (3.10)$$



$$\bar{q} = \left[ \frac{L_s - L}{2} \quad 0 \quad 0 \quad \theta_{x,1} \quad \theta_{y,1} \quad \theta_{z,1} \quad -\frac{L_s - L}{2} \quad 0 \quad 0 \quad \theta_{x,2} \quad \theta_{y,2} \quad \theta_{z,2} \right]^T \quad (3.13)$$

where  $L_s$  is the strained length. Substituting Equation 3.13 into Equation 3.11, we get

$$\begin{aligned} f_{x,a} &= EA(L_s - L)/L, & f_{x,b} &= -f_{x,a} \\ f_{y,a} &= -6EI_z/L^2(\theta_{z,a} + \theta_{z,b}) & f_{y,b} &= -f_{y,a} \\ f_{z,a} &= +6EI_y/L^2(\theta_{y,a} + \theta_{y,b}) & f_{z,b} &= -f_{z,a} \\ \tau_{x,a} &= GJ/L(\theta_{x,b} - \theta_{x,a}), & \tau_{x,b} &= -\tau_{x,a} \\ \tau_{y,a} &= -2EI_y/L(2\theta_{y,a} + \theta_{y,b}), & \tau_{y,2} &= -2EI_y/L(\theta_{y,a} + 2\theta_{y,b}) \\ \tau_{z,a} &= -2EI_z/L(2\theta_{z,a} + \theta_{z,b}), & \tau_{z,a} &= -2EI_z/L(\theta_{z,a} + 2\theta_{z,b}) \end{aligned} \quad (3.14)$$

The above formulas of internal forces have been largely reduced; they are now only the functions of included angles and extended lengths, which can be derived from the beam-ends orientations and the node positions.

#### 3.1.4. Strain Energy

The strain energy can be used as an index to evaluate the result of form-finding or of an optimization. It can be calculated as follows

$$U = \frac{1}{2} \sum \bar{q}_i^T \mathbf{k}_i \bar{q}_i \quad (3.15)$$

where  $\mathbf{k}_i$  is the stiffness matrix of the  $i$ -th beam element. Substituting Equation 3.12 and Equation 3.13 into Equation 3.15, we get

$$\begin{aligned}
U &= U_N + U_{Mx} + U_{My} + U_{Mz} \\
U_N &= \frac{1}{2} \sum \frac{EA}{l_0} (l - l_0)^2 \\
U_{Mx} &= \frac{1}{2} \sum \frac{GJ}{l_0} (\theta_{x,b} - \theta_{x,a})^2 \\
U_{My} &= 2 \sum \frac{EI_y}{l_0} (\theta_{y,a}^2 + \theta_{y,b}^2 + \theta_{y,a} \cdot \theta_{y,b}) \\
U_{Mz} &= 2 \sum \frac{EI_z}{l_0} (\theta_{z,a}^2 + \theta_{z,b}^2 + \theta_{z,a} \cdot \theta_{z,b})
\end{aligned} \tag{3.16}$$

where  $U_N$  is the total axial strain energy,  $U_{Mx}$  the total out-of-plane bending strain energy,  $U_{My}$  the total in-plane bending strain energy, and  $U_{Mz}$  the total torsion strain energy.

### 3.2 Representation of motion

#### 3.2.1 Newtonian dynamics

Our description of a dynamic system is based on the Newtonian dynamics. The motion of a node can be divided into two parts: the translational motion and the rotational motion. The translational motion is governed by

$$\vec{F} = M \vec{a} \tag{3.17}$$

where  $\vec{F}$  is the resultant translational force acting on the node,  $M$  is the nodal mass, and  $\vec{a}$  is the node acceleration, while the rotational motion of a node is governed by

$$\vec{T} = M_\tau \vec{\alpha} + \vec{\omega} \times (M_\tau \vec{\omega}) \tag{3.18}$$

where  $\vec{T}$  denotes the rotation force,  $M_\tau$  the moment of inertia,  $\vec{\omega}$  the angular velocity and  $\vec{\alpha}$  the angular acceleration.

In section 3.1, the structure system has been discretized into a composition of individual nodes and beam elements. Now together with these two equations of motions we should be able to simulate the



node motions. However, the motions of the individual nodes are still continuous in time axis, and it is not possible to solve the motion of a complex system in an algebraic way. A time integration method is thus needed to discretize the motions into time steps and will be introduced in the next section.

### 3.2.2 Time integration methods

The key point to discretize a motion respect to time is to build the relationship of two states of motion across a time interval. In this way, the next state can always be calculated from the information of the previous state. This stepwise approach is called time integration. Among different time integration methods, the central difference method is deployed in our scheme to build the relationship of the two states across a time interval. By the meaning of central difference, we can write down the following equations

$${}^{n+1/2}\vec{d} = {}^{n-1/2}\vec{d} + \Delta t \quad {}^n\vec{v} \quad (3.19)$$

$${}^n\vec{v} = {}^{n-1}\vec{v} + \Delta t \quad {}^{n-1/2}\vec{a} \quad (3.20)$$

Where  $\vec{d}$  denotes the node position,  $\vec{v}$  the node translation velocity, and  $\vec{a}$  the node translation acceleration. The superscript on the left-hand side denotes a specific time step that corresponds to the time point  $t_n = n \Delta t$ , where  $\Delta t$  is the time increment. Substituting Equation 3.17 into Equation 3.20, we get

$${}^n\vec{v} = {}^{n-1}\vec{v} + \Delta t M^{-1} \quad {}^{n-1/2}\vec{F} \quad (3.21)$$

Equation 3.19 and Equation 3.21 are the translation integration formulas for nodes. In the next chapter we will demonstrate our unique way to discretize the rotation motion respect to time.

## Chapter 4

# SIMULATION OF ELASTIC BEAM SYSTEMS OF LARGE DISPLACEMENTS

### 4.1. Introduction

The matrix method is widely used for the simulation/analysis of structure systems, where the displacement  $\bar{Q}$  and the external forces  $\bar{F}_{ext}$  are related by a global stiffness matrix  $\mathbf{K}$

$$\mathbf{K}\bar{Q} = \bar{F}_{ext} \quad (4.1)$$

This linear equation can deal with the systems of small deformations. However, for systems undergoing large deformations, it does not hold anymore. For such a case, the relation between the displacement and the external load becomes nonlinear and can only be solved in an iterative way [17]

$${}^n\mathbf{K}_t {}^{n+1}\bar{\Delta} = {}^n\bar{R} = \bar{F}_{ext} - {}^n\bar{F}_{int} \quad (4.2)$$

where  $\mathbf{K}_t$  is the global tangential stiffness matrix,  $\bar{\Delta}$  is the displacement increment,  $\bar{R}$  is the node residual,  $\bar{F}_{int}$  is the internal force, and the superscript on the left-hand side denotes a specific iteration step. The most common numerical method to solve this nonlinear equation is the Newton-Raphson method (NR).

Dynamic Relaxation (DR) is a way of deriving the static state of a heavily damped system by time integration method (Section 3.2.2). Because it concerns only about the final static equilibrium state, various damping methods and mass terms could be used as controlling factors to speed up the damping process. This concept of solving a static problem by treating it as a heavily damped dynamic system was first proposed Day in 1965 [35]. At that time, DR was used as a tool for structural analysis

and not for form-finding. Since damping and mass terms could be used as an effective way to stabilize the time integration process, DR was then found to be a powerful tool to solve the form-finding problems such as tensile nets and cables [25] [36].

Either using NR or DR, the structure systems of large displacements can only be solved in an iterative way. However, compared to NR, DR's motion update is treated individually for each node and there is no need to solve a global stiffness matrix problem. In DR the node motion is only affected by the physical quantities around the node. The mathematic representation is thus simpler and makes DR an ideal method to deal with local perturbations that are caused by physical contacts or geometric constraints.

As for the calculation efficiency, although NR is proved to be more efficient to deal with structural systems of a smaller number of elements, this advantage stands no more when it goes to a system with a large number of elements. In the latter case, NR exhausts much more time computation time than DR. According to the research of Sauve, the computation time needed for DR is proportional to  $N^{4/3}$  ( $N$  is the number of elements of a system) whereas for NR it is proportional to  $N^{7/3}$  [37]. Besides, because the motion update in DR is treated individually for each node, the technique of parallel computation can thus be applied, which can largely reduce the computation time [38].

In this Chapter, our method is presented in the following manner: After the review of the related work, we first present the core formulations of 6DOF DR. They govern the translation and the rotation motions of dynamic systems. We then introduce the use of the optimized mass matrix and the optimized scalar inertia, which can speed up the convergence rate. The kinetic damping is illustrated subsequently, which is applied to damp the dynamic system to an equilibrium state. In the end, examples are given as the verification of our method.

## 4.2 Related work

DR is a powerful tool for form-finding and analyses of membrane, cable and truss structures. However, the corresponding structural elements possess only three degrees of freedom (3DOF) per node and exhibit no bending or twisting effect. Pian [5] proposed a method that uses equivalent shear forces of bending moment to model the in-plane bending behavior. This method was further developed to investigate spatially curved spline and grid shell structures, such as in the research of Barnes [25],

Wakefield [36], Adriaenssens [39] and Douthe [40]. Due to the lack of rotation DOF, biaxial bending and torsion effects were not considered. To address the torsion effect, Barnes proposed an improved approach, in which an additional torsion factor is required for the coupling of transverse bending and torsion [41].

Without the rotation DOF, certain classic finite elements, such as the Euler-Bernoulli beam element, cannot be applied in DR. Wakefield [36] utilized rotation displacement to describe the three-dimensional rotation in DR and calculate the sway angle using the method proposed by Jonson and Brotton [10]. Another method, first proposed by Williams [42], for updating the orientation by rotating around a pseudo-rotation vector is demonstrated in the work of Adriaenssens, Aberle and D'Amico [7] [43] [44]. Li and Knippers [45] also proposed a different approach that considers rotation mechanism in which the orientation update formula is expressed in a central difference form. Despite these progresses and achievements, uncertainties remain regarding the feasibility of DR with 6DOF per node when the rotational DOF and corresponding physical quantities are coupled with translational quantities [41] [46]. In this chapter the possible cause of the instability observed in the previous research is explained, and the corresponding solution is provided.

### 4.3 Rotation formulations for DR

The translation formulations of DR are given in Chapter 3 already (Equation 3.19 and Equation 3.21). The goal of this section is to derive the rotation formulations of DR. Analogous to the position update formulation (Equation 3.19), we could construct a relationship between a previous and its subsequent node orientations,  ${}^{n-1/2}\mathbf{R}_N$  and  ${}^{n+1/2}\mathbf{R}_N$ , with a transformation matrix  $\mathbf{R}_T$ , which is defined by a rotation vector  $\Delta\bar{\theta} = [\theta_x \quad \theta_y \quad \theta_z]^T$  in the global coordinates as

$${}^{n+1/2}\mathbf{R}_N = \mathbf{R}_T(\Delta\bar{\theta}) {}^{n-1/2}\mathbf{R}_N \quad (4.3)$$

The mathematical meaning of the transformation matrix is that after rotating the previous node orientation with  $|\Delta\bar{\theta}|$  degree around the rotation vector, it will become the subsequent node orientation (Figure 4.1).

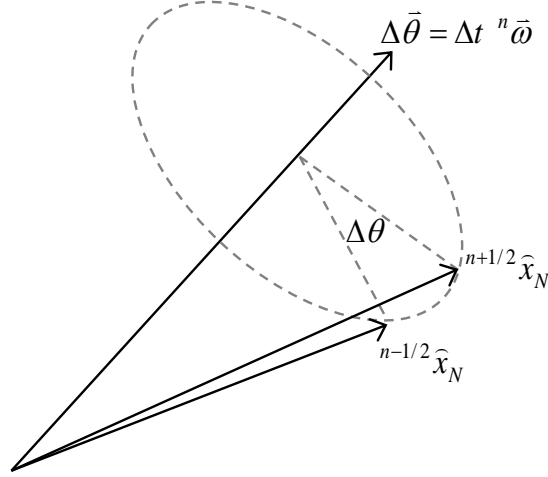


Figure 4.1:  $\mathbf{R}_N$  rotates along a rotation vector  $\Delta\bar{\theta}$ . For simplicity here only  $\hat{x}_N$ , the local x-direction of  $\mathbf{R}_N$ , is shown.  $\hat{y}_N$  and  $\hat{z}_N$  are omitted.

The relationship between the transformation matrix and the rotation vector can be described by the Rodrigues formula [14] as

$$\mathbf{R}_T(\Delta\bar{\theta}) = \begin{bmatrix} c + e_x^2(1-c) & e_x e_y(1-c) - e_z s & e_z e_x(1-c) + e_y s \\ e_x e_y(1-c) + e_z s & c + e_y^2(1-c) & e_y e_z(1-c) - e_x s \\ e_z e_x(1-c) - e_y s & e_y e_z(1-c) + e_x s & c + e_z^2(1-c) \end{bmatrix}, \quad \begin{aligned} c &= \cos|\Delta\bar{\theta}| \\ s &= \sin|\Delta\bar{\theta}| \end{aligned} \quad (4.4)$$

where  $e_x$ ,  $e_y$ , and  $e_z$  are defined as

$$\bar{e} = [e_x \quad e_y \quad e_z]^T = \frac{\Delta\bar{\theta}}{|\Delta\bar{\theta}|} \quad (4.5)$$

By the meaning of central difference, for a short time interval the rotation vector can be approximated by

$$\Delta\bar{\theta} = \int_{t_{n-1/2}}^{t_{n+1/2}} \bar{\omega} dt \approx {}^n \bar{\omega} \Delta t \quad (4.6)$$

Equation 4.3 is then rewritten as

$${}^{n+1/2}\mathbf{R}_N = \mathbf{R}_T(\Delta t \quad {}^n\bar{\omega}) \quad {}^{n-1/2}\mathbf{R}_N \quad (4.7)$$

The above equation is our orientation update formulation for the rotation degrees of freedom, which is analogical to the position update formulation (Equation 3.19) for the translational degrees of freedom. Similar to the velocity update formula, we can build the angular velocity update formulation as

$${}^n\bar{\omega} = {}^{n-1}\bar{\omega} + \Delta t \quad {}^{n-1/2}\bar{\alpha} \quad (4.8)$$

where  $\bar{\omega}$  is the node angular velocity,  $\bar{\alpha}$  is the node angular acceleration. So far, only the kinematics of rotation is discussed. Considering dynamics, the term of the angular acceleration in Equation 4.8 has to be related to the resultant rotation force. However, the equation of rotation motion (Equation 3.18) is not linear. It is difficult to represent the angular acceleration in terms of the rotational force. One way to make the calculation simpler is to apply an isotropic inertia to the system, which implies

$$\bar{\omega} \times (M_\tau \bar{\omega}) = M_\tau \bar{\omega} \times \bar{\omega} = 0 \quad (4.9)$$

Equation 3.18 is then reduced to

$$\bar{T} = M_\tau \bar{\alpha} \quad (4.10)$$

Readers might ask why we may conveniently select the mass and inertia terms. This is because we care about only the final static state and not the dynamic process; the mass and the inertia terms will only effect the node accelerations and velocities and will not impose external load to the system and thus will not influence the equilibrium state.

By substituting the angular acceleration in Equation 4.8 with Equation 4.10, we obtain the angular velocity update formula

$${}^n\bar{\omega} = {}^{n-1}\bar{\omega} + \Delta t \quad M_\tau^{-1} \quad {}^{n-1/2}\bar{T} \quad (4.11)$$

A concise comparison between the translation and rotation formulations of DR is shown in

Table 4.1: Translation and rotation formulations of DR

translational part	rotational part
${}^{n+1/2}\bar{\mathbf{d}} = {}^{n-1/2}\bar{\mathbf{d}} + \Delta t \quad {}^n\bar{\mathbf{v}}$	${}^{n+1/2}\mathbf{R}_N = \mathbf{R}_T(\Delta t \quad {}^n\bar{\boldsymbol{\omega}}) \quad {}^{n-1/2}\mathbf{R}_N$
${}^n\bar{\mathbf{v}} = {}^{n-1}\bar{\mathbf{v}} + \Delta t \quad \mathbf{M}^{-1} \quad {}^{n-1/2}\bar{\mathbf{F}}$	${}^n\bar{\boldsymbol{\omega}} = {}^{n-1}\bar{\boldsymbol{\omega}} + \Delta t \quad \mathbf{M}_\tau^{-1} \quad {}^{n-1/2}\bar{\mathbf{T}}$

Table 4.1.

Remark: The rotation vector, the angular velocity and the angular acceleration could also be represented in the local node coordinates. If it is the case, Equation 4.7 and Equation 4.8 are rewritten as

$${}^{n+1/2}\mathbf{R}_N = {}^{n-1/2}\mathbf{R}_N \mathbf{R}_T(\Delta t \quad {}^n\bar{\boldsymbol{\omega}}') \quad (4.12)$$

$${}^n\bar{\boldsymbol{\omega}}' = {}^{n-1}\bar{\boldsymbol{\omega}}' + \Delta t \quad {}^{n-1/2}\bar{\boldsymbol{\alpha}}' \quad (4.13)$$

where  $\bar{\boldsymbol{\omega}}'$  and  $\bar{\boldsymbol{\alpha}}'$  are the angular velocity and the angular acceleration represented in the local node coordinates respectively.

#### 4.3.1 Tensor inertia

A scalar inertia (isotropic inertia) is applied in the previous section to simplify the equation of rotation motion such that the second term in Equation 3.18 can be dropped. However, the tensor inertia which is according to the actual mass distribution of a structure might still be applied when the structure dynamic response becomes important. Therefore, the corresponding update formulation is illustrated in this section.

Considering the transient state at the (n-1/2)-th time step, Equation 3.18 can be rewritten as

$${}^{n-1/2}\bar{\mathbf{T}} = \mathbf{M}_\tau \quad {}^{n-1/2}\bar{\boldsymbol{\alpha}} + {}^{n-1/2}\bar{\boldsymbol{\omega}} \times (\mathbf{M}_\tau \quad {}^{n-1/2}\bar{\boldsymbol{\omega}}) \quad (4.14)$$

By assuming

$${}^{n-1/2}\bar{\omega} = \frac{{}^{n-1}\bar{\omega} + {}^n\bar{\omega}}{2} = \frac{{}^{n-1}\bar{\omega} + ({}^{n-1}\bar{\omega} + \Delta t \quad {}^{n-1/2}\bar{\alpha})}{2} = {}^{n-1}\bar{\omega} + \frac{\Delta t}{2} \quad {}^{n-1/2}\bar{\alpha} \quad (4.15)$$

and substituting it into Equation 4.14, we get

$$\mathbf{M}_\tau \quad {}^{n-1/2}\bar{\alpha} + ({}^{n-1}\bar{\omega} + \frac{\Delta t}{2} \quad {}^{n-1/2}\bar{\alpha}) \times (\mathbf{M}_\tau \quad ({}^{n-1}\bar{\omega} + \frac{\Delta t}{2} \quad {}^{n-1/2}\bar{\alpha})) - {}^{n-1/2}\bar{T} = 0 \quad (4.16)$$

The only unknown in the above equation is  ${}^{n-1/2}\bar{\alpha}$ , which can be solved by an iteration method [47].

Some researchers report that the 6DOF DR is not numerically stable [41] [46]. It might result from using the tensor inertia but not together with the complete equation of rotation motion. This is because that, if a tensor inertia is in use, even when there is no torque acting on the node, the nodal angular acceleration would still change due to the exist of an angular velocity as shown in Equation 4.14. This formula would feed back the correct change of angular velocity and thus conserve the angular momentum. But, if Equation 4.11 is wrongly applied here, the nodal angular acceleration would then be zero. This would destroy the conservation of angular momentum and might lead the computation to divergence.

#### 4.3.2 Exponential mapping

When using Equation 4.4 to calculate the transformation matrix, special attention should be paid to a very small value of  $|\Delta\bar{\theta}|$ ; when  $|\Delta\bar{\theta}|$  is approaching zero (for example, while system approaches equilibrium),  $\Delta\bar{\theta}/|\Delta\bar{\theta}|$  will produce numerical error and cause the system to diverge. The solution is to avoid calculating  $\Delta\bar{\theta}/|\Delta\bar{\theta}|$  and, instead, to use exponential mapping to calculate the transformation matrix  $\mathbf{R}_T(\Delta\bar{\theta})$

$$\mathbf{R}_T(\Delta\bar{\theta}) = \exp \mathbf{A} = \sum_{k=0}^{\infty} \frac{1}{k!} \mathbf{A}^k \cong \mathbf{I} + \mathbf{A} + \frac{1}{2} \mathbf{A}^2 \quad (4.17)$$

where  $\mathbf{A}$  is a skew-symmetric matrix of rotation vector  $\Delta\bar{\theta}$ , which is defined as



$$\mathbf{A} = \text{Skew}(\Delta\bar{\boldsymbol{\theta}}) \equiv \begin{bmatrix} 0 & -\theta_z & \theta_y \\ \theta_z & 0 & -\theta_x \\ -\theta_y & \theta_x & 0 \end{bmatrix} \quad (4.18)$$

In our algorithm if  $|\Delta\bar{\boldsymbol{\theta}}|$  is smaller than 0.1, then Equation 4.17 is used to calculate the transformation matrix. Otherwise, Equation 4.4 is used.

#### 4.4 Co-rotation of beam-ends

A beam-end orientation will co-rotate like a rigid body with the node to which the beam-end is connected and this co-rotation is realized in our scheme by using the transformation matrix of the corresponding node to update the beam-end orientation

$${}^{n+1/2}\mathbf{R}_{E,j} = \mathbf{R}_T(\Delta t {}^n\bar{\boldsymbol{\omega}}_i) {}^{n-1/2}\mathbf{R}_{E,j} \quad (4.19)$$

where  $\bar{\boldsymbol{\omega}}$  is the angular velocity of node  $i$  to which beam-end  $j$  is connected.

#### 4.5 Residuals of nodes

The translation and rotation residuals of nodes are presented in the global coordinates. These residuals are the sums of internal forces and external forces. Because internal forces are presented in the beam coordinates, prior to their summation to form a node residual, they need to be transferred to the global coordinates. The residual of node  $i$  can thus be represented as

$$\begin{aligned} \bar{\mathbf{F}}_i &= \sum_j \mathbf{R}_{B,k} \bar{\mathbf{f}}_j + \bar{\mathbf{F}}_{ext,i} \\ \bar{\mathbf{T}}_i &= \sum_j \mathbf{R}_{B,k} \bar{\boldsymbol{\tau}}_j + \bar{\mathbf{T}}_{ext,i} \end{aligned} \quad (4.20)$$

where  $\bar{\mathbf{F}}_i$  and  $\bar{\mathbf{T}}_i$  are the node translation residual and the node rotation residual respectively,  $\bar{\mathbf{f}}_j$  and  $\bar{\boldsymbol{\tau}}_j$  are presented in the beam coordinates and are the internal translation force and the internal rotation

force, respectively, at beam-end  $j$  that is connected to node  $i$ ,  $\mathbf{R}_{B,k}$  is the beam orientation of beam element  $k$  to which beam-end  $j$  belongs, and  $\vec{F}_{ext,i}$  and  $\vec{T}_{ext,i}$  are the external translation force and the external rotation force exerted on node  $i$ .

#### 4.6 Optimized mass and inertia

Node mass, node inertia and time increment are crucial for controlling the stability of explicit time integration methods. Larger values of mass and inertia or a smaller time increment can help to stabilize the time integration. However, these settings can also decelerate the process toward an equilibrium. To resolve this dilemma, special approaches, which are introduced in this section, are employed.

##### 4.6.1 Integration stability

To ensure integration stability, we use the inequality suggested by Bathe [48] as

$$\Delta t \leq \frac{2}{\omega_0} \tag{4.21}$$

where  $\omega_0$  is the highest natural frequency in the structure. Bathe used the inequality to determine the optimized mesh length, whereas we use it to determine the lower bound of the node mass: For a linear structure that is composed of uniform axial elements with lumped masses, as shown in Figure 4.2.a,  $\omega_0$  is the eigenfrequency of a single element. It can be calculated as the angular frequency of a simple harmonic motion with a mass of  $M/2$  and an unstrained length of  $L/2$  as shown in Figure 4.2.b and Figure 4.2.c.

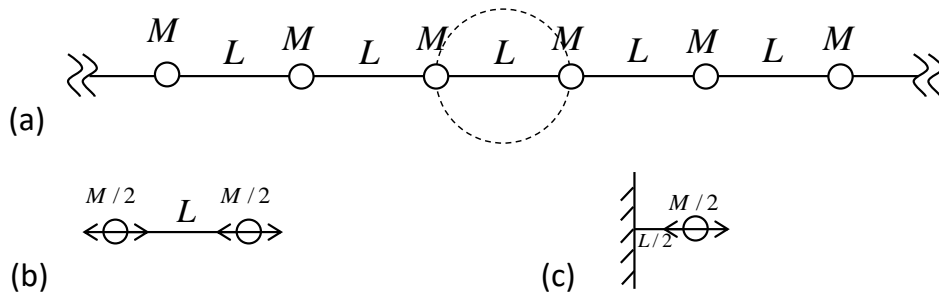


Figure 4.2: (a) Linear structure composed of uniform axial elements with lumped masses; (b) oscillation of one element; (c) equivalent simple harmonic motion

$$\omega_0 = \sqrt{\frac{EA/L}{M/2}} = 2\sqrt{\frac{EA}{LM}} \quad (4.22)$$

where  $E$  is the elastic modulus and  $A$  is the profile area. From the perspective of a single node in the structure,  $EA/L$  and  $M$  denote the node stiffness and the node mass, respectively. Therefore, Eq. (4.22) can be interpreted as the angular frequency of a constrained node as

$$\omega_0 = 2\sqrt{\frac{EA}{LM}} = 2\sqrt{\frac{K}{M}} \quad (4.23)$$

where  $M$  is the node mass and  $K$  is the node stiffness. By substituting  $\omega_0$  in Equation 4.21 with Equation 4.23, Inequality 4.21 can be represented in terms of the node mass and the node stiffness and we can use it to determine the lower bound of the node mass

$$\Delta t \leq \sqrt{\frac{K}{M}} \Leftrightarrow M = \alpha \Delta t^2 K, \quad \alpha \geq 1 \quad (4.24)$$

Similarly, the lower bound of the node inertia is determined by

$$M_r = \alpha \Delta t^2 K_r, \quad \alpha \geq 1 \quad (4.25)$$

where  $K_r$  is the direct node rotation stiffness.

#### 4.6.2 Mass matrix

Considering the direct stiffness of a beam-end, it has different stiffness values in the three local directions

$$\begin{bmatrix} k_x \\ k_y \\ k_z \end{bmatrix} = \begin{bmatrix} \frac{EA}{L} \\ \frac{12EI_z}{L^3} \\ \frac{12EI_y}{L^3} \end{bmatrix} \quad (4.26)$$

where  $k$  is the direct beam-end stiffness in a major local direction and the subscript marked the major local direction. If a scalar/lumped mass term is applied, in order to guarantee the stability in all directions, the mass in Equation 4.24 should be calculated with the maximum stiffness value among the three.

However, if the system is composed of slender elements, such that  $k_x$  is much larger than  $k_y$  or  $k_z$  (the beam-end mass is thus determined by the axial stiffness), the convergence rate will become extremely slow. This is because that the mass is too large for the lateral direction and results in a very small acceleration in that direction.

One solution is to use different mass values in different directions and in the form of a diagonal matrix [36]. Such a scaled mass term in a matrix form is used in our program as an option. For beam-end  $j$ ,  $\mathbf{k}_j$  is its translation stiffness matrix, and  $\mathbf{m}_j$  is its contribution to the translation node mass

$$\mathbf{m}_j = \alpha \Delta t^2 \mathbf{k}_j, \quad \alpha \geq 1, \quad \mathbf{k}_j = \begin{bmatrix} \frac{E_j A_j}{L_j} & 0 & 0 \\ 0 & \frac{12E_j I_{zj}}{L_j^3} & 0 \\ 0 & 0 & \frac{12E_j I_{yj}}{L_j^3} \end{bmatrix} \quad (4.27)$$

where  $\alpha$  is the scale parameter to ensure calculation convergence. This directionally related mass term is presented in the local coordinates of a beam element, and every beam-end will contribute its part to the connected node when composing the node mass matrix

$$\mathbf{M}_i = \sum_j \mathbf{R}_j \mathbf{m}_j \mathbf{R}_j^T \quad (4.28)$$

where  $\mathbf{R}_j$  is the beam orientation for transferring the mass matrix to the global coordinates prior to summation, and the subscript  $j$  indicates all beam elements that are connected to the node  $i$ .

#### 4.6.3 Scalar inertia

For the rotation motion, there are also different rotation stiffness values for the three local directions

$$\begin{bmatrix} k_{\tau,x} \\ k_{\tau,y} \\ k_{\tau,z} \end{bmatrix} = \begin{bmatrix} \frac{GJ}{L} \\ \frac{4EI_y}{L} \\ \frac{12EI_z}{L} \end{bmatrix} \quad (4.29)$$

where  $k_\tau$  is the direct rotation stiffness of a beam-end. Unlike the case of translation motion, the ratios between the three values of rotation stiffness are not related to the length. And with regular sections

and materials, these three values are in the same scale. Therefore, in the majority of cases, using a scalar inertia will not affect the convergence rate. In fact, when an inertia tensor is used, an iteration process is needed for solving the angular acceleration of a single time step (Section 4.3.1). It might take more computation time than using a scalar inertia.

To ensure integration stability in all directions, the scalar inertia is thus determined by the largest rotation stiffness value among the three

$$m_{\tau,j} = \alpha \Delta t^2 k_{\tau,j}, \quad \alpha \geq 1, \quad k_{\tau,j} = \max \left\{ \frac{G_j J_j}{L_j}; \frac{4E_j I_{y_j}}{L_j}; \frac{4E_j I_{z_j}}{L_j} \right\} \quad (4.30)$$

where  $m_{\tau}$  is the beam-end inertia and  $j$  denote the beam-end number. The node inertia is then calculated by summing all the inertia of the beam-ends that are connected to the node  $i$  as

$$M_{\tau,i} = \sum_j m_{\tau,j} \quad (4.31)$$

#### 4.6.4 Transformability between scalar mass and mass matrix

A term of scalar mass could also be applied in the form of the mass matrix. By setting a mass matrix as

$$\mathbf{m}_j = m_j \mathbf{I} = \alpha \Delta t^2 k_j \mathbf{I}, \quad \alpha \geq 1, \quad k_j = \max \left\{ \frac{E_j A_j}{l_j}; \frac{12E_j I_{z_j}}{l_j^3}; \frac{12E_j I_{y_j}}{l_j^3} \right\} \quad (4.32)$$

Equation 4.28 will transform to

$$\mathbf{M}_i = \sum_j \mathbf{R}_j \mathbf{m}_j \mathbf{R}_j^T = \sum_j m_j \mathbf{I} = M_i \mathbf{I} \quad (4.33)$$

This transformability enables the mass terms to have an integral and unified definition in our program, which eases the adoption of different mass terms.

#### 4.7 Time interval independent

The integration will become time interval independent if the optimized terms of mass and inertia are adopted, whether they are in the form of matrix or scalar. This can be proved in the following way:

By substituting Equation 3.21 into Equation 3.19 and considering the time step  $n=1$ , we get

$${}^{1+1/2}\bar{d} = {}^{1-1/2}\bar{d} + \Delta t ({}^0\bar{v} + \Delta t \mathbf{M}^{-1} {}^1\bar{F}) \quad (4.34)$$

With the definition of the optimized mass (Equation 4.28) and assuming that the initial velocity is zero, the above equation changes to

$${}^{1+1/2}\bar{d} = {}^{1-1/2}\bar{d} + \frac{1}{\alpha} {}^1\mathbf{K}^{-1} {}^1\bar{F} \quad (4.35)$$

Because  ${}^{1-1/2}\bar{d}$ ,  ${}^1\mathbf{K}^{-1}$  and  ${}^1\bar{F}$  are values of initial settings, they are time increment independent. Therefore  ${}^{1+1/2}\bar{d}$  is time increment independent. It can be proved in a similar way that  ${}^{1+1/2}\mathbf{R}_N$  is also time increment independent.

For the time step  $n=2$  we have

$${}^{2+1/2}\bar{d} = {}^{1+1/2}\bar{d} + \frac{1}{\alpha} ({}^1\mathbf{K}^{-1} {}^1\bar{F} + {}^2\mathbf{K}^{-1} {}^2\bar{F}) \quad (4.36)$$

Because  ${}^2\mathbf{K}^{-1}$  is a function of  ${}^{1+1/2}\bar{d}$  and  ${}^{1+1/2}\mathbf{R}_N$ ,  ${}^{2+1/2}\bar{d}$  is thus time increment independent. Since all the variable on the right-hand side of Equation 4.36 are time increment independent,  ${}^{2+1/2}\bar{d}$  is thus time increment independent. Following the rule of mathematical induction, we could show that the node positions and the node orientations are always time increment independent.

#### 4.8 Kinetic damping

Through the time integration formulations we are able to simulate dynamic systems. However, without damping, systems will never stop moving and a static equilibrium state will never be reached. We use the kinetic damping method, which sets every translation velocity and the angular velocity to zero once the kinetic energy of the system reaches a local peak. The corresponding kinetic energy is calculated as

$$E_K = E_{K,t} + E_{K,r} \quad (4.37)$$

where  $E_{K,t}$  is the translation kinetic energy, which is defined as

$$E_{K,t} = \frac{1}{2} \sum_i \bar{\mathbf{v}}_i^T \mathbf{M}_i \bar{\mathbf{v}}_i \quad (4.38)$$

and  $E_{K,r}$  is the rotation kinetic energy, which is defined as

$$E_{K,r} = \sum_i m_{r,i} |\bar{\omega}_i|^2 \quad (4.39)$$

## 4.9 Algorithm

### 4.9.1 Equilibrium criteria

The equilibrium condition is satisfied once the residual (including the translation residual and the rotation residual) of each node is less than the given criteria. In the majority of cases, rotation residuals decrease along with translation residuals; therefore, it is practical to use only one of them as the only indicator of convergence. If geometric constraints are involved, only the tangential components of the translation residuals are counted.

### 4.9.2 Computation procedure

The iteration computation procedure (program flowchart) is summarized in Figure 4.3.

## 4.10 Numerical test cases

Five test cases are presented in this section to verify the accuracy of our method for simulating structures that undergo large displacements and rotations. The first case is a curved cantilever subject to an end transversal force. The second case considers is a straight cantilever beam subject to an end torque such that a circle is the geometry of an equilibrium. The third case is a bended elastic rod



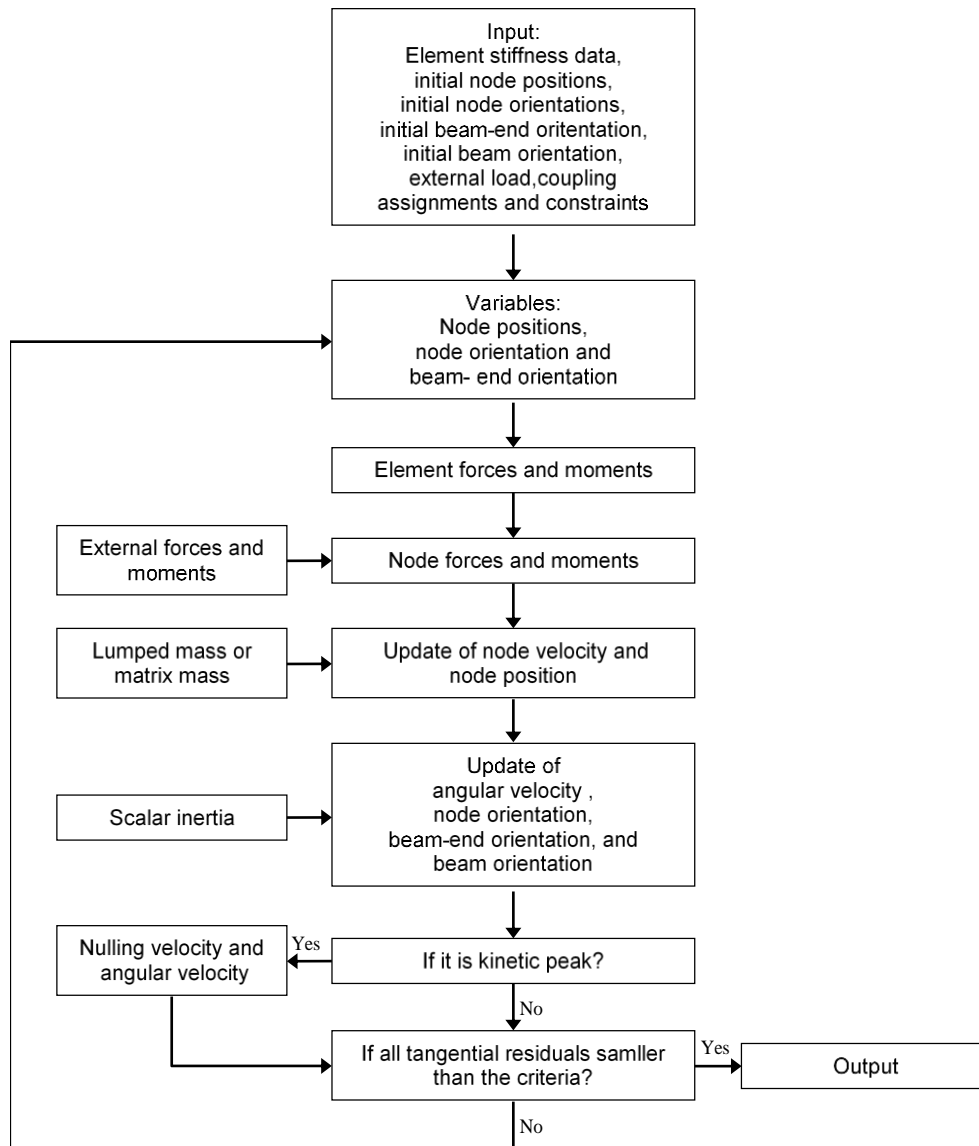


Figure 4.3: Program flowchart

subject to a torsion and lateral force in the middle. The fourth case uses geometry of the first case but changes the material and the profile properties. The fifth case is an extension of the fourth, which has a finer division.

From the discussion in Section 4.6, we know that the mass and inertia terms are calculated automatically according to the optimized terms. And in Section 4.7, we show that the time interval has no influence to the integration result once the optimized mass and inertia terms are applied. Therefore, in our program, there are only two things which could influence the convergence speed and stability. The first is whether to use scalar mass or mass matrix (Section 4.6.2 and Section 4.6.4). The second is the parameter  $\alpha$  in Equation 4.27 and Equation 4.30.

The influence of the choice of scalar mass or mass matrix will be illustrated in Section 5.2, where scalar mass is shown to be more numerically stable than mass matrix. The influence of  $\alpha$  will be illustrated in the sixth example of this section, and it shows that it is a good choice to have  $\alpha = 8$ . As a result, though the first to the fifth examples, scalar mass is applied and  $\alpha$  is set as 8.

#### 4.10.1 Bathe's curved cantilever

The curved cantilever beam proposed by Bathe and Bolourchi exhibits a 45-degree bent geometry with a radius of 100 in. It is composed of eight elements of equal length, lies in the x-y plane and is subject to a concentrated load in the z-direction (Figure 4.4). Elasticity and shear modulus are defined as  $E = 10^7$  psi and  $G = E/2$ , respectively. The cantilever exhibits a uniform square profile with a side length of 1 inch and is subject to an end transverse load of 600 lb in the z-direction. A comparison of the results of Bathe [49], Crisfield [50], Sofistik (commercial FEA software) and ours is provided in Table 4.2. The displacement of our simulation is very close to the results of others. Bathe and Crisfield are pioneers in the development of geometrically nonlinear FEA techniques. Their results are widely used as bench mark tests in the research field.

Table 4.2: End displacement of Bathe's curved cantilever.

	$\Delta x$ [in.]	$\Delta y$ [in.]	$\Delta z$ [in.]
Present	-13.554	-23.859	53.647
Bathe and Bolourchi	-13.4	-23.5	53.4
Crisfield	-13.63	-23.87	53.71
Sofistik	-13.559	-23.552	53.294

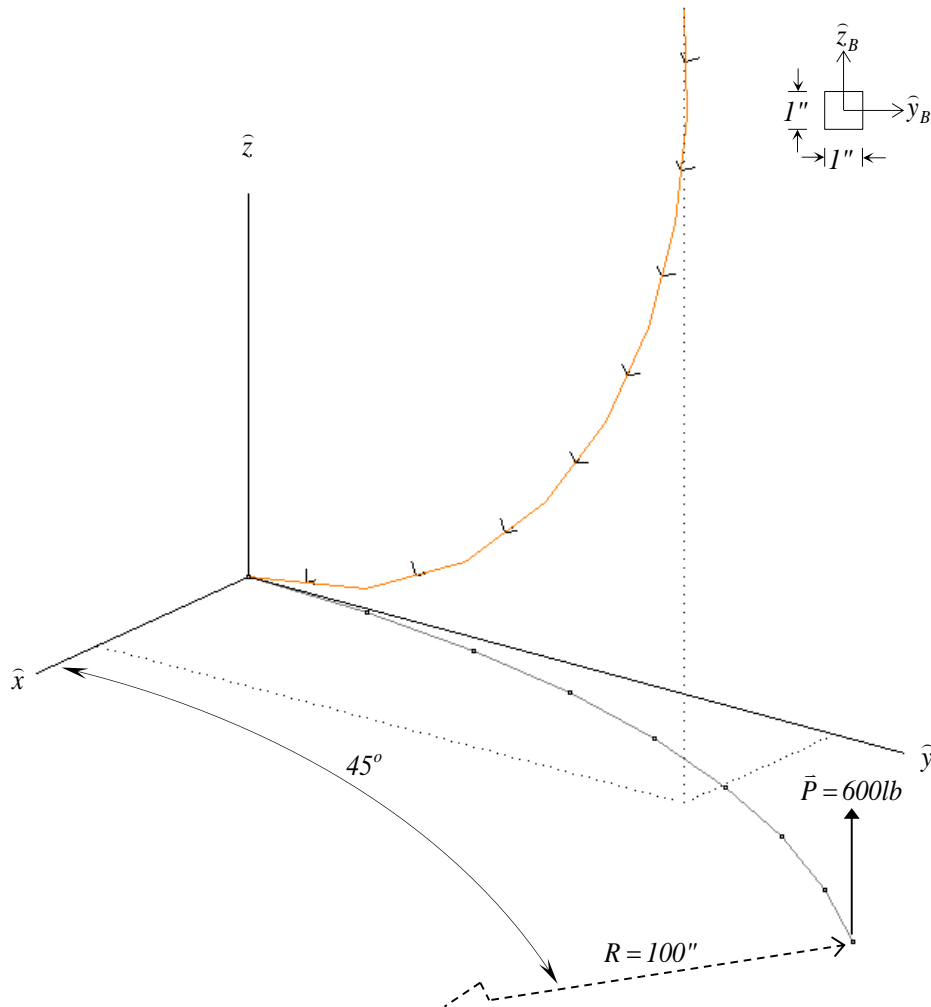


Figure 4.4: The initial geometry (gray) and the deformed geometry (orange) of a curved cantilever, which is subject to a lateral load, is shown here. The short and black line segments attached on the deformed geometry show the local beam orientations.

#### 4.10.2 Roll-up test

The test case proposed by Ibrahimbegovic [51] is a straight cantilever (Figure 4.5) which has a length of 10 (because there are no units in the original research, units are not used in this section) and is subject to an end bending moment  $T$  of a magnitude of  $20\pi$ . The section properties are as follows: axial stiffness  $EA$  is  $10^4$ , bending stiffness  $EI$  is  $10^2$ , and torsional stiffness  $GJ$  is  $10^2$ , which corresponds to a circular section of a diameter of 0.4.

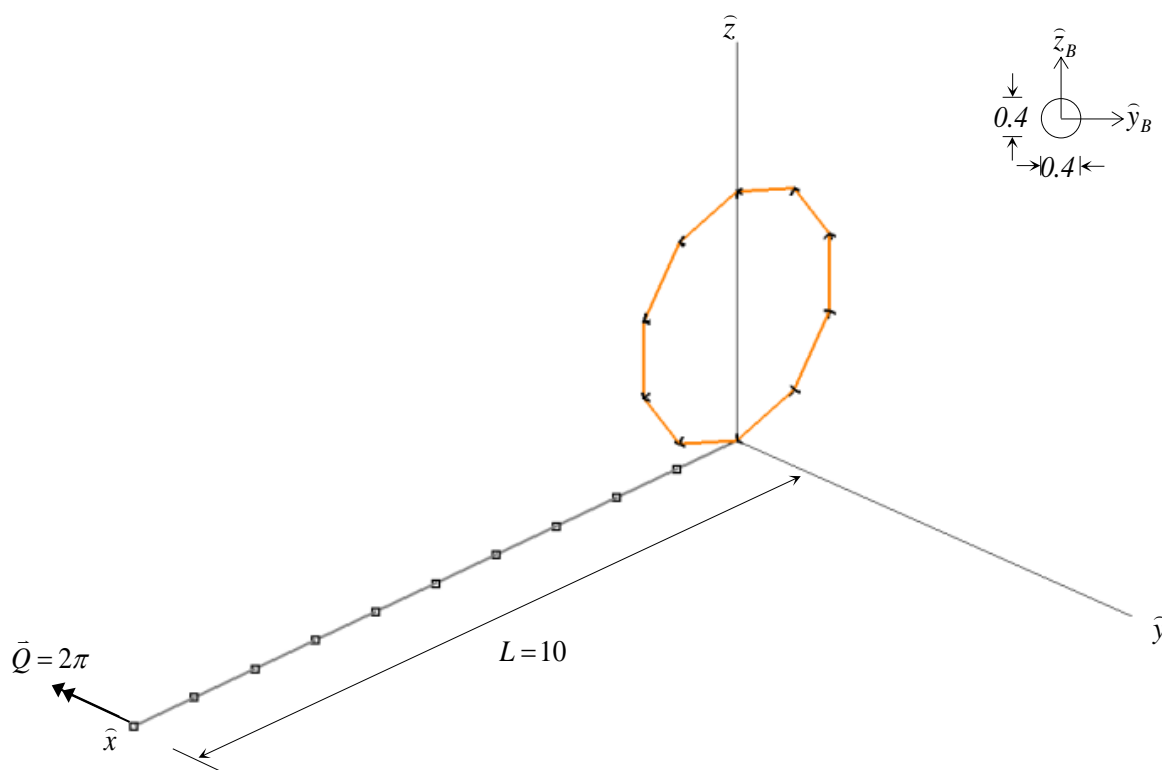


Figure 4.5: The initial geometry (gray) and the deformed geometry (orange) of a cantilever, which is subject to an end moment, is shown here. The short and black line segments attached on the deformed geometry show the local node orientations.

Table 4.3: displacement of cantilever subject to end moment

	$\Delta x$	$\Delta y$	$\Delta z$
present	$-1.7 \cdot 10^{-4}$	0	$9.4 \cdot 10^{-4}$
theoretical	0	0	0

According to the classical Euler formula,  $\theta = \frac{TL}{EI}$ , the end rotation should be exactly  $2\pi$ . Due to symmetry, the end node position should overlap with the supporting point, which is the coordinate origin. Our simulation result of the end position is listed in Table 4.3.

## 4.10.3 D'Amico' beam

The test proposed by D'Amico [7] considers an elastic bended rod subject to a torsion and a lateral force in the mid-span (Figure 4.6). The rod has a length of 10 m and is composed of 32 beam elements. Axial stiffness  $EA$  is set as  $100\text{MN N/mm}^2$ , bending stiffness  $EI$  is  $100\text{ kNm}^2$  ( $EI_x=EI_y=EI$ ), and torsion stiffness  $GJ$  is  $50\text{ kNm}^2$ . The rod is first bended by pushing the two ends toward each other. Then, the two ends are constrained translationally in three major directions and rotationally in global

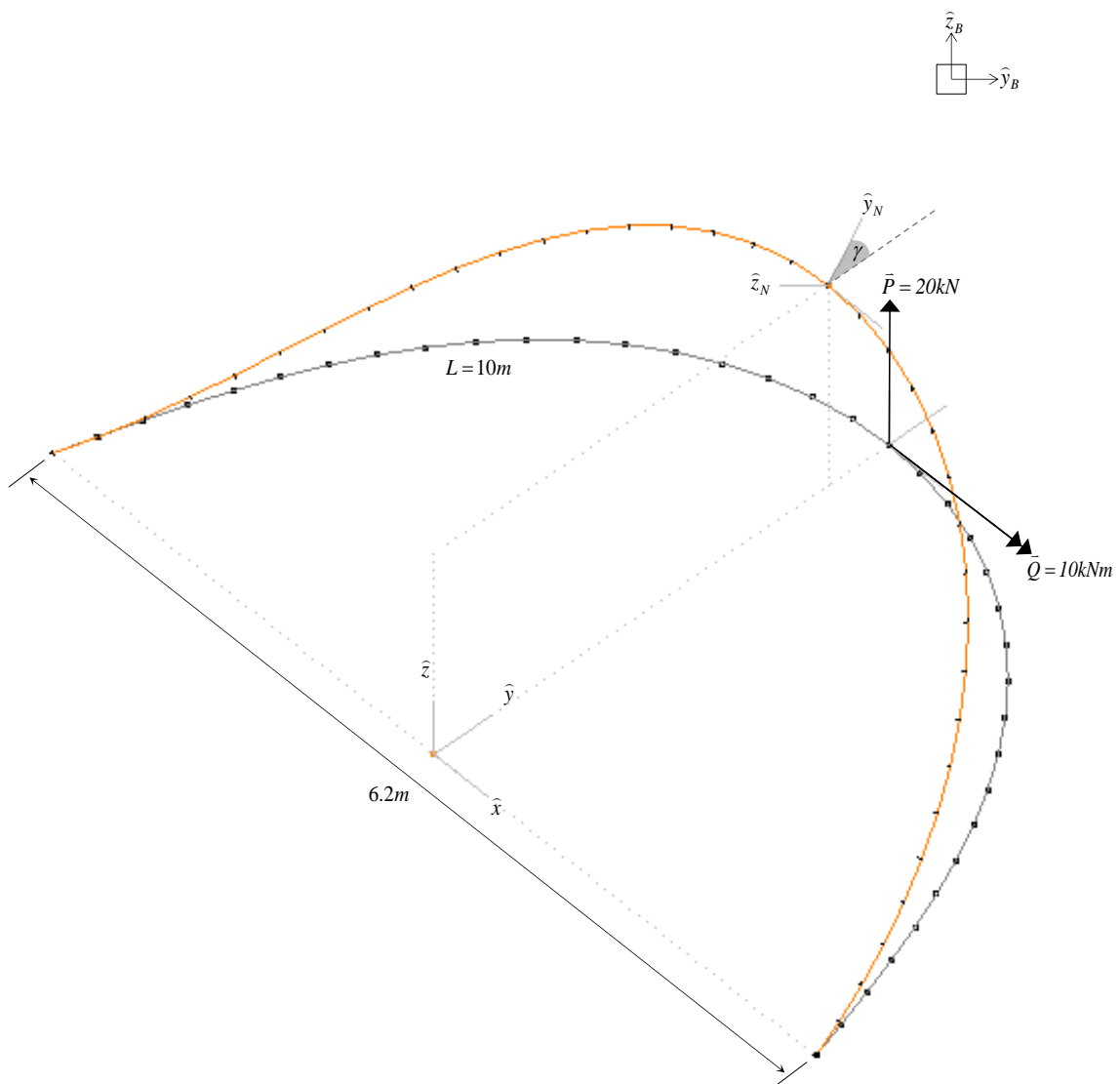


Figure 4.6: D'Amico's beam test. Transient geometry (gray) and final geometry (orange) of an initially straight rod, which is subject to a lateral force and a torque in the mid-span

x and y directions. Transverse load  $P$  in global z-direction and torsion moment  $Q$  in global x-direction are then applied to the mid-span node. The iteration terminates when the maxima node rotation residual is smaller than  $P \cdot 9.5^{-6} = 0.19 \text{ N}$ , as set in D'Amico's research. As shown in Table 4.4 and Table 4.5, the result from our method is very close to the result of D'Amico's.

Table 4.4: Displacement of the mid-span point

	D'Amico		present
	NR	DR	
y/L	0.2975	0.2980	0.2971
z/L	0.1633	0.1621	0.1630
$\gamma(\text{rad})$	0.9498	0.9442	0.9486

Table 4.5: Bending moment of selected elements

Elem. internal reaction [kNm]	Mx			My			Mz		
	D'Amico	present		D'Amico	present		D'Amico	present	
Elem. index	NR	DR		NR	DR		NR	DR	
1	5.03	5.00	5.03	-33.65	-33.38	-33.64	1.12	1.14	1.11
6	5.03	5.00	5.03	-20.75	-20.63	-20.73	13.81	13.84	13.77
11	5.03	5.00	5.03	-10.67	-10.65	-10.63	28.88	28.89	28.82
16	5.03	5.00	5.03	-3.61	-3.58	-3.53	44.56	44.50	44.48
21	-5.03	-5.00	-5.03	-3.61	-3.58	-3.53	44.56	44.50	44.48
26	-5.03	-5.00	-5.03	-10.67	-10.65	-10.63	28.88	28.89	28.82
31	-5.03	-5.00	-5.03	-20.75	-20.63	-20.73	13.81	13.84	13.77
36	-5.03	-5.00	-5.03	-33.65	-33.38	-33.64	1.12	1.14	1.11

#### 4.10.4 Bathe's beam with different sections and stiffness properties

In order to examine the stability and reliability of our method, a more extensive study is adopted, which tests different section profiles and materials and compares the displacements, the orientations and the internal forces derived from our program with the results of SOFISTIK and ANSYS.

The same geometry is taken from the model in Section 4.10.1. But the values of the elasticity and the shear modulus are changed to typical values of a wood material ( $E=1200 \text{ N/mm}^2$  and  $G=E/15=800 \text{ N/mm}^2$ ). The ratio of  $G/E$  is  $1/15$ , which is 7.5 times smaller than of the case in Section 4.10.1, and the rotation generated from torsion is thus expected to be larger. Models of different sections,  $25 \times 25 \text{ mm}$ ,  $100 \times 10 \text{ mm}$  and  $10 \times 100 \text{ mm}$ , are tested.

The results are shown in Figure 4.7 - Figure 4.9 and in Table 4.6 - Table 4.9. All the tests derived convergent results. Therefore, the question about if 6 DOF DR has stability problem against torsion should be answered.

Table 4.6: End displacement

	25x25			100x10			10x100		
	SOFISTIK	ANSYS	present	SOFISTIK	ANSYS	present	SOFISTIK	ANSYS	present
$\Delta x[\text{mm}]$	-2.02E+02	-2.09E+02	-2.08E+02	9.50E+01	9.48E+01	9.57E+01	-2.47E+02	-2.42E+02	-2.47E+02
$\Delta y[\text{mm}]$	-2.29E+02	-2.17E+02	-2.18E+02	-1.84E+02	-1.77E+02	-1.81E+02	-1.95E+02	-1.95E+02	-1.93E+02
$\Delta z[\text{mm}]$	9.11E+02	9.04E+02	9.06E+02	5.20E+02	5.05E+02	5.15E+02	9.17E+02	9.13E+02	9.16E+02
$\theta x[\text{rad}]$	3.04E-01	3.09E-01	2.71E-01	-4.51E-02	-4.36E-02	-8.53E-02	4.76E-01	4.77E-01	4.77E-01
$\theta y[\text{rad}]$	-9.47E-01	-9.28E-01	-9.38E-01	-8.38E-01	-8.19E-01	-8.22E-01	-6.39E-01	-6.27E-01	-6.36E-01
$\theta z[\text{rad}]$	-2.04E-01	-1.58E-01	-1.95E-01	-3.05E-01	-2.91E-01	-3.21E-01	1.12E-02	1.89E-02	-5.36E-03

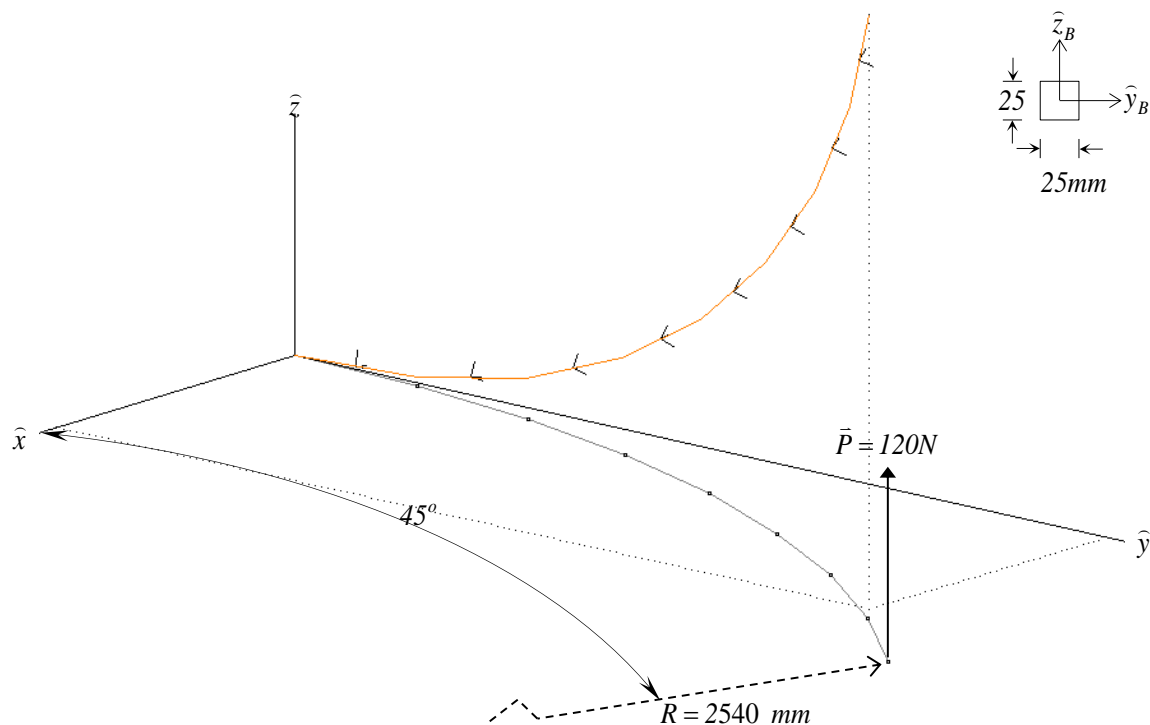


Figure 4.7: The initial geometry (gray) and the deformed geometry (orange) of a curved cantilever of a section profile 25x25mm, which is subject to a lateral load, are shown here. The short and black line segments attached on the deformed geometry show the local beam

Table 4.7.a: Internal forces 25x25

Elem. Nr.	$F_x$ [N]			$F_y$ [N]			$F_z$ [N]		
	SOFISTIK	ANSYS	present	SOFISTIK	ANSYS	present	SOFISTIK	ANSYS	present
1	6.94E+00	6.78E+00	6.97E+00	-1.87E+01	-1.80E+01	-1.84E+01	1.18E+02	1.17E+02	1.18E+02
3	3.87E+01	3.85E+01	3.87E+01	-6.01E+01	-6.08E+01	-6.15E+01	9.64E+01	9.55E+01	9.55E+01
5	6.59E+01	6.54E+01	6.56E+01	-8.38E+01	-6.45E+01	-6.50E+01	5.51E+01	7.72E+01	7.66E+01
7	8.44E+01	8.36E+01	8.36E+01	-7.41E+01	-5.14E+01	-5.19E+01	4.23E+01	6.94E+01	6.87E+01

Table 4.7.b: Internal forces 25x25

Elem. Nr.	$M_x$ [Nmm]			$M_y$ [Nmm]			$M_z$ [Nmm]		
	SOFISTIK	ANSYS	present	SOFISTIK	ANSYS	present	SOFISTIK	ANSYS	present
1	-5.50E+04	-5.48E+04	-5.42E+04	-1.75E+05	-1.75E+05	-1.76E+05	-2.44E+04	-2.16E+04	-2.42E+04
3	-2.78E+04	-2.68E+04	-2.66E+04	-1.11E+05	-1.12E+05	-1.11E+05	-5.81E+04	-5.91E+04	-6.07E+04
5	-1.12E+04	-1.02E+04	-1.01E+04	-4.73E+04	-6.27E+04	-6.21E+04	-5.85E+04	-4.33E+04	-4.40E+04
7	-1.71E+03	-1.67E+03	-1.65E+03	-1.64E+04	-2.56E+04	-2.54E+04	-2.54E+04	-1.69E+04	-1.71E+04



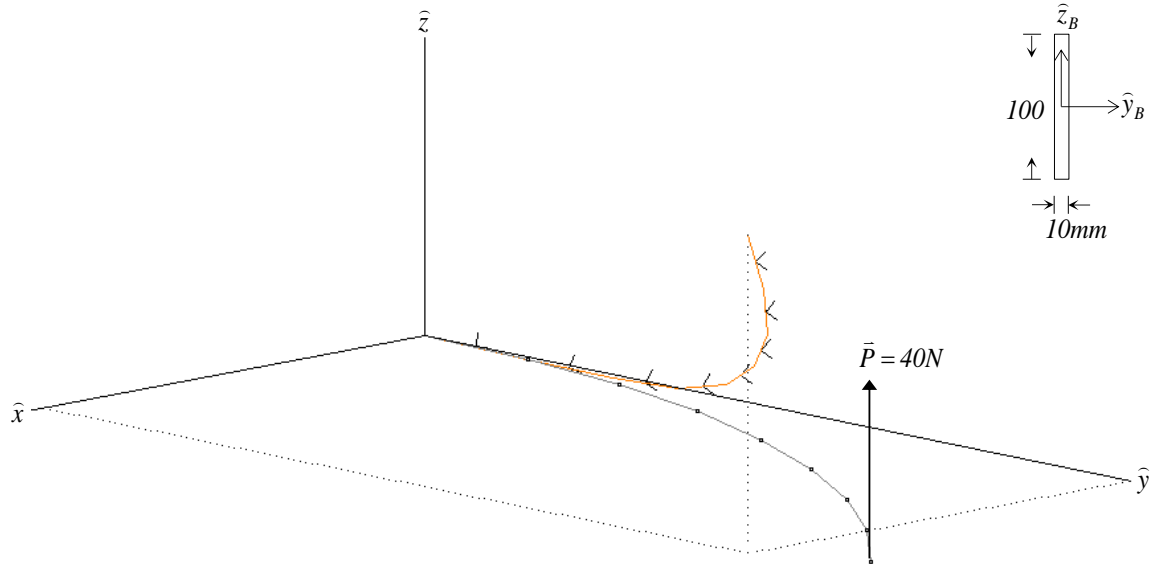


Figure 4.8: The initial geometry (gray) and the deformed geometry (orange) of a curved cantilever of a section profile 100x10mm, which is subject to a lateral load, are shown here. The short and black line segments attached on the deformed geometry show the local beam orientations.

Table 4.8.a: Internal forces 100x10

Elem. Nr.	$\bar{F}_x$ [N]			$\bar{F}_y$ [N]			$\bar{F}_z$ [N]		
	SOFISTIK	ANSYS	present	SOFISTIK	ANSYS	present	SOFISTIK	ANSYS	present
1	7.00E-02	1.11E-01	6.49E-02	-5.87E+00	-5.67E+00	-5.88E+00	3.96E+01	3.92E+01	3.96E+01
3	4.77E+00	4.67E+00	4.74E+00	-2.17E+01	-2.11E+01	-2.16E+01	3.33E+01	3.35E+01	3.33E+01
5	1.23E+01	1.20E+01	1.23E+01	-2.50E+01	-2.47E+01	-2.51E+01	2.87E+01	2.91E+01	2.86E+01
7	1.89E+01	1.83E+01	1.87E+01	-2.66E+01	-2.23E+01	-2.25E+01	2.31E+01	2.78E+01	2.73E+01

Table 4.8.b: Internal forces 100x10

Elem. Nr.	$\bar{M}_x$ [Nmm]			$\bar{M}_y$ [Nmm]			$\bar{M}_z$ [Nmm]		
	SOFISTIK	ANSYS	present	SOFISTIK	ANSYS	present	SOFISTIK	ANSYS	present
1	-2.96E+04	-2.97E+04	-2.96E+04	-6.08E+04	-6.05E+04	-6.09E+04	-8.96E+03	-8.00E+03	-8.99E+03
3	-1.51E+04	-1.54E+04	-1.51E+04	-4.07E+04	-4.13E+04	-4.08E+04	-2.44E+04	-2.36E+04	-2.44E+04
5	-5.34E+03	-5.43E+03	-5.25E+03	-2.41E+04	-2.45E+04	-2.41E+04	-1.87E+04	-1.85E+04	-1.88E+04
7	-7.60E+02	-8.07E+02	-7.51E+02	-8.70E+03	-1.03E+04	-1.02E+04	-9.39E+03	-7.76E+03	-7.87E+03

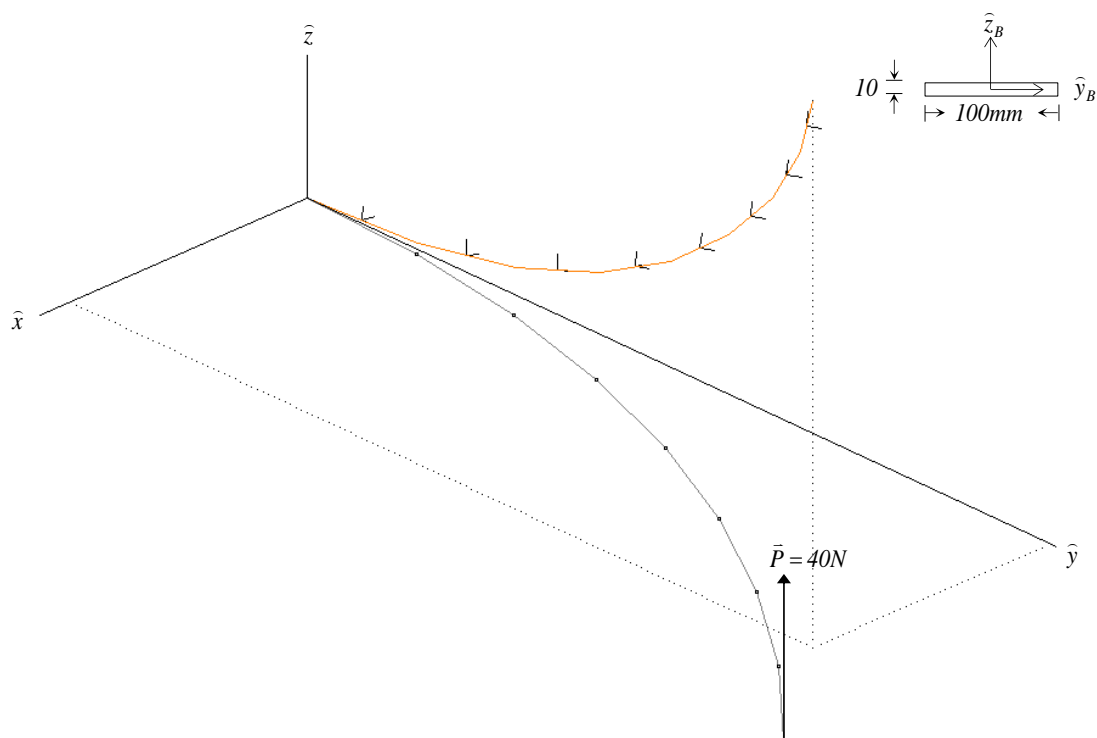


Figure 4.9: The initial geometry (gray) and the deformed geometry (orange) of a curved cantilever of a section profile 10x100mm, which is subject to a lateral load, are shown here. The short and black line segments attached on the deformed geometry show the local beam orientations.

Table 4.9.a: Internal forces 10x100

Elem. Nr.	$F_x[\text{N}]$			$F_y[\text{N}]$			$F_z[\text{N}]$		
	SOFISTIK	ANSYS	present	SOFISTIK	ANSYS	present	SOFISTIK	ANSYS	present
1	3.06E+00	2.96E+00	3.06E+00	-3.36E+00	-3.26E+00	-3.35E+00	3.97E+01	3.95E+01	3.97E+01
3	1.43E+01	1.42E+01	1.43E+01	-1.07E+01	-1.08E+01	-1.11E+01	3.58E+01	3.57E+01	3.57E+01
5	2.22E+01	2.21E+01	2.22E+01	-1.05E+01	-1.12E+01	-1.16E+01	3.15E+01	3.14E+01	3.12E+01
7	2.69E+01	2.67E+01	2.68E+01	-6.81E+00	-7.59E+00	-7.96E+00	2.88E+01	2.88E+01	2.86E+01

Table 4.9.b: Internal forces 10x100

Elem. Nr.	$M_x[\text{Nmm}]$			$M_y[\text{Nmm}]$			$M_z[\text{Nmm}]$		
	SOFISTIK	ANSYS	present	SOFISTIK	ANSYS	present	SOFISTIK	ANSYS	present
1	-1.69E+04	-1.72E+04	-1.69E+04	-5.98E+04	-5.97E+04	-5.99E+04	-3.76E+03	-3.24E+03	-3.75E+03
3	-8.87E+03	-8.91E+03	-8.84E+03	-4.17E+04	-4.17E+04	-4.16E+04	-8.96E+03	-8.92E+03	-9.45E+03
5	-3.74E+03	-3.73E+03	-3.73E+03	-2.53E+04	-2.53E+04	-2.52E+04	-5.82E+03	-6.34E+03	-6.70E+03
7	-6.60E+02	-6.53E+02	-6.63E+02	-1.06E+04	-1.06E+04	-1.05E+04	-1.90E+03	-2.16E+03	-2.31E+03

#### 4.10.5 Bathe's beam with finer division

In order to examine if the difference of the results of SOFISTIK, ANSYS and our method will decrease as the division becomes finer, the models are recreated with a finer division that each cantilever is composed of 32 beam elements instead of 8. The sections and the stiffness properties stay unchanged.

The results are shown in Figure 4.10 - Figure 4.12 and in Table 4.10 - Table 4.13, which show that there is still notable difference between the results of ANSYS and SOFISTIK.

Table 4.10: End displacement

	25x25			100x10			10x100		
	SOFISTIK	ANSYS	present	SOFISTIK	ANSYS	present	SOFISTIK	ANSYS	present
$\Delta x$ [mm]	-2.07E+02	-2.12E+02	-2.14E+02	8.96E+01	9.34E+01	8.94E+01	-2.49E+02	-2.45E+02	-2.50E+02
$\Delta y$ [mm]	-2.34E+02	-2.19E+02	-2.20E+02	-1.87E+02	-1.80E+02	-1.83E+02	-1.96E+02	-1.95E+02	-1.94E+02
$\Delta z$ [mm]	9.19E+02	9.10E+02	9.12E+02	5.32E+02	5.14E+02	5.27E+02	9.19E+02	9.16E+02	9.18E+02
$\theta x$ [rad]	3.03E-01	3.07E-01	2.68E-01	-4.37E-02	-4.27E-02	-8.40E-02	4.75E-01	4.74E-01	4.75E-01
$\theta y$ [rad]	-9.59E-01	-9.36E-01	-9.47E-01	-8.51E-01	-8.26E-01	-8.32E-01	-6.43E-01	-6.31E-01	-6.41E-01
$\theta z$ [rad]	-2.16E-01	-1.59E-01	-1.98E-01	-3.11E-01	-2.93E-01	-3.24E-01	1.05E-02	1.75E-02	-6.16E-03

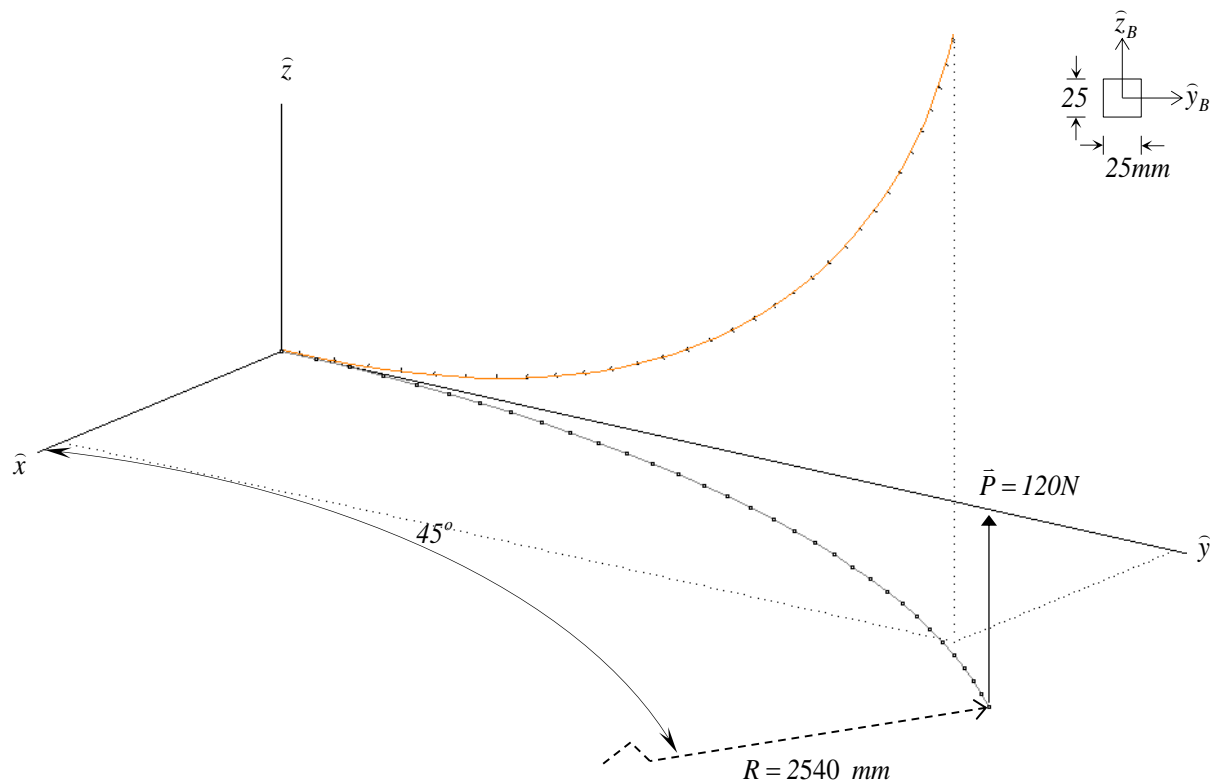


Figure 4.10: The initial geometry (gray) and the deformed geometry (orange) of a curved cantilever of a section profile 25x25mm, which is subject to a lateral load, are shown here. The short and black line segments attached on the deformed geometry show the local beam orientations.

Table 4.11.a: Internal forces

Elem. Nr.	$F_x$ [N]			$F_y$ [N]			$F_z$ [N]		
	SOFISTIK	ANSYS	present	SOFISTIK	ANSYS	present	SOFISTIK	ANSYS	present
1	1.78E+00	1.78E+00	1.79E+00	-5.31E+00	-5.15E+00	-5.23E+00	1.20E+02	1.20E+02	1.20E+02
11	4.10E+01	4.10E+01	4.11E+01	-6.22E+01	-6.28E+01	-6.35E+01	9.41E+01	9.36E+01	9.31E+01
21	7.32E+01	7.27E+01	7.26E+01	-8.70E+01	-6.19E+01	-6.25E+01	3.83E+01	7.31E+01	7.23E+01
31	9.14E+01	9.07E+01	9.03E+01	-5.98E+01	-4.19E+01	-4.24E+01	4.97E+01	6.75E+01	6.67E+01

Table 4.11.b: Internal forces

Elem. Nr.	$M_x$ [Nmm]			$M_y$ [Nmm]			$M_z$ [Nmm]		
	SOFISTIK	ANSYS	present	SOFISTIK	ANSYS	present	SOFISTIK	ANSYS	present
1	-6.21E+04	-6.16E+04	-6.12E+04	-1.84E+05	-1.86E+05	-1.86E+05	-7.25E+03	-6.93E+03	-7.20E+03
11	-2.69E+04	-2.56E+04	-2.54E+04	-1.06E+05	-1.07E+05	-1.06E+05	-5.85E+04	-6.05E+04	-6.13E+04
21	-7.49E+03	-6.88E+03	-6.81E+03	-2.93E+04	-4.97E+04	-4.92E+04	-5.23E+04	-3.53E+04	-3.57E+04
31	-1.00E+02	-1.03E+02	-1.02E+02	-4.69E+03	-6.30E+03	-6.23E+03	-5.46E+03	-3.78E+03	-3.82E+03

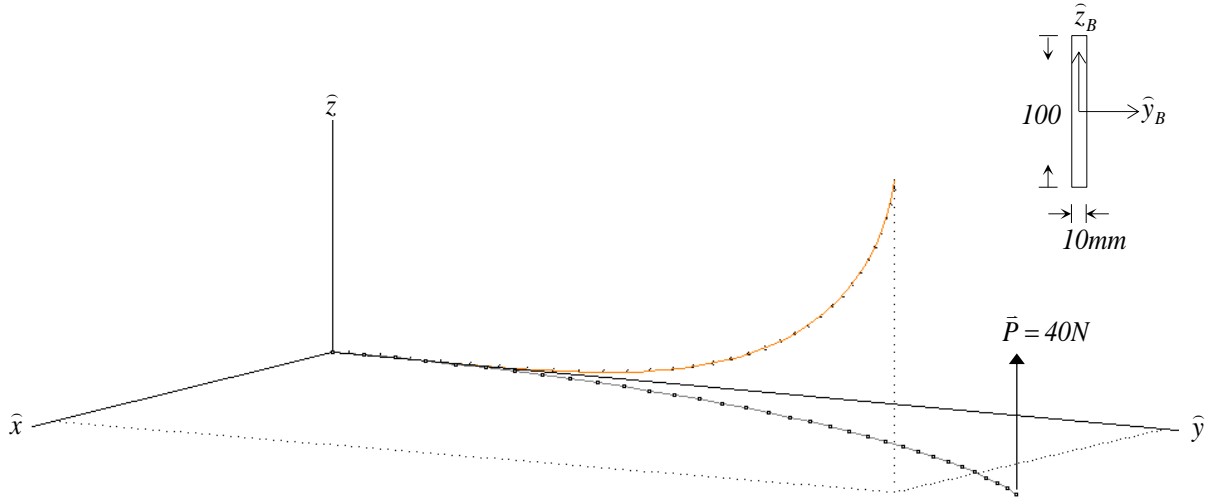


Figure 4.11: The initial geometry (gray) and the deformed geometry (orange) of a curved cantilever of a section profile 100x10mm, which is subject to a lateral load, are shown here. The short and black line segments attached on the deformed geometry show the local beam orientations.

Table 4.12.a: Internal forces

Elem. Nr.	$\underline{F_x[N]}$			$\underline{F_y[N]}$			$\underline{F_z[N]}$		
	SOFISTIK	ANSYS	present	SOFISTIK	ANSYS	present	SOFISTIK	ANSYS	present
1	1.00E-02	8.37E-03	8.96E-03	-1.62E+00	-1.57E+00	-1.62E+00	4.00E+01	3.99E+01	4.00E+01
11	5.39E+00	5.23E+00	5.39E+00	-2.23E+01	-2.20E+01	-2.25E+01	3.28E+01	3.30E+01	3.26E+01
21	1.48E+01	1.44E+01	1.48E+01	-2.86E+01	-2.44E+01	-2.48E+01	2.37E+01	2.82E+01	2.77E+01
31	2.20E+01	2.11E+01	2.16E+01	-2.51E+01	-2.00E+01	-2.02E+01	2.22E+01	2.75E+01	2.69E+01

Table 4.12.b: Internal forces

Elem. Nr.	$\underline{M_x[Nmm]}$			$\underline{M_y[Nmm]}$			$\underline{M_z[Nmm]}$		
	SOFISTIK	ANSYS	present	SOFISTIK	ANSYS	present	SOFISTIK	ANSYS	present
1	-3.25E+04	-3.27E+04	-3.25E+04	-6.35E+04	-6.38E+04	-6.37E+04	-2.56E+03	-2.45E+03	-2.57E+03
11	-1.44E+04	-1.45E+04	-1.44E+04	-3.93E+04	-3.98E+04	-3.93E+04	-2.43E+04	-2.42E+04	-2.47E+04
21	-3.54E+03	-3.48E+03	-3.42E+03	-1.69E+04	-1.98E+04	-1.94E+04	-1.81E+04	-1.54E+04	-1.56E+04
31	-4.00E+01	-4.40E+01	-4.25E+01	-2.08E+03	-2.57E+03	-2.52E+03	-2.31E+03	-1.83E+03	-1.85E+03

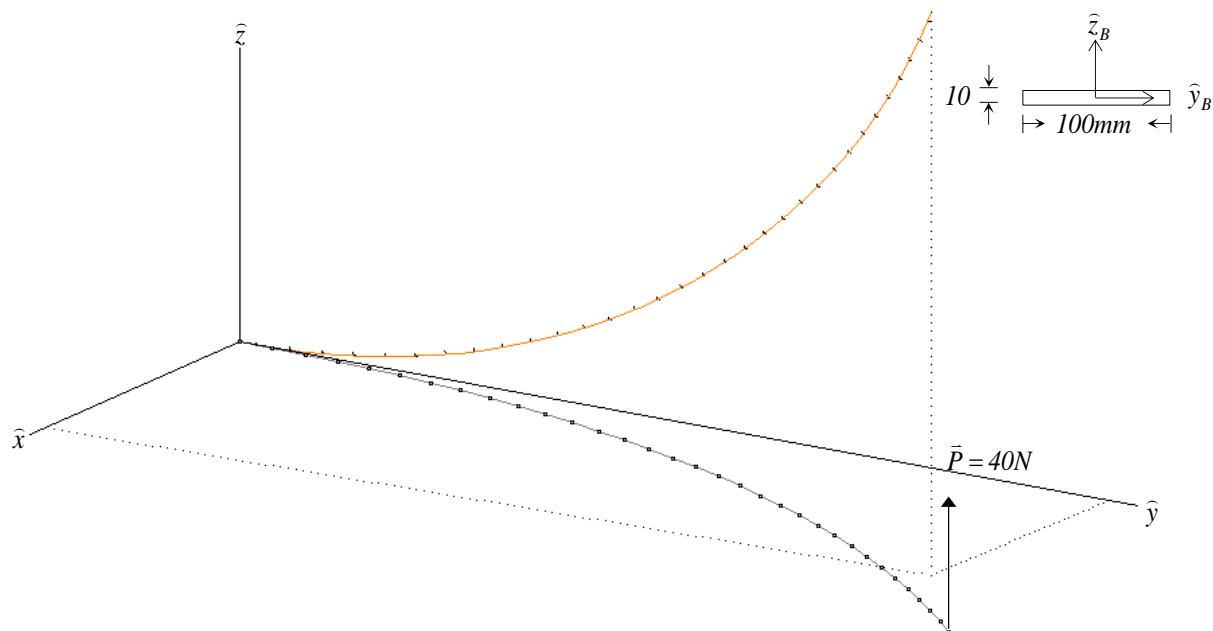


Figure 4.12: The initial geometry (gray) and the deformed geometry (orange) of a curved cantilever of a section profile 10x100mm, which is subject to a lateral load, are shown here. The short and black line segments attached on the deformed geometry show the local beam orientations.

Table 4.13.a: Internal forces

Elem. Nr.	Fx[N]			Fy[N]			Fz[N]		
	SOFISTIK	ANSYS	present	SOFISTIK	ANSYS	present	SOFISTIK	ANSYS	present
1	7.90E-01	7.85E-01	7.91E-01	-9.47E-01	-9.24E-01	-9.46E-01	4.00E+01	4.00E+01	4.00E+01
11	1.50E+01	1.50E+01	1.50E+01	-1.10E+01	-1.12E+01	-1.15E+01	3.54E+01	3.54E+01	3.53E+01
21	2.41E+01	2.40E+01	2.40E+01	-9.70E+00	-1.06E+01	-1.09E+01	3.05E+01	3.02E+01	3.01E+01
31	2.82E+01	2.81E+01	2.81E+01	-4.33E+00	-4.80E+00	-5.16E+00	2.81E+01	2.82E+01	2.80E+01

Table 4.13.b: Internal forces

Elem. Nr.	Mx[Nmm]			My[Nmm]			Mz[Nmm]		
	SOFISTIK	ANSYS	present	SOFISTIK	ANSYS	present	SOFISTIK	ANSYS	present
1	-1.90E+04	-1.92E+04	-1.90E+04	-6.30E+04	-6.30E+04	-6.31E+04	-1.12E+03	-1.04E+03	-1.12E+03
11	-8.52E+03	-8.61E+03	-8.50E+03	-4.05E+04	-4.05E+04	-4.04E+04	-8.96E+03	-9.17E+03	-9.54E+03
21	-2.62E+03	-2.64E+03	-2.61E+03	-2.05E+04	-2.05E+04	-2.04E+04	-4.45E+03	-5.07E+03	-5.31E+03
31	-4.00E+01	-4.26E+01	-4.25E+01	-2.62E+03	-2.63E+03	-2.61E+03	-3.55E+02	-4.06E+02	-4.39E+02

#### 4.10.6 Influence of parameter $\alpha$

The models illustrated in Section 4.10.4 and Section 4.10.3 are used here to show the influence of  $\alpha$  to the convergence speed and stability, which are occurred in Eq. (27) and Eq. (40). As shown in Table 4.14a and Table 4.14b, the iteration number  $n$  increases as  $\alpha$  increases.  $n$  is approximately proportional to  $\sqrt{\alpha}$ .

Table 4.14a: Barthe`s Beam 25x25

$\alpha$	4	8	16	32	64
number of Iteration	div.	32413	47966	59028	80174

Table 4.14b: D`Amico`s Beam

$\alpha$	4	8	16	32	64
Number of Iteration	div.	19977	22218	36136	53507

## Chapter 5

### SIMULATION WITH FICTITIOUS ELEMENTS

#### 5.1 Introduction

As illustrated in Section 4.6.2, the problem of the low convergence rate caused by a small stiffness ratio between the transverse direction and the axial direction may be solved by using mass matrix. However, the application of mass matrix has its own limitation: When the stiffness ratio is small and the included angle exceeds a certain degree, numerical instability occurs. In such a situation, mass matrix is no more applicable, and a corresponding solution is needed.

The stiffness ratio is one of the most important factors which influence the convergence rate. According to our research, the convergence rate reaches the best efficiency when the ratio approaches the value of one. Using this character, a new method is proposed. The method uses fictitious elements of the proper stiffness ratio to simulate the actual systems. The convergence rate is thus optimized.

In this chapter, the influence of the stiffness ratio and the application limitation of mass matrix are first illustrated. The new method using the fictitious elements is then introduced. Related examples are given in the final place.

#### 5.2 Observation of convergence rate and stability

A cantilever structure similar to the model shown in Section 4.10.2 is introduced here to illustrate the valuables which influence the convergence rate. Since the system will become time interval independent when the optimized mass terms are implied (Section 4.7), we could simply set  $\Delta t = 1$  and make it dimensionless. Similarly, if we rescale the geometric size of the system as

$$\bar{q}_0' = \bar{q}_0 / L_{char} \tag{5.1}$$



where  $L_{char}$  is the characteristic length of the system, the acceleration and velocity will become dimensionless too. The convergence rate will then be related to the four ratios only, which are listed below

$$\begin{aligned}
 C_{Ty} &= 12I_z / AL^2 \\
 C_{Tz} &= 12I_y / AL^2 \\
 C_{Ry} &= EI_z / GJ \\
 C_{Rz} &= EI_y / GJ
 \end{aligned} \tag{5.2}$$

The third and the fourth ratios do not change with the element length and are on a scale of 0.1 to 10 in the majority of cases. This is because I and J are on the same scale for solid profiles and closed thin profiles and E/G varies from 0.5 (steel) to 1/15 (timber) for usual structure materials.

The first and the second ratios are largely determined by the element length, which is determined by the division of the system. And these two ratios are the final dominant factors for the convergence rate.

For a rectangular profile,  $C_{Ty}$  can be calculated as

$$C_{Ty} = \frac{12I_z}{AL^2} = \frac{bh^3}{bhL^2} = \left(\frac{h}{L}\right)^2 \tag{5.3}$$

where h and b are the height and the width of the beam element respectively. In the majority of cases,  $\frac{h}{L}$  is a value between 1 and 1/30 and  $C_{Ty}$  is thus a value between 1 and 1/1000. In the following paragraphs, the influence of these ratios to the convergence rate is investigated.

A cantilever structure similar to the model in Section 4.10.2 is adopted here to demonstrate the influence of  $C_{Ty}$  when different mass terms are applied. Two groups of models are tested. The models in the first group have a division of 10 segments and a segment length of 1m. Models in the second group have a division of 20 segments and a segment length of 0.5m. The elastic modulus E is set as 12000 N/mm<sup>2</sup> in both groups.

Table 5.1: Cantilever with a division of 10 segments

b [mm]	31623	10000	3162	1000	316	100	32	10
$C_{Ty}$ [-]	1.0E+03	1.0E+02	1.0E+01	1.0E+00	1.0E-01	1.0E-02	1.0E-03	1.0E-04
Number of Iteration								
scalar mass	div.	3066	2845	2992	6249	18962	44655	121308
mass matrix	none	div.	7363	2992	3905	8631	div.	none

Table 5.2: Cantilever with a division of 20 segments

b [mm]	15811	5000	1581	500	158	50	16	5
$C_{Ty}$ [-]	1.0E+03	1.0E+02	1.0E+01	1.0E+00	1.0E-01	1.0E-02	1.0E-03	1.0E-04
Number of Iteration								
scalar mass	div.	7816	10100	8532	18616	45723	none	352976
mass matrix	none	div.	7071	8532	13794	div.	none	none

In order to test the influence of  $C_{Ty}$ , various section dimensions are tested. The side length  $b$  of the square profile is determined in a way such that  $C_{Ty}$  is varied as a geometric sequence, which is calculated as  $C_{Ty} = \left(\frac{b}{L}\right)^2$ . The applied bending moment at the end is calculated as  $M = \frac{2\pi EI}{L}$ , where  $L$  is the cantilever length, so that the deformed rod will form a closed circle. The iteration is set to terminate when the maxima residual torque of all nodes is smaller than  $M \cdot 10^{-6}$ .

As shown in Table 5.1 and Table 5.2, when  $C_{Ty}$  is close to the value of one, the system reaches its highest convergence rate. Systems with scalar mass exhibit very low convergence rate when  $C_{Ty}$  becomes small. The result also shows that the use of mass matrix can speed up the convergence rate. However, when the value of  $C_{Ty}$  is out of a specific domain, the computation diverges.

### 5.3 Influence of division

When  $C_{Ty}$  is much smaller than one and causes a low convergence rate, a possible solution is to have a finer division such that  $C_{Ty}$  approaches one. However, the convergence rate is proportional to  $1/N^{4/3}$ , where  $N$  is the total number of elements in the system. The drawback caused by the increased number of elements is thus larger than the benefit gained from an optimized value of  $C_{Ty}$  (from Table 5.1, when  $C_{Ty} < 1$ , the convergence rate is proportional to  $C_{Ty}^{2/5}$  approximately).

### 5.4 Method to speed up the convergence rate

We propose a new method which is named as Fictitious Element Dynamic Relaxation (FEDR) to speed up the convergence rate, which uses the fictitious section area to adjust the value of  $C_{Ty}$  to be close to the value of one and uses the fictitious unstrained length to adjust the strained length to be the same as of the actual section area. This method is based upon the fact that the force diagram is a function of the strained geometry. If the strained geometries are the same, the force diagrams are also the same. Therefore, many different physical systems may correspond to the same force diagram. As a result, it is possible to use fictitious elements to replace the actual elements and still get the same result. This idea will be further illustrated in the following section.

#### 5.4.1 One force diagram can be shared by many systems

A force diagram may be related to different physical systems. This idea is illustrated in Figure 5.1, where a force diagram is shared by the two hanging chain systems. The force diagram may be derived from a rather stiff system as shown on the left-hand side of Figure 5.1 or from a rather soft system on the right-hand side. If both systems have the same strained geometry, their force diagrams will be the same and so do their internal forces.

If the simulation convergence rate of the soft system is faster than that of the stiff system, it is better to use the soft system to simulate the stiff one because it is faster and gives the same result.

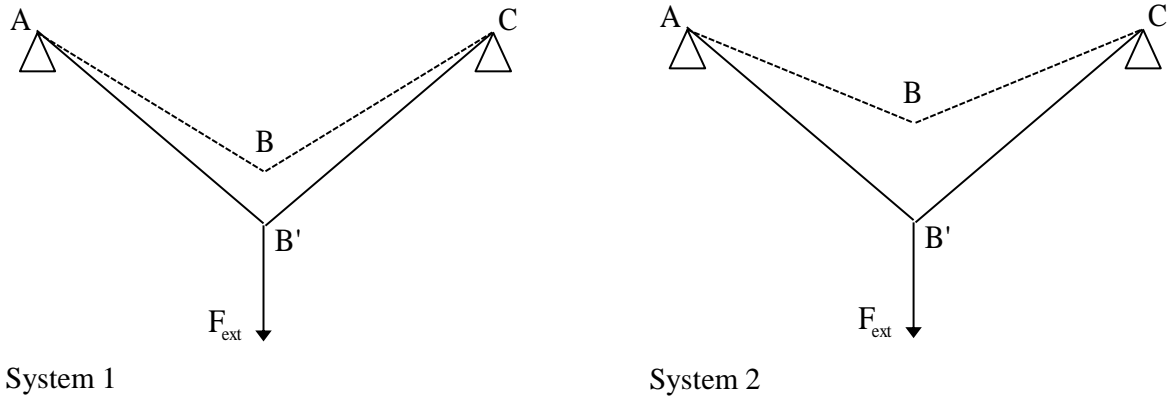


Figure 5.1: Two different systems may have the same strained geometry and thus have the same force diagram and internal forces.

#### 5.4.2 Fictitious section area and fictitious unstrained length

This idea can be applied not only to hanging chain systems but also to the systems composed of elastic beam elements.

In order to adjust  $C_{T_y}$  and  $C_{T_z}$  to the desired value to speed up the convergence rate, the fictitious area  $A_{ficti}$  is used to replace the actual area and is set as

$$A_{ficti} = \frac{12}{L_0^2} \sqrt{I_y \cdot I_z} \quad (5.4)$$

This replacement will affect the axial stiffness and thus effect the strained length. In order to get the same strained length as of the actual section area, the fictitious unstrained length has to be applied.

Unlike  $A_{ficti}$ , the fictitious unstrained length  $L_{0,ficti}$  needs to be decided and assigned iteratively. An additional loop for the length iteration is thus added outside the existing loop. The inner loop is named as the equilibrium iteration loop, and the outer loop is named as the length iteration loop. For each length iteration,  $L_{0,ficti}$  is assigned as

$$\begin{aligned}
L_{0, ficti}^1 &= L_0 \\
L_{0, ficti}^2 &= L_{0, ficti}^1 + (L_{goal}^2 - L_s^1) \\
&\vdots \\
L_{0, ficti}^n &= L_{0, ficti}^{n-1} + (L_{goal}^n - L_s^{n-1})
\end{aligned} \tag{5.5}$$

where  $L_0$  is the actual unstrained length,  $L_{goal}$  is the goal length of this length iteration,  $L_s$  is the strained length derived from the last length iteration and the superscript  $n$  denote the number of the length iteration. In order to generate the same extended length as of the actual area,  $L_{goal}$  is calculated as

$$L_{goal}^n = L_0 \left( 1 + \frac{f_x^{n-1}}{EA} \right) \tag{5.6}$$

where  $f_x$  is the axial internal force derived in the last length iteration and is calculated as

$$f_x = EA_{ficti} \cdot \frac{L_s - L_{0, ficti}}{L_{0, ficti}} \tag{5.7}$$

If the axial deformation is negligible or insignificant,  $L_{goal}$  could be simply assigned as the actual unstrained length  $L_0$ , with which a rigid length is assumed.

Readers might ask why not having the update of  $L_{0, ficti}$  at the end of the inner loop so that the length can be updated in each equilibrium iteration. This idea has been examined and proved by us to be not feasible. The reason is that the frequent change of unstrained lengths simply leads the calculation to a divergence.

### 5.4.3 Precision control

It is obvious that the strained length of a fictitious element  $L_s$  will never approach its goal length  $L_{goal}$  if the value of the equilibrium control  $e_{equi,control}$  is too large. A relation which determines the value of  $e_{equi,control}$  is proposed

$$e_{equi,control} = e_{length,control} \cdot E \cdot A_{ficti} \quad (5.8)$$

where  $e_{length,control}$  is a value which controls the difference between the values of  $L_{goal}$  and  $L_s$ . This difference is defined as

$$e_{length,i} = \frac{|L_{goal,i} - L_{s,i}|}{L_{goal,i}} \quad (5.9)$$

where the subscript i denotes the i-th beam element. If all  $e_{length,i}$  is small than  $e_{length,control}$ , then the fictitious system reaches the required precision so that the strained geometry of the fictitious system is close enough to that of the actual system.

However, it is not necessary and time consuming to have a very small value of  $e_{equi,control}$  for the initial length iterations. Therefore, in our program, there is an option to set  $e_{equi,control}$  as a valuable which decrease gradually: The equilibrium criterion starts from an initial value,  $e_{equi,control} = e_{equi,control}^0$ , and when the inner loop reaches an equilibrium, the following inequality is checked for every elements

$$e_{length,i} \leq e_{length,control} \equiv \frac{e_{equi,control}}{E \cdot A_{ficti}} \quad (5.10)$$

If it is not satisfied for all elements, only the length update is executed. If it is satisfied for all elements,  $e_{equi,control}$  will decrease by a factor of 10, and  $e_{length,control}$  will change accordingly.

#### 5.4.4 Extremely short elements (when the transvers stiffness is much larger than the axial stiffness)

As shown in Table 5.1 and Table 5.2, when  $C_{Ty} \gg 1$  (an extremely short element), the calculation diverges. This is because that, when  $C_{Ty} \gg 1$ , the transverse stiffness is much larger than the axial one, the strained lengths might then be too much compressed and cause the computation unstable. This problem can also be solved by using the fictitious elements and setting the unstrained fictitious length  $L_{goal}$  equal to  $L_0$ . A rigid length is then assumed and the corresponding axial forces could be derived with Equation 5.7.

### 5.5 Computation procedure

Where to place the length iteration loop is illustrated in Figure 5.2.

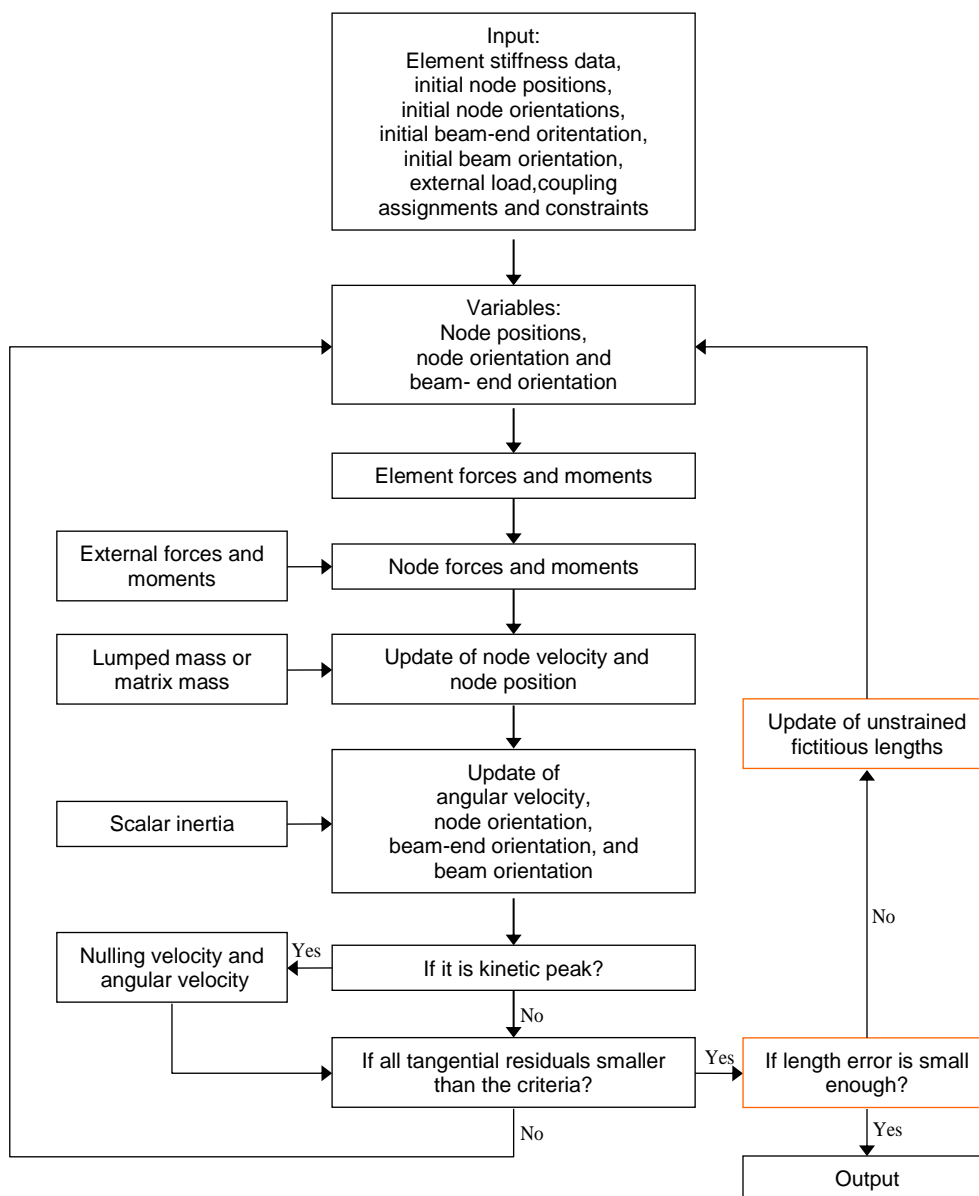


Figure 5.2: Program flowchart which includes the length iteration loop (the orange marks the newly added blocks)



## 5.6 Test cases -- Comparison between DR and FEDR

To test the robustness and the correctness of the method, the test cases introduced in Section 4.10 are recalculated with the new method. The equilibrium iteration loop is terminated when the node residual is smaller than  $P*1E-6$  and the length iteration loop is terminated when the length error ratio is smaller  $1E-7$ .

If FEDR is applied, the use of  $A_{ficti}$  will change the values of  $C_{Ty}$  and  $C_{Tz}$  such that they will be closer to the unit as shown in Table 5.3. A comparison of the convergence rate is done between the cases when different mass terms are applied. The result is shown in Table 5.4 and Table 5.5. The comparisons shows the proposed method does not have convergence problem, and in the majority of cases it convergences faster than that using mass matrix only. To show the correctness of our method, a comparison of the displacement and the orientation of the end node and a comparison of internal forces is also provided. As shown in Table 5.6-Table 5.9, the result of the FEDR is very close to that of DR.

Table 5.3:  $C_{Ty}$  and  $C_{Tz}$ , of DR and FEDR

	25x25		100x10		10x100	
	8	32	8	32	8	32
$C_{Ty}$ (DR)	1.0E-02	1.6E-01	1.6E-01	2.6E+00	1.6E-03	2.6E-02
$C_{Tz}$ (DR)	1.0E-02	1.6E-01	1.6E-03	2.6E-02	1.6E-01	2.6E+00
$reaCA=(C_{Ty}*C_{Tz})^{0.5}$	1.0E-02	1.6E-01	1.6E-02	2.6E-01	1.6E-02	2.6E-01
$C_{Ty}'=C_{Ty}/reaCA$ (FEDR)	1.0E+00	1.0E+00	1.0E+01	1.0E+01	1.0E-01	1.0E-01
$C_{Tz}'=C_{Tz}/reaCA$ (FEDR)	1.0E+00	1.0E+00	1.0E-01	1.0E-01	1.0E+01	1.0E+01

Table 5.4: Comparison of convergence rate (iteration number)

	25x25		100x10		10x100	
	8	32	8	32	8	32
DR with scalar mass	32413	74689	82306	1054618	61681	486744
DR with mass matrix	div.	93441	div.	229008	23622	225019
FEDR with mass matrix	5490	52410	26745	290535	17969	180059

Table 5.5: Comparison of convergence rate (percentage)

	25x25		100x10		10x100	
	8	32	8	32	8	32
DR with scalar mass	1	1	1	1	1	1
DR with mass matrix	none	125%	none	22%	38%	46%
FEDR with mass matrix	17%	70%	32%	28%	29%	37%

Table 5.6: Comparison of end displacements of DR and FEDR

	25x25		100x10		10x100	
	DR	FEDR	DR	FEDR	DR	FEDR
$\Delta x$ [mm]	-2.1414E+02	-2.1411E+02	8.9390E+01	8.9392E+01	-2.4955E+02	-2.4956E+02
$\Delta y$ [mm]	-2.1994E+02	-2.1991E+02	-1.8304E+02	-1.8305E+02	-1.9417E+02	-1.9417E+02
$\Delta z$ [mm]	9.1221E+02	9.1213E+02	5.2742E+02	5.2742E+02	9.1804E+02	9.1804E+02
$\theta x$ [rad]	2.6841E-01	2.6838E-01	-8.3975E-02	-8.3975E-02	4.7475E-01	4.7475E-01
$\theta y$ [rad]	-9.4658E-01	-9.4655E-01	-8.3199E-01	-8.3199E-01	-6.4083E-01	-6.4083E-01
$\theta z$ [rad]	-1.9796E-01	-1.9794E-01	-3.2372E-01	-3.2373E-01	-6.1635E-03	-6.1630E-03

Table 5.7.a: Comparison of internal translation forces of DR and FEDR (profile 25x25)

Elem. Nr.	$F_x$ [N]		$F_y$ [N]		$F_z$ [N]	
	DR	FEDR	DR	FEDR	DR	FEDR
1	1.7945E+00	1.7942E+00	-5.2296E+00	-5.2279E+00	1.1987E+02	1.1987E+02
11	4.1083E+01	4.1077E+01	-6.3545E+01	-6.3543E+01	9.3135E+01	9.3140E+01
21	7.2556E+01	7.2548E+01	-6.2485E+01	-6.2486E+01	7.2327E+01	7.2332E+01
31	9.0304E+01	9.0295E+01	-4.2376E+01	-4.2378E+01	6.6704E+01	6.6708E+01

Table 5.7.b: Comparison of internal rotation forces of DR and FEDR (profile 25x25)

Elem. Nr.	$M_x$ [Nmm]		$M_y$ [Nmm]		$M_z$ [Nmm]	
	DR	FEDR	DR	FEDR	DR	FEDR
1	-6.1196E+04	-6.1199E+04	-1.8604E+05	-1.8604E+05	-7.2002E+03	-7.1969E+03
11	-2.5367E+04	-2.5369E+04	-1.0629E+05	-1.0629E+05	-6.1327E+04	-6.1326E+04
21	-6.8126E+03	-6.8130E+03	-4.9229E+04	-4.9232E+04	-3.5696E+04	-3.5697E+04
31	-1.0197E+02	-1.0197E+02	-6.2324E+03	-6.2328E+03	-3.8213E+03	-3.8215E+03

Table 5.8.a: Comparison of internal translation forces of DR and FEDR (profile 100x10)

Elem. Nr.	$F_x$ [N]		$F_y$ [N]		$F_z$ [N]	
	DR	FEDR	DR	FEDR	DR	FEDR
1	8.9628E-03	8.6424E-03	-1.6168E+00	-1.6171E+00	3.9967E+01	3.9967E+01
11	5.3855E+00	5.3854E+00	-2.2487E+01	-2.2488E+01	3.2639E+01	3.2639E+01
21	1.4753E+01	1.4753E+01	-2.4828E+01	-2.4829E+01	2.7675E+01	2.7675E+01
31	2.1607E+01	2.1607E+01	-2.0199E+01	-2.0199E+01	2.6929E+01	2.6929E+01

Table 5.8.b: Comparison of internal rotation forces of DR and FEDR (profile 100x10)

Elem. Nr.	$M_x$ [Nmm]		$M_y$ [Nmm]		$M_z$ [Nmm]	
	DR	FEDR	DR	FEDR	DR	FEDR
1	-3.2487E+04	-3.2487E+04	-6.3652E+04	-6.3652E+04	-2.5678E+03	-2.5682E+03
11	-1.4360E+04	-1.4360E+04	-3.9266E+04	-3.9266E+04	-2.4684E+04	-2.4684E+04
21	-3.4182E+03	-3.4182E+03	-1.9397E+04	-1.9397E+04	-1.5580E+04	-1.5580E+04
31	-4.2470E+01	-4.2470E+01	-2.5175E+03	-2.5175E+03	-1.8543E+03	-1.8543E+03

Table 5.9.a: Comparison of internal translation forces of DR and FEDR (profile 10x100)

Elem. Nr.	Fx[N]		Fy[N]		Fz[N]	
	DR	FEDR	DR	FEDR	DR	FEDR
1	7.9126E-01	7.9163E-01	-9.4616E-01	-9.4520E-01	3.9981E+01	3.9981E+01
11	1.4965E+01	1.4965E+01	-1.1477E+01	-1.1477E+01	3.5274E+01	3.5275E+01
21	2.4021E+01	2.4021E+01	-1.0919E+01	-1.0919E+01	3.0062E+01	3.0062E+01
31	2.8120E+01	2.8120E+01	-5.1609E+00	-5.1608E+00	2.7975E+01	2.7975E+01

Table 5.9.b: Comparison of internal rotation forces of DR and FEDR (profile 10x100)

Elem. Nr.	Mx[Nmm]		My[Nmm]		Mz[Nmm]	
	DR	FEDR	DR	FEDR	DR	FEDR
1	-1.8999E+04	-1.8999E+04	-6.3053E+04	-6.3053E+04	-1.1160E+03	-1.1150E+03
11	-8.4964E+03	-8.4964E+03	-4.0393E+04	-4.0393E+04	-9.5379E+03	-9.5375E+03
21	-2.6121E+03	-2.6121E+03	-2.0376E+04	-2.0376E+04	-5.3138E+03	-5.3138E+03
31	-4.2453E+01	-4.2453E+01	-2.6135E+03	-2.6135E+03	-4.3947E+02	-4.3947E+02

## Chapter 6

# PRE-STRESSING AND COUPLING OF ELASTIC GRID SHELL

### 6.1 Introduction

Most research of form-finding and analysis of elastic grid shells uses Pian's rod model to simulate the bending mechanism [25] [52] [40]. However, the Pian's rod model is a simplified model which does not take biaxial bending and torsion into consideration. Structural designers have tried to solve this problem with the following method: They first take the forms found by form-finding methods and then rebuild the corresponding structure models with commercial FEA programs. However, if the geometric forms are directly transformed to structure models, there will be no bending pre-stresses in them. How to rebuild the pre-stresses into the structure models is thus one of the most critical challenges of the structure analysis of elastic grid shells and other bending-active structures.

In this chapter we introduce a new method to assign the pre-stresses due to bent or twisted geometries of Euler-Bernoulli beam elements such that we can conveniently select a starting geometry. A complex pre-stressing process, which is common for the simulation of bending-active structures, is thus prevented. We also introduce the way we consider the rotation couplings such that hinges, revolute joints and fixed joints can be simulated. With the pre-stressing technique, the node coupling technique, and the methods that we introduced in the previous chapters, the complete mechanism of elastic girds can be simulated.

### 6.2 Related work

#### Pre-stresses of bending moments and torsions

So far, the only way to precisely assign pre-stresses in bending-active structure models is by repeating a similar erection/formation process in FEA programs; using stretchable cable elements, truss elements and displacement loads, structure models can be deformed from an unstressed state to a pre-stressed state [53]. The method can deal with the pre-stressing precisely. The only drawback is that

when the complexity of a structure increases, the formation process becomes time consuming and difficult. Until now this pre-stressing technique is only applied to relative simple bending-active structure models. Instead of simulating a formation process, our method can assign pre-stresses directly into structure models in one step.

### Technique of rotation coupling

Only after the rotation degrees of freedom are involved, special joint configurations such as revolute joints are then possible. Discussions or examples about how to realize these rotation couplings in 6DOF DR schemes are rare [7] [54]. The main feature of our method is that it is based on an equilibrium configuration and might be able to lead to a convergence of the system more efficiently. In this chapter our coupling method is introduced in detail and examined by examples.

## **6.3 Assigning pre-stress**

The joint discussed here is a rigid joint, which means the orientations of the two consecutive beam ends which connected to the same joint maintain their relative difference in orientation through the transient phase. Therefore, if the orientations which have the correct difference are assigned to the two consecutive beam-ends, the pre-stresses arising from bending and torsion moments are generated.

### 6.3.2 Initial beam-end orientations

For a straight joint, the orientations of the corresponding beam ends remain equivalent throughout the process. Therefore, by assigning equal orientations to the two consecutive beam ends at a joint, as shown in Figure 6.1.a, the pre-stress of an initially straight joint is given. On the other hand, none of pre-stress is created if the beam orientations are assigned to the two consecutive beam ends, as shown in Figure 6.1.b. In the two figures the larger axes mark the beam orientation, while the smaller ones mark the orientation of beam-ends. To better illustrate our concept, the positions of beam-ends axes are slightly shifted inwards. In reality, the two adjacent beam-ends join at the same position in space.

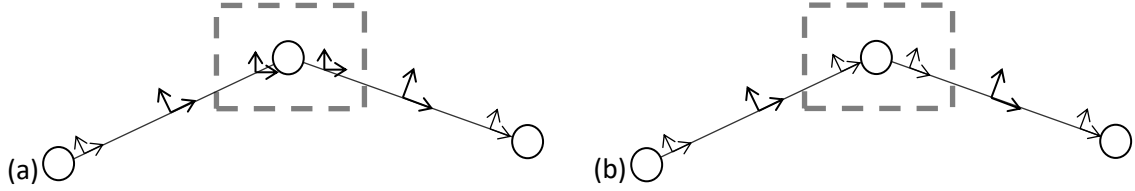


Figure 6.1: (a) In the area enclosed by the dashed line, the orientations of the consecutive beam ends are equivalent. This creates the pre-stress of bending moments and torsions of an initially straight joint. (b) In the area enclosed by the dashed line, the orientations of the two consecutive beam ends are equivalent to its beam orientation; therefore, no pre-stress of moments and torsions is created.

If the initial pre-stress is excessive, the computation may diverge. To prevent this from happening, the assigned initial orientations of the beam ends in Figure 6.1.a should be as close to their beam orientations as possible. The average of the two beam orientations is thus used and its local z-direction is determined by

$${}^0\hat{z}_E = ({}^0\hat{z}_{B,L} + {}^0\hat{z}_{B,R}) / |{}^0\hat{z}_{B,L} + {}^0\hat{z}_{B,R}| \quad (6.1)$$

where  ${}^0\hat{z}_{B,L}$  is the local z direction of the beam element on the left-hand side of the joint,  ${}^0\hat{z}_{B,R}$  the local z direction of the beam element on the right-hand side of the joint, and the super script "o" on the left-hand side marks the initial state. The local y- and x-directions of the beam ends are determined by

$${}^0\hat{y}_E = {}^0\hat{z}_E \times ({}^0\hat{x}_{B,L} + {}^0\hat{x}_{B,R}) / |{}^0\hat{z}_E \times ({}^0\hat{x}_{B,L} + {}^0\hat{x}_{B,R})| \quad (6.2)$$

$${}^0\hat{x}_E = {}^0\hat{y}_E \times {}^0\hat{z}_E \quad (6.3)$$

where  ${}^0\hat{x}_{B,L}$  is the local x-direction of the beam element on the left-hand side of the joint and  ${}^0\hat{x}_{B,R}$  the local x-direction of the beam element on the right-hand side of the joint.

### 6.3.2 Initial beam orientations

Initial orientations of beam ends are determined by initial beam orientations. However, initial beam orientations are not yet given. Two easy ways are adopted in our program to assign initial beam

orientations: The first method, shown in Figure 6.2, is based on assigning the local y-direction of a beam element in reference to the global z-direction as

$${}^0\hat{y}_B = \hat{Z} \times {}^0\hat{x}_B \quad (6.4)$$

where  $\hat{Z}$  is the global z-direction and  ${}^0\hat{x}_B$  the local x direction of the beam element, which is related to the positions of the beam ends and is known already. The local z-direction of the beam element is defined by the crossing product of  ${}^0\hat{x}_B$  and  ${}^0\hat{y}_B$

$${}^0\hat{z}_B = {}^0\hat{x}_B \times {}^0\hat{y}_B \quad (6.5)$$

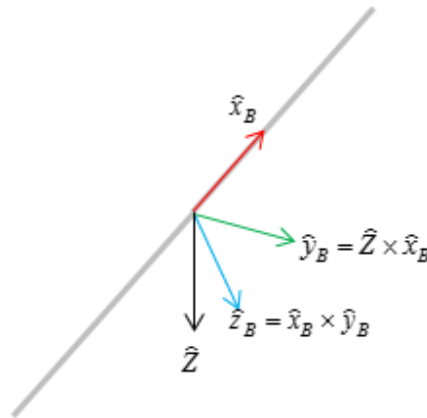


Figure 6.2: Local directions of a beam element are determined as follows:  $\hat{x}_B$  is along the beam axis,  $\hat{y}_B$  is determined by  $\hat{x}_B$  and  $\hat{Z}$ , and then  $\hat{z}_B$  is determined by  $\hat{x}_B$  and  $\hat{y}_B$ .

The second method, shown in Figure 6.3, is based on assigning the local y-direction of a beam element in reference to the surface norm  $\hat{n}$  as

$$\hat{y}_B = \hat{n} \times \hat{x}_B \quad (6.6)$$

This method is especially useful when the initial geometry is related to a surface as illustrated in our numerical test case in Section 6.5.1 and form-finding examples in Section 7.2.4.

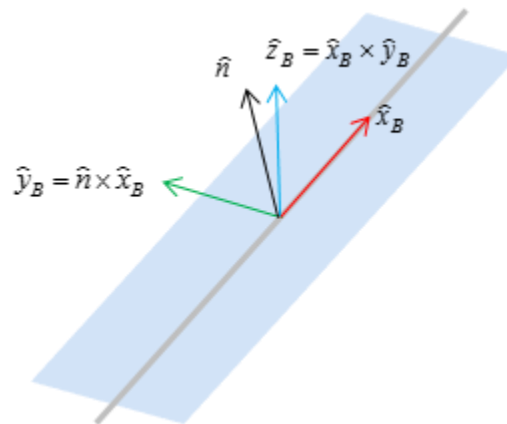


Figure 6.3: Local directions of a beam element can be determined in reference to a surface normal;  $\hat{x}_B$  is along the beam axis,  $\hat{y}_B$  is determined by  $\hat{n}$  and  $\hat{x}_B$ , and  $\hat{z}_B$  is determined by  $\hat{x}_B$  and  $\hat{y}_B$ .

### 6.3.3 Initial node orientations

Thus far we've only mentioned how to assign initial orientations of beam elements and of beam-ends, but the initial orientations of nodes are not given. Actually, if there is no rotation coupling, the initial node orientations are not of importance; they could be any orientations. Special assignment of node orientations related to revolute joints are illustrated in Section 6.4.3.

### 6.3.4 Omission of beam-end orientations

As shown in Figure 6.1.a, the consecutive beam-ends have the same orientations. In such a case, the beam-ends orientations could be omitted and be replaced by the node orientation. These node orientations then need to be assigned with Equation 6.1 - Equation 6.3.

When it comes to structure analysis, actually both situations will be encountered. For example, the lattice part of a grid shell may consist of initially straight joints, while the edge beam may be made of curved laminated timber, which is presented as initially curved joints in the structure analysis model.



### 6.3.5 Validity for both explicit and implicit integration method

Because the argumentation of the above mentioned pre-stressing method does not involve any special technique of either implicit or explicit integration methods, the pre-stressing method can be applied to both integration methods.

## 6.4 Node coupling

Being free of in-plan rigidity is one of the main features of elastic grid structures, which grants them the ability to transform to various shapes from a simple plane grid. However, this feature cannot be achieved without additional degrees of freedom in joints, such as the rotation degree of freedom of revolute joints. In the following sections, we introduce the two most common joints in bending elastic grid shells: the hinge joint and the revolute joint.

### 6.4.1 Translation coupling

A hinge/spherical joint can be modeled by coupling only the translational degrees of freedom of the two nodes and leaving their rotation degrees of freedom uncoupled. By considering the conservation of translational momentum, the coupled position and translational velocity are

$${}^{n+1/2}\bar{d}_a = {}^{n+1/2}\bar{d}_b = {}^{n-1/2}\bar{d}_a + \Delta t \quad {}^n\bar{v}_a \quad (6.7)$$

$${}^n\bar{v}_a = {}^n\bar{v}_b = {}^{n-1}\bar{v}_a + \Delta t (\mathbf{M}_a + \mathbf{M}_b)^{-1} ({}^{n-1/2}\bar{F}_a + {}^{n-1/2}\bar{F}_b) \quad (6.8)$$

where the subscripts “a” and “b” denote the two coupled nodes, Node a and Node b.

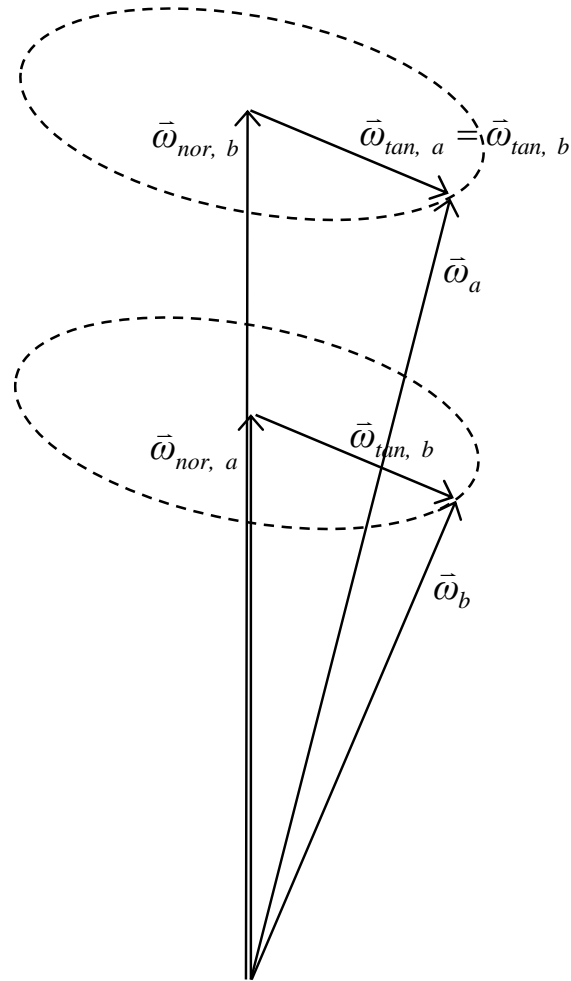


Figure 6.4:  $\vec{\omega}_{nor, i}$  is parallel to the revolute joint axis. And  $\vec{\omega}_{tan, i}$  is enforced to be the same for the coupled nodes.

#### 6.4.2 Rotation coupling (revolute joint)

For a revolute joint, the local z-directions of the two coupled nodes coincide with each other. The two nodes are rotatable along the local z-axis. Considering the coupling behavior, as shown in Figure 6.4 the torque and the angular velocity are decomposed into components in two directions: One is in the normal direction (along the local z-direction) and the other component is in the tangential direction (normal to the local z-direction)

$$\vec{\omega}_{nor, i} = (\vec{\omega}_i \cdot \hat{n})\hat{n} , \quad i = a, b \quad (6.9.a)$$

$$\bar{\omega}_{\tan,i} = \bar{\omega}_i - \bar{\omega}_{\text{nor},i} , \quad i = a, b \quad (6.9.b)$$

$$\bar{T}_{\text{nor},i} = (\bar{T}_i \cdot \hat{n})\hat{n} , \quad i = a, b \quad (6.10.a)$$

$$\bar{T}_{\tan,i} = \bar{T}_i - \bar{T}_{\text{nor},i} , \quad i = a, b \quad (6.10.b)$$

The subscripts “nor” and “tan” denote normal and tangential respectively.

The physical meaning of a revolute joint is that the tangential angular accelerations and tangential angular velocities of the two coupled nodes are always equivalent. By considering the conservation of angular momentum on the tangential plane, the update of the tangential angular velocity is

$${}^n \bar{\omega}_{\tan,a} = {}^n \bar{\omega}_{\tan,b} = {}^{n-1} \bar{\omega}_{\tan,a} + \Delta t (I_a + I_b)^{-1} ({}^{n-1/2} \bar{T}_{\tan,a} + {}^{n-1/2} \bar{T}_{\tan,b}) \quad (6.11)$$

On the other hand, using the uncoupled normal angular accelerations, the updates of the normal angular velocities are calculated as

$${}^n \bar{\omega}_{\text{nor},i} = {}^{n-1} \bar{\omega}_{\text{nor},i} + \Delta t I_i^{-1} {}^{n-1/2} \bar{T}_{\text{nor},i} , \quad i = a, b \quad (6.12)$$

As for the orientation update, to ensure overlapping of the two local z axes we divide the rotation process into two stages of rotation as follows

$${}^{n+1/2} \mathbf{R}_{N,i} = \mathbf{R}_T(\Delta t {}^n \bar{\omega}_{\text{nor},i}) \mathbf{R}_T(\Delta t {}^n \bar{\omega}_{\tan,i}) {}^{n-1/2} \mathbf{R}_{N,i} , \quad i = a, b \quad (6.13)$$

The node orientation  $\mathbf{R}_{N,i}$  first rotates along the tangential angular velocity by multiplying with the transformation matrix  $\mathbf{R}_T(\Delta t {}^n \bar{\omega}_{\tan,i})$  (which is equivalent for the two nodes and ensures that the two local z overlap) and second rotates along the normal angular velocity by multiplying with the transformation matrix  $\mathbf{R}_T(\Delta t {}^n \bar{\omega}_{\text{nor},i})$  (which is in the same direction for the two nodes but does not contain the same scale, and therefore the local z-direction is unchanged and remains overlapping with one another).

### 6.4.3 Initial orientations of coupled nodes and beam-ends of a revolte joint

The norms of the coupled nodes coincide with each other through the transient states, if the initial norm direction of the coupled nodes coincide with each other. For simplicity, we set the local z-directions of the coupled nodes as the norm directions. Therefore, the local z-directions of the coupled nodes should be assigned in the same direction in the very beginning as shown in Figure 6.5.

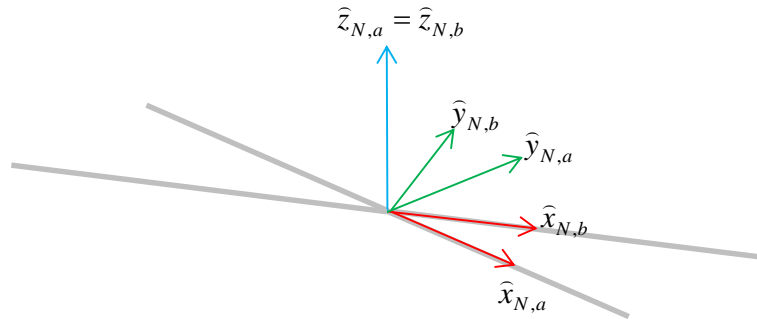


Figure 6.5: Two nodes and four beam-ends join at one revolte joint. The initial local z-directions of the coupled nodes coincide with each other and is assigned as the norm of the revolte joint. Therefore, the local z-directions of the coupled nodes remain overlapping through the transient phase.

### 6.4.4 Coupling more than two nodes

The derivation provided in the previous sections can be applied to multiple nodes. In our program, the maxima number of nodes of coupling is four.

## 6.5 Test cases

### 6.5.1 Relaxed rod

This test case is used to verify the pre-stress assignment as proposed in Section 6.3. If the pre-stress is correct, the strained curved rod will resume a straight line as in Figure 6.6. The diameter of the barrel and the length of the barrel are 20 m and 40 m respectively. The initial geometry of a bended rod is defined as a helix on the barrel. The rod is composed of 36 beam elements with a square profile that has a side length of 5 cm. Each beam element has a length of 141 cm. The elasticity and shear

modulus are defined by  $E=10^7\text{kN/m}^2$  and  $G=E/2$  respectively. The local  $z$ -directions of the beam-end are assigned as normal to the barrel surface.

Once the beam is released, the motion is triggered by the residuals and the system is eventually damped to a static state. The computation terminates once the residual of each node is less than  $10^{-4}$  kN. The variation in strain energy throughout the process is shown in Figure 6.7.

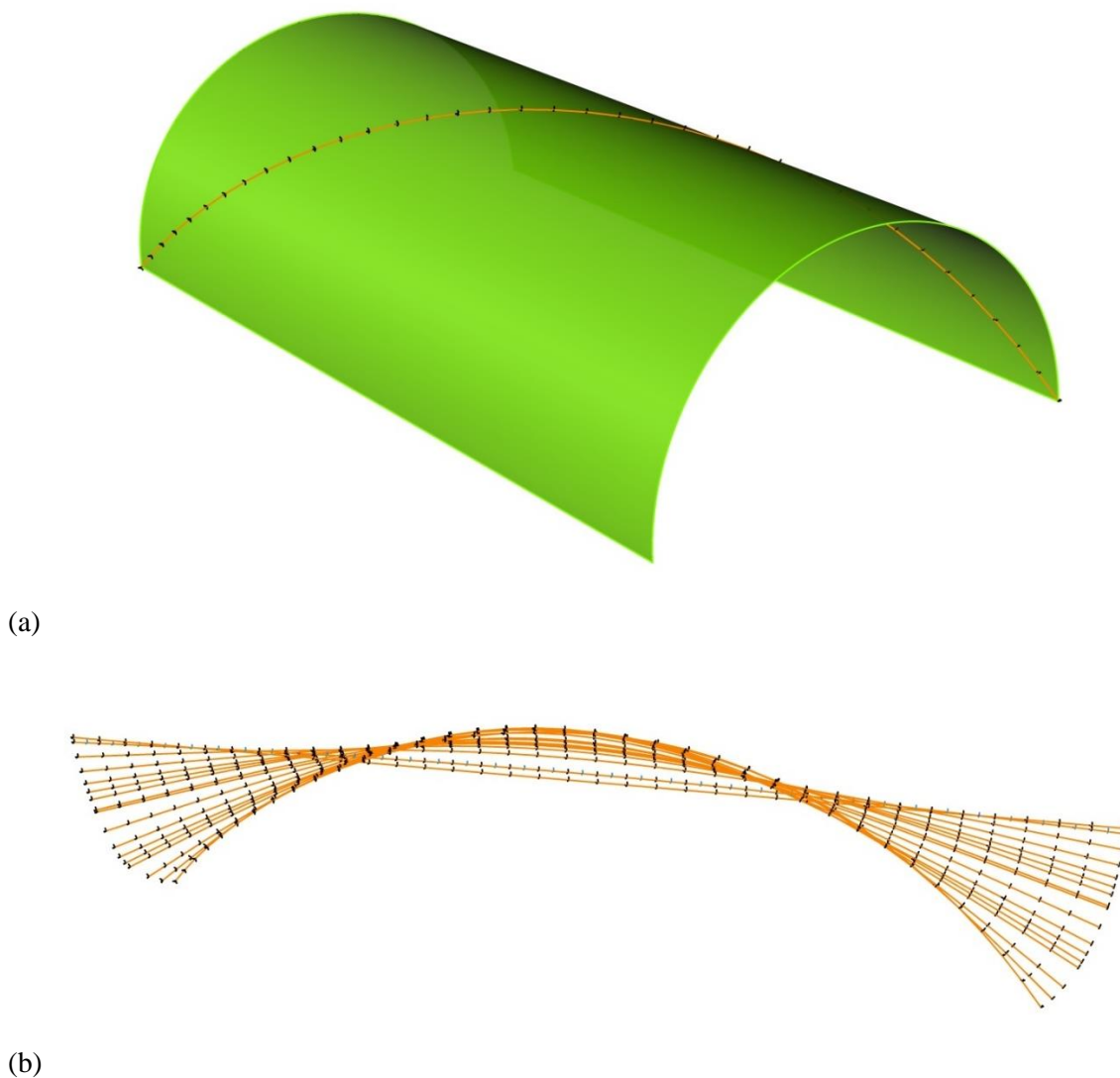


Figure 6.6: (a) Pre-stressed rod of a helix geometry defined by a barrel surface; (b) beam relaxes from the pre-stressed state and resumes a straight line

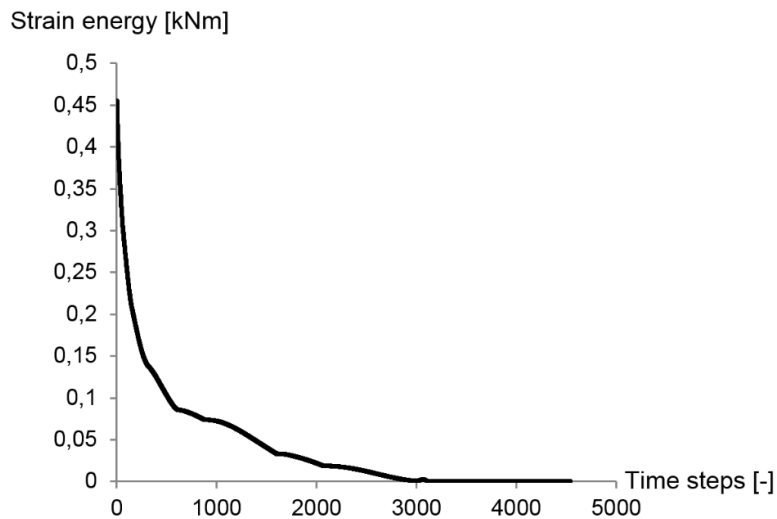


Figure 6.7: Strain energy versus time step of the relaxed rod

### 6.5.2 Relaxed crossing rods joined with a revolute joint

This example shows the relaxed process of two bended rods which are connected together with a revolute joint in their middle length as shown in Figure 6.8.a. This example demonstrates how we check the correctness and the robustness of the simulation of a revolute joint.

To test the robustness, the bended angles of each rod are almost 90 degrees and any three of the four beam elements are not coplanar. Each beam element has a length of 1.225m, the profile and the stiffness properties of which are set to be the same as in the last example. The initial local y-directions of the beam elements are assigned in reference to the global z-direction. The computation terminates once the residual of each node is less than  $10^{-5}$  kN.

When the system reaches equilibrium, the two rods resume straight line and the local z-directions of the two coupled nodes (the blue segment lines) remain overlapping as shown in Figure 6.8.b. The variation in strain energy (Equation 3.16) throughout the process is shown in Figure 6.9.

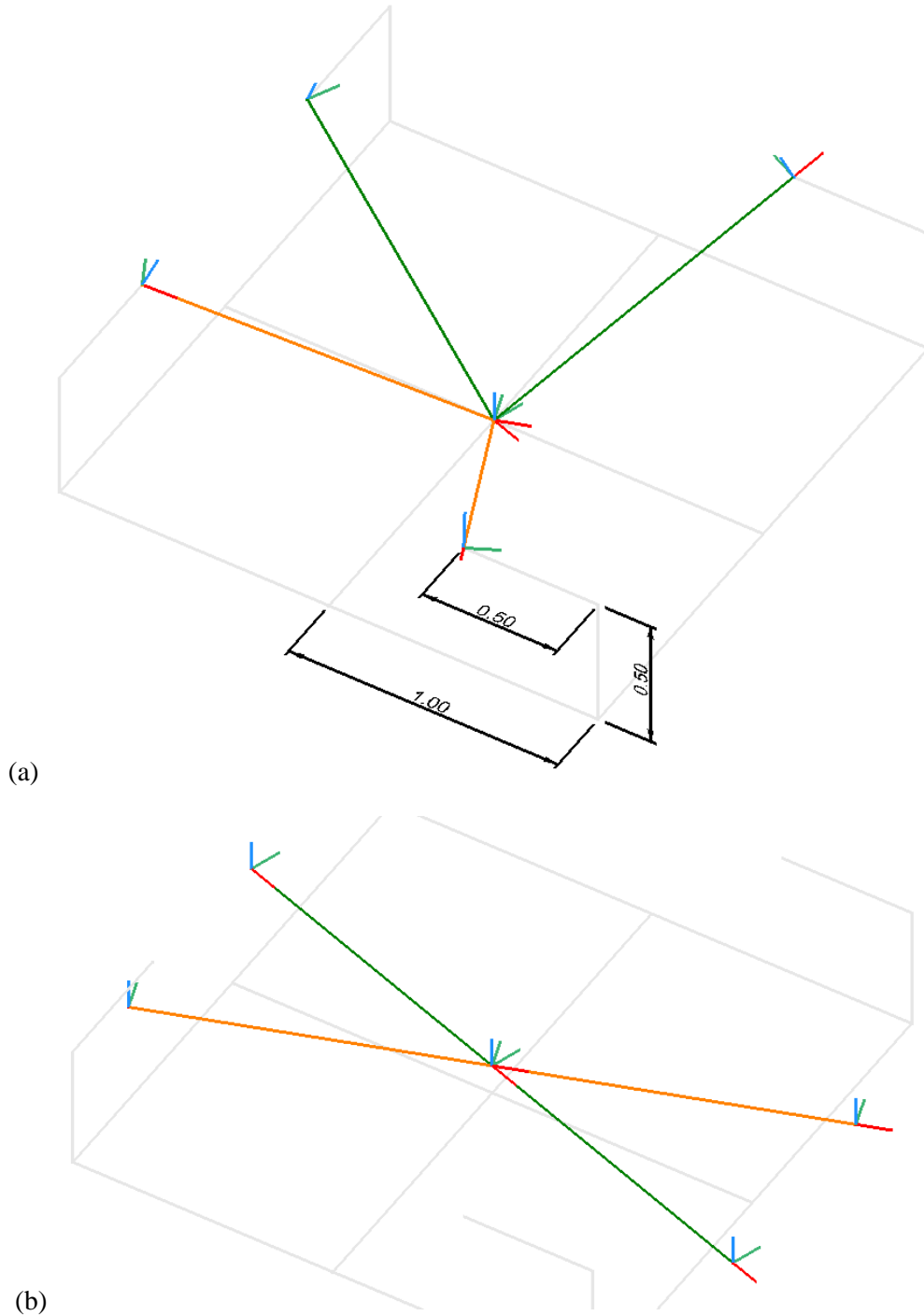


Figure 6.8: (a) Two rods in a strained geometry are jointed together with a revolute joint in the mid-span. The initial local y-directions of the beam elements are assigned in reference to the global z-direction. (b) When the system reaches an equilibrium, the two rods resume straight line and their local z-directions (blue segment lines) remain overlapping.

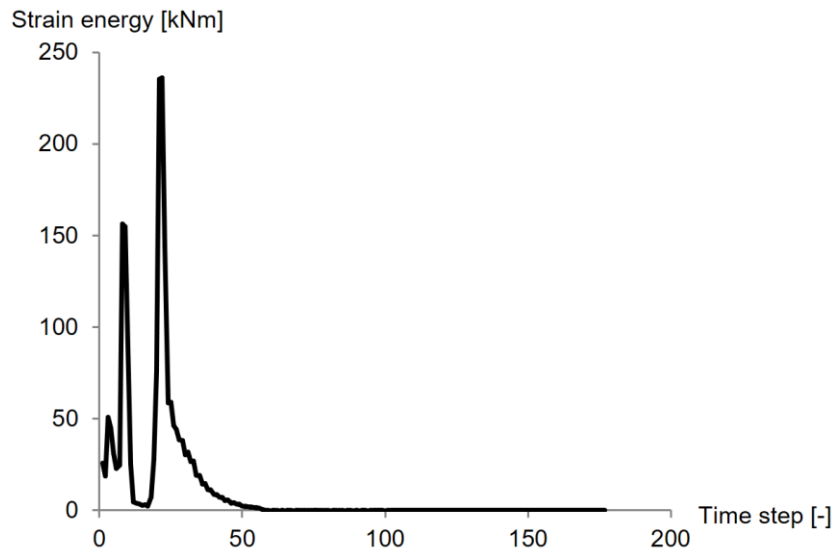
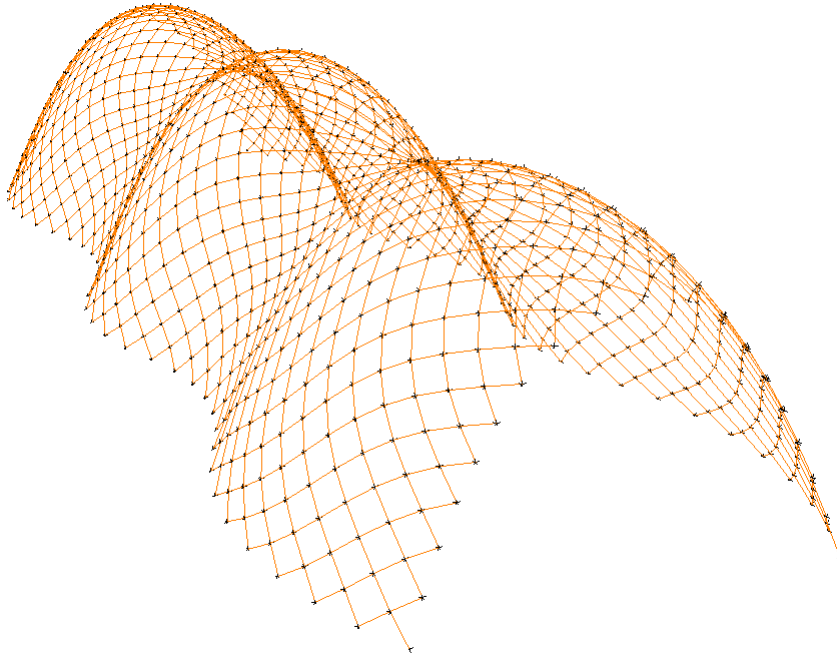


Figure 6.9: Strain energy versus time step of the bended rods jointed with a revolute joint.

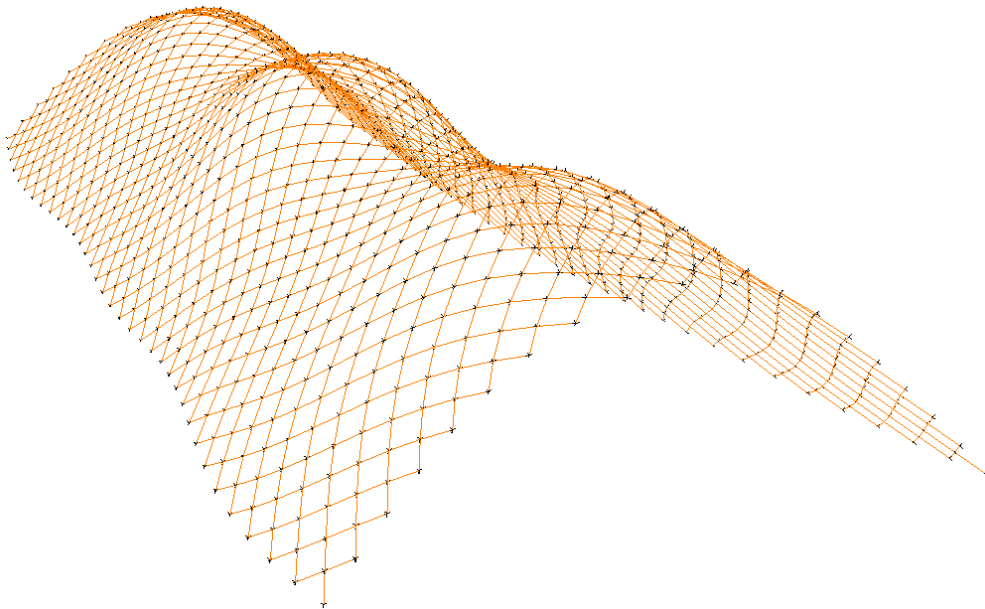
### 6.5.3 Relaxed grid

The relaxed process of a doubly curved grid with pre-stresses is tested in this example as shown in Figure 6.10. The grid size is 1x1m and the local z-direction of each beam element is determined in reference to the global z-direction. The profile and the stiffness properties are set to be the same as in the previous example.



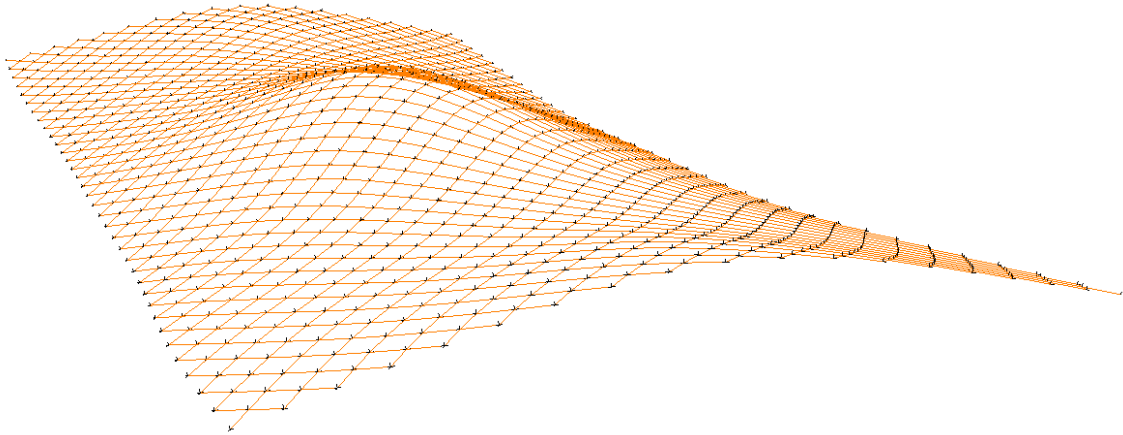


(a)

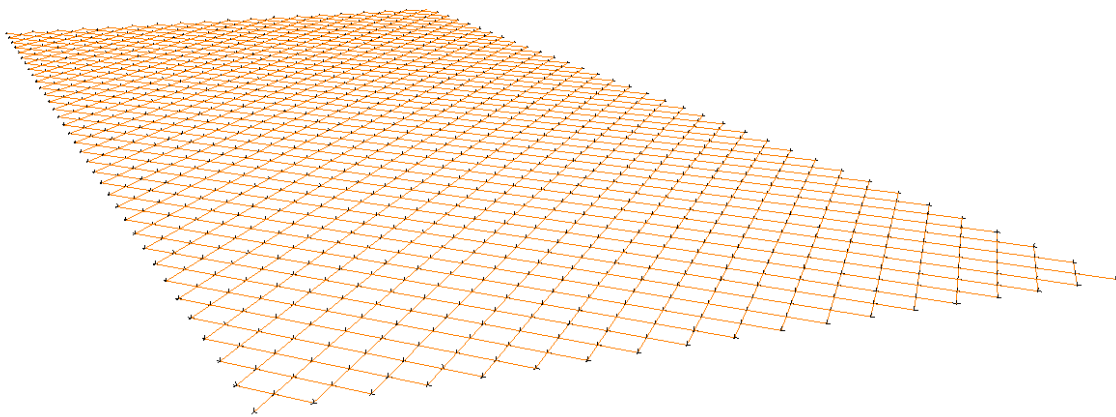


(b)

Figure 6.10: (a) A doubly curved grid structure is jointed with revolute joints and assigned with bending and torsion pre-stresses. The black segment lines show the node orientations. (b) One transient state of the relaxation process



(c)



(d)

Figure 6.11: (a) A later transient state is shown here. (b) When the system reaches an equilibrium, the rods resume straight lines and the local  $z$ -directions of the coupled nodes remain overlapping.

## Chapter 7

# FORM-FINDING BY MANIPULATING GEOMETRIC CONSTRAINTS AND PROFILE STIFFNESS

### 7.1 Introduction

Grid shells with continuous elastic rods have the advantages to generate curved spaces with uniform members and joints. The joints connecting the crossing rods are capable of having in-plane rotations. This allows grids free of the in-plane rigidity so as to take large deformations during erection/formation process. Another advantage is, members in these elastic structures are in bended states, thus when they are all combined together they can easily generate single or double curved space. This character makes elastic grid shell have the potential to be the structures of free-form architectures.

However, as stated in the introduction of Chapter 2, finding the exact boundary conditions of a actively bent grid shell is not an easy task. In this chapter we introduce two major ways to enforce geometric constraints to elastic grids: the projection method and the force method. We present our discoveries that when the projection method is used we can avoid a system from being trapped in local potential wells by using the stiffness of a fictitious profile. And it is necessary at the same time to modify the mass matrix to ensure numerical stability. We also demonstrate that the bending mechanism can play an even more important role in form-finding; it can be used to generate smooth patterns from kinked geometries without the necessity of defaulting target surfaces.

### 7.2 Projection method

By constantly projecting a node to the nearest position of the surface or the curve, the movement of the constrained node is restricted in a small neighbourhood around the surface/curve. To further reduce the space of this neighbourhood, the node residual of motion update is modified such that only the tangential part is considered (Figure 7.1); the motion which is normal to the surface is thus suppressed. The tangential part of the node residual is calculated as

$$\vec{F}_{\text{tan}} = \vec{F} - (\vec{F} \cdot \hat{n}) \hat{n}, \text{ for a surface constraint} \quad (7.1)$$

$$\vec{F}_{\text{tan}} = (\vec{F} \cdot \hat{t}) \hat{t}, \text{ for a curve constraint} \quad (7.2)$$

where  $\vec{F}$  is the residual node force which are the sum of the internal force and the external force,  $\hat{n}$  the normal direction of the constraint surface, and  $\hat{t}$  the tangential direction of the constraint curve. When the system reaches an equilibrium, the resultant grid pattern naturally fulfills the given geometric constraints and has the least strain energy in the solution domain defined by the constraints.

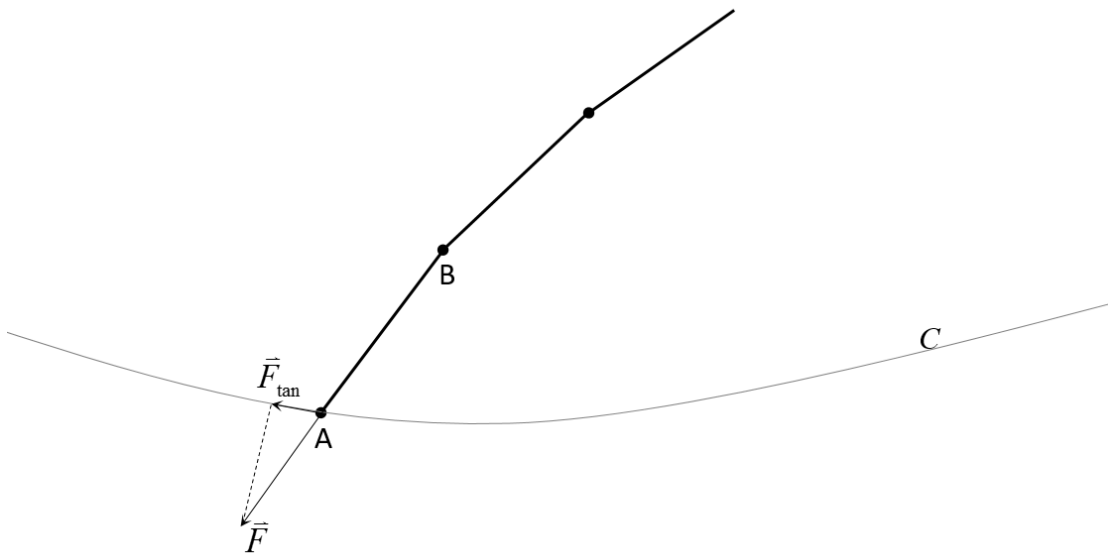


Figure 7.1:  $\vec{F}$ , the residual force of a node A, tends to push the node away from the curve C, where the node B is a consecutive structural node. By considering only  $\vec{F}_{\text{tan}}$ , the tangential part of  $\vec{F}$ , a smoother movement along the geometric constraint can be achieved.

### 7.2.1 Modification of mass matrix

The above mentioned method works well when the scalar mass is applied. However, when the mass matrix is applied and a slender beam element is in use, the projection method does not lead to a

convergent result. This is because the shear residual  $\bar{f}_{tran}$ , which is in the transverse direction of the beam-end, is too large compared with the original shear residual derived from  $\bar{F}$  (Figure 7.2). The large shear residual together with the optimized mass matrix (Section 4.6.2) induce a numerical instability.

The solution is to modify the mass matrix of the beam-end: Two fictitious beam elements are added in the transverse directions of the beam-end (Figure 7.3). The two elements contribute their stiffness to the node stiffness but generate no internal forces to the node residual. In this way, the “transverse

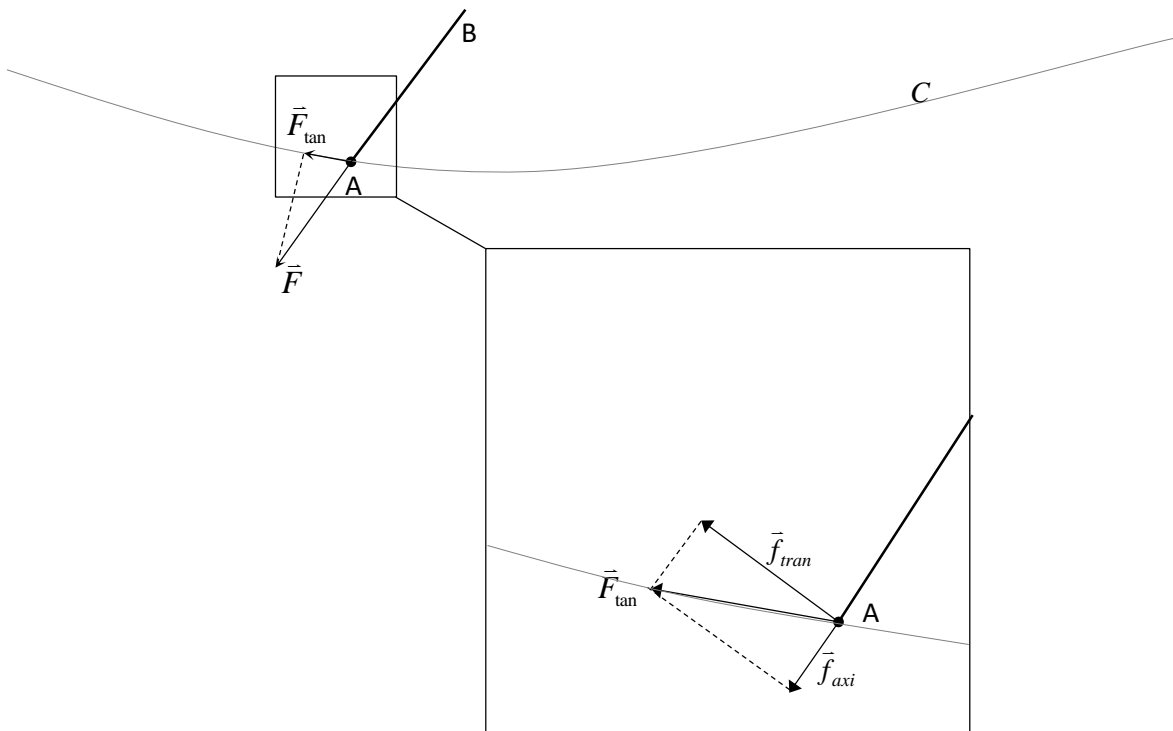


Figure 7.2: The shear residual  $\bar{f}_{tran}$  is in the same scale of the axial residual  $\bar{f}_{axi}$ .

mass” is in the scale of the “axial mass” and can thus deal with the large transverse force. Because the fictitious elements do not affect node residuals, the equilibrium state should not be affected.

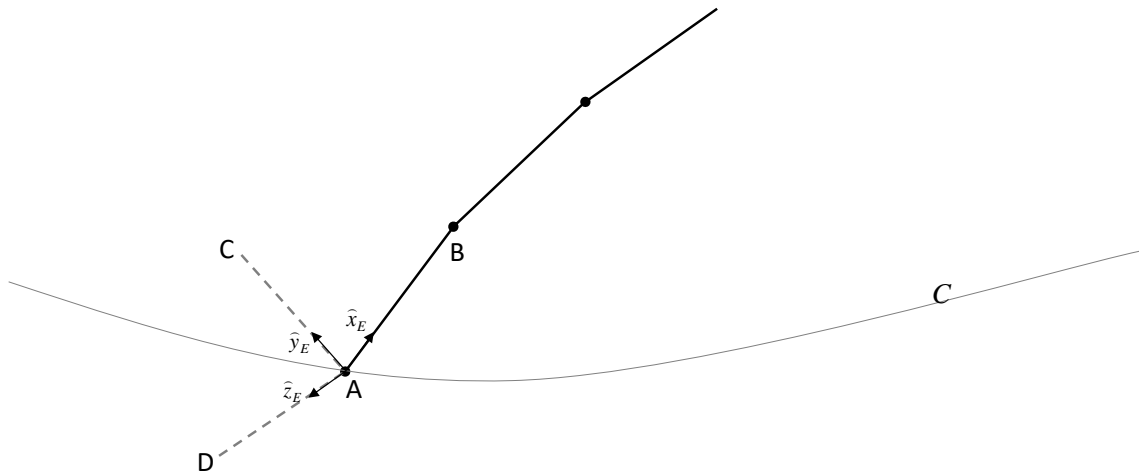


Figure 7.3: The node A is constrained only movable along the curve C. Two fictitious beam elements AC and AD are built in the local y-direction and in the local z-direction of the node respectively.

7.2.2 Computation procedure of projection mechanism

Where to introduce the projection mechanism in the program is illustrated in Figure 7.4.

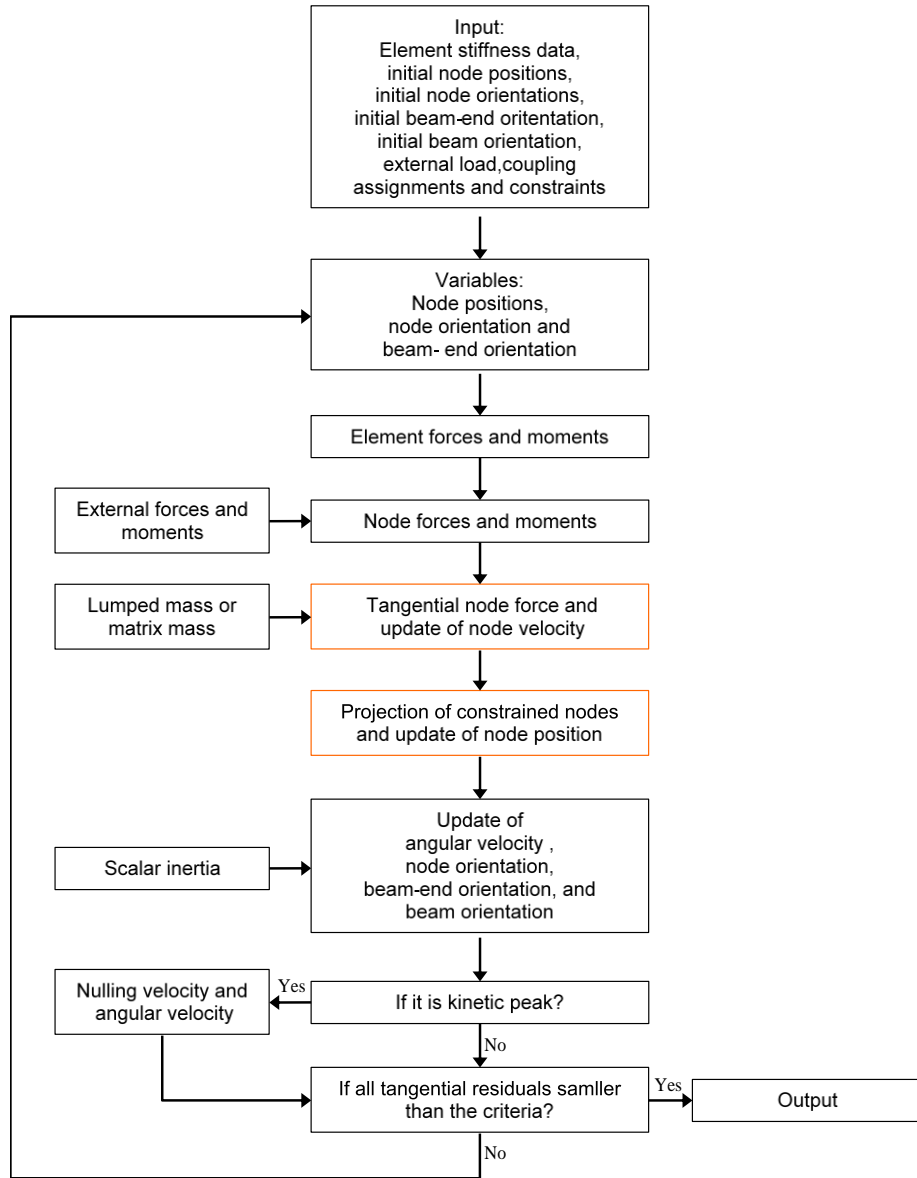


Figure 7.4: Computation procedure including the projection mechanism (the orange color marks the newly added blocks).

### 7.2.3 Potential well

If the calculation starts from a state which is highly pre-stressed, the dynamic process toward equilibrium is easily trapped in a local potential well of a local minimum strain energy. This phenomenon becomes more critical when the axial stiffness  $EA/L$  is much larger than the transverse stiffness  $EI/L^3$ .

Figure 7.5 shows a kinked grid pattern where a surface constraint is imposed on the elastic grid. As shown in Figure 7.6 (the enlarged picture of Figure 7.5), the kinked grid has equal grid lengths but is extremely distorted in some areas. Once the grid reaches a state with such a kinked geometry, the relaxation process will be trapped and cannot get out from the potential well.

We found that we could move the system out of the local potential well by assigning a greater transverse stiffness of a scale similar to the axial stiffness and gradually reducing it to the original stiffness in the transient phase. The reason behind this is that if the axial stiffness is greater, the form-finding process is dominated by axial forces, which tend to maintain the given unstrained lengths of beam elements and could result in a grid pattern of many kinks. And if the transverse

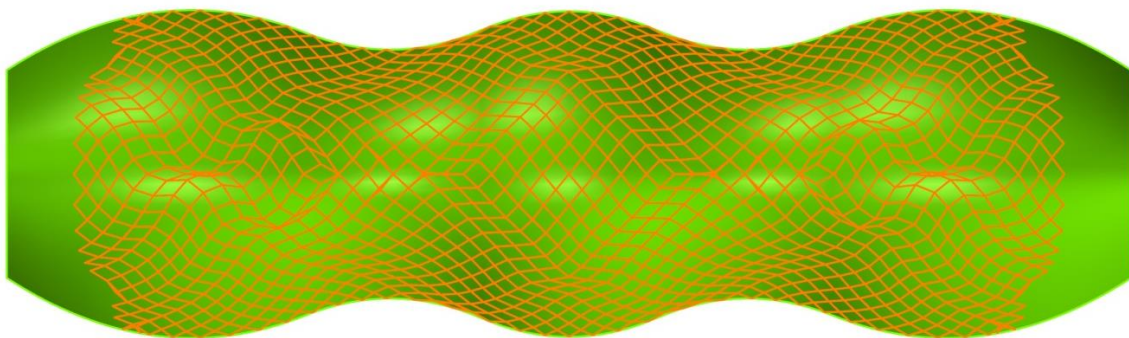


Figure 7.5: A kinked pattern is generated when a surface constraint is imposed on an elastic grid. The grid is in a state of equal grid lengths but highly distorted in some areas. (The beam elements used in this case are based on Pian's rod model with 3DOF per node. When the Euler-Bernoulli beam elements, which has 6DOF per node, are used, the computation diverges.)



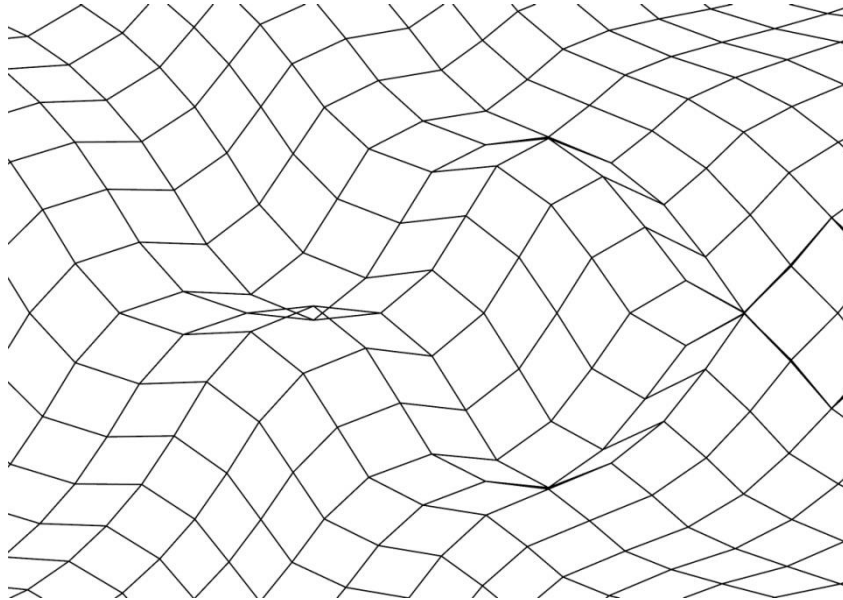


Figure 7.6: An enlarged picture of the distorted area in Figure 7.5

stiffness is greater, then the bending mechanism is dominant, which tends to smooth the grid and diminishes the kinks.

#### 7.2.4 Example-Weald and Downland Gridshell

Downland Gridshell as our first example to demonstrate our form-finding method. The task is to obtain a single-layer grid pattern that complies with the triple-bulb geometry and simultaneously exhibits the lowest strain energy.

The grid, which has a uniform grid length of 1m, is composed of 102 initially straight rods as shown in Figure 7.7.a. Every rod exhibits a square profile with a side length of 5 cm and is composed of numbers of beam elements. Each beam element has an unstrained length of 1m. The connections between the crossing rods are revolute joints, which allow rotations along the local z-directions. The elasticity and shear modulus of the material are defined as  $E=10^7\text{kN/m}^2$  and  $G=E/2$  respectively. Two geometrical constraints are imposed (Figure 7.7 b). First, the grid nodes on the longer sides are

constrained on the curved boundaries. Second, the remaining grid nodes are constrained on the triple-bulb surface.

In this example, the axial stiffness is about five thousand times the value of the transverse stiffness. Because the axial stiffness is significantly greater than the transverse stiffness, the system is easily trapped in a local potential well. To avoid this from happening, the transverse stiffness is assigned with a larger value in the beginning and then reduced gradually: The transverse stiffness is applied on the orders of 1000 times the original value, 100 times the original value, 10 times the original value and with no amplification, and the value changes only after an equilibrium is reached. The final equilibrium state is shown in Figure 7.8.a.

The equilibrium state can also be derived with the FEDR method introduced in Section 5.4. With that method, the axial stiffness is adjusted in the same scale of the transverse stiffness, which enables the bending mechanism to be dominant.

The derived form is transferred to a load-bearing structure after the constraints are removed and the diagonals and hinge supports are added (Figure 7.8.b). The structure is then relaxed once again and deforms slightly due the residual forces. The largest deformation, which is 6 cm, occurs on the top of the opening of the grid shell. Compared with the span of the opening, 11.7m, this value is relatively small. That means the form we found for the three-dimensional elastic grid fits the target surface very well.

We proceed with 6DOF DR to investigate the load-bearing behavior of the structure. Table 7.1 demonstrates the strain energy of the grid structure in different load cases. It shows that as the loading increases, the strain energy due to bending and torsion increases slowly, but the axial strain energy increases rapidly. This means the structure behaves like a shell; external loads are mainly taken by internal axial forces. Another point worth noticing is that the initial bending and torsion strain energy possess large portions of the strain energy, even when an extremely heavy load is applied. This means that for a bending-active structure it is crucial to reduce the initial strain energy (the strain energy due to the bent geometry), and this makes our method, which finds the least strain energy state for given geometric constraints, even more meaningful. Fig. 7.9 shows the deformation of the grid shell under a heavy uneven load.

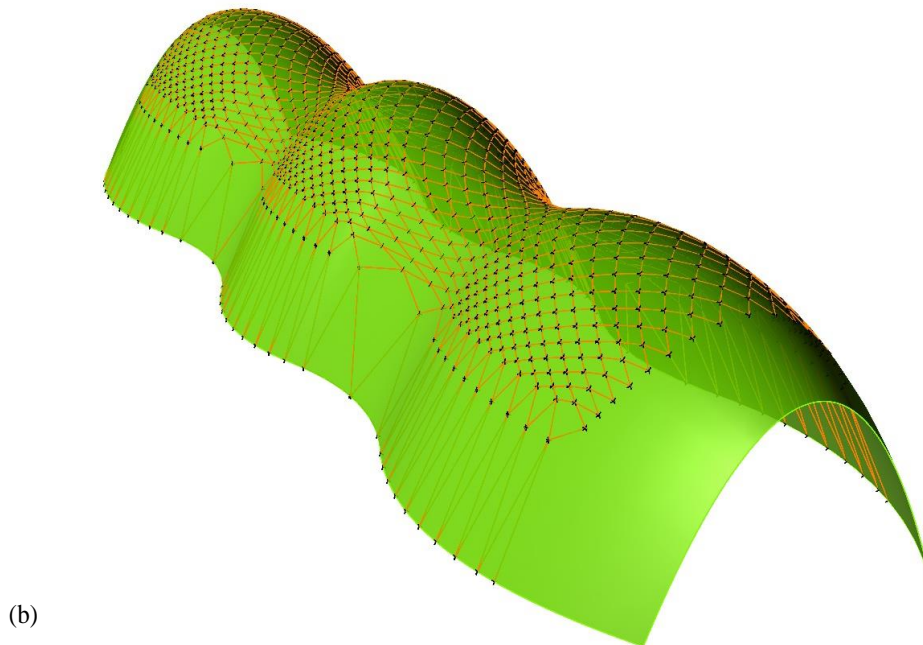
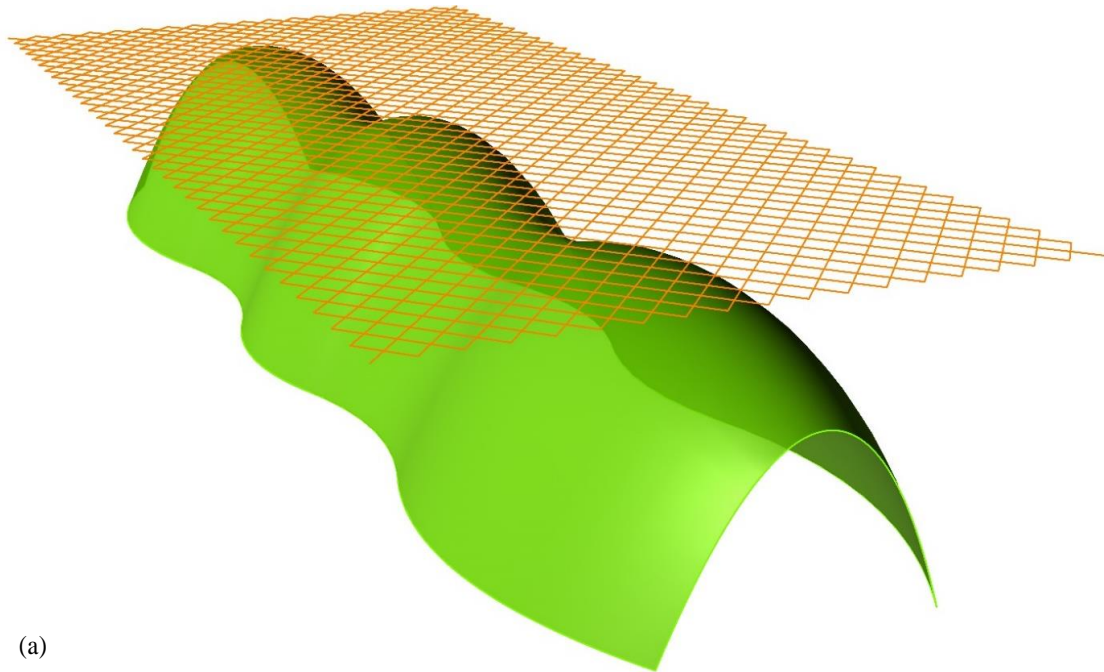


Figure 7.7: (a) Initial grid and geometric constraints; (b) edge nodes are constrained by the boundary curves, and the remaining nodes are constrained by the surface.

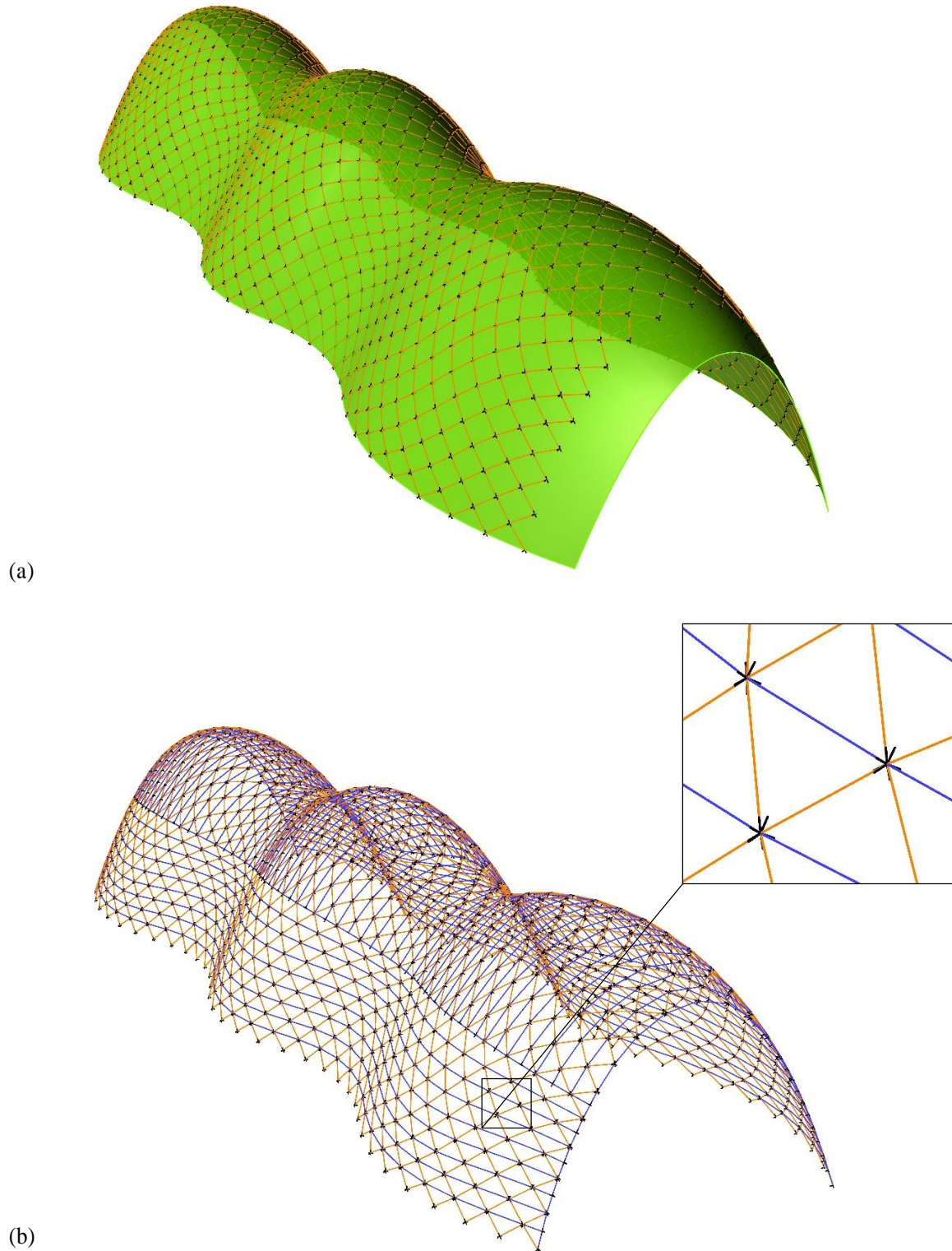


Figure 7.8: (a) Equilibrium state under constraints; (b) a load-bearing structure is accomplished after the constraints are removed and the bracing and support conditions are added; the enlarged part shows the node orientations.

Table 7.1: Strain energy of a grid shell in different load cases

Load type	Load per joint [kN]	Strain energy [kNm]				
		Torsional	Out-of-plane bending	In-plane bending	Axial	Total
Unloaded	0	25,3	121	40,8	1,13	187
Even load*	1,2	25,4	122	40,8	1,46	189
	2,4	32,5	163	41	8,31	245
Uneven load**	1,2	25,3	121	40,8	2,01	190
	2,4	31,2	158	41	13,1	243

\*All joints are applied with the load.

\*\*Only the joints on the left-hand side of the center line are applied with the load.

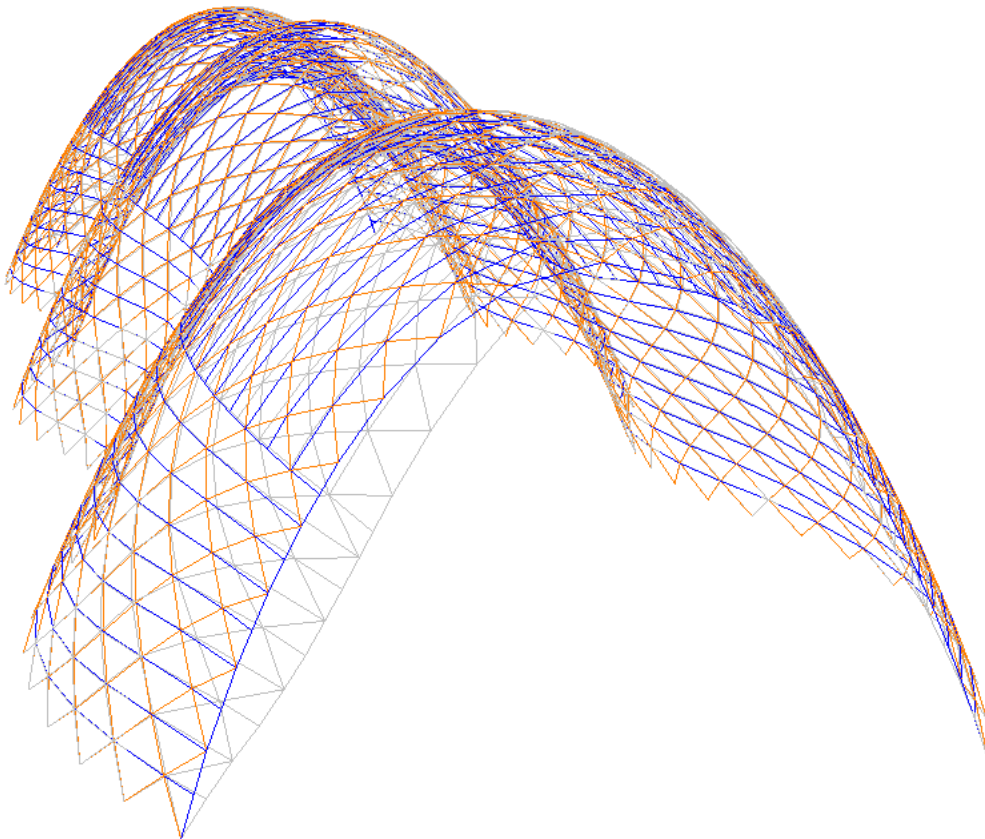


Figure 7.9: Unscaled deformation of the grid shell under an uneven vertical load; every joint on the left-hand side of the center line is applied with a downward vertical force of 2.4kN.

### 7.2.5 Example-2D Hybgrid

Hybgrid, proposed by Truco and Felipe [55], is an innovative double-layer structural type which is composed of three uniform flexible chord members and can generate various geometries by controlling the strut lengths between the chords (Figure 7.10). Currently, the only available form-finding for Hybgrid is based on physical models. Thus, the testing of our method constitutes a significant benchmark.

As shown in Figure 7.11.a. The grid is composed of three chords: the upper chord, the middle chord and the lower chord. Each chord is composed of 40 beam elements with an unstressed length of 12.88 cm. The connections between the chords consist of revolute joints. Each chord has a uniform rectangular profile that exhibits a width of 80 mm and a thickness of 4 mm. The elasticity and shear modulus are defined as  $E=10^7 \text{KN/m}^2$  and  $G=E/2$ , respectively.

The upper chord nodes that are on the top of quadrangles are constrained by the upper curve (only movable on the curve). Similarly, the lower chord nodes that are on the bottom of quadrangles are constrained by the lower curve. The two curve constraints, which contain an interval of 0.375 m

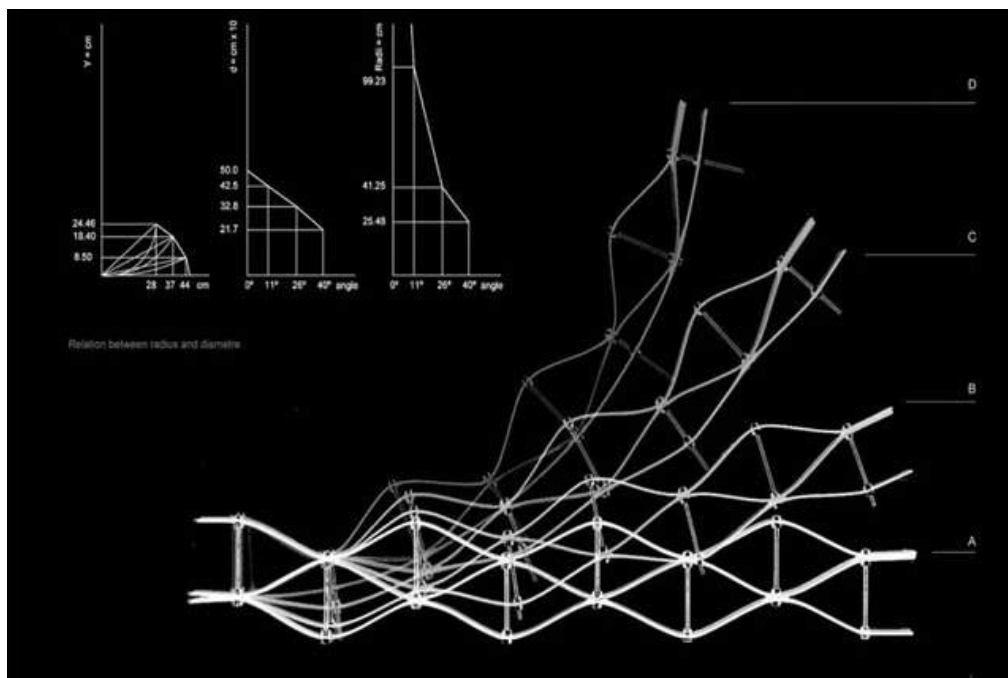


Figure 7.10: A 2D Hybgrid structure can generate various linear geometry by controlling the strut lengths between the chords. (Source: <http://www.achimmenges.net>)

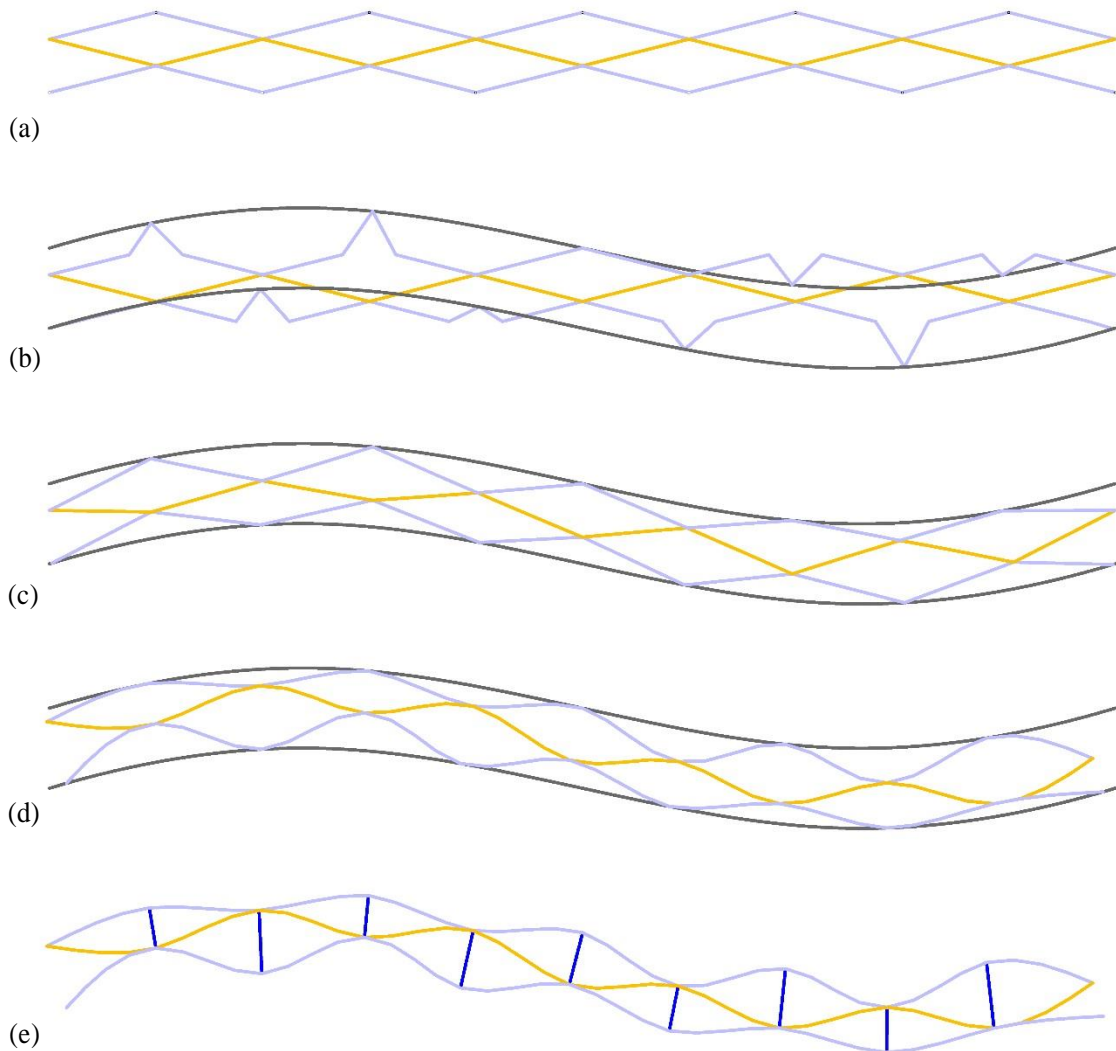


Figure 7.11: (a) Initial geometry of a 2D Hybrid structure; (b) transient state when constrained nodes are projected to the boundaries; (c) transient state derived by the force density method with fixed nodes on the boundaries; (d) equilibrium state of Euler-Bernoulli beams solved by DR using the geometry in Figure 7.11.c as the new initial geometry; constrained nodes are movable on the boundaries; (e) load-bearing structure is accomplished after boundaries are removed and struts and supporting conditions are added in.

between the curves, are equivalent. The curve constraint is defined by two arcs with a curvature of 4.4 m.

After the first projection, the structure becomes largely distorted because we only projected a few nodes to the constraints and the rest nodes remain in their original positions (Figure 7.11.b). A substantially distorted initial state will cause the divergent integration. To adjust the initial geometry to a smoother shape, we fix the constrained nodes and solve a force density solution (the tensile axial force is proportional to the member length) as shown in Figure 7.11.c.

In this example, the ratio between axial stiffness and the transverse stiffness is  $1.26E4$  (the axial stiffness is substantially greater than the transverse stiffness). To prevent the system from being trapped in a local potential well, the relaxation process is divided into stages: The values of the transverse stiffness are applied on the orders of 1000 times the original, 100 times the original, 10 times the original and with no amplification applied (Fig. 7.11.d).

The structure could be transferred to a load-bearing structure once the constraints are removed and the struts and supporting conditions are added as shown in Fig. 7.11.e.

### 7.2.6 Example-3D Hybgrid

We also applied our scheme in the form-finding of a 3D Hybgrid (Figure 7.12). As shown in Figure 7.13.a, the plane grid is composed of 18 composite beams and each composite beam has a structure that is similar to the 2D Hybgrid in the previous example. In plain view, two crossing beams have a 60-degree included angle.

Two types of constraint are applied: the surface constraint and the curve constraint. For the surface constraint, the upper chord nodes that are on the top of quadrangles are constrained by the upper surface. Similarly, the lower chord nodes that are on the bottom of quadrangles are constrained by the lower surface (Figure 7.13.b). The two surfaces are equivalent with an interval of 0.375 m between the surfaces. The surface is defined as a surface of revolution that is generated by an arch of radius of 2.9 m with a revolution of radius of 22.9 m.

For the curve constraint, we constrain four nodes, which are located in the center area of the upper surface, by two curves that are produced by projecting two straight crossing lines with a 60-degree included angle to the upper surface (the dark purple lines in Figure 7.14.b). This constraint helps us to maintain the included angle in the plane view.





Figure 7.12: A 3D Hybrid structure can generate various surface geometry by controlling the strut lengths between the chords. (Source: <http://www.achimmenges.net>)

To obtain a smoother initial geometry, a force density solution is required at the beginning of form-finding (Figure 7.14.a). To prevent the system from being trapped in a local potential well, the subsequent form-finding process is divided into stages with varying transverse stiffness as demonstrated in the previous example. The structure could be transferred to a load-bearing structure once the constraints are removed and the struts and supporting conditions are added, as shown in Figure 7.15.a.

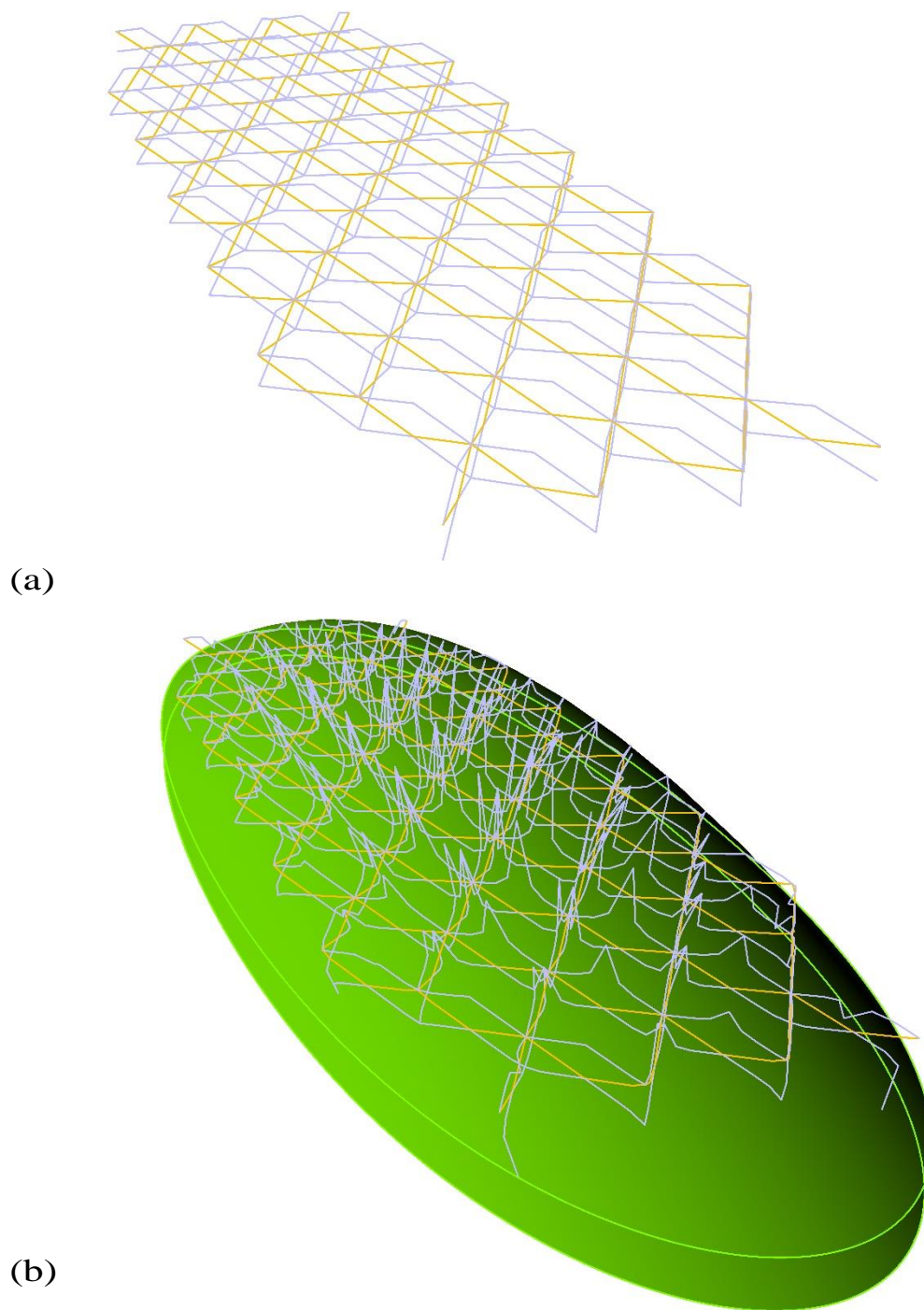


Figure 7.13: (a) Initial geometry of a 3D Hybgrid; (b) transient state when constrained nodes are projected to the surface constraints

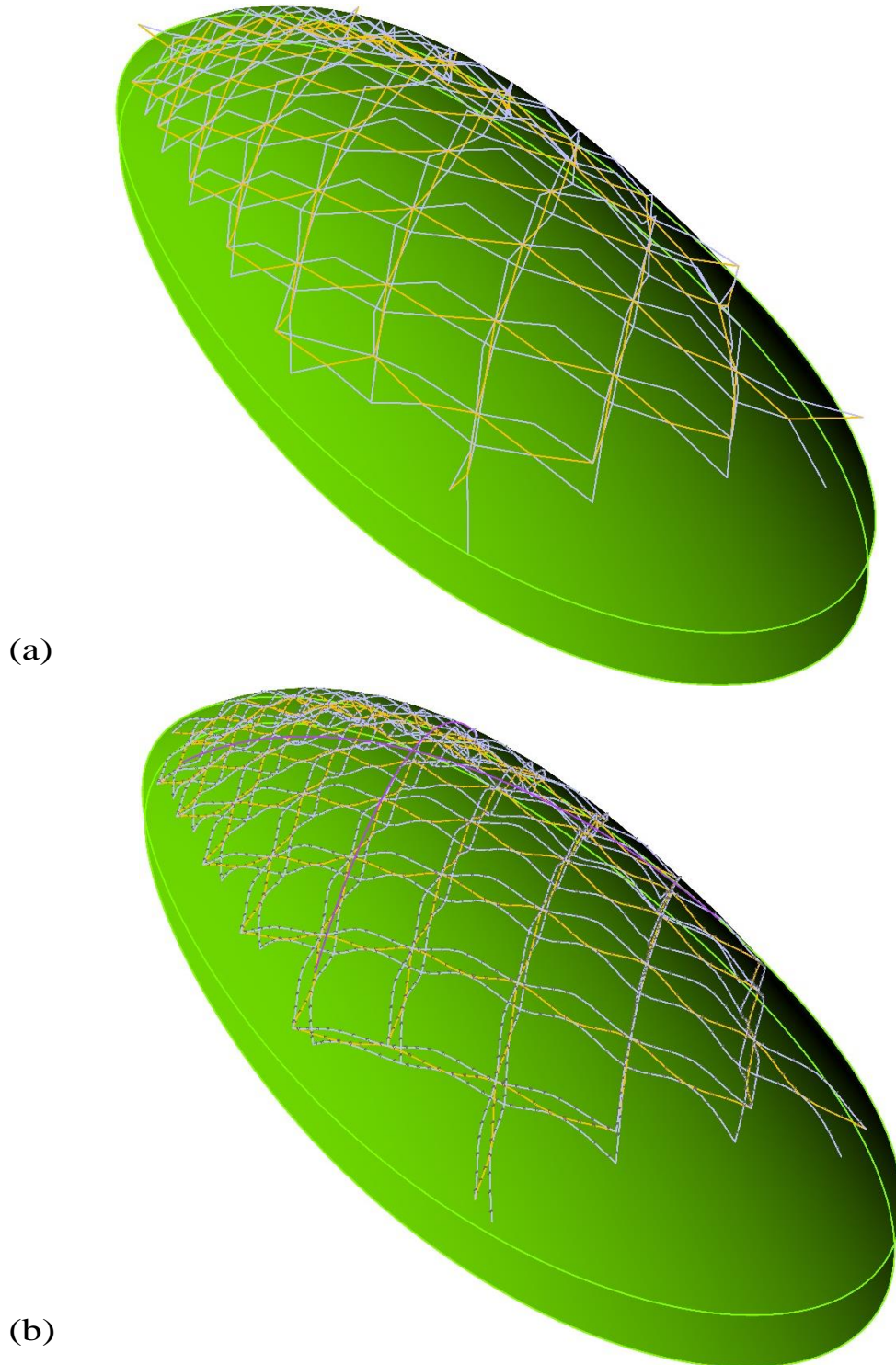
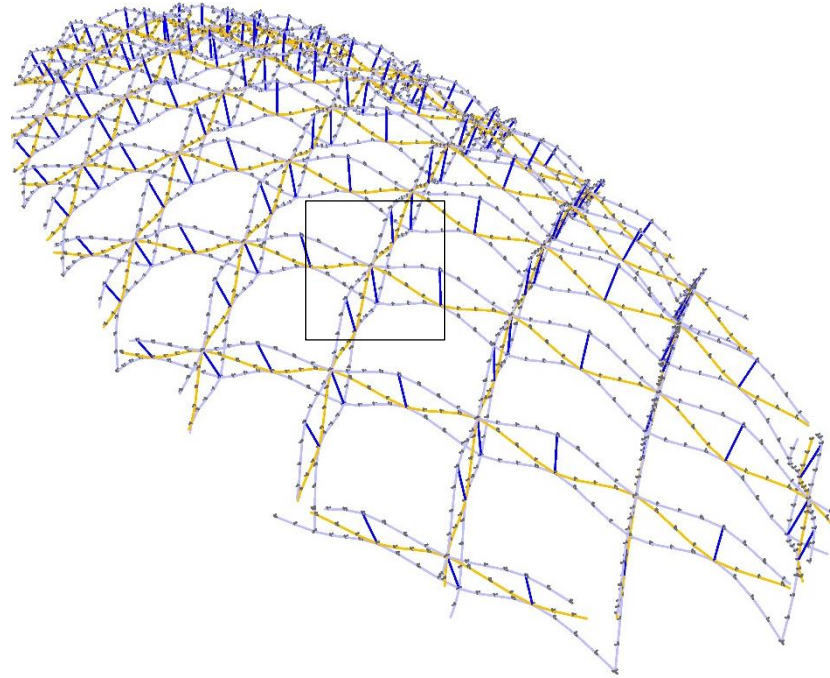
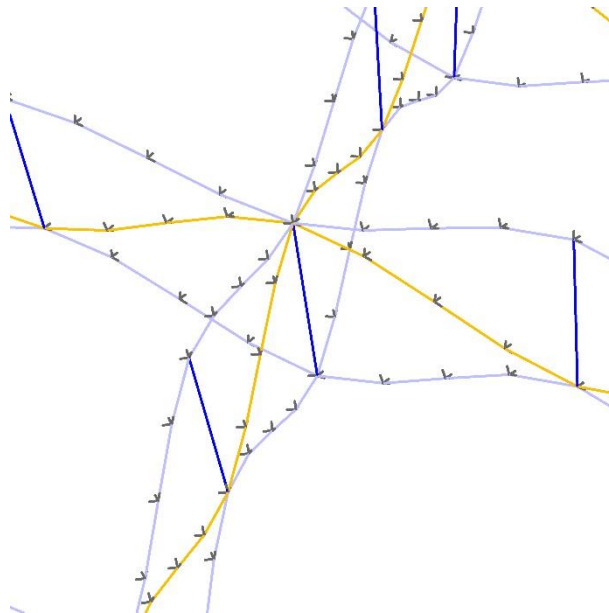


Figure 7.14: (a) Transient state solved by the force density method with the nodes fixed on the constraints. (b) Equilibrium state of Euler-Bernoulli beams solved by 6DOF DR using the geometry derived in Figure 7.14.a as the new initial geometry; constrained nodes are only movable on the surface constraints. Four nodes in the central area are constrained by the two curves (dark purple curves) to keep the in-plane included angles.



(a)



(b)

Figure 7.15: (a) A load-bearing structure is achieved when the constraints are removed and the struts and the support conditions are added. (b) Enlarged area of Figure 7.15.a to show the orientations of the coupled nodes

### 7.3 Force method

By applying traction forces or gravities to grid nodes, the structure will move toward the constraint surface/curve and deform itself to adopt the constraint geometry. Unlike the projection method, which has no control variables, the force method has the magnitude and the direction of the traction force as control variables.

The most intuitive way to define the traction force between the constraint and the node is to use the projection point on the constraint surface/curve. As shown in Figure 7.16.a, a traction force  $\vec{F}_{trac}$  could be defined as

$$\vec{F}_{trac} = f(h)\hat{n} \quad (7.3)$$

where  $\hat{n}$  is the unit vector points from the point  $A$  toward the point  $A'$ ,  $h$  is distance between  $A$  and  $A'$ , and  $f(h)$  is the magnitude of the traction force.

If a gravity force is applied as the traction force, the traction force will not change its magnitude and direction through the process (Figure 7.16.b). Therefore, the contact mechanism is needed to enforce the interaction between the grid structure and the geometric constraint.

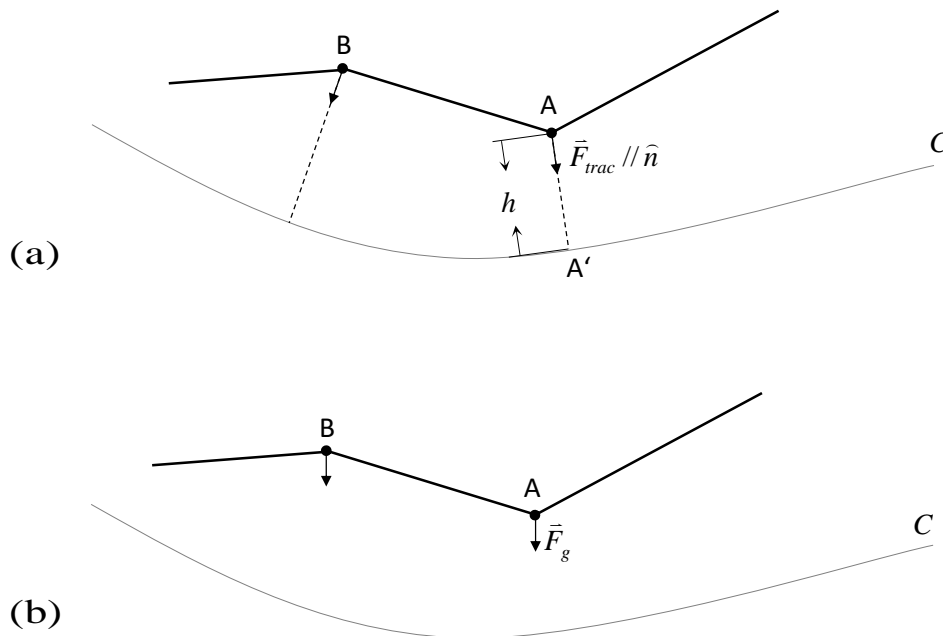


Figure 7.16: (a) a traction force directing to the nearest point on the surface, whose magnitude is a function of the distance; (b) the direction and the magnitude of a gravity force is independent from the constraint surface.

### 7.3.1 Contact mechanism

The contact between a node and a constraint surface takes place when the node position of the next time step would be located in the other side of the contact surface. As shown in Figure 7.17, a node at the  $(n-1/2)$ -th time step is located at the position  $A$  (it can be expressed as  $\overrightarrow{OA} = {}^{n-1/2}\bar{d}$  where the position  $O$  is the origin). If there is no contact mechanism, at the next time step, it should move to the position  $A'$ .

#### Elastic collision

When an elastic collision takes place, the node will rebound to the position  $A''$ , which can be expressed as

$$\overrightarrow{OA''} = \overrightarrow{OA'} + 2\overrightarrow{A'P} \quad \text{or} \quad {}^{n+1/2}\bar{d} = {}^{n+1/2}\bar{d}' - 2h\hat{n} \quad (7.4)$$

where the position  $P$  is the intersection of the segment line  $\overline{A'A''}$  and the surface  $S$ ,  ${}^{n+1/2}\bar{d}' = \overrightarrow{OA'}$  is the node position when there is no collision mechanism,  $h$  is equal to  $\overline{A'P}$ , and  $\hat{n}$  is the unit norm vector at the position  $P$ .

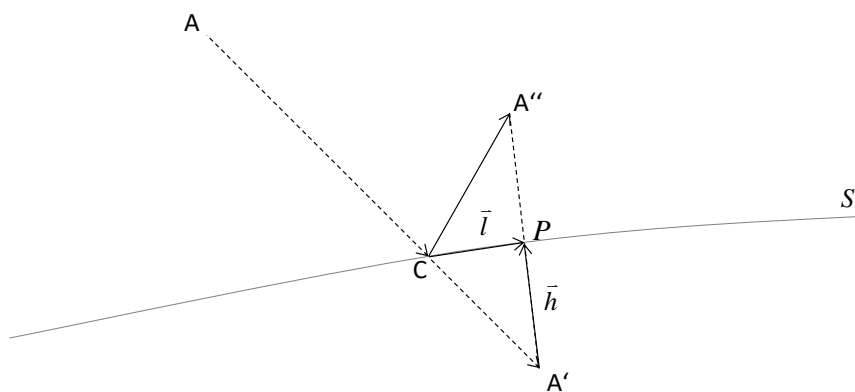


Figure 7.17: Elastic collision on a surface  $S$ ; “ $A$ ” denotes the node position at the  $(n-1/2)$ -th time step, “ $A''$ ” denotes the node position at the  $(n+1/2)$ -th time step after an elastic collision takes place, and “ $A'$ ” denotes the node position if no collision takes place.

The node velocity changes its direction after the collision. Its component in the normal direction will change its sign to the opposite direction. Therefore, the node velocity after the collision is

$${}^n\vec{v} = {}^n\vec{v}' - 2(\vec{v}' \cdot \hat{n})\hat{n} \quad (7.5)$$

where  ${}^n\vec{v}'$  is the node velocity at the n-th time step when there is no collision mechanism.

### Inelastic collision

For an inelastic collision, the position and the velocity of a rebound are not unique. We consider an inelastic collision by simply scaling the tangential velocity and the normal velocity after the collision as follows

$${}^n\vec{v} = c_{\tan} {}^n\vec{v}'_{\tan} - c_{nor} {}^n\vec{v}'_{nor} \quad (7.6)$$

where  ${}^n\vec{v}'_{\tan}$  is the tangential velocity of  ${}^n\vec{v}'$ ,  ${}^n\vec{v}'_{nor}$  the normal velocity of  ${}^n\vec{v}'$ ,  $c_{\tan}$  the scale factor in the tangential direction, and  $c_{nor}$  the scale factor in the norm direction. The reductions in velocities lead to a position

$${}^{n+1/2}\vec{q} = ({}^{n+1/2}\vec{q}' + \vec{h} - \vec{l}) + c_{\tan}\vec{l} + c_{nor}\vec{h} \quad (7.7)$$

Where  $\vec{h}$  is equal to  $\overline{A'P}$  and  $\vec{l}$  is equal to  $\overline{CP}$  (the position  $C$  is the collision point, which is the intersection of the segment line  $\overline{AA'}$  and the surface  $\mathcal{S}$ ). The correctness of Equation 7.6 and Equation 7.7 can be verified by considering two extreme cases: First, when  $(c_{\tan}, c_{nor})$  is equal to  $(1, 1)$ , the two equations transform to equations of the elastic collision. Second, when  $(c_{\tan}, c_{nor})$  is equal to  $(0, 0)$ ,  ${}^{n+1/2}\vec{q}$  is equal to  $\overline{OC}$  and  ${}^n\vec{v}$  is a null vector, which imply a completely inelastic collision. In practice,  $c_{nor}$  has to be a value larger than one to prevent penetration from happening.

### 7.3.2 Example-gravity plus contact mechanism

This example demonstrates the dropping process of an elastic grid on a given surface (Figure 7.18). The grid structure and the surface are the same as defined in the example of Section 7.2.4. In order to

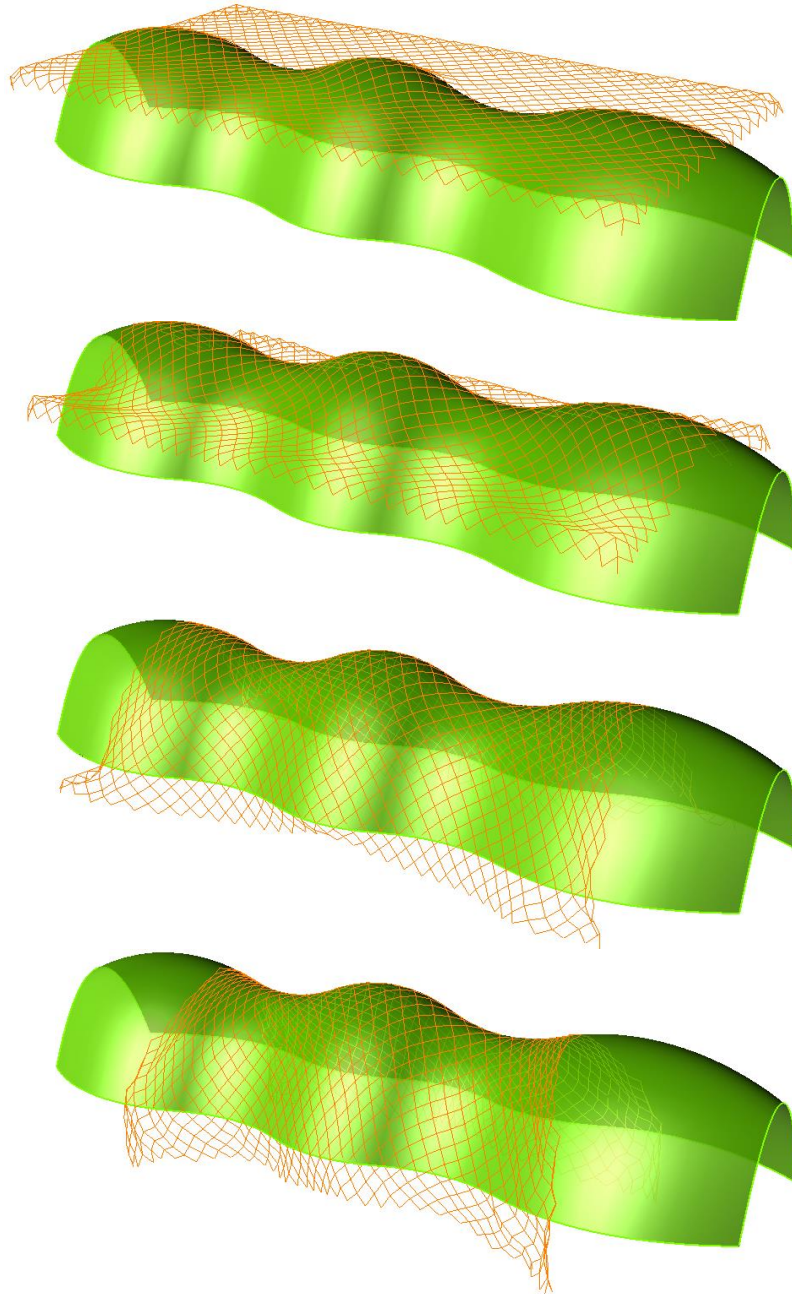


Figure 7.18: Dropping process of an elastic grid

draw the elastic grid toward the surface, a gravity load is applied and is set as 0.2 kN for each node. The scale factors for an inelastic collision are set as  $(c_{tan}, c_{nor}) = (1, 0.1)$ . For simplicity, this example is simulated with the Pien's rod model based on the 3DOF DR scheme.



### 7.3.3 Force method vs. projection method

The force method and the projection method have their own advantages and disadvantages. Therefore, it is important to choose the appropriate one for each different case. The greatest advantage of the projection method is its simplicity. There is no need to calculate additional coefficients when applying this method, and a grid could fit the target geometry without compromise.

If there is a need to further reduce the strain energy, the grid should be allowed to leave the constrain surface in certain degree such that the out-of-plane bending strain energy can be reduced. However, this is not possible by the projection method. The force method could be used here as a solution, where relatively weak traction forces are applied to the grid such that the grid could approach the target geometry in a smooth way and not be too much bended. Finding a right way to apply these traction forces and determining their appropriate magnitudes are the additional cost of this method.

### 7.4 Bending as a dominant factor in form-finding

Most of form-finding methods are based on optimizing the axial strain energy of a system, such as the force density method and the hanging chain method. What will be the result of form-finding if the bending strain energy is the only target to be optimized?

As we found in Section 7.2.4, if we want the bending mechanism to be a dominant factor in form-finding, the ratio between the transverse stiffness and the axial stiffness needs to be enlarged. When the ratio is large enough, the transverse stiffness (bending mechanism) will become dominant and the beam elements will become very tensile. They will then be able to change their lengths in a large degree to compose/form a better global geometry to minimize the bending strain energy.

What will be the corresponding physical model of this phenomenon? According to the above description, the rod should be able to freely extend or shorten its length. The corresponding physical model for this can be a continuous rod which passes through the constraint points without frictions. Because there is no friction, the rod can slip through the points and adjust the lengths such that the bending strain energy is minimized. Besides, because of no friction, there should be no axial forces in the rod too. This brings out an important conclusion: The bending dominant form-finding process should not only minimize the bending strain energy but also null the axial strain energy of the system.

The following examples are introduced to further illustrate this concept.

#### 7.4.1 Example-smoothing a kinked polyline with a bending mechanism

This example demonstrates how to use the bending mechanism to derive a smooth polyline which passes through the four pre-defined points in space (Figure 7.19). The procedure is as follows: Firstly, a kinked polyline that passes through the four points is built up (by increasing the division number of the polyline, the resulting curve can be smoother). Secondly, the bending mechanism and the point constraint on the four nodes are assigned. The point constraint will keep the positions of the constrained nodes unchanged.

The ratio between the transverse stiffness and axial stiffness is about 2, which is  $10^4$  times larger than the ratio of a beam element with a square profile of a side length of 5cm and an unstrained length of 1m (if the stiffness properties of the realistic profile is adopted, the beam element will be much less tensile and the derived polyline will not be smooth). For simplicity, this example is simulated with the Pien's rod model based on the 3DOF DR scheme.

#### 7.4.2 Example-smoothing a kinked grid with a bending mechanism

The same test can be applied to a kinked grid. The grid is composed of continuous rods oriented in three directions with a grid length of 0.5m (Figure 7.20). The ratio between the transverse stiffness and axial stiffness of the beam elements is the same as in the last example.

An initially kinked geometry is generated by extruding the central part of the plane grid downwards. Then, the beam elements of the extruded part are divided into numbers of elements for generating smoother curves.

The orange nodes are fixed as the only constraint in the model for maintaining the directions of the beam elements on the edges (Figure 7.21). For simplicity, this example is simulated with the Pien's rod model based on the 3DOF DR scheme.

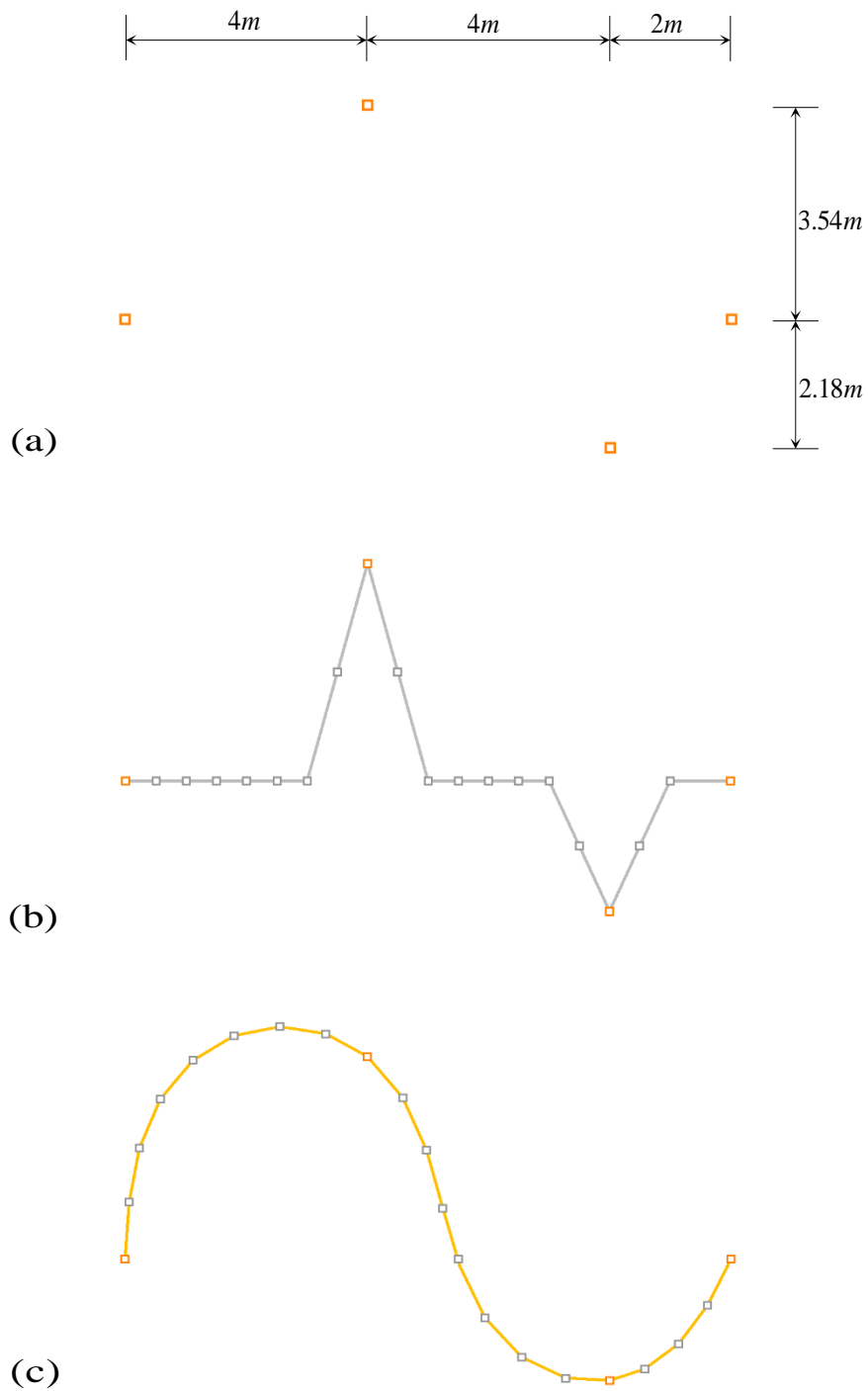


Figure 7.19: (a) Positions of the constrained points; (b) kinked polyline that passes through the constrained points; (c) curved polyline after relaxation

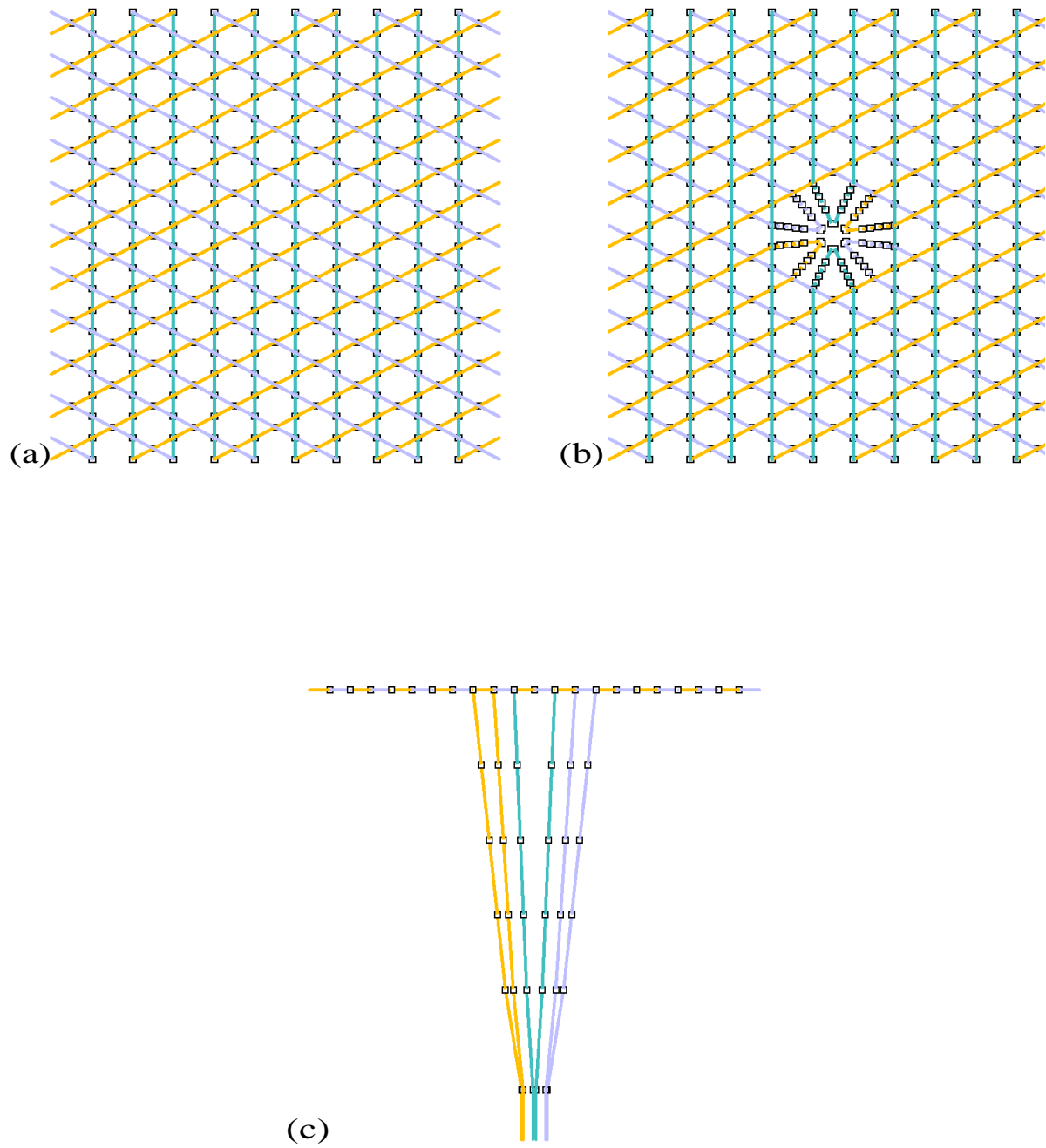


Figure 7.20: (a) Top view of a plane grid; (b) top view of an extruded grid; (c) side view of an extruded grid

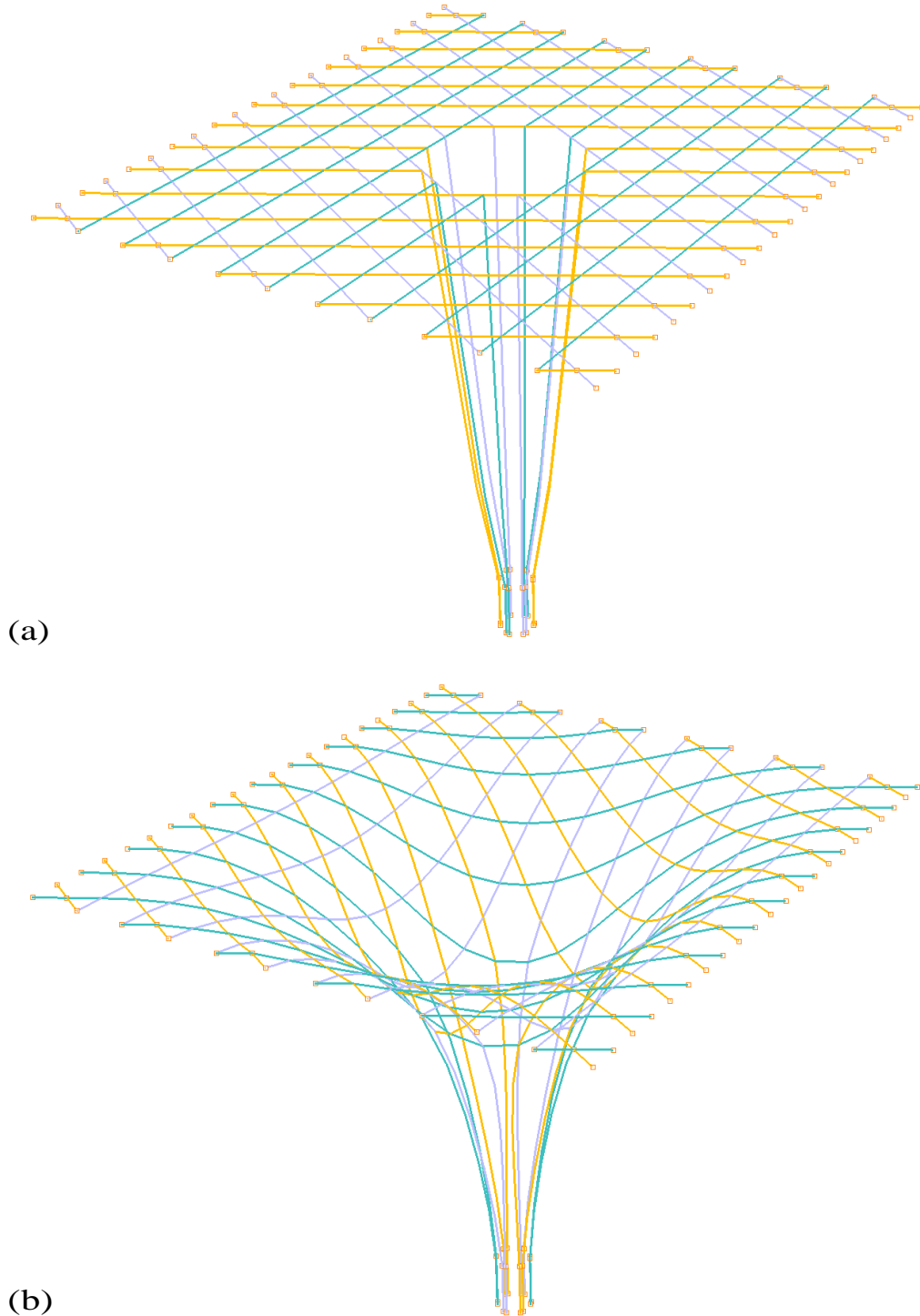


Figure 7.21: (a) Perspective view of an extruded grid; the orange nodes are imposed with the point constraint. (b) Perspective view of an extruded grid after relaxation

### 7.4.3 Example-Downland Gridshell with irregular grid lengths

If there is no requirement of having uniform member lengths, the freedom of optimizing residuals of elastic grid shells is larger. The fictitious stiffness of a profile can then be used as a variable in the form-finding process. The stiffness of a fictitious profile could enable a grid to have a larger range of strained lengths, which facilitates the reduction of bending stresses and generates smoother grid patterns.

In this example, a fictitious stiffness properties is used in the form-finding process; a factor of  $10^4$  is applied to the bending and torsional stiffness to enable the beam element to have a larger range of the strained length. This fictitious stiffness setting is only used in the form-finding stage. And once the form is found, the actual stiffness is recovered and the strained lengths of the form found are taken as the new unstrained grid lengths.

The comparison of the strain energy between the two forms, which are found with the real stiffness setting and the fictitious stiffness setting, is showed in Table 7.2, and the comparison of their geometries is showed in Figure 7.22. The in-plane bending strain energy of the irregular grid shell is largely reduced, which is only 25% of the in-plane bending strain energy of the regular grid shell. The axial strain energy is largely reduced too, which supports the argument we made in Section 7.4.1 that the bending dominant form-finding process will null the axial strain energy of the system.

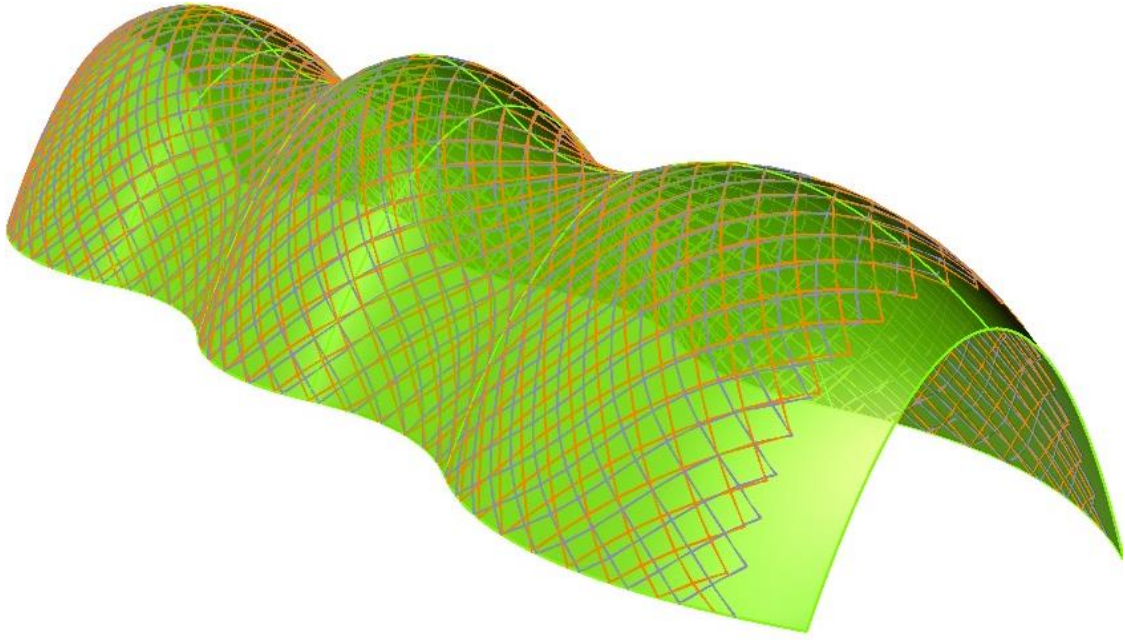


Figure 7.22: Comparison of the two grid patterns of the irregular grid and the regular grid, which are presented in the orange colour and the purple colour respectively. Both grid patterns are smooth, but the irregular grid (orange) has less in-plane bending curvatures.

Table 7.2: Comparisons of the grid length and the strain energy between the regular grid and the irregular grid

	max. length[m]	min. length[m]	strain energy [kNm]	axial strain energy [kNm]	torsional strain energy [kNm]	out-of- plane bending strain energy [kNm]	in-plane bending strain energy [kNm]
regular grid	1.0003	0.9996	9.5E+01	5.2E-01	2.5E+01	3.6E+01	3.2E+01
irregular grid	1.0602	0.9308	6.7E+01	3.2E-03	2.6E+01	3.3E+01	8.2E+00

PART III    SEGMENTAL TIMBER  
PLATE SHELL



## Chapter 8

### Introduction

Shell structures have excellent structural performance. However, due to high manufacturing costs, continuous shell structures are rarely built today. Segmental plate shells, composed of prefabricated planar panels, might offer an interesting alternative. Unlike single layer grid shells, which usually need bending-stiff joints to stabilize the structure, segmental plate shells could generate local bending stiffness without the help of bending-stiff joints. This property helps segmental plate shells to generate a relative simple connectivity, which makes this type of structures more competitive.

#### 8.1 The study of Segmental Timber Plate Shells

##### Plate shells

Because of the limited thickness of a plate shell, designing a practical connection for it has been a challenging task [18]. Plate shells of larger scales are thus rare in building construction, and only a few segmental plate shells have been built so far [56] [57] [58] [59]. Only a few studies on this subject can be found [60] [61] [57]; these involve either the use of adhesives for joining or the application of combined mechanical/adhesive techniques.

##### Inspiration from nature

Because experiences gained from the construction of segmental plate shells are limited, plate structures in nature can be used as concept generators for the design of such structures. Similar to the problem faced in man-made plate structures, the structural discontinuity between hard tissues and soft tissues of natural shells causes losses in structural performance [62]. Nevertheless, through the process of evolution, these shells have developed corresponding features to increase their strength capacity.

The shells of sand dollars, which are highly adapted sea urchins, have been studied in parallel with the development of the Landesgartenschau Exhibiton Hall. Their shells consist of modular polygonal

plates linked at the edges by finger-like calcite protrusions and organic fibers (Figure 8.1). They have soft tissues at the sutures between hard plates allowing their individual plates to grow and the bounded spaces to expand continuously. Their plate layouts have trivalent patterns that are featured to give kinematic stability when adapted into plate structures. The high load-bearing capacity of the sand dollar skeleton is well adapted to high energy environments. This is achieved through morphological features that are also attractive for many shells in building construction. The sand dollar can thus serve as a suitable model for shells in building construction. A detailed biomechanical analysis and simulation of the morphological features of the sand dollar is still pending and subject of ongoing biomimetic research.

#### The Landesgartenschau Exhibition Hall in Schwäbisch Gmünd

In 2013, ICD, ITKE, and the Institute of Engineering Geodesy (IIGS, Prof. Volker Schwieger) were commissioned by the forestry administration of Baden-Württemberg (ForstBW) to initiate a timber shell research project. One of the production of this research would be the design and construction of an exhibition hall for the annual Landesgartenschau, which took place in Schwäbisch Gmünd in 2014. This hall provided a place in which to promote the use and the function of the forest of Baden-

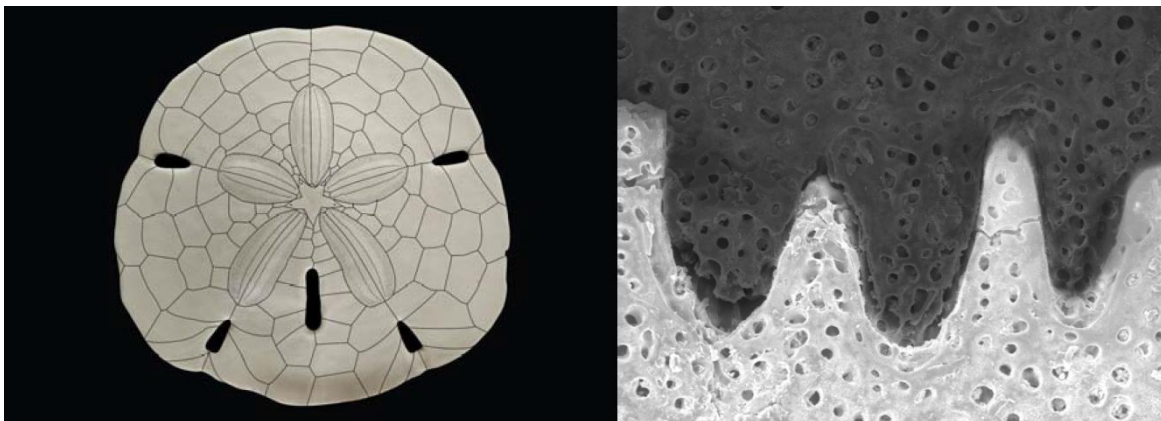


Figure 8.1 Left: Top view of a sand dollar with highlighted topology (James Nebelsick, 2014). Right: Microscopic view of the plate edge of a sand dollar (James Nebelsick, 2014).

Württemberg (Figure 8.2). And the design goal is to use the building itself as the best demonstration of the newest technologies of timber construction. The exhibition hall is proposed to stand on site as

long as possible and is therefore designed to meet the respective wind and snow load requirements. It is the first permanent segmental timber plate shell built so far.

## **8.2 Contributions**

### Innovative connection for plate structures

We propose a practical connection design for thin plate structures. This connection is composed of finger joints and crossing screw joints that could be easily fabricated and installed.

### Study of the bending stiffness of trivalent patterns

A simplified model is introduced to estimate the bending stiffness of trivalent patterns. The result shows that the bending stiffness of the hexagonal patterns and of the star-like patterns is similar. And for each pattern the bending stiffness in the two major directions are also similar.

### Improved form-finding method of trivalent polyhedrons

A form-finding method based on the principles of the Dupin duality for trivalent polyhedrons has been adopted in this research. New mechanisms are added to the method such that the smoothness and the direction of the triangulation could be better controlled.

## **8.3 Structure of Part III**

Part III consists of six chapters, from chapter eight to chapter thirteen. The structure of Part III unfolds as below: In chapter eight, we illustrate the current state of the study, our research interest and our contribution to the research of segmental timber plate shells. In chapter nine, we introduce the geometric properties of trivalent polyhedrons. In chapter ten, we show the form-finding method. In chapter eleven, we demonstrate our innovative connection design of segmental timber plate shells. In chapter twelve, we show how to build a global FE model and how to simulate connections with spring elements. In chapter thirteen, we illustrate the installation compatibility and the erection process.



Figure 8.2: Landesgartenschau Exhibition Hall, Schwäbisch Gmünd, 2014. Project Team: Inst. for Computational Design (ICD, Prof. Menges), Inst. of Building Structures & Structural Design (ITKE, Prof. Knippers), Inst. of Engineering Geodesy (IIGS, Prof. Schwieger), University of Stuttgart

## Chapter 9

### Form of Trivalent Polyhedrons

#### 9.1 Trivalent polyhedron

Given a free-form surface many corresponding polyhedrons could be found. Among them, planar hexagonal meshes (P-Hex meshes) are of particular interests because of the regularity of their geometries and their dual property with triangular meshes [63].

A PH-mesh belongs to the group of trivalent polyhedrons, whose vertex is the intersection from the three nearby polygons. The characteristic that the offset of a trivalent polyhedron remains a trivalent polyhedron makes it advantageous, compared to other polyhedral surfaces, when applied in a free-form building with multi-layer structures [64].

For a PH-mesh, according to a specific free-form surface, in the area of a positive Gaussian curvature ( $k > 0$ ), the corresponding segmental pattern is always hexagonal, while in the area of a negative Gaussian curvature ( $k < 0$ ), the corresponding segmental pattern is a star-like geometry (Figure 9.1). In the area of transition, where the Gaussian curvature approaches zero, either one side of a hexagonal pattern or one side of a star pattern will approach a straight line (Figure 9.2). This might cause mechanical instability in the structure and will be further illustrated in the following sections.

#### 9.2 Stability inherent from trivalent geometries

For a plate structure with a trivalent geometric pattern, when three plates meet at one point and are hinged at the three intersection lines, each plate is constrained by the other two. The bending stiffness is created even though the joints themselves are only hinged connections [60] [59].

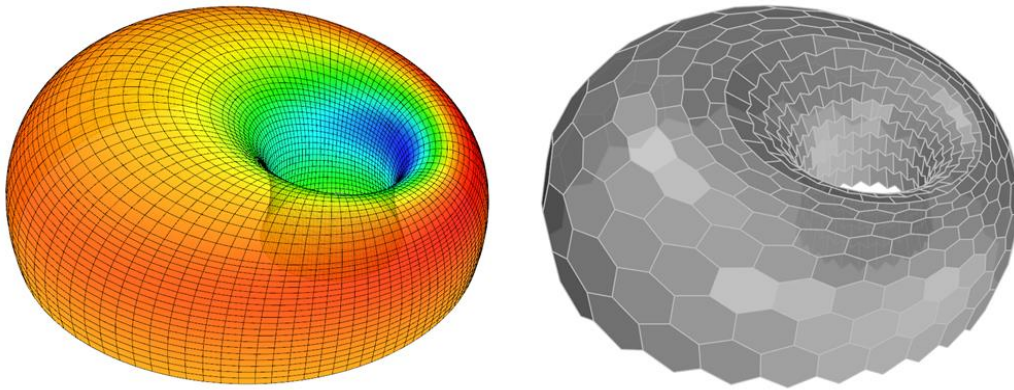


Figure 9.1 Left: Gaussian curvature analysis of a torus geometry (orange color means positive Gaussian curvature, blue means negative Gaussian curvature, and green means the Gaussian curvature approaches zero). Right: PH-mesh corresponding to the torus geometry.

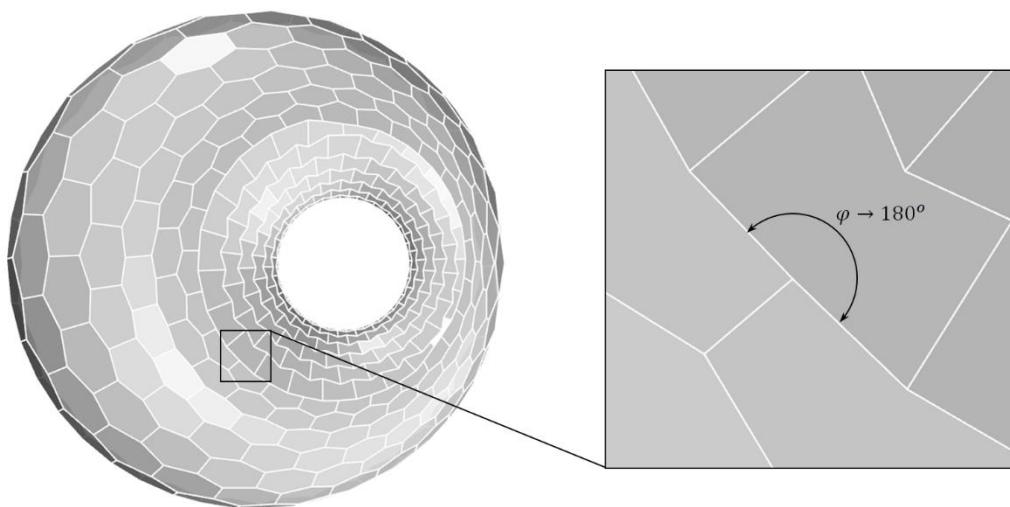


Figure 9.2: Trivalent pattern at the transition zone, where the Gaussian curvature approaches zero. Right: Enlarged figure, where the included angle approaches 180 degrees

A simplified analysis model is introduced here to facilitate the understanding of the mechanism and also for estimating the bending stiffness. As shown in Figure 9.3, the model consists of seven rows of polygons, where end A is subject to a bending moment  $M$  and end B is fixed. Because the bending moment  $M$  is transferred from end A to end B, each row of polygons generates a relative rotation around the axis.

In the marked region, one edge, which consists of four joints, is selected for a detailed analysis. The rotation stiffness  $K_{\theta, \text{ per edge}}$  of this edge around the global X-axis is defined and calculated as

$$K_{\theta, \text{ per edge}} = \frac{M_{\text{ per edge}}}{\theta} = \frac{\sum V_{Z,i} \cdot Y_i}{\theta} \quad (9.1)$$

where  $M_{\text{ per edge}}$  is the bending moment in the global X-direction taken by the edge,  $\theta$  is the relative rotation of the two plates around the X-axis,  $V_{Z,i}$  is the out-of-plane shear force of the  $i$ th joint caused by the relative rotation and  $Y_i$  is the distance from the X-axis to the  $i$ th joint. The shear force can be calculated as

$$V_{Z,i} = K_z \cdot \Delta z_i = K_z \cdot (Y_i \cdot \theta) \quad (9.2)$$

where  $K_z$  is the joint stiffness in the global Z-direction (derived from physical tests, see [8]) and  $\Delta z_i$  is the relative displacement of the joint in the z-direction. Substitute  $V_{Z,i}$  in Equation 9.1 with Equation 9.2, we get

$$K_{\theta, \text{ per edge}} = K_z \cdot \sum Y_i^2 \quad (9.3)$$

With  $Y_i = r_i \cdot \cos \varphi$  where  $r_i$  is the distance from the center of the edge to the joint and  $\varphi$  is the angle between the local y-direction and the global Y-direction, the above equation is transformed to

$$K_{\theta, \text{ per edge}} = \cos^2 \varphi \cdot K_z \cdot \sum r_i^2 \quad (9.4)$$

Since there are twelve edges along one rotation axis, the bending stiffness of all the joints along the axis is

$$K_{\theta, \text{ per axis}} = 12 \cdot K_{\theta, \text{ per edge}} \quad (9.5)$$

The corresponding rotation around the axis is thus

$$\theta_{\text{ per axis}} = \frac{M}{K_{\theta, \text{ per axis}}} \quad (9.6)$$

Because between end A and end B there are six such rotatable axes, the rotation of end A is as follows (elastic bending of the plates is neglected)

$$\theta_{end A} = \frac{6M}{K_{\theta, \text{ per axis}}} = \frac{6M}{12K_{\theta, \text{ per edge}}} = \frac{6}{12} \cdot \frac{M}{\cos^2(60^\circ) \cdot K_z \cdot \sum r_i^2} \quad (9.7)$$

One can see that when  $\varphi$  approaches  $90^\circ$ ,  $\theta_{end A}$  will approach infinite. This implies a zero bending stiffness and will cause instability in plate shells as mentioned previously.

The bending stiffness and the rotation of end A of the second pattern (Figure 9.4), which is generated by rotating the first pattern by 90 degrees, can also be analyzed and calculated in a similar way. Since, for the second pattern, there are ten rotatable axes between end A and end B and each axis has six edges, the rotation of end A is calculated as

$$\theta_{end A} = \frac{10}{6} \cdot \frac{M}{\cos^2(30^\circ) K_z \sum r_i^2} \quad (9.8)$$

Interestingly, the ratio between the rotations of the two patterns is close to unit

$$\frac{\frac{6}{12 \cos^2(60^\circ)}}{\frac{10}{6 \cos^2(30^\circ)}} = 0,90 \quad (9.9)$$

This means the two patterns have similar bending stiffness per unit area which is not easy to see without calculation. Because the second pattern is generated by a 90-degree rotation of the first pattern, it also means that the hexagonal patterns have similar bending stiffness in the two major directions.

Similar detailed rotation analysis can also be applied to the star patterns (Figure 9.5). The result shows that the bending stiffness and the rotation of end A of the first star pattern and of the second star pattern (derived by rotating the first star pattern by  $90^\circ$ ) are exactly the same as of the first hexagonal pattern and of the second hexagonal pattern respectively. Therefore, their appearance in the structure should not weaken the bending resistance.



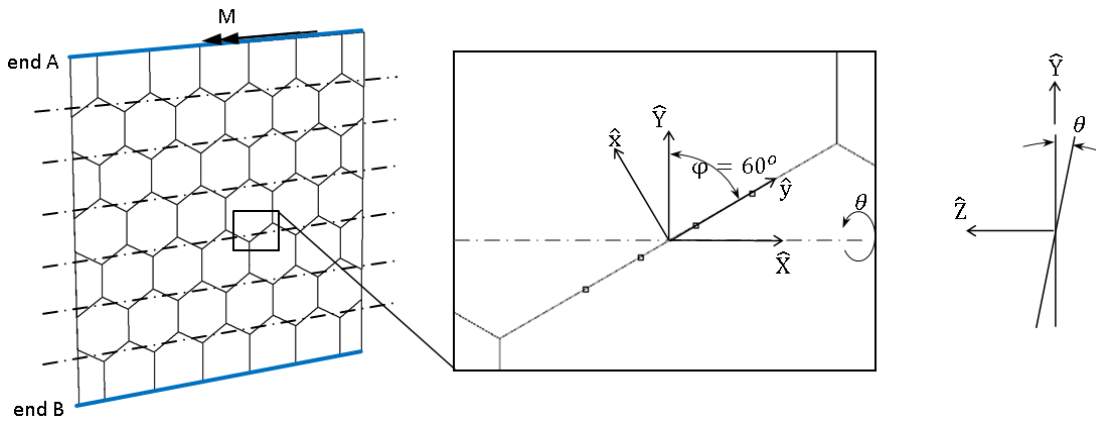


Figure 9.3 Left: Simplified bending model of the first hexagonal pattern. Middle: Selected edge for detailed analysis, which consists of four joints. Right: Section view of the selected edge

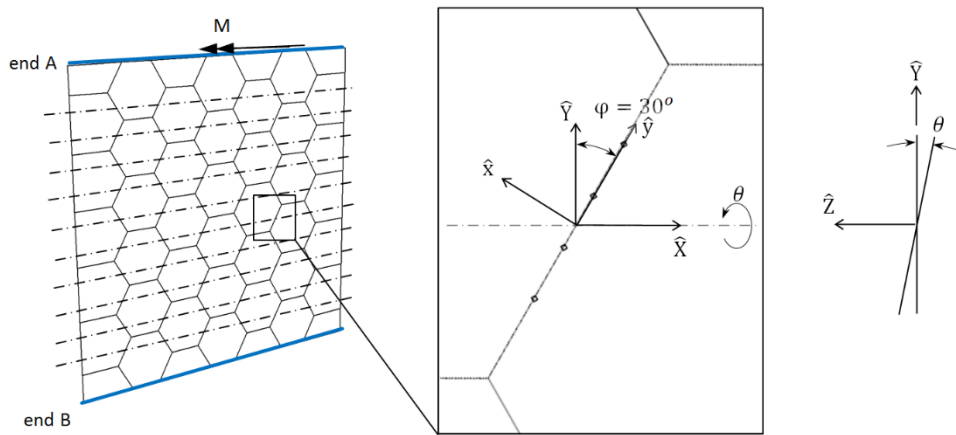


Figure 9.4 Left: Simplified bending model of the second hexagonal pattern (7m x 7m). Middle: Selected edge for detailed analysis, consists of four joints. Right: Section view of the selected edge

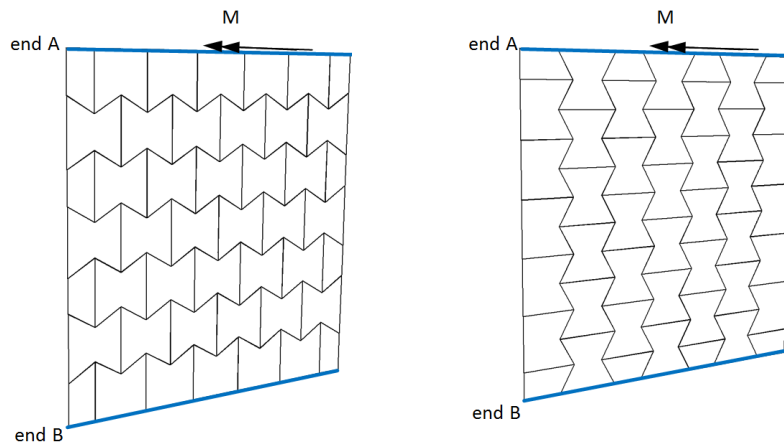


Figure 9.5: Simplified bending models of the first and of the second star-like patterns.

The result from the simplified model is further checked by the FE-models (Figure 9.6 and Figure 9.7). The plate material properties in the non-linear FE-models are set to be 10 times the stiffness of the Landesgartenschau Exhibition Hall (as shown in Chapter 11 and Chapter 12) such that the rotation within the plates can be neglected. The comparison between the FE-model and the simplified model is listed in Table 9.1. The rotation derived from the simplified model is similar to the values from the FE-models. In both cases the stiffness of all four patterns is quite similar.

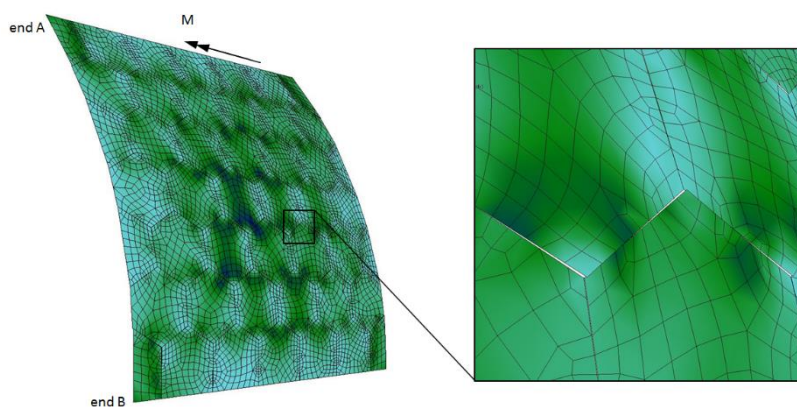


Figure 9.6 Left: Bending simulation of the first hexagonal pattern (7m x 7m). Right: Enlarged figure shows the gaps due to relative rotation.

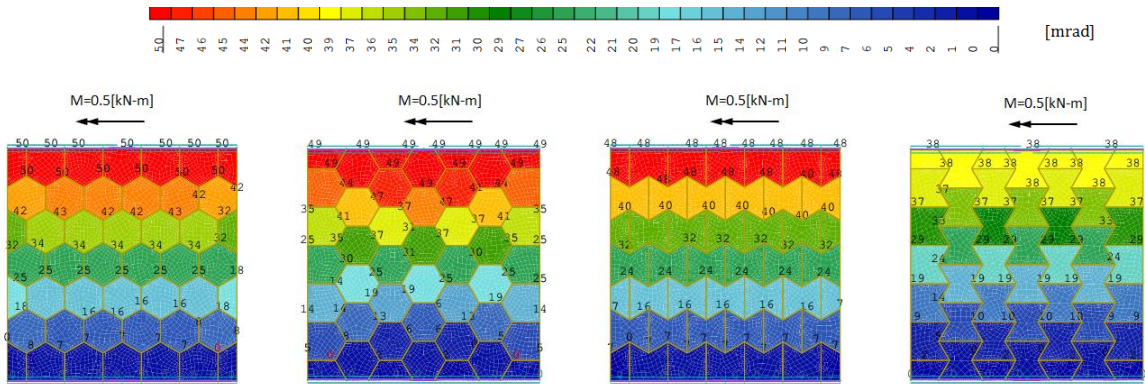


Figure 9.7: Result of bending simulation of the four patterns

rotation of end A [mrad]	$\theta_{1st\ hexa}$	$\theta_{2nd\ hexa}$	$\theta_{1st\ star}$	$\theta_{2nd\ star}$
FE-model	41	41	43	39
simplified model	44	49	44	49

Table 9.1: Rotation of end A of the four patterns

### 9.3 Patterns and Force Transfer

The pattern of segmental plates will affect the force transfer in shell structures. It defines the locations of all connections, which are the weak points in the structure. Because the material is not continuous at connections, forces will be redirected when they pass through the connections. Besides, the joint stiffness also affects the force path largely, because when the joints are stiffer, larger forces will be attracted to flow through. The geometric pattern and the joint stiffness thus determine where and how the internal forces are transferred in segmental plate shells. Four FE-models are built to investigate the phenomenon mentioned above. Each model is applied with a downward force on the top to observe how the force is transferred in the segmental elements (Figure 9.8). The joint stiffness of the models is set such that the contact mechanism of the finger joint connection (Chapter 11) is considered, which means joint stiffness in the local y-direction is much larger than the remaining two directions (in Figure 9.3 and Figure 9.4 the local coordinates of a connection are defined).

One can observe that the forces flow through the edges in a parallel way (not at a right angle to the edges). This tells us that the forces shown in Figure 9.8 are mainly transferred through edges in the

form of in-plane shear forces in the local coordinates of connections. Besides, the pattern on the left (the first hexagonal pattern) can better distribute the downward load than the pattern on the right (the second hexagonal pattern), since its stresses and reaction forces on the bottom is more uniform than of the right pattern. Similar behaviors can be observed in the star-like patterns (Figure 9.9).

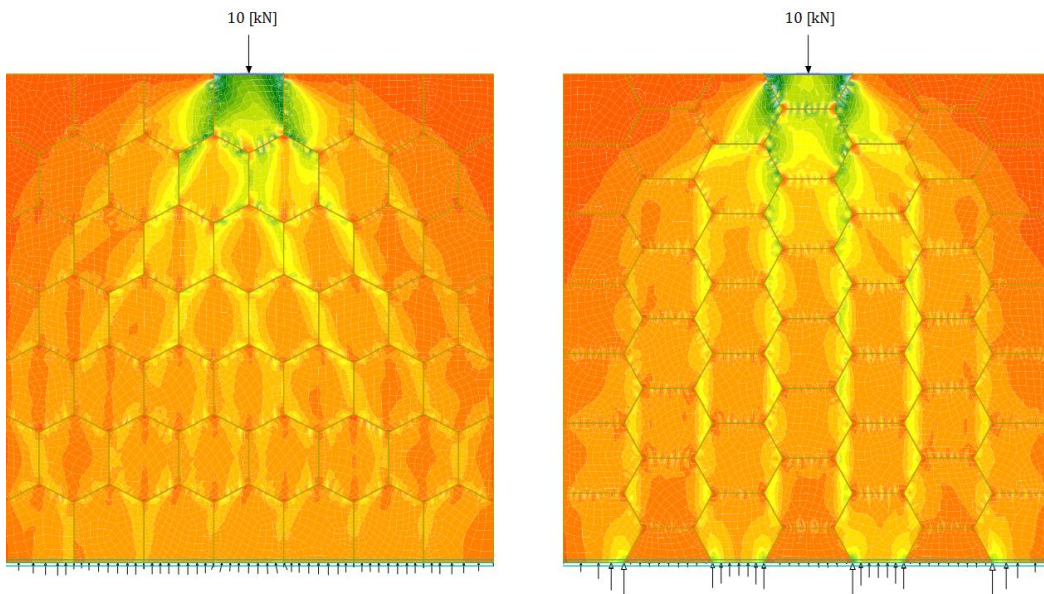


Figure 9.8: Principle stresses and reaction forces of the first and of the second hexagonal patterns

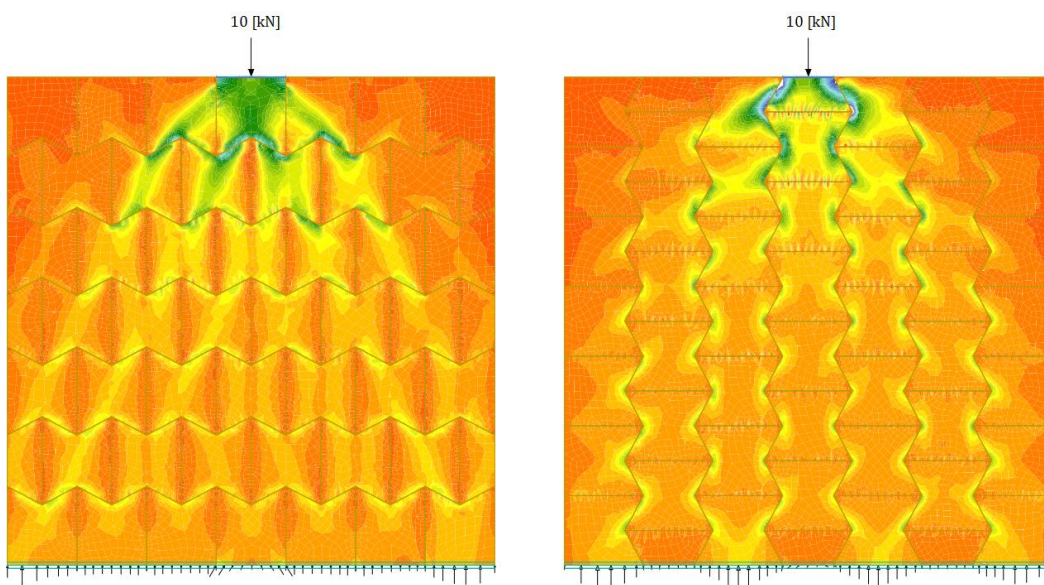


Figure 9.9: Principle stresses of the first and of the second star-like patterns

## Chapter 10

### Form-finding of Trivalent Polyhedrons

#### 10.1 Introduction

The most intuitive way to create a trivalent polyhedron of a free-form surface is through the intersection of tangent planes [65]. The intersection of a set of tangent planes of a curved surface forms a specific trivalent polyhedron (Figure 10.1). This method could be further improved by adding penalty functions such that the normal direction and the offset distance of each tangent surface could be slightly adjusted to optimize the polyhedral patterns [66]. This method, however, has two main disadvantages. First, the size and the geometry of each polygon are nearly random. Second, without using penalty functions a solution might not be found in anticlastic areas.

A method using Dupin duality is developed to deal with such difficulties [63]. This method divides the derivation of a trivalent polyhedron into two stages. First, a specific triangulation would be found by using the properties of Dupin duality. This triangulation would generate a corresponding hexagonal mesh that each hexagon is nearly flat. Second, this hexagonal mesh would be further planarized to derive a planar hexagonal mesh (P-Hex mesh). Recently, a varied version of this method

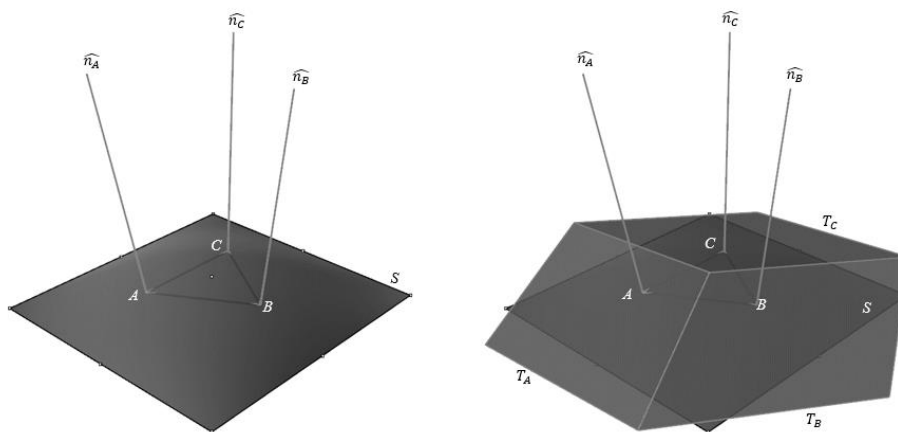


Figure 10.1: The intersection of a set of tangent planes of a curved surface forms a specific trivalent polyhedron. Points A, B and C are located on a surface S.  $\hat{n}_i$  is its normal direction and  $T_i$  is its tangent plane.

has been proposed. It is also a two-stage approach, but the initial triangulation is replaced with a planar quadrilateral mesh [67] [68].

These two-stage approaches are proved to be able to produce a better mesh, which is smoother and more regular than that of the tangent plane method. The method used in this research is based on this two-stage approach and is further improved to better adopt free form geometries.

## 10.2 Initial triangulation

### Regular and irregular P-Hex meshes

A hexagonal mesh could be generated from a triangular mesh whose vertices are of valence six (Figure 10.2). However, a hexagon from such a hexagonal mesh is not necessarily planar. After planarization the mesh geometry could change quite a lot or even self-intersected. Therefore, the initial hexagonal mesh should be as planar as possible such that the geometry after planarization would be similar to the initial hexagonal mesh geometry.

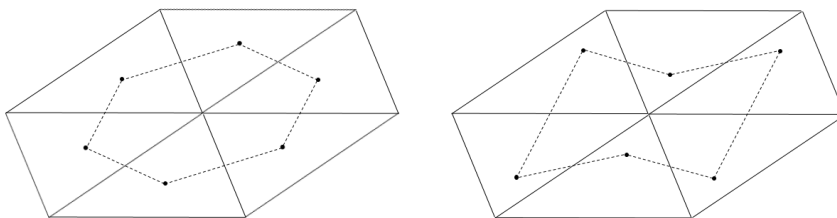


Figure 10.2: A hexagonal mesh could be generated from a triangular mesh whose vertices are of valence six. Different pattern of hexagon could be created by choosing a specific location in a triangle as the vertices of hexagons.

A relation between a triangular mesh and the corresponding P-Hex mesh could be created through the intersections of the local tangent planes of vertices as shown in Figure 8.1. However, the P-Hex mesh may be very irregular if the triangular mesh is randomly chosen. A vertex of such a P-Hex mesh may be far away from the gravity center of the corresponding triangle, and this might result a very irregular P-Hex mesh. The key point of the Dupin duality method thus is to find an ideal triangulation whose hexagonal mesh is quasi planar and has vertices that each vertex is very close to the Dupin center of the corresponding triangle. Such a triangle is also named here as an ideal triangle.

Smoothness assumption

Under the smoothness assumption, a small region of a free-form surface could be always described by two Gaussian curvatures, which are the curvature in the major directions. For a segment  $AB$  on  $S$ , an offset tangent plane  $P$  of the mid of  $AB$  would intersect with the local surface and form an ellipse for  $k > 0$  or a hyperbola for  $k < 0$  (Figure 8.3). The tangent planes of the ends  $AB$  would intersect at line  $L$ . This line could be treated as a line on plane  $P$  when  $\overline{AB}$  short enough is, and the direction of  $L$  is then the conjugate direction of  $\overline{AB}$ . This is because that, when the ratio of  $\overline{AB}/r$  approaches zero, the ratio of  $h/\overline{AB}$  will approach zero too, where  $h$  is the distance between  $L$  and  $AB$  and  $r$  is the radius of the surface curvature. This smoothness assumption simplify transfer a 3D problem into a 2D problem.

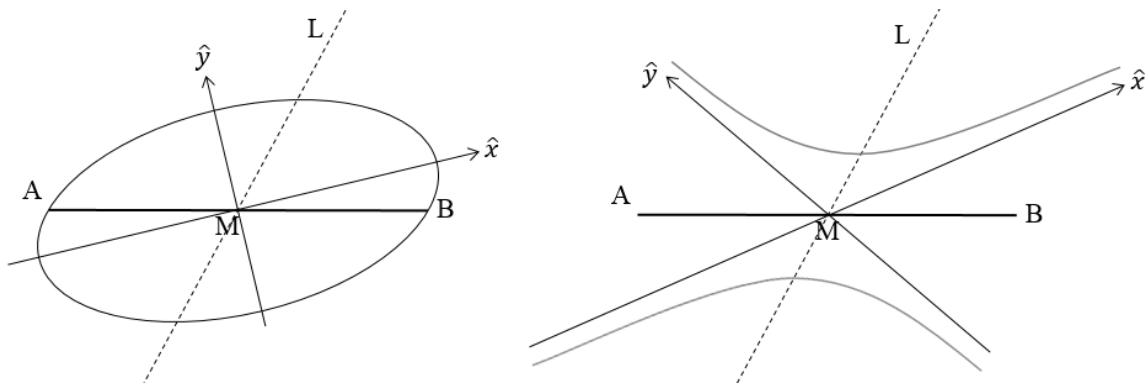


Figure 10.3: An offset tangent plane  $P$  of the mid of  $AB$  would intersect with the curved surface and form an ellipse for  $k > 0$  or a hyperbola for  $k < 0$ . The direction of line  $L$  is the conjugate direction of  $\overline{AB}$ . Vectors  $\hat{x}$  and  $\hat{y}$  are the major directions of the curved surface.

Ideal triangle and ideal triangulation

A triangle  $ABC$  has its bottom vertices  $A$  and  $B$  and top vertex  $C$  on a surface  $S$ . The tangent planes of  $A$  and  $B$  intersect at a line  $L1$ . And the tangent planes of  $B$  and  $C$  intersect at a line  $L2$  (Figure 10.4). When  $ABC$  is an ideal triangle of surface  $S$ ,  $C$  shall locate at  $L1$  and  $A$  shall locate at  $L2$ . If  $A$  and  $B$  are fixed, the procedure of finding  $C$  will be to adjust the position of  $C$  on  $L1$  iteratively until  $L2$  is pointing toward  $A$  for  $k > 0$  or until  $\overline{CO} = 2\overline{CM}/3$  for  $k < 0$ . Beside the iterative method, point  $C$  could also be solved analytically [63]. The solution is illustrated in Figure 10.5.

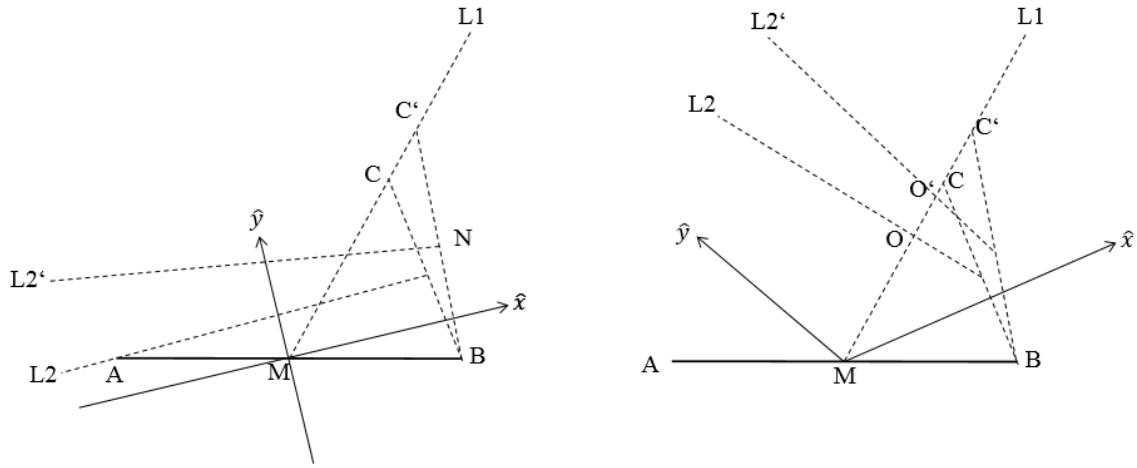


Figure 10.4 Left:  $k > 0$ ; Right:  $k < 0$ . In both cases, the tangent planes of  $A$  and  $B$  intersect at a line  $L1$ . And the tangent planes of  $B$  and  $C$  intersect at a line  $L2'$ . The procedure of finding  $C$  will be to adjust the position of  $C$  on  $L1$  iteratively until  $L2$  is pointing toward  $A$  for  $k > 0$  or until  $\overline{CO} = 2\overline{CM}/3$  for  $k < 0$ .

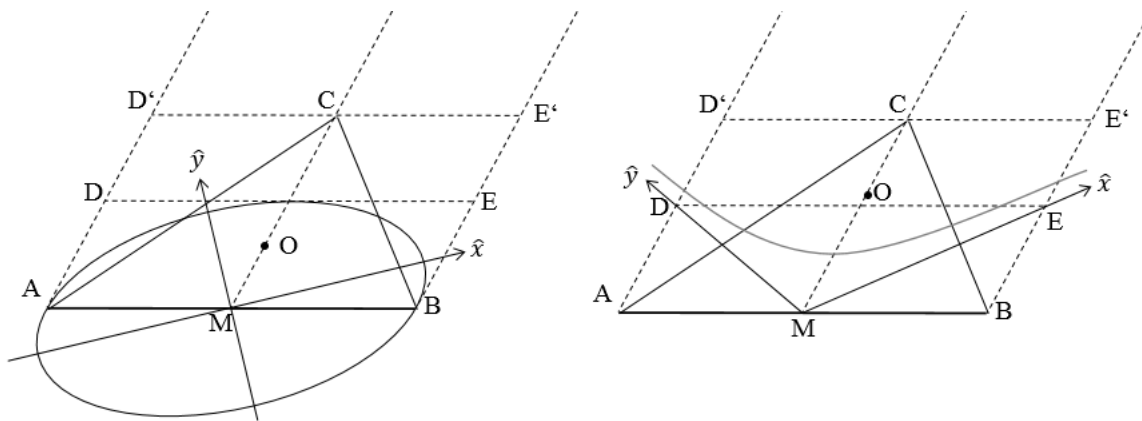


Figure 8.5 Left:  $k > 0$ ; Right:  $k < 0$ . In both cases,  $C$  is the intersection point of  $\overline{MC}$  and  $\overline{D'E'}$ , where  $\overline{MC}$ ,  $\overline{AD'}$  and  $\overline{BE'}$  are parallel with  $\overline{AB}$ 's conjugate direction and  $\overline{DE}$  and  $\overline{D'E'}$  are parallel with  $\overline{AB}$ . The position of  $D'$  is determined by setting  $\overline{AD'}/\overline{AD} = \sqrt{3}$ . However, the position of  $D$  is determined differently. For  $k > 0$ ,  $D'$  is determined by letting  $\overline{DE}$  a tangent to the ellipse. For  $k < 0$ ,  $D'$  is determined by finding the intersection of ray  $\hat{y}$  and a ray which passes through  $A$  and parallel with  $\overline{MC}$ .



One may note from the figure that, for an anticlastic surface zone, the intersection of L1 and L2 of an ideal triangle is no more at the gravity center but at the middle point between the gravity center and C. For both cases of synclastic areas and anticlastic areas, the intersection point of L1 and L2 is all named as the Dupin center of the triangle.

An ideal triangulation, which are composed of ideal triangles, could be derived by the conjugate network method [63]. This method starts from a base curve  $C_0$  which is composed of segments of a uniform length usually. Using the method illustrated in the last paragraph, the corresponding top vertex of each segment could be determined. All these newly generated vertices will form a new base curve  $C_1$ . The rest curves could be formed in a similar manner (Figure 10.6 and Figure 10.7).

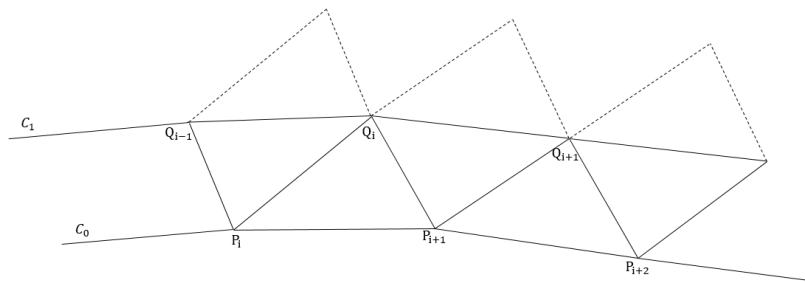


Figure 10.6: An ideal triangulation starts from a base curve  $C_0$ . The corresponding top vertex of each segment could be determined by the method illustrated in this section and all these newly generated vertices will form a new base curve  $C_1$ .

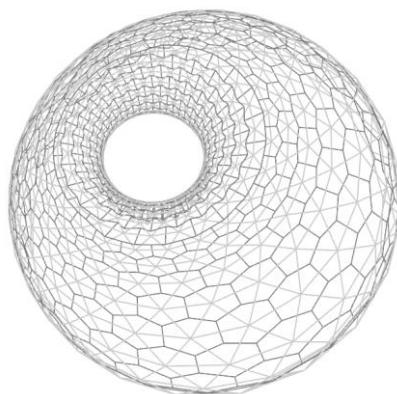


Figure 10.7: The ideal triangulation (light gray) can generate a quasi P-Hex mesh (dark grey).

However, this method usually results in a mesh which is not smooth, especially when the curvature experiences a large change in a small distance. Some mechanisms have to be added into the triangulation process to smooth the curve. In this research, a bending stiffness is added into the curve to adjust the smoothness.

When the conjugate direction is parallel to the main direction of  $S$ , the resulted mesh will be normal to the base curves and generate a normal, not affine, hexagon geometry. However, even when the initial base curve is parallel with the main direction, the later base curves will gradually deviate from the main direction and cause an oblique triangulation. Therefore, additional nodal forces are assigned to the vertices of a base curve segment when its direction is not parallel with the main direction of the surface curvature in order to adjust the base curve's direction closer to the main direction. 3DOF DR is used here as a solver to find such the solution.

#### Transition zone

The above mentioned triangulation procedure faces another challenge when the Gaussian curvature changes its sign or approaches zero. When the Gaussian curvature approaches zero,  $CM$  ( $M$  is the middle point of  $AB$ ), will be much longer or much smaller than  $AB$ . Both cases will cause a bad triangulation. The solution applied here is through setting the upper bound and the lower bound of the ratio  $q = \overline{MC}/\overline{AB}$  (Figure 10.8) to limit the variation.

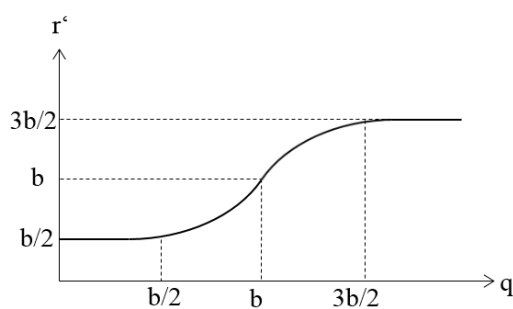


Figure 10.8: The definition of the ration  $r'$ , which is the actual value in use to relocate point  $C$ .

The ratio  $r'$  is the actual value in use. Point  $C$  is relocated such that  $r' = \overline{MC}/\overline{AB}$  but the unit vector  $\widehat{MC}$  remains unchanged.  $r'$  defined as follows

$$\begin{aligned}
 & \frac{b}{2} + \frac{q^2}{2b}, \text{ for } 0 < q \leq b \\
 & \frac{3b}{2} - \frac{(q-2b)^2}{2b}, \text{ for } b < q \leq 2b \\
 & \frac{3b}{2}, \text{ for } 2b < q
 \end{aligned} \tag{8.1}$$

Where the coefficient  $b$  could be simply taken as a value one.

### 10.3 Planarization

A hexagon mesh could be generated out of an ideal triangulation by connecting the Dupin centers of all the triangles. But this hexagonal mesh is only nearly planar and needed to be further planarized. This planarization is done by assigning a bending mechanism to the quad elements of each hexagon, where the hexagon is divided into six quad elements (Figure 10.9). And only quad edges within the hexagon have bending stiffness. Edges between hexagons are hinged. The solver applied here is also 3DOF DR.

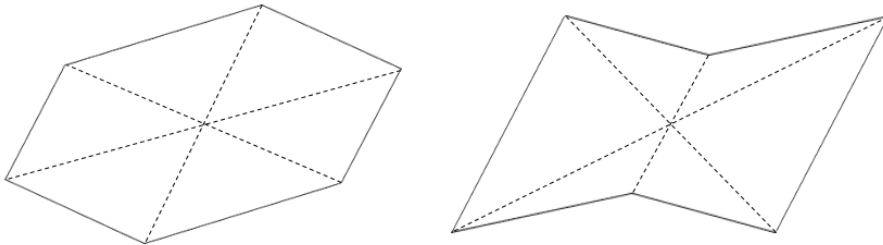


Figure 10.9: Each hexagon is divided into six quad elements. Only quad edges within the hexagon have bending stiffness. Edges between hexagons are hinged.

## Chapter 11

## Connection Design

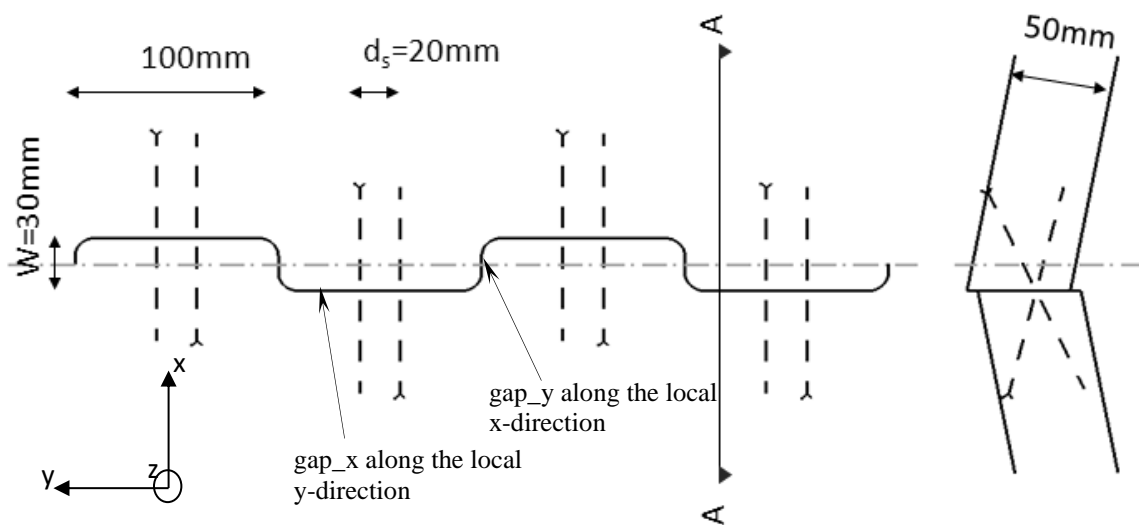


Figure 11.1 Left: Top view of a connection; a connection consists of numbers of finger joints and crossing screw joints in its local coordinates. Right: Section view AA.

The design of a feasible connection that provides sufficient strength and stiffness between panels with a thickness of only 50 mm was one of the key challenges of the project. Our objective that the connection could ultimately be applied to the building industry also meant that we had to follow the building code during the development process. Our research has thus led to a novel connection design for plate structures: finger joints are used in connections to resist decisive in-plane shear forces, whereas the smaller axial forces and out-of-plane shear forces are taken up by crossing screw joints (Figure 11.1). The crossing screws lie in parallel planes, normal to the edge, with distance  $d_s=20$  mm to each other. The screws intersect with each other with a specific angle in the side view.

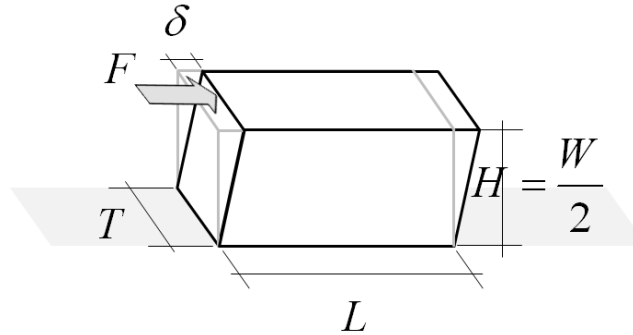


Figure 11.2: The shear deformation model of a finger joint; the thrust force will be taken by the contact surface and be transferred to the shear plane at the bottom. The stiffness and the capacity of the finger joint can be estimated from this model.

As shown in Figure 11.1, two kinds of gaps are considered in the connection model. One is parallel with the local y-axis (gap\_x), and the other is parallel with the local x-direction (gap\_y). Their functions are explained in the following sections.

### 11.1 In-plane shear resistance

The stiffness generated from a single wooden block of a finger joint,  $K_{y,contact}$ , can be estimated by a shear deformation model as in Figure 11.2 and is calculated as

$$K_{y,contact} = \frac{F}{\delta} = \frac{GLT}{H} \quad (11.1)$$

where  $F$  is the in-plane shear force,  $G$  is the shear modulus,  $\delta$  is the shear displacement, and  $H$ ,  $L$ , and  $T$  are its height, length, and thickness, respectively. Because the contact mechanism is generated by a pair of wooden blocks that behave like a series of springs, despite the stiffness of a finger joint, the displacement has to be doubled, and the stiffness of the finger joint becomes

$$K_{y,contact} = \frac{GLT}{2H} \quad (11.2)$$

The capacity of the finger joint in the local y-direction,  $F_{y,contact,Rd}$ , can be calculated by considering the shear failure of the bottom surface of the wooden block as

$$F_{y,contact,Rd} = \frac{k_{mod}}{\gamma_M} f_{V,k} LT \quad (11.3)$$

where  $k_{mod}$  is the modification factor for the duration of the load and the moisture content,  $\gamma_M$  is the partial factor for the material properties, and  $f_{V,k}$  is the characteristic shear strength of the plywood (all notations are according to DIN EN 1995-1-1 2010). A more careful study of the performance of a finger joint, under the influence of the grain direction of the surface ply, was conducted by building an FE-model of the finger joint and analyzing its membrane stresses. The results show that the maximum membrane forces and the shear displacement in the finger joint are not strongly related to the grain direction of the surface ply.

If there is a gap along the local x-direction of a connection (gap\_y in Figure 11.1), the wooden finger joint can only generate resistances after the contact takes place. Before that, the shear resistance is provided only by the crossing screw joint. The shear stiffness,  $K_{y,screw,ser}$ , of a crossing screw joint could be calculated as (DIN EN 1995-1-1 2010)

$$K_{y,screw,ser} = 2\rho_m^{1.5} d / 23 \quad (11.4)$$

where  $\rho_m$  is the mean density of the plywood, d is the outer diameter measured on the threaded part, and the factor two arises from the number of screws per joint. According to the code, the stiffness  $K_{y,screw}$  used for calculating the ultimate limit states is adjusted as follows

$$K_{y,screw} = \frac{2}{3} K_{y,screw,ser} \quad (11.5)$$

As stated in the code, the shear capacity of the crossing screw joint in the local y-direction,  $F_{y,screw,Rd}$ , can be calculated by the failure of the screwed joint in the plywood

$$F_{y,screw,Rd} = 2 \frac{k_{mod}}{\gamma_M} \left( 1,15 \sqrt{2M_{y,Rk} f_{h,k} d} + \frac{F_{ax,k}}{4} \right) \quad (11.6)$$

where  $M_{y,Rk}$  is the characteristic fastener yield moment,  $f_{h,k}$  is the characteristic embedment strength in the plywood, and  $F_{ax,k}$  is the characteristic withdrawal capacity of the screw.

## 11.2 Axial force and out-of-plane shear resistance

Neglecting the in-plane shear in the connection and considering only the axial force and the out-of-plane shear, the analysis of the internal forces and the corresponding stiffness of a crossing screw joint can be reduced to a two-dimensional force diagram problem; a simplified model first introduced by Blaß [69] is adapted here, in which the crossing screws are analyzed as a truss structure subjected to axial forces, as shown in Figure 11.3. The stiffness provided by the left side of the crossing screw joint,  $K_{z,r}$ , along the local z-direction of the joint, can be calculated as follows: by assuming a displacement,  $\Delta_{z,r}$ , along the local z-direction of the joint, the work,  $W$ , done by the external force,  $F_z$ , is

$$W = F_z \Delta_{z,r} / 2 \quad (11.7)$$

whereas the strain energy,  $U$ , stored in the screws is

$$U = (K_{ax,1} \sin^2 \theta_1 + K_{ax,2} \sin^2 \theta_2) \Delta_{z,r}^2 / 2 \quad (11.8)$$

where  $\theta_i$  is the angle between the screw axis and the local x-direction of the joint, and  $K_{ax,i}$  is its withdrawing stiffness (Figure 11.3). For a static system, the work is equal to the strain energy

$$F_z \Delta_{z,r} / 2 = (K_{ax,1} \sin^2 \theta_1 + K_{ax,2} \sin^2 \theta_2) \Delta_{z,r}^2 / 2 \quad (11.9)$$

By rearranging the above equation and defining  $K_{z,r}$  as  $F_z / \Delta_{z,r}$ , we obtain

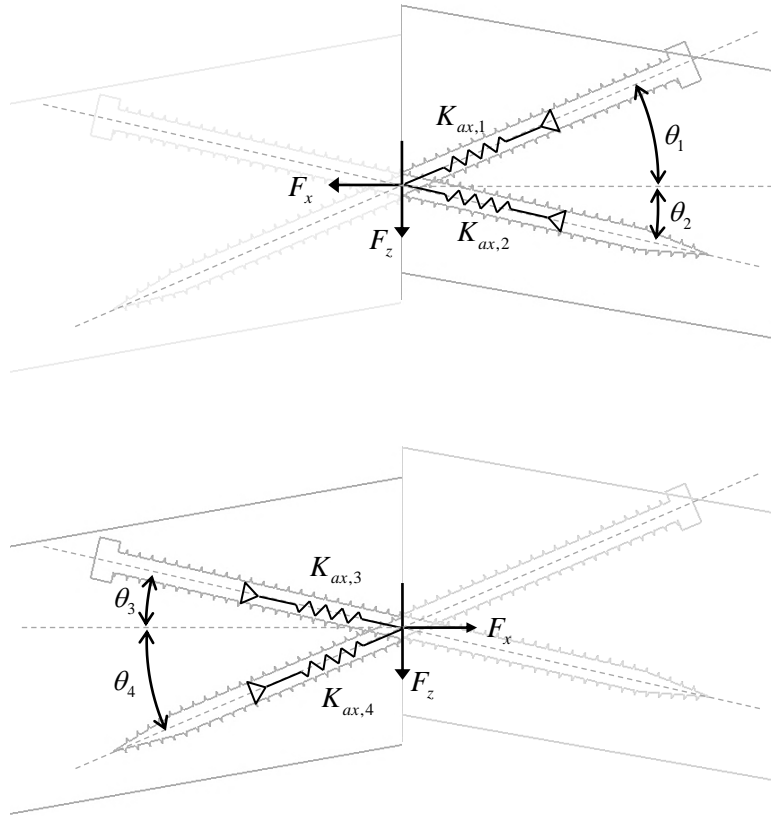


Figure 11.3: Simplified truss model of a crossing screw joint; the stiffness and design capacities of a crossing screw joint can be derived by using this model.

$$K_{z,r} = (K_{ax,1} \sin^2 \theta_1 + K_{ax,2} \sin^2 \theta_2) \quad (11.10)$$

Similarly, the stiffness in the local z-direction, provided by the left side of the crossing screw joint,

$K_{z,screw,l}$ , can be derived as

$$K_{z,l} = (K_{ax,3} \sin^2 \theta_3 + K_{ax,4} \sin^2 \theta_4) \quad (11.11)$$

Readers should note that  $\theta_1$  and  $\theta_2$  are equal to  $\theta_4$  and  $\theta_3$ , respectively. However, for a better comprehension,  $\theta_3$  and  $\theta_4$  are still preserved in the following derivation.



Because the crossing screw joint lies between two plates, the stiffness provided by the two sides of the joint should be considered as series springs. The spring stiffness,  $K_{z,screw}$ , of a crossing screw joint along the local z-direction is thus

$$K_{z,screw} = \frac{K_{z,l}K_{z,r}}{K_{z,l} + K_{z,r}} = \frac{(K_{ax,1} \sin^2 \theta_1 + K_{ax,2} \sin^2 \theta_2)(K_{ax,3} \sin^2 \theta_3 + K_{ax,4} \sin^2 \theta_4)}{\sum_{i=1}^4 K_{ax,i} \sin^2 \theta_i} \quad (11.12)$$

The design capacity,  $F_{z,screw,Rd}$ , of a screw joint in the local z-direction is determined by the one that is the first to reach its withdrawing capacity of the four penetration parts

$$F_{z,screw,Rd} = \min \left\{ \frac{(K_{ax,1} \sin^2 \theta_1 + K_{ax,2} \sin^2 \theta_2)F_{ax,Rd,1}}{K_{ax,1} \sin \theta_1}, \frac{(K_{ax,1} \sin^2 \theta_1 + K_{ax,2} \sin^2 \theta_2)F_{ax,Rd,2}}{K_{ax,2} \sin \theta_2}, \right. \\ \left. \frac{(K_{ax,3} \sin^2 \theta_3 + K_{ax,4} \sin^2 \theta_4)F_{ax,Rd,3}}{K_{ax,3} \sin \theta_3}, \frac{(K_{ax,3} \sin^2 \theta_3 + K_{ax,4} \sin^2 \theta_4)F_{ax,Rd,4}}{K_{ax,4} \sin \theta_4} \right\} \quad (11.13)$$

where  $F_{ax,Rd,i}$  is the withdrawing design capacity of the  $i$  th penetration part. In a similar way, the spring stiffness,  $K_{x,screw}$ , and the design capacity,  $F_{x,screw,Rd}$ , along the local x-direction of a crossing screw joint can be derived as

$$K_{x,screw} = \frac{(K_{ax,1} \cos^2 \theta_1 + K_{ax,2} \cos^2 \theta_2)(K_{ax,3} \cos^2 \theta_3 + K_{ax,4} \cos^2 \theta_4)}{\sum_{i=1}^4 K_{ax,i} \cos^2 \theta_i} \quad (11.14)$$

$$F_{x,screw,Rd} = \min \left\{ \frac{(K_{ax,1} \cos^2 \theta_1 + K_{ax,2} \cos^2 \theta_2)F_{ax,Rd,1}}{K_{ax,1} \cos \theta_1}, \frac{(K_{ax,1} \cos^2 \theta_1 + K_{ax,2} \cos^2 \theta_2)F_{ax,Rd,2}}{K_{ax,2} \cos \theta_2}, \right. \\ \left. \frac{(K_{ax,3} \cos^2 \theta_3 + K_{ax,4} \cos^2 \theta_4)F_{ax,Rd,3}}{K_{ax,3} \cos \theta_3}, \frac{(K_{ax,3} \cos^2 \theta_3 + K_{ax,4} \cos^2 \theta_4)F_{ax,Rd,4}}{K_{ax,4} \cos \theta_4} \right\} \quad (11.15)$$

In a special case, where  $F_{ax,Rd,1} = F_{ax,Rd,2} = F_{ax,Rd,3} = F_{ax,Rd,4} = F_{ax,Rd}$ ,

$K_{ax,1} = K_{ax,2} = K_{ax,3} = K_{ax,4} = K_{ax}$ , and  $\theta_1 = \theta_2 = \theta_3 = \theta_4 = \theta/2$ , the stiffness and the design capacity of a crossing screw joint are reduced to

$$\begin{aligned} K_{x,screw} &= K_{ax} \cos^2(\theta/2) \\ K_{z,screw} &= K_{ax} \sin^2(\theta/2) \end{aligned} \quad (11.16)$$

$$\begin{aligned} F_{x,screw,Rd} &= 2F_{ax,Rd} \cos(\theta/2) \\ F_{z,screw,Rd} &= 2F_{ax,Rd} \sin(\theta/2) \end{aligned} \quad (11.17)$$

### 11.3 Influence of screw orientation in plywood

In the simplified model of a crossing screw joint, the most important components for the calculation of its stiffness and capacity are the stiffness and the capacity of an axially loaded screw. However, in building codes, rules governing the stiffness and the capacity of an axial loaded screw are not sufficient. These values have thus been determined by experiments conducted by the authors.

Because connections occur all around a plate, the screws enter the plywood from various directions. Moreover, because of the varied jointed angles between two adjacent plates and the crossing arrangement of screws, each screw possesses a special inclining angle relative to the norm of the plate. Two angles are thus defined to describe this specific orientation: the inclining angle,  $\alpha$ , which is defined as the angle between the axial direction of the screw and the norm of the surface ply; the sway angle,  $\beta$ , which is defined as the angle between the projected vector of the axial direction of the screw to the surface ply and the grain direction of the surface ply (Figure 11.4).

To determine the influence of the screw orientation on the withdrawing performance (stiffness and capacity), a series of withdrawing tests, with various screw orientations, was conducted. According to the developed structural layout, the possible screw orientations in the plywood were bounded by the following angles: the inclining angle,  $\alpha$ , varied from  $60^\circ$  to  $90^\circ$ , and the sway angle,  $\beta$ , varied from  $0^\circ$  to  $45^\circ$ . Combinations of  $\alpha$  and  $\beta$  were thus selected in order to cover this range;  $\{(\alpha, \beta)\} = \{(90,0), (90,45), (90,90), (60, 0), (60, 45)\}$ . The screw had an outer diameter of 6 mm, a total length

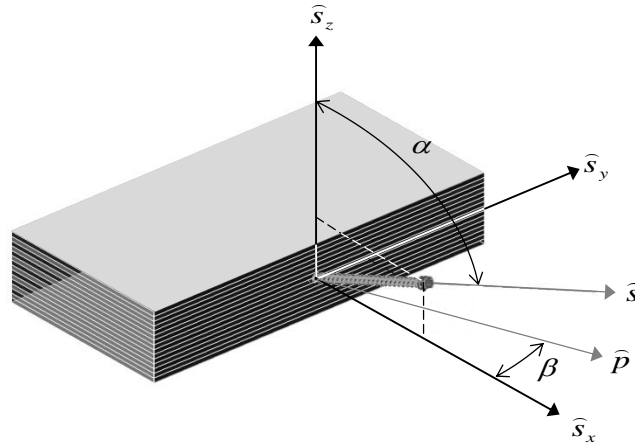


Figure 11.4: Definitions of the inclining angle,  $\alpha$ , and the sway angle,  $\beta$ .  $\hat{s}$  is the axial direction of the screw;  $\hat{P}$  is the grain direction of the surface ply;  $\hat{s}_x$  is the projected vector of  $\hat{s}$  to the surface ply;  $\hat{s}_z$  is the norm of the surface ply;  $\hat{s}_y$  is defined as  $\hat{s}_z \times \hat{s}_x$ .

Table 11.1: The characteristic values of the withdrawing capacity,  $F_{ax,k}$ , and the mean values of the withdrawing stiffness,  $K_{mean}$ , related to various orientations of screws in plywood.

$(\alpha, \beta)$	(90,0)	(90,45)	(90,90)	(60,0)	(60,45)
$F_{ax,k}$ [N]	12713	13391	12574	12713	13442
$K_{mean}$ [N/mm]	4000	3810	4848	4500	3100

of 120 mm, and a penetration length of 60 mm. These settings were exactly the same as in the developed details of crossing screw joints.

For each orientation five specimens were tested. As shown in Table 11.1, the mean withdrawing stiffness of a single screw,  $K_{mean}$ , varies from 3100 to 4848 [N/mm], whereas its characteristic capacity,  $F_{ax,k}$ , varies from 12574 to 13442 [N]; the characteristic capacity is not sensitive to the screw orientation in the plywood, whereas the stiffness obviously changes with the screw orientation. For other possible orientations, the values of  $K_{mean}$  and  $F_{ax,k}$  can be calculated by applying the interpolation functions and by using the values in Table 11.1 as nodal values.

### 11.4 Function of gaps

Three reasons can be given for having gaps between panels. First, gap width can cover the dimension deviation caused by fabrication or moisture. Second, the existence of gaps makes the installation easier; it creates buffer zones that facilitate the positioning of plates to the target geometry. The third reason is to prevent the level effect in the screwed joint and is discussed in the next section. The existence of gaps might reduce the overall performance of the structure. A careful study of the influence of the gap width is thus necessary and is illustrated in Section 11.5.

### 11.5 Bending stiffness in the joint

As stated in Chapter 9, the bending stiff connections are not required in general, if a trivalent geometry is adapted for plate shells. However, a trivalent polyhedral plate structure will become locally kinematically unstable if one of the three angles of a vertex is close to 180 degrees (Figure 11.5). For these areas, additional bending stiffness in connections can effectively improve the structural performance. Therefore, bending stiffness in connections still needs to be considered in the structural analysis of the Landesgartenschau Exhibition Hall.

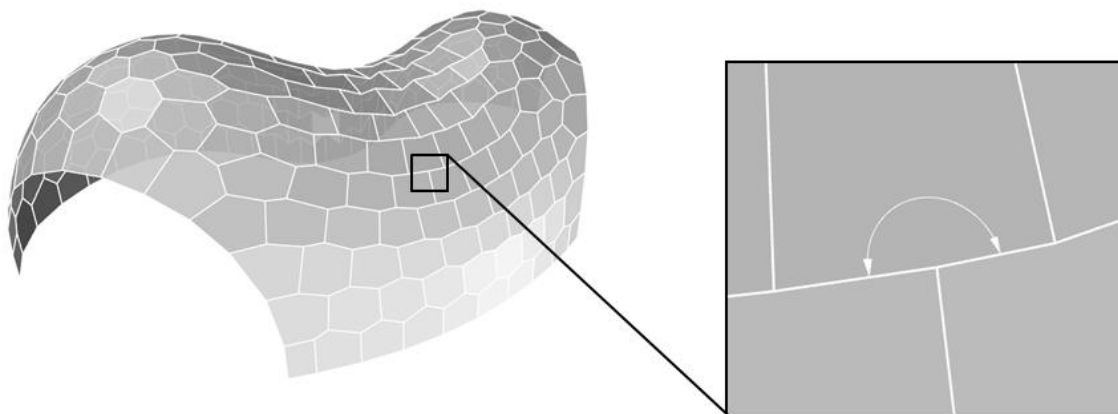


Figure 11.5 Left: A trivalent pattern at the transition zone, where the Gaussian curvature approaches zero. Right: Enlarged figure, where the included angle approaches 180 degrees.

The bending stiffness of a screwed finger joint is determined by a four-point-bending experiment. With the increase of the rotation, two edge surfaces will contact each other and thus create a lever effect that generates pulling out forces on screws. This lever effect is designed to be avoided, and only the bending stiffness before the contact is considered. To prevent a contact taking place, the following inequality is checked

$$\theta_y \leq \frac{d_x - \Delta_x}{t/2} \quad (11.18)$$

where  $\theta_y$  is the relative rotation between the plates,  $d_x$  is the unstressed gap width,  $\Delta_x$  is the displacement of the connection along the local x-direction, and  $t$  is the plate thickness (Figure 11.6). When the inequality holds, no contact will occur between the surfaces of gap\_x.

### 11.6 Minima distances and spacing of screws

In the European Technical Approvals, rules have been laid down concerning minima distances and the spacing of screws (ETA-12/01 14 2012). Although the case illustrated in the approval is not exactly the same as that here, similar rules are still applied here in the joint design to prevent potential splitting failures:

$$\begin{aligned} a_{2,c} &\geq 2.5 \cdot d \\ a_{3,c} &\geq 5 \cdot d \\ a_{4,c} &\geq 3 \cdot d \\ a_{4,c}' &\geq 2.5 \cdot d \\ \alpha_k &\geq 30^\circ \end{aligned} \quad (11.19)$$

where  $a_{2,c}$ ,  $a_{3,c}$ ,  $a_{4,c}$ , and  $a_{4,c}'$  are defined by the centroid of the part of the screw in the plywood (Figure 11.7), and  $d$  is the outer thread diameter of the screw.

These rules are helpful when deciding the penetration point and the angle of the screw. They are not difficult to follow in areas of positive Gaussian curvature. However, in areas of negative Gaussian

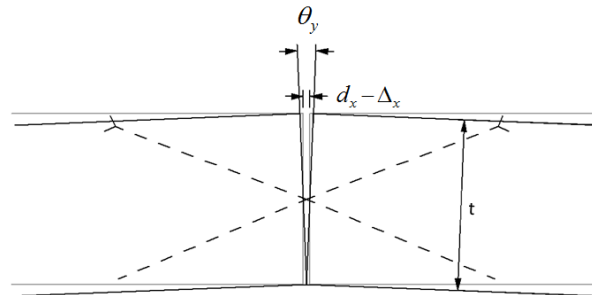


Figure 11.6: The relationship between the rotation angle, the gap width and the plate thickness of a bended screwed joint.

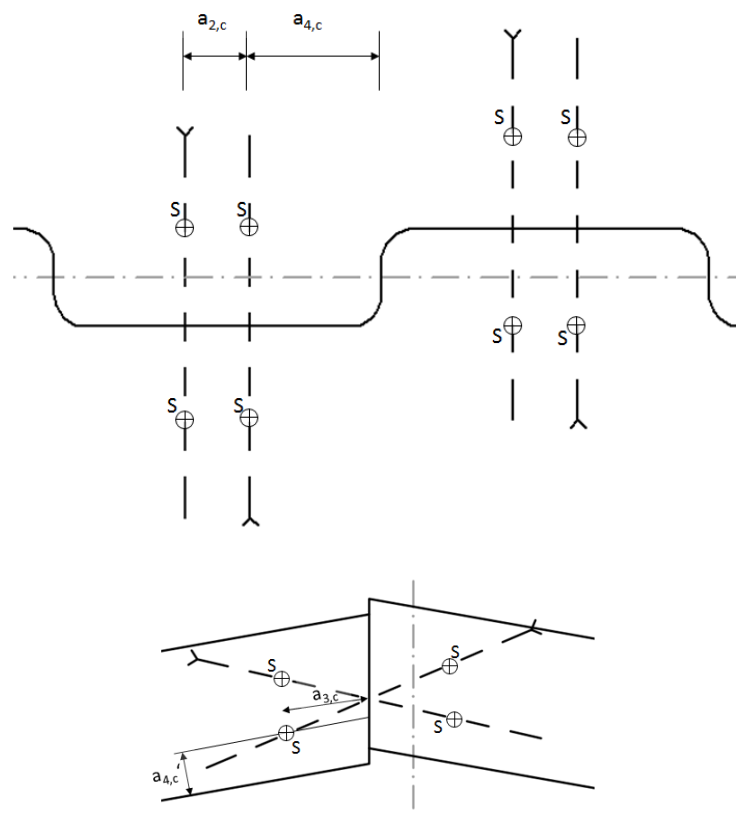


Figure 11.7: The top view and the section view of a connection; S is the centroid of the penetration length of the screw.

curvature, if the screws are installed from the outside of the structure, the guiding slot will become extremely long. To solve this problem, a shorter screw with a length of 80mm is used.

## Chapter 12

### Structural Analysis

#### 12.1 FE-model

The whole structural simulation of the Landesgartenschau Exhibition Hall is carried out with the FE program, Sofistik. The following sections introduce in detail how the connection and the plate are simulated.

##### 12.1.1 Spring element

Because the structural performance of a plate shell is highly correlated with the properties of its connections, a proper simulation of its connections is thus important. In the developed finite element (FE) model, the stiffness of the connections is simulated by spring elements: every connection, which consists of a finger joint and a pair of crossing screws, is simulated by four spring elements that act on the two nodes situated at the opposite sides of two adjoining plates (Figure 12.1 Right). Three springs are used for simulating the axial resistance, the in-plane shear resistance, and the out-of-plane

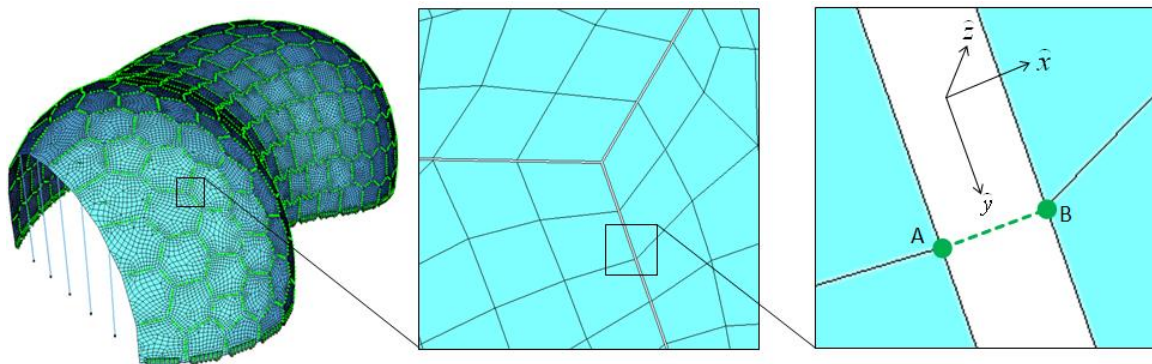


Figure 12.1. Left: The global FE model of the pavilion. Right: Spring elements act on two nodes, A and B, situated at the two opposite sides of neighboring panels. Axes  $x$ ,  $y$ , and  $z$  are the directions of the axial force, the in-plane shear, and the out-of-plane shear, respectively. Axis  $y$  is also the axis of bending resistance.

shear resistance, respectively, whereas the fourth spring is used for simulating the bending resistance. Each spring is assigned with a specific direction of action (Figure 12.1 Right) and a specific spring coefficient. The internal forces of these spring elements are used for examining whether any joint exceeds the design capacity.

The contour of each plate is a simple polygon; the detailed geometries of finger joints are not implied (Figure 12.1 Middle). This is because the inclusion of the detailed geometries of the finger joints will largely increase the number of plate elements and cause the simulation to be highly inefficient.

### 12.1.2 Simulation of gap

The in-plane shear in a connection will be completely taken up by the crossing screw joint if the in-plane displacement of the connection is smaller than the gap width, but once the displacement reaches the gap width, contact occurs, and the finger joint starts to take the force. Therefore, the in-plane shear resistance of a connection,  $K_y$ , cannot be simulated with a constant spring coefficient. Instead, it has to be simulated with a step function

$$\text{For } |\Delta_y| \leq d_y, K_y = K_{y,screw} \quad (12.1.a)$$

$$\text{For } |\Delta_y| > d_y, K_y = K_{y,screw} + K_{y,contact} \quad (12.1.b)$$

where  $\Delta_y$  is the connection displacement along the local y-direction of the connection,  $d_y$  is the gap width related to in-plane shears, and  $K_{y,screw}$  and  $K_{y,contact}$  are the values of stiffness of the in-plane resistances provided by a crossing screw joint and the contact mechanism of a finger joint, respectively. The subscript  $y$  means that the in-plane shear resistance acts in the local y-direction of the connection.

Gaps are also present in the local x-directions of connections. When the compression force is large enough, the opposite surfaces will contact each other and generate resisting forces. The corresponding axial stiffness,  $K_x$ , is then expressed as

$$\text{For } \Delta_x \leq -d_x, K_x = K_{x,screw} \quad (12.2.a)$$



$$\text{For } \Delta_x > -d_x, K_x = K_{x,screw} + K_{x,contact} \quad (12.2.b)$$

where  $\Delta_x$  is the connection displacement along the local x-direction of the connection,  $d_x$  is the gap width related to axial forces,  $K_{x,screw}$  is the value of stiffness of the axial resistance provided by the crossing screw joint, and  $K_{x,contact}$  is the value of stiffness of the axial resistance provided by the contact mechanism of the finger joint. The subscript  $x$  means that the axial resistance acts in the local x-direction of the connection. However, to ensure the functionality of the screwed joint this contact should be avoided and the gap width should be controlled as mentioned in Section 11.4 and Section 115.

### 12.1.3 Simulation of plywood

The shell element in Sofistik is based on Mindlin Plate Theory and is extended by a non-conforming formulation to calculate the membrane forces. By Sofistik shear locking is prevented, and both thin plate and thick plate can be properly simulated (Sofistik 2007).

Because each ply of plywood can be seen as a transversely isotropic material, the overall material properties and behavior of plywood can thus be approximated and described by the classic lamination theory (CLT). For those FE analysis programs in which CLT has been integrated, such as SOFISTIK and ANSYS, multi-layer fibrous materials can be properly simulated.

## 12.2 Failure criteria of a connection

A connection is constituted by a finger joint and a crossing screw joint. In this section, the calculations of failure criteria for both types of joints are illustrated.

### 12.2.1 Failure criterion of crossing screw joint

As mentioned previously, a crossing screw joint provides the axial resistance, the out-of-plane shear resistance, and the in-plane shear resistance. Therefore, when calculating the failure criterion of a

crossing screw joint, all of the contributions from these three forces should be considered. The contribution of the in-plane shear resistance is calculated as

$$\left| \frac{F_{y,screw,Ed}}{F_{y,screw,Rd}} \right| \quad (12.3)$$

where  $F_{y,screw,Ed}$  is the in-plane shear resistance provided by the crossing screw joint and  $F_{y,screw,Rd}$  is the corresponding design capacity (Equation 11.6).  $F_{y,screw,Ed}$  can only be derived from  $\Delta_y$  indirectly and is calculated as

$$F_{y,screw,Ed} = K_{y,screw} \Delta_y \quad (12.4)$$

where  $\Delta_y$  is the displacement of the in-plane shear spring and is defined as to the connection displacement of a connection along the local y-direction.

Comparing this with Equation 12.3, the contribution of the axial resistance and the out-of-plane shear resistance is calculated as

$$\left| \frac{F_{x,Ed}}{F_{x,screw,Rd}} \right| + \left| \frac{F_{z,Ed}}{F_{z,screw,Rd}} \right| \quad (12.5)$$

where  $F_{x,Ed}$  is the axial force of the connection (derived from the axial spring) and  $F_{z,Ed}$  is the out-of-plane shear of the connection (derived from the out-of-plane shear spring). Because  $F_{x,screw,Rd}$  and  $F_{z,screw,Rd}$  are directly related to the axial withdrawing capacity of a screw (Equation 11.13 and Equation 11.15), their contributions to the failure criterion should be linearly additive as shown in Equation 12.5.

When considering the screw failure criteria from two perpendicular internal forces in its major directions, the quotients of the contributions should be squared before addition. Therefore, the failure criterion of a crossing screw joint is evaluated as

$$\left( \left| \frac{F_{x,Ed}}{F_{x,screw,Rd}} \right| + \left| \frac{F_{z,Ed}}{F_{z,screw,Rd}} \right| \right)^2 + \left( \frac{F_{y,screw,Ed}}{F_{y,screw,Rd}} \right)^2 \leq 1 \quad (12.6)$$

where the first part on the left-hand side of the inequality is the contribution from the axial forces of the screws, and the second part is the contribution from the lateral forces of the screws.

### 12.2.2 Failure criterion of finger joint

The failure criterion of a finger joint is evaluated as

$$\left| \frac{F_{y,contact,Ed}}{F_{y,contact,Rd}} \right| \leq 1 \quad (12.7)$$

where  $F_{y,contact,Ed}$  is the in-plane shear resistance provided by the contact mechanism of a finger joint and is calculated as

$$F_{y,contact,Ed} = F_{y,Ed} - F_{y,screw,Ed} \quad (12.8)$$

where  $F_{y,Ed}$  is the in-plane shear of a connection (derived from the in-plane shear spring).

## 12.3 Stress and failure criteria of plywood

Because plywood is a fibrous material, and because every plywood plate in a plate shell structure generates both the membrane action and the plate action, there are multi-ways of potential failures. According to the building code (DIN EN 1995-1-1/NA 2013), the stresses caused by internal forces should be calculated for each ply layer and should be smaller than the corresponding design values as follows (Figure 12.2):

$$\begin{aligned}
\sigma_{x,i} &= \sigma_{xM} - \sigma_{xB,i} \leq f_{m,Rd} \\
\sigma_{y,i} &= \sigma_{yM} - \sigma_{yB,i} \leq f_{m,Rd} \\
\tau_{xy,i} &= \tau_{xyM} - \tau_{xyB,i} \leq f_{V,Rd} \\
\tau_{xz,i} &\leq f_{R,Rd} \\
\tau_{yz,i} &\leq f_{R,Rd}
\end{aligned} \tag{12.9}$$

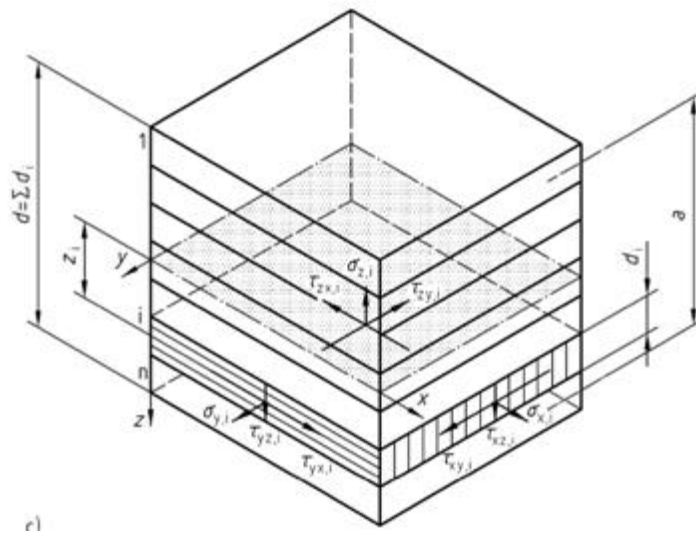


Figure 12.2: Definitions of stresses in each ply (DIN EN1995-1-1/NA).  $x$  marks the local  $x$ -direction of the plate, which is the grain direction of surface ply;  $z$  marks the local  $z$ -direction of the plate, which is the normal direction of the plate; the subscript  $y$  marks the local  $y$ -direction of the plate, which is defined as  $\hat{y} = \hat{z} \times \hat{x}$ .

where  $\sigma_{x,i}$  and  $\sigma_{y,i}$  are the overall normal stresses, in the  $i$ th layer, caused by the membrane force and plate bending in the local  $x$ -direction and in the local  $y$ -direction, respectively,  $\tau_{xy,i}$  is the overall shear stress, in the  $i$ th layer, caused by in-plane shear and plate twisting,  $\tau_{xz,i}$  and  $\tau_{yz,i}$  are the shear stresses, in the  $i$ th layer, caused by the differentiation of plate bending in the local  $x$ -direction and in the local  $y$ -direction, respectively,  $\sigma_{xB,i}$  and  $\sigma_{yB,i}$  are the normal stresses, in the  $i$ th layer, caused by plate bending in the local  $x$ -direction and in the local  $y$ -direction, respectively;  $\tau_{xyB,i}$  is the shear stress, in the  $i$ th layer, caused by twisting in the plate;  $\sigma_{xM}$  and  $\sigma_{yM}$  are the normal stresses caused

by membrane force in the local x-direction and in the local y-direction, respectively,  $\tau_{xyM}$  is the shear stress caused by the membrane shear, and  $f_{m,Rd}$ ,  $f_{V,Rd}$ , and  $f_{R,Rd}$  are the bending design stress, the shear design stress, and the roll shear design stress, respectively, of a single ply.

The checking process can be further simplified by only checking the stresses in the outmost layers and the center layer; this is because the maximum stresses, caused by plate bending or twisting, always take place at the outermost layers, and the maximum horizontal shear always takes place in the center layer. The corresponding checking inequalities are thus reduced to

$$\begin{aligned}
 \sigma_{x,o} &= \sigma_{xM} - \sigma_{xB} \leq f_{m,Rd} \\
 \sigma_{y,o} &= \sigma_{yM} - \sigma_{yB} \leq f_{m,Rd} \\
 \tau_{xy,o} &= \tau_{xyM} - \tau_{xyB} \leq f_{V,Rd} \\
 \sigma_{x,u} &= \sigma_{xM} + \sigma_{xB} \leq f_{m,Rd} \\
 \sigma_{y,u} &= \sigma_{yM} + \sigma_{yB} \leq f_{m,Rd} \\
 \tau_{xy,u} &= \tau_{xyM} + \tau_{xyB} \leq f_{V,Rd} \\
 \tau_{xz,c} &\leq f_{R,Rd} \\
 \tau_{yz,c} &\leq f_{R,Rd}
 \end{aligned} \tag{12.10}$$

where  $\sigma_{x,o}$  and  $\sigma_{x,u}$  are the overall normal stresses of the top layer and of the bottom layer, respectively, in the local x-direction of the plate,  $\sigma_{y,o}$  and  $\sigma_{y,u}$  are the overall normal stresses of the top layer and of the bottom layer, respectively, in the local y-direction of the plate,  $\tau_{xy,o}$  and  $\tau_{xy,u}$  are the overall shear stresses of the top layer and of the bottom layer, respectively, in the local xy-plane,  $\tau_{xz,c}$  and  $\tau_{yz,c}$  are the overall shear stresses of the center layer in the local xz-plane and in the local yz-plane, respectively,  $\sigma_{xB}$  and  $\sigma_{yB}$  are the normal stresses, in the outermost layers, caused by plate bending in the local x-direction and in the local y-direction, respectively, and  $\tau_{xyB}$  is the shear stress in the outermost layers, which is caused by twisting in the plate.

By assuming that the ply thickness is much smaller than the plywood thickness and that  $E_0$  (the stiffness in the grain direction of the ply) is much larger than  $E_{90}$  (the stiffness perpendicular to the

grain direction of the ply), the unknown stresses in Equation 12.10 can be approximated as follows (Figure 12.3):

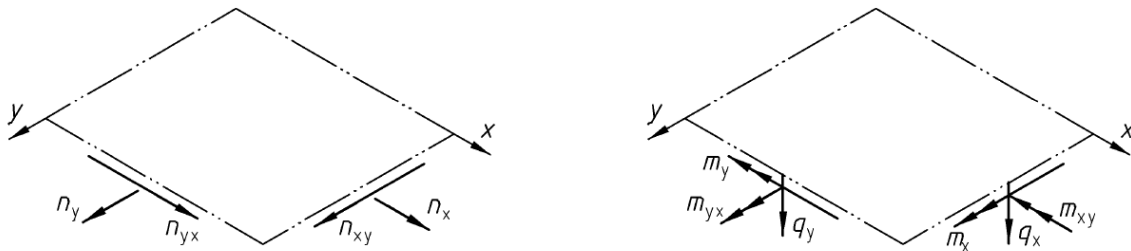


Figure 12.3. Left: Definitions of membrane forces; right: Definitions of plate forces (DIN EN1995-1-1/NA).

$$\sigma_{xB} = 12m_{xx}/T^2 \quad (12.11.a)$$

$$\sigma_{yB} = 12m_{yy}/T^2 \quad (12.11.b)$$

$$\tau_{xyB} = 6m_{xy}/T^2 \quad (12.11.c)$$

$$\sigma_{xM} = 2n_x/T \quad (12.11.d)$$

$$\sigma_{yM} = 2n_y/T \quad (12.11.e)$$

$$\tau_{xyM} = n_{xy}/T \quad (12.11.f)$$

$$\tau_{xz,c} = (3/2)q_x/T \quad (12.11.g)$$

$$\tau_{yz,c} = (3/2)q_y/T \quad (12.11.h)$$

where  $m_{xx}$  and  $m_{yy}$  are the bending moments in the local  $x$ -direction and in the local  $y$ -direction, respectively,  $m_{xy}$  is the twisting moment,  $n_x$  and  $n_y$  are the normal forces in the local  $x$ -direction and in the local  $y$ -direction, respectively,  $n_{xy}$  is the membrane shear in the local  $xy$ -plane, and  $q_x$  and  $q_y$  are the out-of-plane shears in the local  $yz$ -plane and in the local  $xz$ -plane, respectively.

One may notice that compared with the corresponding stress of a isotropic material with the stiffness  $E = E_0$ , (12.11.a) is twice the value of it. This is because that the bending moment is taken here only by half number of the layers and the maximal normal stress is thus doubled. Meanwhile, (12.11.c) remains the same when compared with the corresponding stress in the isometric material. This is because the torsion is taken by all the layers (the in-plane shear stiffness  $G$  of a plywood layer is the

same in both major directions). The same argument and comparison can be made for other stresses in Equation 12.11.

## 12.4 Structural performance

Three limit load analyses were conducted to test the influence of the gap width on overall structural stability and performance. Three different settings have been compared: case A with gap width  $d_y = 0$  [mm] (the contact mechanism generates resistances immediately once the structure is loaded), case B with  $d_y = 1$  [mm], and case C with  $d_y = \text{infinity}$  (the in-plane resistance is provided by screw joints only). For all of these three cases, the gap width  $d_x$  is 1 mm.

The selected load case for testing the limit load of the structure is  $L = 1.35D + 1.5S$ , which is one of the most critical load cases in the analysis, where  $D$  is the self-weight of the building and  $S$  is the un-symmetric snow load. The un-symmetric snow load is distributed in a triangulate way as shown in Figure 12.4: in the concave area, the peak value is 2.84 [kN/m<sup>2</sup>], whereas in the convex areas, it is 1.42 [kN/m<sup>2</sup>]. The values of the material stiffness and the values of the joint stiffness are factored with  $1/\gamma_M$  and  $2/(3\gamma_M)$ , respectively (DIN EN 1995-1-1).

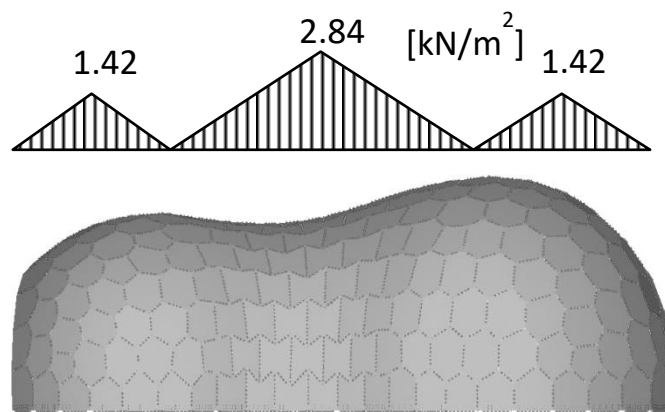


Figure 12.4: The un-symmetric snow load applied to the shell structure for the pushover tests.

Table 12.1: Comparison of forces in connections of case B and case C for load factor  $c = 1$ 

[kN]	maximum tension force in screw joints	maximum in-plane shear in screw joints	maximum in-plane shear in finger joints
case C (dy=infinite)	4.61	2.45	none
case B (dy=1)	3.32	0.73	9.09

The process of the limit-load iteration proceeds by increasing the load factor  $c_n$  (subscript  $n$  is the iteration number) in a geometric progression:  $c_1 = 0.25$ ;  $c_2 = 0.5$ ; if  $n > 2$  and the system converges at the previous iteration, then  $c_n = c_{n-1} + 2(c_{n-1} - c_{n-2})$ ; if  $n > 2$  and the system diverges at the previous iteration, then  $c_n = c_{n+1} + 0.5(c_{n-1} - c_{n-2})$ . The iteration process is terminated if the iteration number is larger than 20.

As shown in Table 12.1, the application of finger joints can largely reduce the in-plane shears in crossing screw joints from 2.45 to 0.73 [kN]. Meanwhile, the maximum tension force in crossing screw joints is reduced from 4.61 to 3.32 [kN]. The reasons for these two positive effects from finger joints are as follows: First, because of the high stiffness of finger joints, the in-plane displacement can hardly further increase after contact, and the maximum in-plane shear taken by a screw joint is thus bounded and will not be over-loaded. Second, this high in-plane resistance of finger joints will change the transfer of force in the structure; more forces will be transferred across connections in the form of in-plane shears, instead of axial forces, and as a result, the axial forces in connections, which are completely taken up by screw joints, are reduced.

The application of finger joints can also effectively make the plate shell stiffer and stronger (Figure 12.5): when the load factor reaches the value of 1, the vertical maximum displacements of case A and of case B are 42% and 77% of case C, respectively; the ultimate loads of case A and of case B are 1.59 times and 1.18 times more than case C, respectively.

Readers should also note that case B is not more advantageous than case C in the initial loading process. This is because no contact takes place in case B for small loading; the benefit of the finger joints becomes apparent only after the structure is further loaded and the contacts of the finger joints take place.



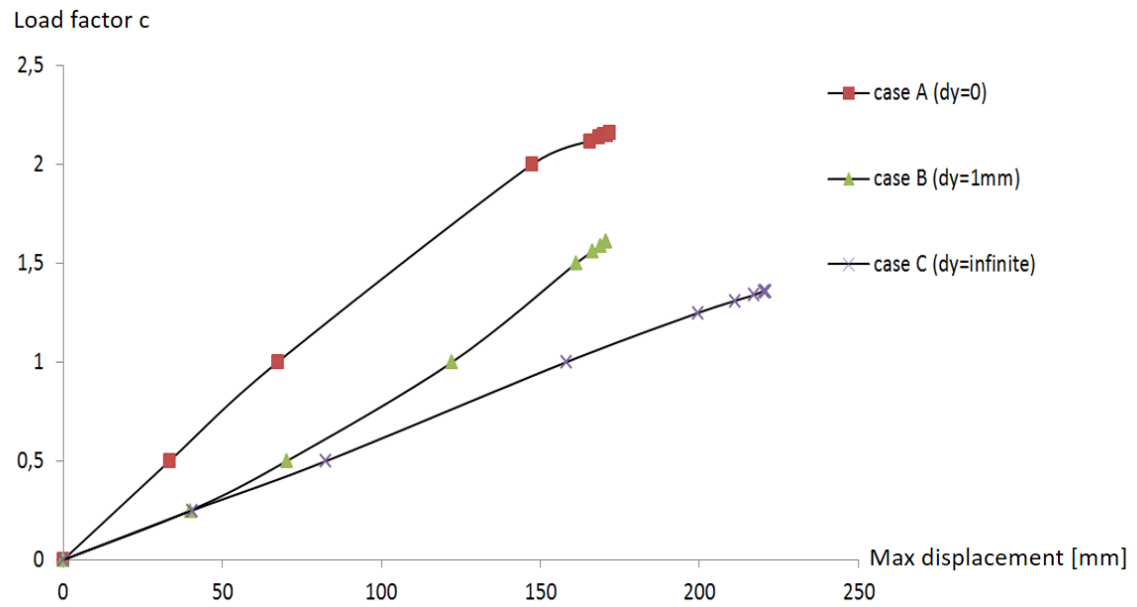


Figure 12.5: Limit load analyses of the three structures with three different settings of gap width

## Chapter 13

### Pre-fabrication and Erection

#### 13.1 Geometric compatibility for installation

For a plate situated in the zone of positive Gaussian curvature, the surfaces of gap\_x are defined as being perpendicular to the local x-axis, and the surfaces of gap\_y are defined as being perpendicular to the local y-direction (Fig 13.1). If the plate is installed along its normal axis from the outside of the surface, no geometrical incompatibility will occur, and no special installation sequence is required.

For a plate situated in the zone of negative Gaussian curvature, a special installation sequence with other plates is needed. Moreover, the orientation of gap surfaces also needs to be slightly adjusted: the surfaces of gap\_x at the left edge of the plate are defined as being parallel with the norm of the plate and the local y-direction (Figure 13.2), and the surfaces of gap\_x at the right edge of the plate are defined as being parallel with the norm of the adjacent plate and the local y-direction. The remaining surfaces of other gaps are defined as in the case of positive Gaussian curvature. With these definitions, no geometrical incompatibility occurs if the plate is installed along its norm from the outside of the surface and in a specific order from the plate on the right to the plate on the left.

#### 13.2 Erection Process

Each plate was prefabricated by a timber construction company. First, the polygonal plates were cut out from rectangular plywood panels by a CNC machine; then, with the help of a robot-arm, the finger joints and the brackets for screws were milled out. The guiding holes for screws were subsequently drilled by the robot-arm. The gap width between the panels was set to be 1 mm (both for  $d_x$  and  $d_y$ ), which was taken into consideration during the panel fabrication and the installation.

On the construction site, the wooden sills were positioned by adjusting their upper faces in the same horizontal plane and aligning their outer faces to the layout contour. They were then fastened onto the concrete foundation with concrete anchors.

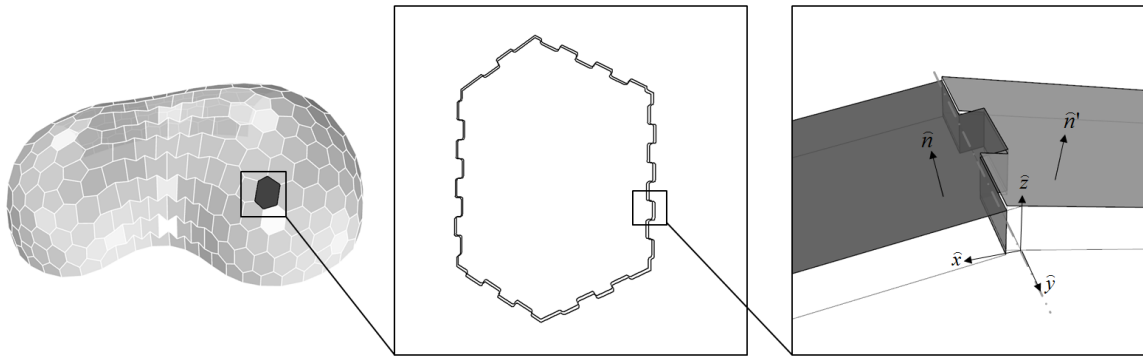


Figure 13.1 Left: A plate located in the zone with a positive Gaussian curvature. Right: The surfaces of gap\_x are perpendicular to the local x-direction, and the surfaces of gap\_y are perpendicular to the local y-direction, where the local z-direction is defined by the sum of the norms of the two plates,  $\hat{n}$  and  $\hat{n}'$ ,  $\hat{y}$  is parallel with the edge of the plate, and  $\hat{x}$  is defined as  $\hat{y} \times \hat{z}$ .

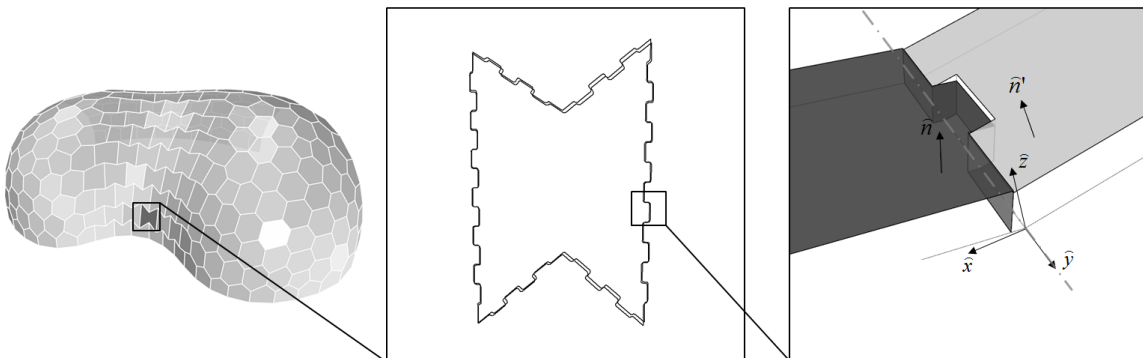


Figure 13.2 Left: A plate located in the zone with a negative Gaussian curvature. Right: The surfaces of gap\_x are parallel with  $\hat{y}$  and  $\hat{n}$ , and the surfaces of gap\_y are perpendicular to  $\hat{y}$ .

The installation of the plates started from the plate at the corner of the building and then proceeded, row by row, until the last plate was installed. A temporary supporting frame work with the section geometry of the inner surface of the plate shell was used to facilitate the correct positioning of each plate during assembly (Figure 13.3 Left).

The remaining parts of the building were installed in the following order: the vapor barrier, the prefabricated modules of thermal isolation and waterproofing (Figure 13.2 Right), the timber roof, columns, and the glass façade.



Figure 13.3 Top: Temporary supporting frame work with the section geometry of the inner surface of the plate shell is used here to facilitate the correct positioning of each plate during installation. Bottom: The prefabricated modules of thermal isolation and waterproofing are installed.



## PART IV CONCLUSION

## Chapter 14

### CONCLUSION AND FUTURE WORK

For reducing the manufacturing cost of timber shells, two strategies, actively bent grid shells and segmental plate shells, are investigated in this research. Both of these construction strategies do not require bending stiff joints and thus largely reduce the joint complexity and the manufacturing cost.

The advantages brought from these construction strategies are all related to their special geometries: An actively bent grid shell is made of initially straight rods and thus needs a geometry which could reduce the pre-stresses due to bending. A segmental plate shell relies on the trivalent pattern to provide stability and thus needs a trivalent polyhedral geometry. All these special geometries could only be found by corresponding form-finding techniques. The cost of having these advantages is thus the extra knowledge and techniques of form-finding.

In this this thesis, we show that DR is capable of being the fundamental base for developing the form-finding techniques for both shell structures. We also show that the structural analysis could also be accomplished under the scheme of DR. This is because that form-finding and structural analysis are essentially the same. They are all simulation results of static equilibrium. The only difference between them is at the stiffness properties of the considered systems.

#### 14.1 Conclusion of Part II

A general scheme for the form-finding and analysis of elastic grid shells is presented in Part II. Within the scheme, structure models are able to interact with the geometric constrains whether by the projection method or the force method. Our scheme can thus be utilized by designers as a powerful tool to consider the material aspect and simultaneously satisfying geometric design requirements.

In chapter 4, we showed that DR is a reliable and convenient method for simulating elastic beams which undergo large rotations and displacements. We proposed new integration formulas for the rotational movement, which are expressed in a central difference form which makes the formula easier to be used and comprehended. With the rotational degrees of freedom, the Euler-Bernoulli beam element is then able to be integrated in our scheme such that biaxial bending and torsion mechanisms

can be considered. Different from some previous research, where the inertia is expressed as a 3x3 matrix, the inertia in our scheme is expressed as a scalar. We showed the necessity of using a scalar inertia and pointed out that if a matrix term is used, the integration shall diverge. This is because that if a matrix inertia is used, the rotation equation of motion stays no longer linear (analogical to the translation equation of motion) and the second term in the rotation equation of motion should be considered. With respect to numerical stability and efficiency, we demonstrate how to use a mass matrix to accelerate the slow motion caused by the low stiffness in the transverse direction. Furthermore, we point out that if both the optimized mass matrix and the optimized scalar inertia are applied, the transient positions and orientations will become time-increment independent.

In Chapter 5, we showed that the ratio between the axial stiffness and transverse stiffness of beam-ends has a large influence to the convergence rate and the best convergence rate occurs when the ratio approaches the value of one. Using this character, a new method is proposed. The method uses fictitious elements of the proper stiffness ratio to simulate the actual systems. The convergence rate is thus optimized.

In chapter 6, we showed an easy way to assign the pre-stresses out of a bent or twisted geometry. This method expands the choice of a starting geometry. We can conveniently select a starting geometry either that is closer to an equilibrium state or that facilitates the assignment of constraints. We are no longer restricted from beginning in an unstrained state. This freedom enables us to begin with a geometry derived from other methods, such as the force density or compass method. To simulate different joint types for elastic grid shells, we presented a new way of node couplings, which is based on an equilibrium configuration. A hinge can be simulated with translation couplings, whereas a revolute joint can be simulated with additional rotation couplings.

In Chapter 7, we presented two major ways to enforce geometric constraints to elastic grids: the projection method and the force method. According to our research, the first is regarded as a more efficient way to apply geometric constraints. We pointed out that the mass matrix will induce numerical instability with the projection method and need corresponding adjustments. We also found that if the initial pre-stress is excessive, the system will be easily trapped in a local potential well and the solution is to apply a greater transverse stiffness in the beginning and gradually reduce it to the original value. Besides, we demonstrated that the bending mechanism can play an even more



important role in form-finding; it can be used to generate smooth linear or surface patterns from kinked geometries without the help of target surfaces.

## **14.2 Conclusion of Part III**

A new construction type of timber shells, named segmental timber plate shells, is proposed in Part III. The geometric properties and the corresponding form-finding methods are studied. An innovative connection for free-form plate structures, which requires a relative thin thickness for connections, is also presented. The analysis and the realization of the Forstpavillion project shows a great potential of this new construction type.

In chapter nine, a simplified model is introduced to estimate the bending stiffness of trivalent patterns. The result shows that the values of bending stiffness of the hexagonal patterns and of the star-like patterns are similar. And for each pattern the bending stiffness in the two major directions are also similar. These patterns have thus a quite similar performance in terms of bending stiffness. However, when it comes to the transfer performance of in-plane forces, one direction of a pattern is always better than the other direction. Therefore, if the major direction of in-plane forces is known, there is a preference of how to orientate the plate pattern direction.

In chapter ten, an improved form-finding method is introduced. New mechanisms are added to the method such that the smoothness and the direction of the triangulation could be better controlled. The results from this improved method are not always satisfying. Usually, a satisfied form could only be found after many times of changing initial settings, including the initial triangulation and the boundary condition.

In chapter eleven, we propose a practical connection design for thin plate structures. This connection is composed of finger joints and crossing screw joints that could be easily fabricated and installed. The analysis shows that the application of finger joints effectively increases the in-plane stiffness and the strength capacity of the connections.

In chapter twelve, the structural analysis of Forstpavillion is presented. We have learned that, when determining the shell thickness, the minimum space for the connection design is more critical than other issues because of the least distance required by the building codes. The result also shows that

the gaps between plates weakens the global structure. If these gaps are inevitable, the benefit brought by the finger joint is limited.

In chapter thirteen, the geometric compatibility and the installation sequence are illustrated. The normal directions of plate edges and the installation sequence are carefully designed for the anticlastic areas, otherwise a 50 mm thick plate could not fit into the boundaries which is defined by the built part. The existing of 1mm-wide caps is proved to be very helpful to speed up the installation process because it covers the variations caused by shrinkage and errors.

### **14.3 Future work**

#### A common scheme for beam systems, quad systems and the mixture

The program we developed in this research supports the form-finding of beam systems (grid shells) and quad systems (plate shells). However, for the structural analysis, it supports only beam systems. It would be more powerful if it could support the structural analysis of quad systems. A larger group of actively bent structures, which are made of plate structures, could then be analyzed and geometrically processed under the same scheme. The pre-stress process would also be easier as what we have shown for the actively bent grid shells.

#### FEDR in the application of interaction design

FEDR is robust to deal with the difficult situation where the initial state of a bending active system is highly distorted and far away from an equilibrium. It converges to the neighborhood of the exact solution rapidly and the rest steps are used for increasing the solution precision. This would be a very good property when used in interaction design because it is stable and fast to get a first result, and in the same time it is always toward the exact solution. In the future, we would try to integrate an interactive user interface into our program.

### Innovative erection process of elastic grid shells

The existing erection methods are not satisfying. When working with the existing erection methods, structure designers need to use a large number of specialized scaffolds to impose out-of-plane forces on grid nodes during formation process, which largely reduce the deployment capability of grid shells. Besides, the intermediate states between the initial geometry (plane grid) and the final geometry are still difficult to define. The existing methods introduced so far are not satisfying. An improper geometry of intermediate state will induce large stresses in elastic members and cause breakages.

In facing with this problem, we may try to define a series of intermediate states by observing the relaxation process of a grid shell from a curved geometry to a plane grid. These intermediate states could possibly be used as a clear path of how to pre-stress the grid during the formation/erection process.

### Kinetic grid shells

An elastic grid can adopt many different shapes, and thus it should be possible to transform from one shape to another, making a kinetic grid shell possible. We would like to ask what the controlling process is and if it is possible to complete the transformation by applying only in-plane forces. Different shapes of a kinetic grid structure can be defined by different target surfaces, and our scheme could be used to find the grid patterns that have the same grid configurations and supporting conditions according to these target surfaces. If a smooth transformation between the target surfaces are known, we could solve the transient states of grid patterns according to these surfaces. And with the information of the transient states, a kinetic process could be fully described.

### Construction alternative of segmental plate shells for larger scale

The segmental plate system proposed in this research is using 50mm thick plywood panels as the fundamental structure. However, this may not be the most economic and structurally efficient way when the shell scale goes larger. A composite plate system, such as a sandwich system, might be a

good solution. It could reduce the structural weight and be easier to strengthen the connectivity at edges. It is also interesting to know what is the span limit of this type of structure.

#### Ways of filling

Gaps between segmental plates are necessary for installation reasons. However, the exist of gaps weakens the structure. This would not be a problem if the gaps are filled after installation. An ideal way of filling should be easy to apply and, in the same time, bring no damage to the appearance.

## Bibliography

- [1] T. Herzog, J. Natterer and M. Volz, *Holzbauatlas Zwei*, 2001.
- [2] C. J. Chen, T. L. Lee and D. S. Jeng, "Finite element modeling for the mechanical behavior of dowel-type timber joints," *Computers & structures*, pp. 81(30), 2731-2738, 2003.
- [3] B. H. Xu, M. Taazount, A. Bouchaïr and P. Racher, "Numerical 3D finite element modelling and experimental tests for dowel-type timber joints," *Construction and building materials*, pp. 23(9), 3043-3052, 2009.
- [4] K. U. Gliniorz, K. M. Mosalam and J. Natterer, "Modeling of layered timber beams and ribbed shell frameworks," *Composites Part B: Engineering*, pp. 33(5), 367-381, 2002.
- [5] J. Lienhard, S. Schleicher and J. Knippers, "Bending-active structures—Research pavilion ICD/ITKE," in *Proceedings of the International Symposium of the IABSE-IASS Symposium*, 2011.
- [6] W. Kübler, "Das neue Elefantenhaus im Zoo Zürich," *Bautechnik*, pp. 91(1), 51-57, 2014.
- [7] B. D'Amico, A. Kermani and H. Zhang, "Form finding and structural analysis of actively bent timber grid shells," *Engineering Structures*, pp. 81, 195-207., 2014.
- [8] J. M. Li and J. Knippers, "Segmental Timber Plate Shell for the Landesgartenschau Exhibition Hall in Schwäbisch Gmünd—the Application of Finger Joints in Plate Structures," *International Journal of Space Structures*, pp. 30(2), 123-139, 2015.
- [9] C. Douthe and O. Baverel, "Design of nexorades or reciprocal frame systems with the dynamic relaxation method," *Computers & Structures*, pp. 87(21), 1296-1307, 2009.
- [10] J. M. Li and J. Knippers, "Form-finding of grid shells with continuous elastic rods," in *Proceedings of the International Symposium of the IASS-APCS Symposium*, 2011.
- [11] P. Block, M. DeJong and J. Ochsendorf, "As hangs the flexible line: Equilibrium of masonry arches," *Nexus Network Journal*, pp. 8(2), 13-24, 2006.
- [12] C. Müller, *Holzleimbau*, Birkhauser, 2000.

- [13] S. Chow, "Adhesive developments in forest products," *Wood Science and Technology*, pp. 17(1), 1-11, 1983.
- [14] E. Schatzberg, "Ideology and technical choice: the decline of the wooden airplane in the United States, 1920-1945," *Technology and Culture*, pp. 35(1), 34-69, 1994.
- [15] F. Otto, E. Schauer, J. Hennicke and T. Hasegawa, "IL 10 Gitterschalen / Grid Shells," Stuttgart, Germany, 1974.
- [16] E. Happold and W. I. Liddell, "Timber lattice roof for the Mannheim Bundesgartenschau," *The structural engineer*, pp. 53(3), 99-135, 1975.
- [17] J. Stalnaker and E. Harris, *Structural design in wood*, Springer Science & Business Media, 1997.
- [18] C. Robeller, *Integral mechanical attachment for timber folded plate structures*, 2015.
- [19] R. Magna, M. Gabler, S. Reichert, T. Schwinn, F. Waimer, A. Menges and J. Knippers, "From nature to fabrication: biomimetic design principles for the production of complex spatial structures," *International Journal of Space Structures*, pp. 28.1: 27-40, 2013.
- [20] S. Bechert, J. Knippers, O. D. Krieg, A. Menges, T. Schwinn and D. Sonntag, "Textile Fabrication Techniques for Timber Shells: Elastic Bending of Custom-Laminated Veneer for Segmented Shell Construction Systems," in *Advances in Architectural Geometry*, 2016.
- [21] M. F. Ashby and D. Cebon, "Material selection in mechanical design," *Le Journal de Physique IV*, pp. 3, C7-1, 1993.
- [22] E. Popov, "Geometri Approach to Chebyshev Net Generation Along an Arbitrary Surface Represented By NURBS," in *International Conference Graphicon 2002*, Russia, 2002.
- [23] L. Du Peloux, J. F. Caron, F. Tayeb and O. Baverel, "The ephemeral cathedral of Créteil: a 350m<sup>2</sup> lightweight structure made of a GFRP composite gridshell.," in *19èmes Journées Nationales sur les Composites*, 2015.
- [24] R. Graefe, "Zur formgebung von bogen und gewölben," *Architectura*, pp. 16, 50-67, 1986.
- [25] M. R. Barnes, "Form finding and analysis of tension structures by dynamic relaxation," *International journal of space structures*, pp. 14(2), 89-104, 1999.
- [26] S. M. L. Adriaenssens and M. R. Barnes, "Tensegrity spline beam and grid shell structures," *Engineering structures*, pp. 23(1), 29-36, 2001.

- [27] C. Douthe, O. Baverel and J. F. Caron, "Form-finding of a grid shell in composite materials," *Journal-International association for shell and Spatial Structures*, pp. 150, 53.
- [28] L. Du Peloux, F. Tayeb, O. Baverel and J. F. Caron, "Faith can also move composite gridshells," in *IASS Symposium 2013*, 2013.
- [29] L. Bouhaya, O. Baverel and J. F. Caron, "Mapping two-way continuous elastic grid on an imposed surface: Application to grid shells.," in *IASS Symposium*, Valencia, 2009.
- [30] T. H. H. Pian and A. Balmer, "Dynamic buckling of a circular ring constrained in a rigid circular surface," in *In Dynamic Stability of Structures: Proceedings of an International Conference Held at Northwestern University*, 1965.
- [31] H.-J. Schek, "The force density method for form finding and computation of general networks.," *Computer methods in applied mechanics and engineering*, pp. 3.1: 115-134, 1974.
- [32] M. Hazewinkel, ed., "Rotation", *Encyclopedia of Mathematics*, Springer, 2001
- [33] Y. B. Yang and S. R. Kuo, *Theory and analysis of nonlinear framed structures*, 1994.
- [34] W. McGuire, R. H. Gallagher and R. D. Ziemian, *Matrix structural analysis*, 2000.
- [35] A. S. Day, "An introduction to dynamic relaxation," *The Engineer*, pp. 219:218-221, 1965.
- [36] D. Wakefield, *Dynamic relaxation analysis of pre-tensioned networks supported by compression arches*, (Doctoral dissertation, City University London), 1980.
- [37] R. G. Sauvé and D. R. Metzger, "Advances in Dynamic Relaxation Techniques for Nonlinear Finite Element Analysis," *Journal of Pressure Vessel Technology*, pp. 117: 170-176, 1995.
- [38] J. O. Hallquist, *LS-DYNA theory manual*, Livermore software Technology corporation, 2006.
- [39] S. Adriaenssens, M. Barnes and C. Williams, "A new Analytic and Numerical basis for the Form-finding and Analysis of Spline and Grid-shell," in *Computing Developments in Civil and Structural Engineering*, Civil-Comp Press, 1999, pp. 83-91.
- [40] C. Douthe, O. Baverel and J. F. Caron, "Form-finding of a grid shell in composite materials," *Journal-International association for shell and Spatial Structures*, pp. 150, 53, 2006.

- [41] M. R. Barnes, S. Adriaenssens and M. Krupka, "A novel torsion/bending element for dynamic relaxation modeling," *Computers & Structures*, pp. 119, 60-67, 2013.
- [42] C. Williams. [Online]. Available: <http://people.bath.ac.uk/abscjkw/>.
- [43] S. M. L. Adriaenssens, Stressed spline structures, (Doctoral dissertation, University of Bath), 2000.
- [44] M. Aberle, The nonlinear analysis of shear-weak gridshells, (Doctoral dissertation, University of Cambridge), 2001.
- [45] J. M. Li and J. Knippers, "Rotation formulations for dynamic relaxation—with application in 3D framed structures with large displacements and rotations," in *IASS-APCS Symposium*, 2012.
- [46] L. Du Peloux, F. Tayeb, B. Lefevre, O. Baverel and J. F. Caron, "Formulation of a 4-DoF torsion/bending element for the formfinding of elastic gridshells," in *IASS Symposium*, 2015.
- [47] P. Krysl and L. Endres, "Explicit Newmark/Verlet algorithm for Time Integration of the Rotational Dynamics of Rigid Bodies," *International journal for numerical methods in engineering*, pp. 62.15: 2154-2177, 2005.
- [48] K. J. Bathe, Finite element procedures, 2006.
- [49] K. J. Bathe and S. Bolourchi, "Large displacement analysis of three-dimensional beam structures," *International Journal for Numerical Methods in Engineering*, pp. 14(7), 961-986, 1979.
- [50] M. A. Crisfield, "A consistent co-rotational formulation for non-linear, three-dimensional, beam-elements," *Computer methods in applied mechanics and engineering*, pp. 81(2), 131-150, 1990.
- [51] A. Ibrahimbegović, F. Frey and I. Kožar, "Computational Aspects of Vector-like Parameterization of Three-dimensional Finite Rotations," *International Journal for Numerical Methods in Engineering*, pp. 38(21), 3653-3673, 1995.
- [52] S. M. L. Adriaenssens and M. R. Barnes, "Tensegrity spline beam and grid shell structures," *Engineering structures*, pp. 23(1), 29-36, 2001.
- [53] J. Lienhard, H. Alpermann, C. Gengnagel and J. Knippers, "Active bending, a review on structures where bending is used as a self-formation process," *International Journal of Space Structures*, pp. 28(3-4), 187-196, 2013.



- [54] J. M. Li and J. Knippers, "Designing Regular and Irregular Elastic Gridshells by Six DOF Dynamic Relaxation," in *Proc Int Conf of the Design Modeling Symposium Berlin*, Berlin, 2013.
- [55] J. Truco and S. Felipe, "HybGrid- Form generation and form finding of adaptable structures," in *Architectural Design (Emergent Technologies and Design)*, 2004, pp. 74(3):62-63.
- [56] L. Blandini, *Structural use of adhesives in glass shells*, Verlag Grauer, 2005.
- [57] A. Bagger, *Plate shell structures of glass*, Technical University of Denmark (DTU), 2010.
- [58] H. Almegaard, A. Bagger, J. Gravesen, B. Jüttler and Z. Šír, "Surfaces with piecewise linear support functions over spherical triangulation," in *IMA International Conference on Mathematics of Surfaces*, 2007.
- [59] R. La Magna, F. Waimer and J. Knippers, "Nature-inspired generation scheme for shell structures," in *IASS-APCS Symposium 2012*.
- [60] T. Wester, "Nature teaching structures," . *International Journal of Space Structures*, pp. 17(2-3), 135-147, 2002.
- [61] F. A. Veer, J. Wurm and G. J. Hobbelman, "The design, construction and validation of a structural glass dome," in *Proceedings of the Glass Processing Days. Poster, 12.*, 2003.
- [62] O. Ellers, A. S. Johnson and P. E. Moberg, "Structural strengthening of urchin skeletons by collagenous sutural ligaments," in *The Biological Bulletin*, 1998.
- [63] W. Wang, Y. Liu, D. Yan, B. Chan, R. Ling and F. Sun, "Hexagonal meshes with planar faces," Dept. of CS, HKU, Tech. Rep., 2008.
- [64] H. Pottmann, C. Jiang, M. Höbinger, J. Wang, P. Bompas and J. Wallner, "Cell packing structures," *Computer-Aided Design*, pp. 60, 70-83, 2015.
- [65] C. Troche, "Planar hexagonal meshes by tangent plane intersection," in *Advances in architectural geometry*, 2008.
- [66] H. Zimmer, M. Campen, R. Herkrath and L. Kobbelt, "Variational tangent plane intersection for planar polygonal meshing," in *Advances in Architectural Geometry*, Wien, 2012.
- [67] Y. Li, Y. Liu and W. Wang, "Planar Hexagonal Meshing for Architecture," *IEEE Transactions on Visualization and Computer Graphics*, pp. 21(1):95-106, 9 2015.

- [68] A. Vaxman and M. Ben-Chen, "Dupin meshing: A parameterization approach to planar hex-dominant meshing," Tech. Rep. CS-2015-01, 2015.
- [69] H. J. Blass and I. Bejtka, *Selbstbohrende Holzschrauben und ihre Anwendungsmöglichkeiten*. Holzbau Kalender, 2004.
- [70] O. Kelly, R. Harris and M. Dickson, "The construction of the downland gridshell," *The Structural Engineer*, pp. 79(17), 25-33., 2001.
- [71] J. Rowe and H. R., "The structural engineering of the Downland Gridshell," in *IABSE Conference: Innovative Wooden Structures and Bridges*, Lahti, Finland, 2001.
- [72] Y. B. Yang and S. R. Kuo, *theory and analysis of nonlinear framed structures*, 1994.
- [73] J. Schlaich, H. Schober and K. Kürschner, "New Trade Fair in Milan—Grid Topology and Structural Behaviour of a Free-Formed Glass-Covered Surface," *International Journal of Space Structures*, pp. 20(1), 1-14, 2005.
- [74] M. u. N. B.-W. LUBW (Landesanstalt für Umwelt, "WALD Einführung WALD," 2014. [Online]. Available: [http://www.lubw.baden-wuerttemberg.de/servlet/is/41578/11\\_wald.pdf?command=downloadContent&filename=11\\_wald.pdf](http://www.lubw.baden-wuerttemberg.de/servlet/is/41578/11_wald.pdf?command=downloadContent&filename=11_wald.pdf).
- [75] O. D. Krieg, T. Schwinn, A. Menges, J. M. Li, J. Knippers, A. Schmitt and V. Schwieger, "Biomimetic lightweight timber plate shells: Computational integration of robotic fabrication, architectural geometry and structural design," in *Advances in Architectural Geometry 2014*.
- [76] S. I. G. & C. KG, European Technical Approval ETA-12/0114: Self-tapping screws for use in timber, ETA-Denmark A/S, 2013.
- [77] D. Johnson and D. M. Brotton, "A finite deflection analysis for space structures," in *International Conference on Space Structures*, 1966.
- [78] C. Jiang, C. Tang, A. Vaxman, P. Wonka and H. Potmann, "Polyhedral Patterns," *ACM Transactions on Graphics*, p. 34(6), 11 2015.
- [79] E. L. Hernández, C. Gengnagel, S. Sechelmann and T. Rörig, "On the materiality and structural behaviour of highly-elastic gridshell structures," in *Computational Design Modelling*, 2011.

- [80] R. Harris and J. Rowe, "The structural engineering of the downland gridshell," in *IABSE Symposium Report. International Association for Bridge and Structural Engineering*, 2001.
- [81] H. & C. AG, Allgemeine bauaufsichtliche Zulassung Z-9.1-841 "Sperrholz aus Buchefurnieren", 2013.
- [82] A. h. t. f. l. E. o. m. arches, "Block, P.; DeJong, M.; Ochsendorf, J.," *Nexus Network Journal*, pp. 8(2), 13-24, 2006.
- [83] "The Spruce Goose," [Online]. Available: <http://www.evergreenmuseum.org/the-spruce-goose>.

## List of Abbreviations

DOF degrees of freedom  
DR dynamic relaxation  
FEA finite element analysis  
FEDR fictitious element dynamic relaxation  
NR Newton-Raphson method  
NURBS non-uniform rational B-spline  
P-Hex Mesh planar hexagon mesh

## List of Notations

- $\vec{d}$  node position vector  
 $\mathbf{R}$  node orientation, which is represented by a 3x3 matrix  
 $\mathbf{R}_B$  beam orientation  
 $\mathbf{R}_E$  beam-end orientation  
 $\mathbf{R}_T$  transformation matrix  
 $\hat{x}, \hat{y}, \hat{z}$  three local directions of a node orientation  
 $\hat{x}_E, \hat{y}_E, \hat{z}_E$  three local directions of a beam-end orientation  
 $\hat{x}_B, \hat{y}_B, \hat{z}_B$  three local directions of a beam orientation  
 $\vec{d}$  node position  
 $\Delta_x, \Delta_y, \Delta_z$  displacements in three local directions  
 $\theta_x, \theta_y, \theta_z$  angles of rotation in three local directions  
 $\Delta\vec{\theta}$  rotation vector  
 $\Delta\theta$  rotation angle (absolute value of a rotation vector)  
 $\vec{r}$  internal forces (end reactions) of a beam element  
 $f_x, f_y, f_z$  translation forces in three local directions  
 $\tau_x, \tau_y, \tau_z$  rotation forces (torques) in three local directions  
 $\mathbf{k}$  stiffness matrix  
 $\vec{q}$  general displacement in local coordinates  
 L beam length  
 $L_0$  unstrained beam length  
 $L_s$  strained beam length  
 E elastic modulus  
 G shear modulus  
 U strain energy  
 $E_K$  kinetic energy  
 R radius  
 $\vec{F}$  translation force in global coordinates  
 M mass  
 $\mathbf{M}$  Mass matrix  
 $\vec{a}$  acceleration in global coordinates  
 $\vec{v}$  velocity in global coordinates  
 $\vec{T}$  rotation force/torque in global coordinates  
 $\mathbf{A}$  skew-symmetric matrix  
 $\vec{\omega}$  angular velocity in global coordinates  
 $\vec{\omega}'$  angular velocity in local coordinates

$\bar{\alpha}$  angular acceleration in global coordinates

$\bar{\alpha}'$  angular acceleration in local coordinates

$M_\tau$  moment of inertia in global coordinates

$n$  number of time step

$\Delta t$  time interval of a time step

$K$  node direct stiffness

$\alpha$  convergence parameter

$I$  second moment of inertia of a beam section

$A$  area of a beam section

$C_T$  translation stiffness ratio

$C_R$  rotation stiffness ratio

$b$  width of a rectangular beam section

$h$  height of a rectangular beam section

$\hat{Z}$  global z-direction

$\hat{n}$  normal direction



## Curriculum Vitae

2014

structural engineer at Knippers Helbig Consulting Engineers, Germany

2013-2014

research and structural design for Forstpavillion of Landesgartenschau in Schwäbisch Gmünd

2010-2014

PhD candidate, scientific researcher and employee at the Institute of Building Structures and Structural Design (ITKE), University of Stuttgart, Germany

2008-2010

structural engineer at Knippers Helbig Consulting Engineers, Germany

2006 - 2007

Project researcher, Graduate Institute of Urban Design and Architecture, National University of Kaohsiung, Taiwan

2003 - 2006

founder of Living-with-Wood Community, Taiwan

leader of design-build projects: Pavilion Design commissioned by Jiang-Shi B&B, Commercial Furniture Design commissioned by Homemakers Union, Art Studio Renovation commissioned by Tsing Hua University

2003 - 2006

master of science, studies of physics and civil engineering at National Taiwan University, Taiwan

2001 - 2003

military service

1999 - 2003

architectural design and cabinet making apprenticeship

1995 - 2001

bachelor of Science, Dept. of Physics, National Tsing Hua University, Taiwan

1977

born in Taipei, Taiwan





## Zusammenfassung

Kontinuierlich gekrümmte Schalenstrukturen sind aufgrund des Lastabtrags vorwiegend über Membrankräfte hocheffiziente Tragwerke; die bauliche Umsetzung hingegen ist schwierig und kostenintensiv. Biegeaktive Gitterschalen oder segmentierte Plattenschalen stellen Alternativstrukturen dar. Bei ersteren wird eine kontinuierlich gekrümmte Form mit Vierecksmaschen aus aktiv gebogenen Balken erzeugt, wodurch die Komplexität der Knotenverbindungen reduziert wird. Letztere nutzen die den trivalenten, räumlichen Geometrien eigene Stabilität zur Erzeugung eines Schalentragswerks mit biegeweichen Kantenverbindungen. In beiden Fällen können die Herstellungskosten gegenüber klassischen Schalenstrukturen erheblich gesenkt werden, weshalb diese Typen Thema der vorliegenden Forschungsarbeit sind.

Forschungsbedarf besteht insbesondere bei numerischen Formfindungsmethoden und -werkzeugen, welche das tatsächliche Verhalten sowohl biegeaktiver Gitterschalen als auch segmentierter Plattenschalen vollständig abbilden vermögen. Basis hierfür ist in dieser Arbeit die wichtige Methode der dynamischen Relaxation (DR), für welche ein neuer Gleichungslöser unter Einschluss des Balkenverhaltens mit Biegung und Torsion entwickelt wurde. Die vorliegende Forschung belegt, dass mit dieser neuen Methode nicht nur die Formfindung, sondern auch geometrisch nichtlineare Analysen möglich sind.

Die Dissertation besteht aus vier Teilen: Nach der Einleitung (Abschnitt I) werden in den Teilen II und III die entwickelten Analyse- und Formfindungsmethoden anhand des Beispiels von zwei Holzschalenstrukturen als segmentierte Plattenschale und als biegeaktive Gitterschale dargelegt. Der vierte Teil bietet eine Zusammenfassung der Ergebnisse und einen Ausblick.

